Dynamics and Control of Newtonian and Viscoelastic Fluids

A DISSERTATION
SUBMITTED TO THE FACULTY OF THE GRADUATE SCHOOL
OF THE UNIVERSITY OF MINNESOTA
BY

Binh K. Lieu

IN PARTIAL FULFILLMENT OF THE REQUIREMENTS
FOR THE DEGREE OF
Doctor of Philosophy

August 2014

Dynamics and Control of
Newtonian and Viscoelastic Fluids

Copyright © 2014

by

Binh K. Lieu

ALL RIGHTS RESERVED

To Ling, our parents, and my sister

Acknowledgements

I cannot begin to thank the many people who helped me throughout my graduate studies, but let me first express my deepest gratitude to my graduate advisor Professor Mihailo R. Jovanović for being an outstanding teacher and a wonderful friend to me during my study at the University of Minnesota. My work and achievements have been a direct consequence of his excellent guidance. His ingenuity, patience, open-mindedness have given me the inspiration to work hard and find my true potential. His kindness and friendship have helped me shape the character I am today. It has been my greatest honor and privilege to have work with you, Mihailo. Thank you for everything, especially all the fun time playing tennis with you.

I would also like to express my gratitude to Professor Satish Kumar from the Department of Chemical Engineering and Material Sciences. My discussions with him have sparked many new research topics in the area of viscoelastic fluids which are presented in Part II of this dissertation.

Many thanks to Professor Tryphon Georgiou. I have benefited immensely from my interactions with him and from the classes taught by him. Professor Tryphon Georgiou's classes on Linear Systems/Optimal Control and Nonlinear Systems have laid the foundation of the work presented in this dissertation. My gratitude extends to Professors Murti Salapaka and Mostafa Kaveh for serving on my dissertation committee.

It has been the greatest privilege to get to know and work with my office mates Rashad Moarref and Fu Lin. I am extremely grateful to Rashad who played a crucial role in the projects presented in Chapters 3 and 4 of this dissertation and to Mr. Fu for the many discussions on optimization and sparsity that led to Chapter 4. Thank you, Rashad and Mr. Fu, for all the good memories and fun times; both of you have made my graduate experience one of the greatest periods of my life.

I would also like to thank the rest of the members of the control research group: Neil Dhingra, Armin Zare, Xiaofan Wu, Eric Dahlberg, Lipeng Ning, Yong Xin Chen, Dr. Shahrouz Takyar, Dr. Xianhua Jiang, and Dr. Donatello Materassi. Thank you everyone for the many laughters, enriching discussions, and fun times. Guys and Gals, it has been my pleasure to have known you.

Special thanks to Spencer, Christine, and Lucas Chow for all their help over this past six years. I have been so blessed to have received your kindness and generosity. Thank you for always making Ling and I feel like we are part of your family.

I would like to thank my (outrageously large) family: Grandma and Grandpa; Aunt My and Uncle Jerry; Aunt Yen and Uncle Fat; Aunt Nikie and Uncle Jeremy; Aunt Hao and Uncle Cam; and cousins Justino, Dustino, Cassidy, and Desmond. Thank you for always believing in me and helping me through the tough times. I'm especially grateful to Aunts My, Yen, and Nikie for taking care of me throughout high school and college. This dissertation would not have been possible without your continuous support.

My warmest thanks to my parents and sister. My mom and dad have always taught me to work hard and pursue my dreams and their sacrifices have given me the opportunity to do just that. I owe my success to my sister who without doubt believed in me even during times when no body does. Thank you mom, dad, and Ai for always being there for me. You made me who I am today.

I would also like to thank my mother-in-law, Yan Ping Zhang, for always being there for Ling and me. I think it was your cooking that kept Ling and I together for all these years. Without your help, Ling would have me out on the street.

Finally, I would like to thank the most important person in my life. Ling has been my best friend and the most loving wife throughout the years. This dissertation would not have been possible without her continuous support, understanding, and endless love. Her advice and guidance have helped me find my way when things seem lost. Her intellectual brilliance and hard working personality have inspired me to be the best in everything I do. Thank you Ling for lifting me up to be more than I can be.

Abstract

Transition to turbulence represents one of the most intriguing natural phenomena. Flows that are smooth and ordered may become complex and disordered as the flow strength increases. This process is known as transition to turbulence. In this dissertation, we develop theoretical and computational tools for analysis and control of transition and turbulence in shear flows of Newtonian, such as air and water, and complex viscoelastic fluids, such as polymers and molten plastics.

Part I of the dissertation is devoted to the design and verification of sensor-free and feedback-based strategies for controlling the onset of turbulence in channel flows of Newtonian fluids. We use high fidelity simulations of the nonlinear flow dynamics to demonstrate the effectiveness of our model-based approach to flow control design.

In Part II, we utilize systems theoretic tools to study transition and turbulence in channel flows of viscoelastic fluids. For flows with strong elastic forces, we demonstrate that flow fluctuations can experience significant amplification even in the absence of inertia. We use our theoretical developments to uncover the underlying physical mechanism that leads to this high amplification. For turbulent flows with polymer additives, we develop a model-based method for analyzing the influence of polymers on drag reduction. We demonstrate that our approach predicts drag reducing trends observed in full-scale numerical simulations.

In Part III, we develop mathematical framework and computational tools for calculating frequency responses of spatially distributed systems. Using state-of-the-art automatic spectral collocation techniques and new integral formulation, we show that our approach yields more reliable and accurate solutions than currently available methods.

Contents

Acknowledgements **iv**

Abstract **vi**

List of Tables **xii**

List of Figures **xiii**

1 Introduction **1**
- 1.1 Motivation . . . 1
- 1.2 Main topics of the dissertation . . . 3
  - 1.2.1 Model-based control of Newtonian fluids . . . 3
  - 1.2.2 Importance of roll and streak structure in transition and turbulence flows . . . 7
  - 1.2.3 Transition to turbulence in channel flows of viscoelastic fluids . . . 7
  - 1.2.4 Polymer induced drag reduction in turbulent channel flows . . . 10
  - 1.2.5 Computation of frequency responses of PDEs . . . 11
- 1.3 Dissertation structure . . . 12
- 1.4 Key contributions . . . 13

I Controlling the onset of turbulence in channel flows of Newtonian fluids **17**

2 Preliminaries: Incompressible channel flows of Newtonian fluids **18**
- 2.1 Navier-Stokes equations . . . 18
  - 2.1.1 Linearized NS equations . . . 19
  - 2.1.2 Evolution model . . . 20
- 2.2 Direct numerical simulations . . . 22
  - 2.2.1 Base-fluctuation decomposition . . . 22
  - 2.2.2 Time-stepping schemes . . . 23
  - 2.2.3 Tau-equations and influence-matrix method . . . 27

2.2.4 Boundary actuations 29

3 Controlling the onset of turbulence by streamwise traveling waves: direct numerical simulations 31
3.1 Introduction 31
3.2 Problem formulation and numerical method 33
3.2.1 Governing equations 33
3.2.2 Numerical method 34
3.2.3 Base flow and nominal net efficiency 35
3.3 Avoidance/promotion of turbulence by streamwise traveling waves . . . 38
3.3.1 Small initial energy 39
3.3.2 Moderate initial energy 41
3.3.3 Large initial energy 46
3.3.4 Energy amplification mechanisms 48
3.3.5 Flow visualization 50
3.4 Relaminarization by downstream waves 52
3.5 Concluding remarks 58

4 Optimal localized control of transitional channel flow 61
4.1 Introduction 61
4.2 Problem formulation 62
4.2.1 Governing equations 62
4.2.2 Actuation along the discrete lattice 64
4.3 Design of optimal localized feedback gains 65
4.3.1 Computation of the structured optimal feedback gains 68
4.4 Localized control of transition 69
4.4.1 Receptivity of the controlled flows 69
4.4.2 Direct numerical simulations 70
4.5 Concluding remarks 73

5 Dynamics of the roll and streak structure in transition and turbulence 74
5.1 Introduction 75
5.2 Modeling framework 76
5.3 Relation of 2D/3C and QL to SSST 77
5.4 Analysis of the models and prior results 79
5.5 Numerical Approach 80
5.6 Results 81
5.7 Concluding remarks 86

II Dynamics of transitional and turbulent channel flows of viscoelastic fluids **88**

6 Worst-case amplification of disturbances in inertialess Couette flows of viscoelastic fluids **89**
- 6.1 Introduction 89
- 6.2 The role of uncertainty: an illustrative example 92
- 6.3 Problem formulation 95
  - 6.3.1 Governing equations 96
  - 6.3.2 Model in the evolution form 98
  - 6.3.3 Spatio-temporal frequency responses 99
- 6.4 Frequency responses of 3D velocity fluctuations 102
- 6.5 Dynamics of streamwise-constant velocity fluctuations 105
  - 6.5.1 Dependence of worst-case amplification on We and L 106
  - 6.5.2 Dominant flow structures 112
  - 6.5.3 Physical mechanisms 114
- 6.6 Dynamics of streamwise-constant polymer stress fluctuations 116
- 6.7 Concluding remarks 120
- 6.8 Appendix: Underlying operators in 3D shear-driven channel flow of FENE-CR fluids 122
- 6.9 Appendix: Explicit scaling of worst-case amplification of streamwise-constant velocity fluctuations 123
- 6.10 Appendix: Frequency response operators from body forces to polymer stresses in streamwise-constant Couette flow of FENE-CR fluids 126

7 Slow-fast decomposition of an inertialess flow of viscoelastic fluids **127**
- 7.1 Introduction 127
- 7.2 Governing equations 128
- 7.3 Evolution equations and low-pass versions of the stream functions 131
- 7.4 Singular perturbation analysis of the 2D inertialess channel flow 134
  - 7.4.1 Singularly perturbed form of the evolution model 134
  - 7.4.2 Block-diagonal form: slow-fast decomposition of the evolution model 135
  - 7.4.3 Analysis of slow and fast subsystems 136
- 7.5 Frequency responses of a 2D inertialess flow of viscoelastic fluids 137
- 7.6 Concluding remarks 138
- 7.7 Appendix: System operators 139

8 Model-based analysis of polymer-induced drag reduction in turbulent channel flow **141**
- 8.1 Introduction 141
- 8.2 Problem formulation 143
  - 8.2.1 Governing equations 144

8.2.2 Mean flow equations 145
8.2.3 Mean flow analysis 146
8.3 Stochastically forced flow with polymers: fluctuation dynamics 150
8.4 Results and discussion 153
8.4.1 Drag reduction by polymers 154
8.4.2 Turbulent mean velocity and fluctuations' statistics 155
8.4.3 Contribution of fluctuations' statistics to mean polymer stresses, turbulent velocity, and drag 157
8.4.4 Energy amplification of velocity and polymer stress fluctuations . 160
8.5 Concluding remarks 163
8.6 Appendix: The underlying operators in a 3D pressure-driven channel flow of FENE-P fluids 166
8.7 Appendix: Mean flow equations with second-order statistics of flow fluctuations 169

III Computational tools for analysis of spatially distributed systems 170

9 Computation of frequency responses for linear time-invariant PDEs on a compact interval 171
9.1 Introduction 171
9.2 Motivating examples and problem formulation 174
9.2.1 Motivating examples 174
9.2.2 Problem formulation 177
9.3 Two point boundary value representations of $\mathcal{T}$, $\mathcal{T}^\star$, and $\mathcal{T}\mathcal{T}^\star$ 180
9.3.1 Representations of the frequency response operator $\mathcal{T}$ 180
9.3.2 Representations of the adjoint operator $\mathcal{T}^\star$ 182
9.3.3 Representations of $\mathcal{T}\mathcal{T}^\star$ 184
9.4 Computation of the largest singular value of $\mathcal{T}$ 185
9.4.1 An illustrative example 186
9.4.2 Integral form of a system of high-order differential equations . . 188
9.4.3 Integral form of a spatial state-space representation 191
9.5 Examples 192
9.5.1 Three-dimensional incompressible channel flows of Newtonian fluids 192
9.5.2 Inertialess channel flow of viscoelastic fluids 195
9.6 Concluding remarks 197
9.7 Appendix: Conversion to a spatial state-space realization 200
9.8 Appendix: Implementation of eigenvalue problems in integral formulation using Chebfun 201
9.9 Appendix: Representations of the frequency response operator for the linearized Navier-Stokes equations 206

9.10 Appendix: Representations of the frequency response operator for the inertialess channel flow of viscoelastic fluids 207
9.11 Appendix: Frequency response of an Euler-Bernoulli beam 208

References **212**

List of Tables

2.1 Time-stepping coefficients of the Crank-Nicolson/Adams-Bashforth and 3rd-order Runge-Kutta methods. 25

2.2 Time-stepping coefficients of the Adams-Bashforth/Backward-Differentiation (ABBDk) schemes. 26

3.1 The computational domain and spatial discretization considered in simulations of the uncontrolled flow, DTWs with ($c = 5$, $\omega_x = 2$, $\alpha = \{0.035, 0.050, 0.125\}$), and UTWs with ($c = -2$, $\omega_x = 0.5$, $\alpha = \{0.015, 0.050, 0.125\}$). Symbols identify the corresponding flow in figures that follow. The box sizes in the streamwise and spanwise directions are denoted by L_x and L_z, respectively. The number of grid points in the streamwise, wall-normal, and spanwise directions are represented by N_i, $i = \{x, y, z\}$, respectively. 35

3.2 Nominal results in Poiseuille flow with $R_\tau = 63.25$. The nominal flux, $U_{B,N}$, and skin-friction drag coefficient, $C_{f,N}$, are computed using the base flow described in Section 3.2.3. The produced power, $\%\Pi_{prod}$, required power, $\%\Pi_{req}$, and net power, $\%\Pi_{net}$, are normalized by the power required to drive the uncontrolled flow. The produced and net powers are computed with respect to the laminar uncontrolled flow. 37

3.3 Results of 3D simulations in Poiseuille flow with $R_\tau = 63.25$ for initial conditions of small, moderate, and large energy (respectively, $E(0) = 2.25 \times 10^{-6}$, $E(0) = 5.0625 \times 10^{-4}$, and $E(0) = 2.5 \times 10^{-3}$). The values of C_f, $\%\Pi_{prod}$, $\%\Pi_{req}$, and $\%\Pi_{net}$ correspond to $t = 1000$. For small initial energy, the produced and net powers are computed with respect to laminar uncontrolled flow; for moderate and large initial energies, they are computed with respect to turbulent uncontrolled flow. 39

6.1 Worst-case amplification of streamwise velocity fluctuations arising from the wall-normal and spanwise forces in the limit of infinitely large maximum extensibility of polymer chains L or infinitely large Weissenberg number We. 111

6.2 Worst-case amplification of τ_{13}, τ_{12}, and τ_{11} arising from d_2 and d_3 in the limit of infinitely large maximum extensibility or infinitely large Weissenberg number. 120

List of Figures

1.1 Visualization in a flat-plate boundary-layer flow of a Newtonian fluid [1]. In laminar flows flow patterns are very regular, and in turbulent flows they are complex and disordered. 1
1.2 (a) Transition from laminar to turbulence over an aircraft wing. Photo taken from efluids by Miguel Visbal. (b) The wake from upstream turbines affects those downstream of wind. 2
1.3 **Sensorless flow control strategies:** (a) Blowing and suction along the walls in the form of a streamwise traveling wave with α, ω_x, and c denoting the amplitude, frequency, and speed of the wave; (b) Transverse wall-oscillations with α and T denoting the amplitude and period of the oscillation. 4
1.4 **Controlling the onset of turbulence via streamwise traveling waves**: Energy amplification of the most energetic structures of the uncontrolled flow with Reynolds number $R = 2000$, in the presence of (a) upstream traveling waves; and (b) downstream traveling waves. The symbols ● and ■, respectively, denote ($c = -2$, $\omega_x = 0.5$) (as selected in [2]) and ($c = 5$, $\omega_x = 2$). Figures are taken from Moarref & Jovanović [3]. . . 5
1.5 (a) An array of distributed hot-film shear-stress sensors and wall-deformation actuators for feedback flow control [4]; (b) Sketch of a localized control strategy where the actuator placed at (r, s) uses information from only the nearest neighbors on the two-dimensional lattice. 6

1.6 Swirling flow and microfluidic channel experiments of Groisman and Steinberg. (a) A weakly inertial swirling flow between parallel discs considered in [5]. Flow of a Newtonian fluid is steady and ordered (laminar), with no structure to it. Flow of a viscoelastic fluid is complex and disordered with a broad range of spatial and temporal scales; flow resistance is increased 20 times compared to a Newtonian fluid. (b) A schematic drawing of a curvilinear channel used in the mixing experiment (top) and snapshots of mixing at different stages considered in [6]. If the liquids contain no polymer molecules (the viscous Newtonian solvent), the flow remains laminar; no mixing occurs and the two working fluids are identical, with a small amount of a fluorescent dye added to one of them. When small amount of high-molecular-weight polymers is added to a Newtonian fluid, the irregular 3D flow stirs the liquid (photos at $N = 8$ and 29) and provides efficient mixing. At the end of the channel, at $N = 54$, the dye distribution becomes rather homogeneous. 9
1.7 Demonstration of increase water throughput in fire hoses using polymer additives. Photo taken from the final presentation of the Center for Turbulence 2012 Summer Research Program. 10
1.8 Preview of Chapter 3: controlling the onset of turbulence via streamwise traveling waves. First row: channel flow geometry with a contour of the streamwise velocity at the center of the channel. Second row: velocity fluctuations in the streamwise direction at time $t = 300$ for the uncontrolled flow with Reynolds number $R = 2000$ and flows subject to downstream and upstream traveling waves (generated by blowing and suction along the walls). Third row: kinetic energy of velocity fluctuations as a function of time t. The downstream traveling waves prevent the flow from becoming turbulent by suppressing growth of fluctuations' energy, while the uncontrolled flow and the upstream traveling waves trigger transition to turbulence by promoting growth of fluctuations' energy. In flows that are not turbulent flow patterns are very regular (downstream waves), and in turbulent flows they are complex and disordered (uncontrolled and upstream waves). 14
2.1 Channel flow geometry. Fluid flows between two rigid walls at $y = \pm 1$. The boundary conditions are periodic in the streamwise (x) and spanwise (z) directions and no-slip at the walls. The mean flow $\bar{u}(y)$ is driven in the x-direction by either a mean pressure gradient or a mean shear. . . . 19
3.1 A channel flow with blowing and suction along the walls. 33

3.2 Mean streamwise base velocity, $\overline{U}(y)$, obtained in 2D simulations of the uncontrolled Poiseuille flow with $R_\tau = 63.25$, ×, and controlled flows subject to: (a) DTWs with □, ($c = 5$, $\omega_x = 2$, $\alpha = 0.035$); ○, ($c = 5$, $\omega_x = 2$, $\alpha = 0.05$); ◇, ($c = 5$, $\omega_x = 2$, $\alpha = 0.125$); and (b) UTWs with ◁, ($c = -2$, $\omega_x = 0.5$, $\alpha = 0.015$); ▽, ($c = -2$, $\omega_x = 0.5$, $\alpha = 0.05$); △, ($c = -2$, $\omega_x = 0.5$, $\alpha = 0.125$). 36

3.3 Energy of the velocity fluctuations, $E(t)$, for the initial condition with small energy: (a) ×, uncontrolled; ○, a DTW with ($c = 5$, $\omega_x = 2$, $\alpha = 0.05$); and (b) UTWs with ◁, ($c = -2$, $\omega_x = 0.5$, $\alpha = 0.015$); ▽, ($c = -2$, $\omega_x = 0.5$, $\alpha = 0.05$); △, ($c = -2$, $\omega_x = 0.5$, $\alpha = 0.125$). . . . 40

3.4 (a) Skin-friction drag coefficient, C_f; (b) normalized required power, $\%\Pi_{req}$; (c) normalized produced power, $\%\Pi_{prod}$; and (d) normalized net power, $\%\Pi_{net}$, for the initial condition with small energy: ×, uncontrolled flow; ○, DTW with ($c = 5$, $\omega_x = 2$, $\alpha = 0.05$); and UTWs with ◁, ($c = -2$, $\omega_x = 0.5$, $\alpha = 0.015$); ▽, ($c = -2$, $\omega_x = 0.5$, $\alpha = 0.05$); △, ($c = -2$, $\omega_x = 0.5$, $\alpha = 0.125$). 42

3.5 (a) Energy of the velocity fluctuations, $E(t)$; (b) skin-friction drag coefficient, $C_f(t)$; (c) normalized required power, $\%\Pi_{req}$; and (d) normalized net power, $\%\Pi_{net}$, for the initial condition with moderate energy: ×, uncontrolled; and UTWs with ◁, ($c = -2, \omega_x = 0.5, \alpha = 0.015$); ▽, ($c = -2, \omega_x = 0.5, \alpha = 0.05$); △, ($c = -2, \omega_x = 0.5, \alpha = 0.125$). 43

3.6 (a) Energy of the velocity fluctuations, $E(t)$; (b) skin-friction drag coefficient, $C_f(t)$; (c) normalized required power, $\%\Pi_{req}$ (solid), normalized produced power, $\%\Pi_{prod}$ (dashed); and (d) normalized net power, $\%\Pi_{net}$, for the initial condition with moderate energy: DTWs with □, ($c = 5, \omega_x = 2, \alpha = 0.035$); ○, ($c = 5, \omega_x = 2, \alpha = 0.05$). 45

3.7 (a) Energy of the velocity fluctuations, $E(t)$; (b) skin-friction drag coefficient, $C_f(t)$; (c) normalized required power, $\%\Pi_{req}$ (solid), normalized produced power, $\%\Pi_{prod}$ (dashed); and (d) normalized net power, $\%\Pi_{net}$, for the initial condition with large energy: ×, uncontrolled; DTWs with ○, ($c = 5, \omega_x = 2, \alpha = 0.05$); and ◇, ($c = 5$, $\omega_x = 2$, $\alpha = 0.125$). 47

3.8 (a) and (b) Production, $P_E(t)$ (solid), and dissipation, $D_E(t)$ (dashed), of kinetic energy in Poiseuille flow with $R_\tau = 63.25$ for the initial condition with small energy: (a) ×, uncontrolled; ○, DTW with ($c = 5$, $\omega_x = 2$, $\alpha = 0.05$); and (b) ▽, UTW with ($c = -2$, $\omega_x = 0.5$, $\alpha = 0.05$); △, UTW with $\alpha = 0.125$. (c) $P_E(t) + D_E(t)$ for the UTW with ($c = -2$, $\omega_x = 0.5$, $\alpha = 0.05$). 49

3.9 Streamwise velocity fluctuations, $u(x, z)$, at $y = -0.5557$ ($y^+ = 28.11$), (a), (c), (e) $t = 50$, and (b), (d), (f) $t = 120$ for initial condition with moderate energy: uncontrolled flow; UTW with ($c = -2$, $\omega_x = 0.5$, $\alpha = 0.05$); and DTW with ($c = 5$, $\omega_x = 2$, $\alpha = 0.05$). 51

3.10 Simulation of the uncontrolled flow for the initial condition with moderate energy. (a) - (c) 3D visualizations of the isosurfaces of the discriminant, $D > 10^{-6}$ (blue), $D > 10^{-5}$ (green), and $D > 10^{-4}$ (red). (d) - (f) 2D visualizations of the crossflow velocity vectors (arrows) and the x-averaged streamwise vorticity (color plots). 53
3.11 Simulation of the DTW with ($c = 5$, $\omega_x = 2$, $\alpha = 0.05$) for the initial conditions with moderate energy. (a) - (c) 3D visualizations of the isosurfaces of the discriminant, $D > 10^{-6}$ (blue), $D > 10^{-5}$ (green), and $D > 10^{-4}$ (red). (d) - (f) 2D visualizations of the crossflow velocity vectors (arrows) and the x- averaged streamwise vorticity (color plots). . 54
3.12 Simulation of the UTW with ($c = -2$, $\omega_x = 0.5$, $\alpha = 0.05$) for the initial condition with moderate energy. (a) - (c) 3D visualizations of the isosurfaces of the discriminant, $D > 10^{-6}$ (blue), $D > 10^{-5}$ (green), and $D > 10^{-4}$ (red). (d) - (f) 2D visualizations of the crossflow velocity vectors (arrows) and the x-averaged streamwise vorticity (color plots). Only one quarter of the channel ($x \in [0, 2\pi]$) is shown. 55
3.13 3D visualizations of the isosurfaces of the discriminant, $D > 10^{-5}$ (blue), $D > 10^{-4}$ (green), and $D > 10^{-3}$ (red) for the uncontrolled flow (left figures) and the UTW with ($c = -2$, $\omega_x = 0.5$, $\alpha = 0.05$) (right figures) for the initial condition with moderate energy. Only one quarter of the channel ($x \in [0, 2\pi]$) is shown for the UTW. 56
3.14 Energy of velocity fluctuations around base flows of Section 3.2.1. Simulations are initiated by a fully developed turbulent flow with $R_c = 2000$: ×, uncontrolled; DTWs with □, ($c = 5, \omega_x = 2, \alpha = 0.035$); ○, ($c = 5, \omega_x = 2, \alpha = 0.05$); and ◇, ($c = 5$, $\omega_x = 2$, $\alpha = 0.125$). 57
3.15 (a) Energy of velocity fluctuations around base flows of Section 3.2.1, $E(t)$; and (b) skin-friction drag coefficient, $C_f(t)$. Simulations are initiated by a fully developed turbulent flow with $R_c = 4300$: ×, uncontrolled; DTWs with □, ($c = 5, \omega_x = 2, \alpha = 0.035$); ○, ($c = 5, \omega_x = 2, \alpha = 0.05$); and ◇, ($c = 5$, $\omega_x = 2$, $\alpha = 0.125$). 58
3.16 Mean velocity, $\overline{U}(y)$, and streamwise velocity (shaded plots) at $y = -0.7518$. Simulations are initiated by a fully developed turbulent flow with $R_c = 4300$: ×, $t = 0$; •, $t = 100$; *, $t = 900$. The dashed line identifies the laminar mean velocity induced by the DTW with ($c = 5$, $\omega_x = 2$, $\alpha = 0.125$). 59
4.1 A periodic channel with size $L_x \times 2 \times L_z$. 63
4.2 Sketch of a localized control strategy where the actuator placed at (r, s) uses information from only the nearest neighbors on the two-dimensional lattice. 67

4.3 Energy density of the velocity fluctuations $E(k_n)$ for the uncontrolled flow with $R_c = 2000$ ($\circ$), optimal centralized ($\Box$), truncated centralized ($\triangledown$), and optimal localized ($\diamond$) controllers for (a) $k_m = 0$; (b) $k_m = 0.5$; (c) $k_m = 1$; and (d) $k_m = 1.5$. The truncated controller is unstable for $k_m = \{0.5, 1\}$ and $k_n = \{0, 1\}$ and the energy density is not defined for any combination of these wavenumbers. Note: The energy density is computed at the discrete set of wavenumbers k_n and k_m (symbols) and the lines are plotted for visual aid. 71

4.4 (a) Energy of the velocity fluctuations $E(t)$; and (b) skin-friction drag coefficient $C_f(t)$ for the flow with no control ($\circ$) and optimal centralized ($\Box$), truncated centralized ($\triangledown$), and optimal localized ($\diamond$) controllers. The results are obtained using DNS with $R_c = 2000$. 72

5.1 In both the 2D/3C (5.4) and QL (5.2) (and its associated ensemble mean SSST model) the perturbations ($\vec{u}$) influence the dynamics of the mean flow ($\vec{U}$). This coupling is denoted pathway (1) in the block diagram. The SSST model augments the 2D/3C formulation with feedback from the mean flow to the perturbation dynamics, which is illustrated through pathway (2). 78

5.2 Turbulent mean velocity profiles (based on a streamwise, spanwise and time averages) obtained from DNS with the $L_x = 4\pi$ channel (solid line), the QL model (line with an x marker) and the 2D/3C model (dashed line), all at R=1000. The forcing f in the 2D/3C model is 0.065. There is no forcing applied to the DNS or QL during the time interval used to generate the profile, (i.e. the QL is in the self-sustaining state). 80

5.3 Roll, streak and perturbation development during transition and turbulence at $R = 1000$.Shown are (a) RMS streak velocity $\sqrt{U_s^2}$, (b) RMS roll velocity $\sqrt{V^2 + W^2}$,(c) RMS perturbation velocity $\sqrt{u^2 + v^2 + w^2}$, and (d) RMS velocity departure from the laminar flow. All figures show DNS for boxes with $L_x = 1.2\pi$ (solid line) and $L_x = 4\pi$ (cross-marker with line), QL forced with $f = 0.04$ at $k_x = 1.67$ (dash-dot line) and the 2D/3C with $f = 0.04$ (dashed line). The perturbation forcing of the QL simulation was stopped at $t = 500$ demonstrating that after transition, the QL self-sustains. 83

5.4 The self sustaining state in the QL simulation. In all plots the QL was forced with amplitude $f = 0.04$ until $t = 500$. At $t = 500$ the same QL was was evolved under no forcing $f = 0$ (solid), with $f = 0.04$ (dashed) and with $f = 0.1$ (dashed-dot). Shown are: the RMS perturbation velocity $\sqrt{u^2 + v^2 + w^2}$ (left) and the RMS roll velocity $\sqrt{V^2 + W^2}$ (right). This shows that after the QL enters the self sustaining state, the statistics are independent of f. When the QL is on this turbulent attractor the dynamics are strongly regulated by the interaction between the perturbations and the roll/streak structure. 84
5.5 Initial development of the roll and streak structure during transition to turbulence at $R = 1000$. Shown are the RMS values of (a) the streak velocity $\sqrt{U_s^2}$ and (b) the roll velocity $\sqrt{(V^2 + W^2)}$ for DNS (solid line), QL (dashed-dot), 2D/3C (dashed line). All simulations were initialized from a laminar state. A stochastic perturbation forcing with amplitude $f = 0.04$ was introduced to instigate transition. This figure shows that the QL and DNS exhibit exponential growth of the roll/streak structure in accordance with the roll/streak instability predicted by SSST with the predicted overshoot and subsequent establishment of the feedback regulated turbulent state. The 2D/3C produces continued algebraic growth of the roll/streak structure because of the lack of feedback from the mean flow to the perturbations, pathway (2) in figure 5.1. 84
5.6 A y-z plane cross-section of the flow at a single snapshot in time (a) the $k_x = 0$ mode of the DNS, (b) the QL, and (c) the 2D/3C simulations, all at $R = 1000$. All panels show contours of the streamwise component of the mean flow U with the velocity vectors of (V, W) superimposed. The QL is self-sustaining ($f = 0$), and the 2D3C is forced with an amplitude $f = 0.065$. 85
5.7 A $k_x = 0$ snapshot of the DNS with the longer ($L_x = 4\pi$) channel showing contours of the streamwise velocity field U with the velocity vectors of (V, W) superimposed. The averaging effect caused by the longer channel is clearly evident in the more regularized features versus the plots in figure 5.6 86
6.1 Block diagrams of (a) system (6.1); and (b) system (6.1) connected in feedback with norm-bounded unstructured uncertainty Γ. Here, $s \in \mathbb{C}$ denotes the temporal Laplace transform variable, and the transfer function, from d to φ, is determined by $H(s) = R/\big((s + \lambda_1)(s + \lambda_2)\big)$. 93
6.2 Block diagram of a system connected in feedback with norm-bounded unstructured uncertainty Γ. 94
6.3 Geometry of a three-dimensional shear-driven channel flow. 97

6.4 Worst-case amplification from $\mathbf{d}$ to $\mathbf{v}$ in Couette flow with $\beta = 0.5$, $We = \{10, 50, 100\}$, and $L = \{10, 50, 100\}$: first row, $We = 10$; second row, $We = 50$; and third row, $We = 100$. 103
6.5 Component-wise worst-case amplification from d_j to s in Couette flow with $s = \{u, v, w\}$, $j = \{1, 2, 3\}$, $\beta = 0.5$, $We = 50$, and $L = 50$. The symbol ($\bullet$) identifies the largest value of the corresponding plot. 104
6.6 Functions characterizing worst-case amplification from d_2 and d_3 to v and w at $k_x = 0$; $g_{sj}(k_z)$ with $\{s = v, w;\ j = 2, 3\}$. 108
6.7 Maximum singular values of the frequency response operators from d_j to u as a function of ω in streamwise-constant Couette flow with $j = \{1, 2, 3\}$, $k_z = 1.5$, $\beta = 0.5$, $L = 10$, and $We = [10, 100]$. The symbol ($\circ$) identifies the peak values of the corresponding curves. 109
6.8 Worst-case amplification from d_j to u in streamwise-constant Couette flow: first row, $L = 10$ and $We = [10, 100]$; and second row, $L = 100$ and $We = [10, 1000]$. The symbol ($\bullet$) shows the worst-case amplification from d_j to u in the limit of infinitely large We. 110
6.9 Functions characterizing worst-case amplification from d_2 and d_3 to u at $k_x = 0$ and $\omega = 0$: g_{u2} ($\circ$); and g_{u3} (solid). 111
6.10 First row: body forcing fluctuations in d_2 and d_3 leading to the largest amplification of u. Second row: streamwise velocity fluctuations obtained by forcing the inertialess Couette flow with the body force fluctuations shown in (a) and (b), respectively. 113
6.11 Spanwise frequency responses from d_j to the polymer stress fluctuations τ_{22} (g_{1j}), τ_{23} (g_{2j}), and τ_{33} (g_{3j}) with $j = \{2, 3\}$. The function $g_{12} = g_{32}$ and the function $g_{13} = g_{33}$: (a) g_{12}, g_{32} ($\circ$) and g_{13}, g_{33} (solid); and (b) g_{22} ($\circ$) and g_{23} (solid). 117
6.12 Maximum singular values of the streamwise-constant frequency responses operator from d_j to τ_{13} ($\mathbf{G}_{4j}$), τ_{12} ($\mathbf{G}_{5j}$), and τ_{11} ($\mathbf{G}_{6j}$) as a function of ω for $j = \{2, 3\}$, $k_z = 1.5$, $\beta = 0.5$, $L = 10$ and $We = [10, 100]$. 118
6.13 Spanwise frequency responses from d_j to the polymer stress fluctuations τ_{13} (g_{4j}), τ_{12} (g_{5j}), and τ_{11} (g_{6j}) for $j = \{2, 3\}$. The function $g_{52} = g_{62}$ and the function $g_{53} = g_{63}$: (a) g_{42} ($\circ$) and g_{43} (solid) for $\beta = 0.5$; and (b) g_{52}, g_{62} ($\circ$) and g_{53}, g_{63} (solid). 119
7.1 Channel flow geometry. We consider the dynamics of two-dimensional flow fluctuations in the (x, y)-plane. 129
7.2 The temporal frequency dependence of $\Pi_{\psi f}$ and Π_{ψ} in flows with $k_x = 1$, $\beta = 0.5$, and $\epsilon = \{0.02, 1 \times 10^{-2}, 5 \times 10^{-3}\}$. The lines represent the results for Π_{ψ}. The symbols represent the results for $\Pi_{\psi f}$ which is the response from only the fast system. 138
8.1 Channel flow geometry. 144

8.2 Mean velocity as a function of the distance from the wall in flows with (a) no polymers $U_0(y^+)$; and with polymers $U(y^+)$ for: (b) $L = 100$ and $We_\tau = 25$ ($\times$), $We_\tau = 50$ ($+$), $We_\tau = 100$ ($\triangleleft$), $We_\tau = 200$ ($\bullet$); and (c) $We = 100$ and $L = 25$ ($\Box$), $L = 50$ ($\diamond$), $L = 100$ ($\triangle$), $L = 200$ ($\bigtriangledown$). For Newtonian fluids, the result is obtained for flows with $R_\tau = 186$ and $\beta = 1$. In addition, we also show the linear wall asymptote, $U = y^+$, and the logarithmic inertial sublayer asymptote, $U = 2.5\ln(y^+) + 5.5$. For flows with polymers, results are obtained for flows with $R_\tau = 186$, $\beta = 0.9$, and $D_0 = 3.25$ using the assumption that turbulent viscosity ν_{T0} captures the behavior of fluctuations. 149

8.3 Percent drag reduction as a function of the friction Weissenberg number. Results are obtained using the turbulent mean velocity U for flows with $R_\tau = 186$, $\beta = 0.9$, $D_0 = 3.25$, and $L = [10, 1000]$ with the assumption that turbulent viscosity ν_{T0} captures the behavior of fluctuations. 149

8.4 (a) Percent drag reduction as a function of the friction Weissenberg number. Results are obtained using the turbulent mean velocity U for flows with $R_\tau = 186$, $\beta = 0.9$, $D_0 = 3.75$, and $L = [30, 130]$ with second-order flow statistics ($\overline{uv}$, Γ_{12}, Λ_{12}) correction to the mean flow equations. (b) Drag reduction normalized by $\max\left(DR\left(We_\tau = 130, L\right)\right) = 0.33$. Symbols represent the normalized polymer drag reduction data from direct numerical simulations [7] of fully developed turbulent flow with $R_\tau = 125$, $\beta = 0.9$, $D_0 = 3.75$, $L = 30\,(\circ)$, $L = 60\,(\Box)$, $L = 85\,(\bigtriangledown)$, $L = 120\,(\triangle)$. . . 155

8.5 Turbulent mean velocity obtained using method presented in Section 8.3 for flows with $R_\tau = 186$, $\beta = 0.9$, and $D_0 = 3.75$. Result for flow without polymers is represented by the dashed line. The symbol ($\circ$) represents data obtained using DNS for flows with $DR = 33\%$. 156

8.6 Turbulent mean viscosity, Reynolds shear stress, and root-mean-squared velocity fluctuations obtained using method presented in Section 8.3 for flows with $R_\tau = 186$, $\beta = 0.9$, $D_0 = 3.75$, and $DR = 33\%$. Results for the flow without polymers are represented by dashed lines. The symbol ($\circ$) represents data obtained from DNS for flows with 33% drag reduction. 157

8.7 Variation of Reynolds shear stress ($\overline{uv}$) and polymer shear stress (T_{12}) as a function of the distance from the wall for $R_\tau = 186$, $\beta = 0.9$, $D_0 = 3.75$, $We_\tau = 110$, and $L = \{30, 70, 110, 130\}$. 158

8.8 Variation of Λ_{12}, Γ_{12}, and T_{12} as a function of the distance from the wall for $R_\tau = 186$, $\beta = 0.9$, $D_0 = 3.75$, $We_\tau = 110$, (a) $L = 30$, (a) $L = 70$, (a) $L = 110$, and (a) $L = 130$. 159

8.9 Variation of (a) Reynolds shear stress ($\overline{uv}$) and (b) polymer shear stress (T_{12}) as a function of the distance from the wall for $R_\tau = 186$, $\beta = 0.9$, $D_0 = 3.75$, $L = 110$, and $We_\tau = \{30, 70, 110, 130\}$. 160

8.10 Premultiplied DNS-based energy spectrum of the turbulent flow of Newtonian fluids, $k_x k_z E_{v0}$, at $R_\tau = 186$ [8]. 161
8.11 Contribution to the normalized energy spectrum of velocity fluctuations induced by polymers, $\bar{E}_{vp}(\boldsymbol{\kappa})$, for $We_\tau = 130$, $R_\tau = 186$, $\beta = 0.9$, $D_0 = 3.25$: (a) $L = 10$; (b) $L = 70$; and (c) $L = 130$. All figures are shown in log-log-log scale. 162
8.12 Contribution to the normalized energy spectrum of the fluctuating conformation tensor from Newtonian fluids' dynamics, $\bar{E}_{c0}(\boldsymbol{\kappa})$, for $We_\tau = 130$, $R_\tau = 186$, $\beta = 0.9$, $D_0 = 3.25$: (a) $L = 10$; (b) $L = 70$; and (c) $L = 130$. All figures are shown in log-log-log scale. 163
8.13 Contribution to the normalized energy spectrum of the fluctuating conformation tensor induced by polymers, $\bar{E}_{cp}(\boldsymbol{\kappa})$, for $We_\tau = 130$, $R_\tau = 186$, $\beta = 0.9$, $D_0 = 3.25$: (a) $L = 10$; (b) $L = 70$; and (c) $L = 130$. All figures are shown in sign preserving log-log-log scale. 164
9.1 We consider the dynamics of flow fluctuations in the (x, y)-plane of the channel. 176
9.2 Block diagrams of (a) the frequency response operator $\mathcal{T}$: $\mathbf{d} \mapsto \boldsymbol{\varphi}$; and (b) the adjoint operator $\mathcal{T}^\star$: $\mathbf{f} \mapsto \mathbf{g}$. 180
9.3 A cascade connection of $\mathcal{T}^\star$ and $\mathcal{T}$ with $\mathcal{T}\mathcal{T}^\star$: $\mathbf{f} \mapsto \boldsymbol{\varphi}$. 183
9.4 Channel flow geometry. 193
9.5 Two largest singular values of the frequency response operator for the linearized Navier-Stokes equations as a function of the temporal frequency ω in the flow with $R = 2000$, $k_x = 1$, and $k_z = 1$: blue $\times$, $\sigma_1(\mathcal{T})$; and red $\circ$, $\sigma_2(\mathcal{T})$. 193
9.6 Streamwise velocity fluctuation development for largest singular value of the frequency response operator in a pressure-driven channel flow with R = 2000, $k_x = k_z = 1$, (a) $\omega = -0.385$, and (b) $\omega = -0.982$. High and low velocity regions are represented by red and green colors. Isosurfaces of u are taken at ± 0.55. 194
9.7 Streamwise velocity (color plots) and vorticity, $\omega_x = \partial_y w - \partial_z v$, (contour lines) fluctuation development for largest singular value of the frequency response operator in the cross section of a pressure-driven channel flow with $R = 2000$, $k_x = k_z = 1$, (a) $\omega = -0.385$, and (b) $\omega = -0.982$. Red color represents high speed and blue color represents low speed streaks. 194
9.8 The largest singular values of the frequency response operator for an inertialess shear-driven channel flow of viscoelastic fluids as a function of We at $k_x = 1$, $\beta = 0.5$, and $\omega = 0$. Results are obtained using: (a) and (b) Pseudo-spectral method with $N = 100$, blue $\circ$; $N = 150$, red *; and $N = 200$, green $\square$; (c) and (d) Chebfun with integral forms of input-output differential equations, blue $\triangle$; and spatial state-space representations, red ∇. 196

9.9 Principal singular functions of the frequency response operator for inertialess shear-driven flow of viscoelastic fluids with $We = 20$, $k_x = 1$, and $\beta = 0.5$. First column: real part of $u_{\max}$; second column: imaginary part of $v_{\max}$. Results are obtained using: (a) and (b) Pseudo-spectral method with $N = 50$, red $\times$; $N = 100$, blue $\circ$; $N = 200$, green $\square$; (c) and (d) Chebfun with integral form of input-output differential equations. 198
9.10 An Euler-Bernoulli beam that is clamped at the left end and subject to a boundary actuation at the other end. 209
9.11 Frequency response of the Euler-Bernoulli beam (9.59)-(9.60) with the output determined by the vertical displacement of the beam at the right end. (a) magnitude of the frequency response $|\mathcal{T}(\omega)|$; (b) phase of the frequency response $\angle \mathcal{T}(\omega)$. 210

Chapter 1

Introduction

1.1 Motivation

This dissertation deals with modeling, analysis, and control of transitional and turbulent shear channel flows of Newtonian and viscoelastic fluids. In particular, we are interested in the development of theoretical and computational methods for studying these complex flows. However, before going into the mathematics and physics of turbulence, it is worthwhile to first discuss the motivation behind this dissertation.

Transition to turbulence is one of the most intriguing natural phenomena. Flows that are smooth and ordered (laminar) may become complex and disordered (turbulent) as the flow strength increases; see Figure 1.1 for an illustration. This process is known as transition to turbulence.

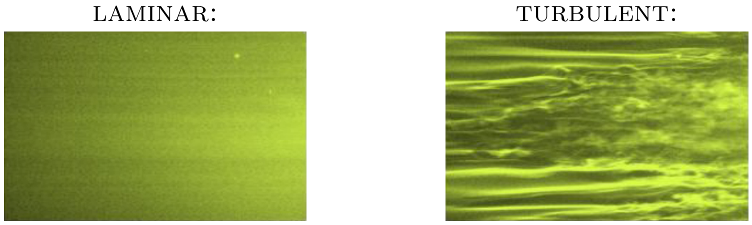

Figure 1.1: Visualization in a flat-plate boundary-layer flow of a Newtonian fluid [1]. In laminar flows flow patterns are very regular, and in turbulent flows they are complex and disordered.

Despite the endeavors of generations of engineers, applied mathematicians, and physicists, understanding of transition and its triggering mechanisms still contains major mysteries. Progress in this area is important not only from a theoretical standpoint, but also because it is essential for effective implementation of flow control strategies. In some applications, suppression of turbulence is desired (e.g., for increased energy

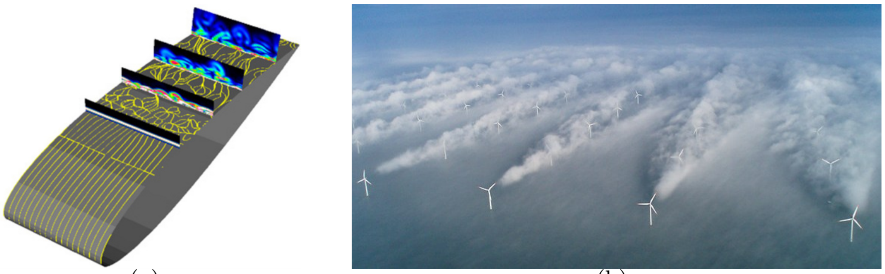

(a) (b)

Figure 1.2: (a) Transition from laminar to turbulence over an aircraft wing. Photo taken from efluids by Miguel Visbal. (b) The wake from upstream turbines affects those downstream of wind.

efficiency), whereas in other applications promotion of turbulence is needed (e.g., for improved mixing). This dissertation focuses on the dynamics and control of transition and turbulence in flows of Newtonian, such as air and water, and complex viscoelastic fluids, such as polymers and molten plastics.

For Newtonian fluids, turbulent flow around cars, airplanes, and ships increases resistance to their motion. An aerodynamically perfect wing of an aircraft would have laminar flow all the way from its leading edge to its rear. However, wings are not perfect, and at some point the flow will become turbulent; see Figure 1.2(a). As a result, about half of the fuel required to maintain the aircraft at cruise conditions is used to overcome the resistance to motion imposed by the turbulent flow. Similarly, in wind farms, turbulence reduces the aerodynamic efficiency of the blades, thereby decreasing the energy capture; see Figure 1.2(b). Thus, there is a critical demand for development and utilization of advanced turbulence suppression techniques. Currently available strategies combine physical intuition with extensive numerical simulations and experiments in order to control transition to turbulence. Even though simulations and experiments offer valuable insights into the performance of control strategies, their effectiveness can be significantly enhanced by a model-based approach to flow control design.

My study of complex viscoelastic fluids is motivated by recent findings showing that transition to turbulence can occur even at small flow rates [9]. This is in contrast to Newtonian fluids where transition takes place only when the fluid is moving at a high speed. Improved understanding of transition mechanisms in viscoelastic fluids is important for polymer manufacturing and micro/nano-fluidic mixing [10]. In manufacturing, turbulence is undesirable because it compromises quality of polymer products. In micro/nano-fluidic devices, the addition of polymers can trigger turbulence, thereby leading to a mixing enhancement [6]. Efficient mixing of macromolecular solutions containing DNA or globular proteins is of fundamental importance in biotechnology where these devices are increasingly being used.

To tackle the aforementioned problems, this dissertation utilizes tools from two major disciplines: control systems theory and fluid mechanics. Control theory is an interdisciplinary branch of engineering and mathematics that deals with dynamical systems and their control. On the other hand, fluid mechanics is a branch of physics that studies the motion and behavior of fluids and the effect of forces acting on them. We illustrate, in this dissertation, that the combination of these two disciplines can lead to many new and exciting discoveries in the area of turbulence research. The remainder of this chapter provides a summary of the main topics, the layout, and the major contributions of the dissertation.

1.2 Main topics of the dissertation

In this section, we discuss the main topics of the dissertation.

1.2.1 Model-based control of Newtonian fluids

In many engineering applications that involve fluid flows, turbulence plays a significant role in control design. When flows transition from laminar to turbulent state, complex fluid motions appear and have two practical consequences:

1. Mixing enhancement. In smooth laminar flow, the process of mixing of two fluids can only occur through diffusion which is often a very slow process. On the other hand, the wide range of temporal and spatial scales of turbulent flows allow the process of mixing to occur at a much higher rate.

2. Drag increase. For moving bodies, the friction of the fluid on solid surfaces is significantly increased in turbulent regime compared to laminar regime. This property is of particular importance in applications that deal with water, where friction drag is as significant as profile drag.

Depending on the specific application, the control objective may be to promote or suppress turbulence. Here, we discuss a number of flow strategies for controlling the onset of turbulence in shear flows of Newtonian fluids. The ability to manipulate turbulence is desirable in many practical applications like in air- and water-transportations, and wind turbines.

Designing fuel-efficient air- and water-vehicles has become increasingly important due to the global energy crisis. Turbulence around the wings of an aircraft increases drag and results in larger fuel consumption. In particular, the skin-friction drag is responsible for 50% and 90% of fuel consumption in passenger aircrafts and in submarine, respectively. Another important application concerns renewable energy sources, such as wind energy. The renewed interest in environmentally-friendly energy sources stems from the desire to achieve fossil-fuel independence, thereby indirectly addressing both the global warming and global energy crises. In order to increase productivity and efficiency, wind turbines are becoming progressively larger which poses significant

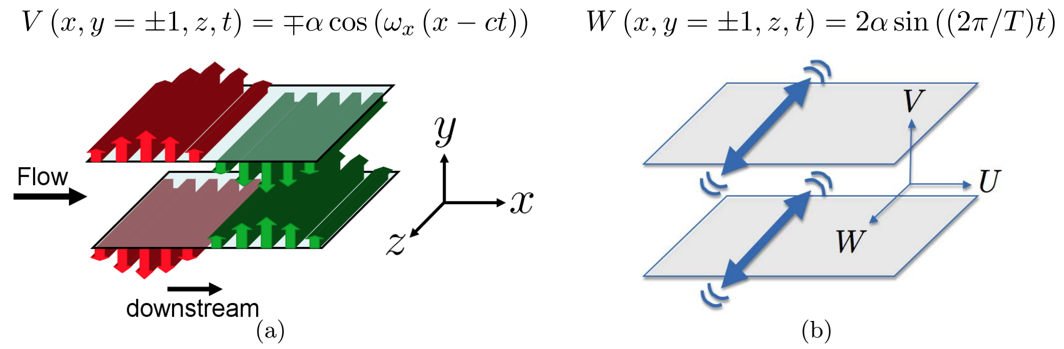
$V\left(x, y=\pm 1, z, t\right)=\mp\alpha\cos\left(\omega_x\left(x-ct\right)\right)$
$W\left(x, y=\pm 1, z, t\right)=2\alpha\sin\left((2\pi/T)t\right)$
Flow
downstream
y
x
z
V
U
W

(a) (b)

Figure 1.3: **Sensorless flow control strategies:** (a) Blowing and suction along the walls in the form of a streamwise traveling wave with α, ω_x, and c denoting the amplitude, frequency, and speed of the wave; (b) Transverse wall-oscillations with α and T denoting the amplitude and period of the oscillation.

technological challenges for their design and control. During its operation, a wind turbine is subject to severe uncertainties arising from atmospheric turbulence, near-ground effects, and spatial variations in wind. These effects play an integral role in efficiency and longevity of turbines. In view of these global issues, there is a critical demand for development and utilization of advanced theoretical and computational turbulence suppression techniques.

In this dissertation, we address the aforementioned issues by developing techniques for design and evaluation of vibrational (sensorless) flow control strategies, where the dynamics are impacted by zero-mean oscillations, and for feedback flow control strategies, where measurements are used to achieve the desired objective.

Sensorless flow control strategies

Flow control by means of sensorless mechanisms, that is without measurement of any flow quantities, is a promising technology for implementation. They represent a simpler alternative to feedback flow control which requires wall-mounted devices for sensing and actuations; instead, sensorless flow control relies on the fundamental understanding of flow physics and control designs. Examples of these sensorless schemes include transverse wall-oscillations and wall-transpirations in the form of streamwise traveling waves; see Figure 1.3 for illustrations. Both wall-oscillations and wall-transpirations belong to a class of vibrational control, where the system's dynamical properties are altered by introducing zero-mean vibrations into the system's coefficients. It has been shown using high-fidelity simulations that both wall-oscillations and wall-transpirations have promising drag reduction properties. In particular, blowing and suctions in the form of an upstream traveling waves can lead to a sustained sub-laminar drag (below the level achieved in laminar flow) in a fully developed turbulent channel flow [2].

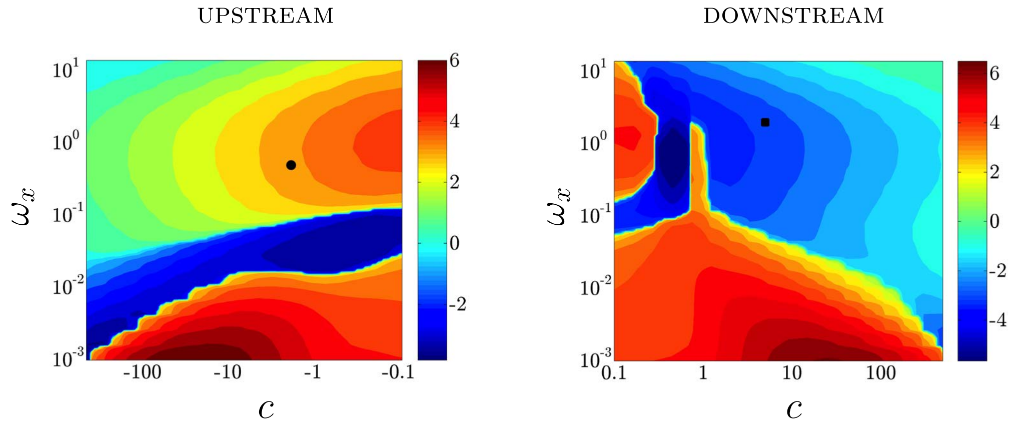

(a) (b)

Figure 1.4: **Controlling the onset of turbulence via streamwise traveling waves**: Energy amplification of the most energetic structures of the uncontrolled flow with Reynolds number $R = 2000$, in the presence of (a) upstream traveling waves; and (b) downstream traveling waves. The symbols ● and ■, respectively, denote ($c = -2$, $\omega_x = 0.5$) (as selected in [2]) and ($c = 5$, $\omega_x = 2$). Figures are taken from Moarref & Jovanović [3].

In this dissertation, we show that properly designed streamwise traveling waves are capable of preventing flows from transitioning to turbulence in low Reynolds number regime. Chapter 3 along with [3] represents a two-part flow control design process where a model-based method is used for designing flow control parameters and high-fidelity simulations are used for validating the theoretical predictions. In Part 1, Moarref & Jovanović [3] used the stochastically forced Navier-Stokes equations linearized around the nominal velocity that is induced by wall-actuation to study the effect of traveling wave parameters (amplitude α, frequency ω_x, and speed c of the wave) on flow receptivity. Their results obtained using perturbation analysis, illustrate that reducing the flow receptivity (sensitivity to disturbances) represents a powerful paradigm for controlling the onset of turbulence. They showed that carefully selected downstream traveling waves are capable of reducing the energy amplification of the most energetic structures of the uncontrolled flow; see Figure 1.4 for details. On the other hand, the velocity fluctuations around the upstream traveling wave (selected by [2] to sustain sub-laminar drag) exhibit larger receptivity to disturbances. Hence, Moarref & Jovanović concluded that the downstream traveling waves with properly designed speed and frequency are well-suited for controlling the onset of turbulence. In contrast, the upstream traveling waves can promote turbulence.

In Chapter 3, we use high-fidelity simulations of the nonlinear dynamics to validate

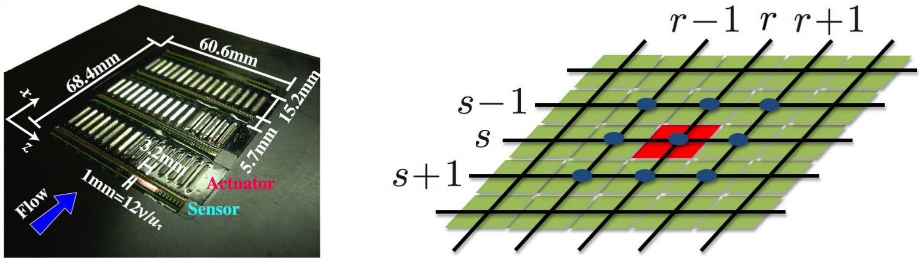

(a)

(b)

Figure 1.5: (a) An array of distributed hot-film shear-stress sensors and wall-deformation actuators for feedback flow control [4]; (b) Sketch of a localized control strategy where the actuator placed at (r, s) uses information from only the nearest neighbors on the two-dimensional lattice.

the theoretical predictions made in [3]. The numerical results of this dissertation elucidate the predictive power of the model-based control method developed in [3] and suggest that the linearized Navier-Stokes equations with uncertainty represent an effective control-oriented model for preventing transition.

Feedback flow control strategies

In contrast to sensorless flow strategies, feedback control utilizes flow information from measurements to manipulate the flow fields to achieve a desired performance (e.g., prevent flow from transitioning to turbulence or reduce drag). Feedback flow control strategies are made possible by the recent developments in micro-electro-mechanical devices [4]. The relevant flow quantities such as velocity, pressure, and shear stresses are measured by sensors and the flow is actuated by wall-deformation actuators and compliant surfaces via a feedback rule. Feedback strategies for control of fluid flows involve individual system components that are capable of sensing, computation, and actuation; see Figure 1.5(a). Therefore, an important question in design of flow controllers is related to the interconnection structure between these components. A centralized controller yields best performance at the expense of excessive communication and computation. A fully decentralized controller, while advantageous from a communications perspective, may sacrifice performance. A reasonable middle ground between these competing approaches is offered by localized strategies where each component exchanges information with a limited number of nearby components. For example, Figure 1.5(b) illustrates a situation where information from only the nearest neighbors is used. In Chapter 4, we have designed a localized optimal controller for preventing transition to turbulence.

1.2.2 Importance of roll and streak structure in transition and turbulence flows

The Navier Stokes (NS) equations provide a comprehensive model of the dynamics of turbulence. Unfortunately, these equations are analytically intractable. They have, however, been extensively studied computationally since the early work of Kim, Moin, and Moser [11] and a number of highly resolved numerical simulations exist, see e.g. [12–15]. Ever increasing computing power promises to make possible simulation of an even wider range of turbulent flows. However, a complete understanding of the physical mechanisms underlying turbulence in the NS equations, even in simple parallel flow configurations, remains elusive. Thus, considerable effort has been devoted to the search for more tractable models for studying the dynamics of turbulence.

The prominence of streamwise elongated structures in wall-bounded shear flow turbulence previously motivated turbulence investigations using streamwise constant (2D/3C) and streamwise averaged (SSST) models. Results obtained using these models imply that the statistical mean turbulent state is in large part determined by streamwise constant structures, particularly the well studied roll and streak. In Chapter 5, the role of streamwise structures in transition and turbulence is examined by comparing theoretical predictions of roll/streak dynamics made using 2D/3C and SSST models with direct numerical simulations. The results confirm that the 2D/3C model accurately obtains the turbulent mean velocity profile despite the fact that it only includes one-way coupling from the cross-stream perturbations to the mean flow. The SSST system augments the 2D/3C model through the addition of feedback from this streamwise constant mean flow to the dynamics of streamwise varying perturbations. With this additional feedback, the SSST system supports a perturbation/mean flow interaction instability leading to a bifurcation from the laminar mean flow to a self-sustaining turbulent state. Once in this self-sustaining state the SSST collapses to a minimal representation of turbulence in which a single streamwise perturbation interacts with the mean flow. Comparisons of high-fidelity simulation data with simulations of this self-sustaining state demonstrate that this minimal representation of turbulence produces accurate statistics for both the mean flow and the perturbations. These results suggest that SSST captures fundamental aspects of the mechanisms underlying transition to and maintenance of turbulence in wall-bounded shear flows.

1.2.3 Transition to turbulence in channel flows of viscoelastic fluids

In low-inertial flows the nonlinearities provided by the polymer stresses of viscoelastic fluids can provide nontrivial dynamics that is commonly observed in turbulent flows of Newtonian fluids. This “elastic turbulence” phenomenon is nicely captured in the experiments by Groisman & Steinberg [5, 6]. They showed that dilute polymer suspensions being sheared in simple flow geometries can exhibit time-dependent dynamics and show efficient fluid mixing; see Figure 1.6 for details. On the other hand, the same experiments using Newtonian fluids do not show such complex dynamics and properties. Since viscoelastic fluid flows are often encountered in commercially important settings, understanding transition to *elastic turbulence* in such flows may therefore have critical effects from both fundamental and technological standpoints.

Newtonian fluids are characterized by a static-in-time linear relation between stresses and velocity gradients. In viscoelastic fluids, however, this relation generally depends on the entire flow history and is often nonlinear. The simplest models for dilute solutions of viscoelastic fluids are obtained from kinetic theory by representing each polymer molecule by a spring connecting two spherical beads [16,17]. Different spring properties lead to different constitutive equations: the Oldroyd-B (infinitely extensible Hookean spring) and the FENE-P (finitely extensible, nonlinear elastic, with the Peterlin statistical closure for the restoring force) models are most commonly used. The constitutive equations determine the influence of velocity gradients on the time-evolution of stresses, and they introduce six additional equations for the components of the conformation tensor. The most notable property of viscoelastic fluids is that the stresses do not immediately disappear when fluid motion is brought to rest; rather, they decay to zero with some characteristic relaxation time.

In addition to the Reynolds number, which represents the ratio of inertial to viscous forces, the properties of viscoelastic fluids are characterized by several additional parameters. The *Weissenberg number* captures the importance of the fluid relaxation time relative to the characteristic flow time, the *viscosity ratio* measures the ratio of solvent viscosity to total viscosity, and the *finite extensibility parameter* determines the extensibility of polymer molecules in the FENE-P model. Note that while the Reynolds number determines the strength of nonlinear inertial terms in the equations of fluid motion, the Weissenberg number quantifies the strength of nonlinear stress terms in the constitutive equations.

Transition in the experiments described in Figure 1.6 is initiated by a linear elastic instability that arises from the presence of curved streamlines [18]. However, the question as to whether and how transition can occur in channel flows of viscoelastic fluids with straight streamlines remains wide open. This is an intriguing question because such flows are linearly stable when inertial effects are negligible; yet, they exhibit complex dynamical responses in strongly elastic regimes [19–21]. In this thesis, we utilize systems theoretic tools to study this phenomenon. In particular, our analysis presented in Chapter 6 shows that flow fluctuations can experience significant amplification even in the absent of inertial forces. The results demonstrate that inertialess shear flows of viscoelastic fluids exhibit poor robustness to disturbances. We show that the underlying mechanism responsible for large amplification and poor robustness comes from the interaction between polymer stress fluctuations with base shear, and it represents a close analog of the lift-up mechanism that initiates a bypass transition in inertial flows of Newtonian fluids.

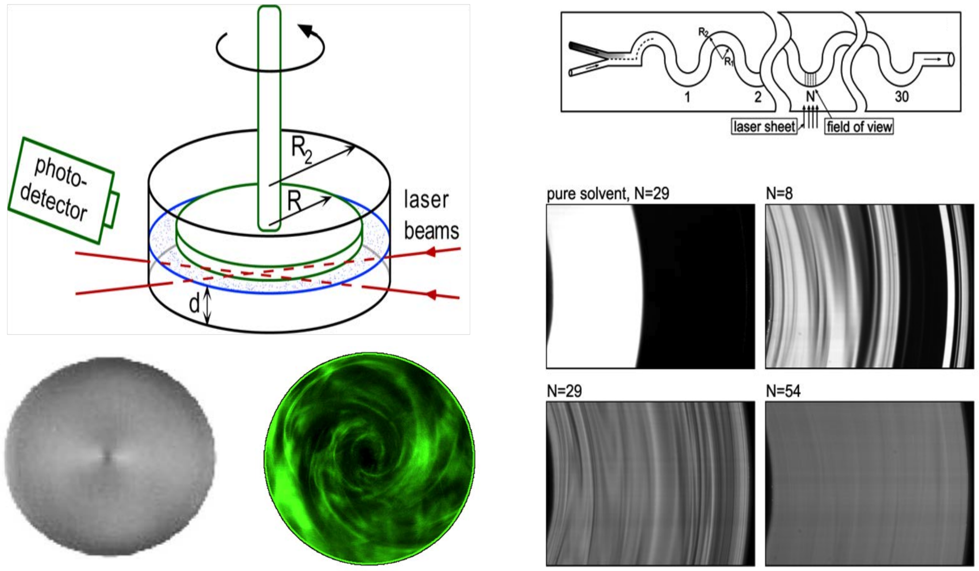

(a) (b)

Figure 1.6: Swirling flow and microfluidic channel experiments of Groisman and Steinberg. (a) A weakly inertial swirling flow between parallel discs considered in [5]. Flow of a Newtonian fluid is steady and ordered (laminar), with no structure to it. Flow of a viscoelastic fluid is complex and disordered with a broad range of spatial and temporal scales; flow resistance is increased 20 times compared to a Newtonian fluid. (b) A schematic drawing of a curvilinear channel used in the mixing experiment (top) and snapshots of mixing at different stages considered in [6]. If the liquids contain no polymer molecules (the viscous Newtonian solvent), the flow remains laminar; no mixing occurs and the two working fluids are identical, with a small amount of a fluorescent dye added to one of them. When small amount of high-molecular-weight polymers is added to a Newtonian fluid, the irregular 3D flow stirs the liquid (photos at $N = 8$ and 29) and provides efficient mixing. At the end of the channel, at $N = 54$, the dye distribution becomes rather homogeneous.

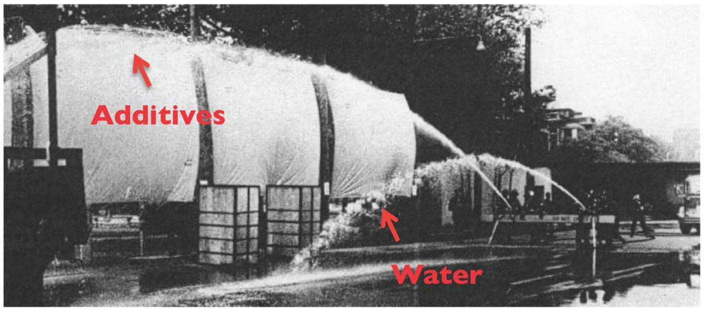

Figure 1.7: Demonstration of increase water throughput in fire hoses using polymer additives. Photo taken from the final presentation of the Center for Turbulence 2012 Summer Research Program.

1.2.4 Polymer induced drag reduction in turbulent channel flows

Viscoelastic fluids can also have significant influence on the dynamics of turbulent flows. It is well known that the addition of a minute amount of long-chain polymer molecules to turbulent shear flows is an effective means for reducing skin-friction losses. Study of polymer drag reduction is of both practical and fundamental importance. From applied point of view, the injection of high-molecular weight polymers to flowing liquids in pipe flows and marine vessels can have tremendous benefits. Figure 1.7 shows an experiment demonstrating how polymer additives were used to increase the water throughput in fire hoses. In addition, polymer drag-reducing additives have been used in the Trans-Alaska Pipeline System to increase throughput and to maintain throughput with off-line pumping stations [22]; polymer ejection has been used in US Navy submarine testings to reduce hull drag and increase speed by 10%–15% [23]. From fundamental point of view, understanding mechanisms of polymer drag reduction may shed light into the essential turbulent flow physics and open new ways of controlling turbulence via active or passive means.

The drag reduction by polymers has been extensively studied over the past sixty years [23] and most of our understanding comes from numerical and experimental studies. Even though direct numerical simulations have offered new insights on the interactions of polymers and turbulence [24, 25], maximum drag reduction [7, 26], and coherent structures [27–30], the development of computationally attractive models that are suitable for analytical developments and optimization has been lagging behind. Deeper theoretical understanding in conjunction with computationally attractive turbulence modeling can help improve the understanding of fundamental flow physics and expand utility of polymer drag reduction. We consider this issue by developing a model-based approach to studying polymer drag reduction in turbulent channel flows in Chapter 8.

1.2.5 Computation of frequency responses of PDEs

In many physical systems there is a need to examine the effects of exogenous disturbances on the variables of interest. The frequency response analysis represents an effective means for quantifying the system's performance in the presence of a stimulus, and it characterizes the steady-state response of a stable system to persistent harmonic forcing. At each temporal frequency, the frequency response of finite dimensional linear time-invariant systems with scalar input and output is a complex number that determines the magnitude and phase of the output relative to the input. In systems with many inputs and outputs (multi-variable systems), the frequency response is a complex matrix whose dimension is determined by the number of inputs and outputs. In systems with infinite dimensional input and output spaces, the frequency response is an operator. It is well-known that the singular values of the frequency response matrix (in multi-variable systems) or the frequency response operator (in infinite dimensional systems) represent proper generalization of the magnitude characteristics for single-input single-output systems. At a specific frequency, the largest singular value determines the largest amplification from the input forcing to the desired output. Furthermore, the associated left and right principal singular functions identify the spatial distributions of the output (that exhibits this largest amplification) and the input (that has the strongest influence on the system's dynamics), respectively.

Frequency response analysis has many potential applications in numerical analysis, physics, and engineering, especially in systems with generators that do not commute with their adjoints [31]. In these systems, standard modal analysis may fail to capture amplification of exogenous disturbances, low stability margins, and large transient responses. In contrast, singular value decomposition of the frequency response operator represents an effective tool for identifying these non-modal aspects of the system's dynamics. In particular, wall-bounded shear flows of both Newtonian and viscoelastic fluids have non-normal dynamical generators of high spatial order and the ability to accurately compute frequency responses for these systems is of paramount importance.

Computation of frequency responses for partial differential equations (PDEs) is typically done numerically using finite-dimensional approximations of the operators in the evolution equation. Pseudo-spectral methods represent a powerful tool for discretization of spatial differential operators, and they possess superior numerical accuracy compared to approximation schemes based on finite differences [32–35]. In spite of their advantages, pseudo-spectral methods may produce unreliable results and even fail to converge upon grid refinement when dealing with systems that contain differential operators of high order; this lack of convergence is attributed to the loss of accuracy arising from ill-conditioning of the discretized differentiation matrices [36]. Furthermore, implementation of general boundary conditions may be challenging. We address these issues in Chapter 9 where we introduce a method for computing frequency responses of linear time-invariant PDEs that avoids the need for finite dimensional approximations of differential operators in the evolution equation. Our mathematical framework facilitates the use of recently developed computing environment, `Chebfun` [37], that is capable of solving boundary value problems and eigenvalue problems with superior accuracy.

1.3 Dissertation structure

The dissertation is organized into three parts. Each part contains individual chapters that describe various projects that were carried out in my graduate studies. Note that each chapter is self-contained with sections dedicated to providing necessary background, concluding remarks, future research, and miscellaneous information.

Part I is devoted to control and dynamics of transitional channel flows of Newtonian fluids, and it contains Chapters 2 – 4. Chapter 2 gives a brief description of the governing equations for incompressible channel flows of Newtonian fluids. In particular, it illustrates how the linearized Navier-Stokes equations can be put into an evolution form that is amendable for analysis and computation. Furthermore, it provides an overview of the mathematics behind Channelflow [38] which is a collection of C++ codes used to conduct high-fidelity or direct numerical simulations of the full-nonlinear Navier-Stokes equations in a channel geometry. We have also included a brief description on the implementation of boundary actuations for 3D channel flows in numerical simulations. For controlling the onset of turbulence: (i) Chapter 3 uses direct numerical simulations to assess the efficacy of blowing and suction in the form of streamwise traveling waves; and (ii) Chapter 4 studies the design of localized optimal state-feedback controllers. Chapter 5 analyzes the influence of roll and streak structures in transition and turbulence.

Part II considers transitional and turbulent channel flows of viscoelastic fluids. It contains three projects that involve using systems theoretic tools to model and analyze these complex fluids. For inertialess shear-driven channel flows of viscoelastic fluids: (i) Chapter 6 studies the worst-case amplification of velocity and polymer stress fluctuations in flows driven by external disturbances; and (ii) Chapter 7 uses singularly perturbation methods to study the slow-fast decomposition of the flow system. In Chapter 8, we utilize a model-based method to study the influence of polymers on drag reduction in a turbulent channel flow.

Part III discusses the development of computational tools for analysis of spatially distributed systems. We present a reliable method in Chapter 9 for computations of frequency responses of time-invariant partial differential equations in which an independent spatial variable belongs to a compact interval. We demonstrate the utility of Chebfun [37] which is a powerful Matlab toolset for numerical computation with functions of real variable. Chebfun is a collection of Matlab programs which implement an automatic Chebyshev collocation method and it is based on the idea of overloading Matlab commands for vectors and matrices to functions and operators.

1.4 Key contributions

In what follows, we discuss the major contributions of this dissertation.

Part I

Controlling the onset of turbulence by streamwise traveling waves: direct numerical simulations. We highlight the effects of the modified base flow on the dynamics of velocity fluctuations and net power balance. Our simulations show that the upstream traveling waves promote turbulence even when the uncontrolled flow stays laminar. On the other hand, our selected downstream traveling waves are capable of reducing the fluctuations' kinetic energy, thereby maintaining the laminar flow, see Figure 1.8 for an illustration. In flows driven by a fixed pressure gradient, a positive net efficiency as large as 25 % relative to the uncontrolled turbulent flow can be achieved with downstream waves. Furthermore, we show that these waves can also relaminarize fully developed turbulent flows at low Reynolds numbers.

Optimal localized control of a transitional channel flow. We consider actuation generated by blowing and suction at the walls, and the actuators are placed along a two-dimensional lattice of equally spaced points with each actuator using information from only a limited number of nearby neighbors. We utilize recently developed tools for designing structured optimal feedback gains to reduce receptivity of velocity fluctuations to flow disturbances in the presence of control. Our simulation results, conducted at a low Reynolds number, show that this approach can indeed maintain the laminar flow. This is in contrast to the localized strategies obtained by spatial truncation of optimal centralized controllers, which may introduce instability and promote transition even in the situations where the uncontrolled flow stays laminar.

Dynamics of roll and streak structures in transition and turbulence. The dynamical significance of streamwise elongated structures in wall-turbulence is supported by a growing body of work pointing to their central role in both transition to turbulence and maintenance of turbulent flows. Streamwise coherent "roll cells" associated with streamwise elongated regions of low and high streamwise momentum have been observed in both direct numerical simulations of turbulent channel flow as well as in boundary layer and pipe flow experiments. These so-called streak structures are of great interest because they account for a substantial portion of the turbulent kinetic energy and have been shown to modulate the activity of near-wall structures. Here, to study the role of roll and streak structure in transition and turbulence, we develop tools for running high-fidelity numerical simulations of the streamwise constant (2D/3C) and streamwise averaged (SSST) models. Our numerical simulations confirm that the 2D/3C model accurately obtains the turbulent mean velocity profile despite the fact that it only includes one-way coupling from the cross-stream perturbations to the mean flow. The SSST system augments the 2D/3C model through the addition of feedback from this streamwise constant mean flow to the dynamics of streamwise varying perturbations.

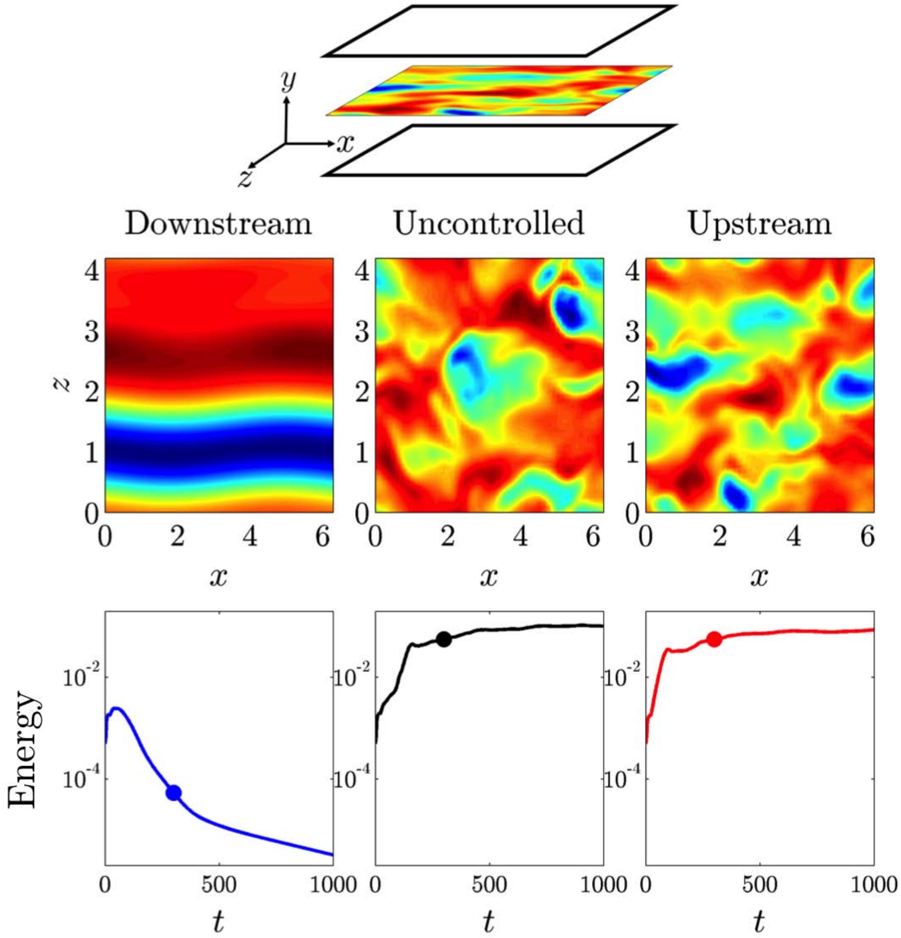

Figure 1.8: Preview of Chapter 3: controlling the onset of turbulence via streamwise traveling waves. First row: channel flow geometry with a contour of the streamwise velocity at the center of the channel. Second row: velocity fluctuations in the streamwise direction at time $t = 300$ for the uncontrolled flow with Reynolds number $R = 2000$ and flows subject to downstream and upstream traveling waves (generated by blowing and suction along the walls). Third row: kinetic energy of velocity fluctuations as a function of time t. The downstream traveling waves prevent the flow from becoming turbulent by suppressing growth of fluctuations' energy, while the uncontrolled flow and the upstream traveling waves trigger transition to turbulence by promoting growth of fluctuations' energy. In flows that are not turbulent flow patterns are very regular (downstream waves), and in turbulent flows they are complex and disordered (uncontrolled and upstream waves).

With this additional feedback, the SSST system supports a perturbation/mean flow interaction instability leading to a bifurcation from the laminar mean flow to a self-sustaining turbulent state. Once in this self-sustaining state the SSST collapses to a minimal representation of turbulence in which a single streamwise perturbation interacts with the mean flow. Comparisons of high-fidelity numerical data with simulations of this self-sustaining state demonstrate that this minimal representation of turbulence produces accurate statistics for both the mean flow and the perturbations. These results suggest that SSST captures fundamental aspects of the mechanisms underlying transition to and maintenance of turbulence in wall-bounded shear flows.

Part II

Worst-case amplification of disturbances in an inertialess shear-driven channel flow of viscoelastic fluids. We study the amplification of deterministic disturbances in an inertialess Couette flow of viscoelastic fluids by analyzing the frequency responses from spatio-temporal body forces to the velocity and polymer stress fluctuations. In strongly elastic flows, we show that disturbances with large streamwise length scales may be significantly amplified even in the absence of inertia. For fluctuations without streamwise variations, we derive explicit analytical expressions for the dependence of the worst-case amplification (from different forcing to different velocity and polymer stress components) on the Weissenberg number (We), the maximum extensibility of the polymer chains (L), the viscosity ratio, and the spanwise wavenumber. For the Oldroyd-B model, the amplification of the most energetic components of velocity and polymer stress fields scales as We^2 and We^4. On the other hand, finite extensibility of polymer molecules limits the largest achievable amplification even in flows with infinitely large Weissenberg numbers: in the presence of wall-normal and spanwise forces the amplification of the streamwise velocity and polymer stress fluctuations is bounded by quadratic and quartic functions of L. This high amplification signals low robustness to modeling imperfections of inertialess channel flows of viscoelastic fluids. The underlying physical mechanism involves interactions of polymer stress fluctuations with a base shear, and it represents a close analog of the lift-up mechanism that initiates a bypass transition in inertial flows of Newtonian fluids.

Slow-fast decomposition of an inertialess flow of viscoelastic fluids. We study the frequency responses of an inertialess two-dimensional channel flow of viscoelastic fluids. By rewriting the evolution equations in terms of low-pass filtered versions of the stream function, we show that strongly-elastic flows can be brought into a standard singularly perturbed form that exhibits a slow-fast decomposition. In high-Weissenberg number regime, which is notoriously difficult to study numerically, we demonstrate that the frequency responses are reliably captured by the dynamics of the fast subsystem. We use numerical computations to validate our theoretical findings and to illustrate that our formulation does not suffer from spurious numerical instabilities.

Analysis of polymer drag reduction in a turbulent channel flow. We develop a model-based approach for studying the influence of polymers on drag reduction in a turbulent channel flow. Our simulation-free method utilizes turbulence modeling in conjunction with the analysis of stochastically forced linearized equations to capture the effect of velocity and polymer stress fluctuations on the turbulent viscosity and drag. Compared to traditional methods, that relies on numerical simulations, we determine the turbulent mean velocity from the second-order statistics of the linearized model driven by white-in-time stochastic forcing. The spatial power spectrum of the forcing is selected to ensure that the linearized model for the flow without polymers reproduces the turbulent energy spectrum. We show that the essential drag-reducing trends and turbulent mean velocity observed in direct numerical simulations are captured by our approach. This demonstrates that our model-based approach has the potential for capturing underlying physical mechanisms responsible for polymer induced drag reduction. Furthermore, the proposed model is expected to pave for way for future analysis of polymer induced turbulent channel flows at higher Weissenberg number and finite-extensibility of the polymer chains than currently possible.

Part III

Computation of frequency responses for linear time-invariant PDEs on a compact interval. We develop the mathematical framework and computational tools for calculating frequency responses of linear time-invariant PDEs in which an independent spatial variable belongs to a compact interval. In conventional studies this computation is done numerically using spatial discretization of differential operators in the evolution equation. Instead, we introduce an alternative method that avoids the need for finite-dimensional approximation of the underlying operators. Our approach has two advantages over currently available schemes: first, it avoids numerical instabilities encountered in systems with differential operators of high order and, second, it alleviates difficulty in implementing boundary conditions. We provide examples from Newtonian and viscoelastic fluid dynamics to illustrate utility of the proposed method. In addition, we have developed easy-to-use softwares that are available at

`www.umn.edu/~mihailo/sofware/chebfun-svd/`.

Part I

Controlling the onset of turbulence in channel flows of Newtonian fluids

Chapter 2

Preliminaries: Incompressible channel flows of Newtonian fluids

In this chapter we summarize the basic mathematical frameworks of incompressible channel flows of viscous Newtonian fluids that are relevant to Chapters 3 and 4. We first present the governing equations and show how to obtain the evolution equations that are amenable for analysis and computation. We then provide a discussion on the spectral method used for simulating three-dimensional channel flows of viscous Newtonian fluids.

2.1 Navier-Stokes equations

We confine our attention to incompressible channel flows of a viscous Newtonian fluid where the velocity and pressure fields satisfy the Navier-Stokes (NS) and the continuity equations given in their non-dimensional form by

$$\mathbf{u}_t \;=\; -\left(\mathbf{u}\cdot\boldsymbol{\nabla}\right)\mathbf{u} \,-\, \boldsymbol{\nabla}p \,+\, \frac{1}{R}\Delta\mathbf{u}, \tag{2.1a}$$

$$0 \;=\; \boldsymbol{\nabla}\cdot\mathbf{u}, \tag{2.1b}$$

where $\mathbf{u}$ is the velocity vector, p is the pressure, R denotes the Reynolds number, $\boldsymbol{\nabla}$ is the gradient, and $\Delta = \boldsymbol{\nabla}\cdot\boldsymbol{\nabla}$ is the Laplacian. Each field is assumed to vary both temporally and spatially, e.g. $\mathbf{u} = \mathbf{u}(x, y, z, t)$. The system of equations (2.1a) exhibits a steady-state solution for the velocities,

$$\bar{\mathbf{u}} \;=\; \left[\begin{array}{ccc} U(y) & 0 & 0 \end{array}\right]^T, \tag{2.2}$$

where $U(y) = y$ in shear-driven (Couette) flow and $U(y) = 1 - y^2$ in pressure-driven (Poiseuille) flow, see figure 2.1 for an illustration.

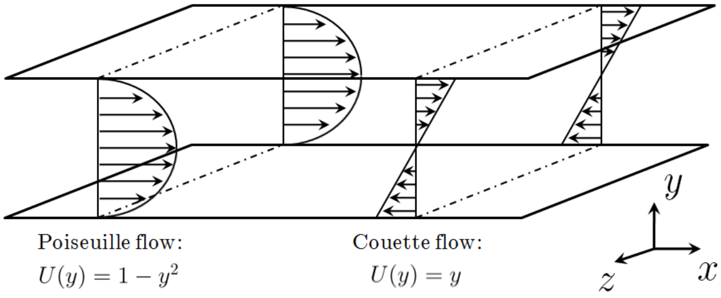

Figure 2.1: Channel flow geometry. Fluid flows between two rigid walls at $y = \pm 1$. The boundary conditions are periodic in the streamwise (x) and spanwise (z) directions and no-slip at the walls. The mean flow $\bar{u}(y)$ is driven in the x-direction by either a mean pressure gradient or a mean shear.

2.1.1 Linearized NS equations

The linearized Navier-Stokes (LNS) equations are obtained by first decomposing the velocity and pressure fields into their respective nominal and fluctuating parts

$$\mathbf{u} \;=\; \bar{\mathbf{u}} + \tilde{\mathbf{u}}, \quad p \;=\; \bar{p} + \tilde{p}. \tag{2.3}$$

Substitution of (2.3) into (2.1a) yields

$$\tilde{\mathbf{u}}_t \;=\; -\left(\bar{\mathbf{u}} \cdot \boldsymbol{\nabla}\right)\tilde{\mathbf{u}} \,-\, \left(\tilde{\mathbf{u}} \cdot \boldsymbol{\nabla}\right)\bar{\mathbf{u}} \,-\, \left(\tilde{\mathbf{u}} \cdot \boldsymbol{\nabla}\right)\tilde{\mathbf{u}} \,-\, \boldsymbol{\nabla}\tilde{p} + \frac{1}{R}\Delta\tilde{\mathbf{u}}. \tag{2.4}$$

The LNS equations that describe the dynamics of infinitesimal velocity and pressure fluctuations are obtained by neglecting the second order term $\left(\tilde{\mathbf{u}} \cdot \boldsymbol{\nabla}\right)\tilde{\mathbf{u}}$,

$$\tilde{\mathbf{u}}_t \;=\; -\left(\bar{\mathbf{u}} \cdot \boldsymbol{\nabla}\right)\tilde{\mathbf{u}} \,-\, \left(\tilde{\mathbf{u}} \cdot \boldsymbol{\nabla}\right)\bar{\mathbf{u}} \,-\, \boldsymbol{\nabla}\tilde{p} + \frac{1}{R}\Delta\tilde{\mathbf{u}}, \tag{2.5a}$$

$$0 \;=\; \boldsymbol{\nabla} \cdot \tilde{\mathbf{u}}. \tag{2.5b}$$

In addition, we consider the LNS equations in the presence of external forces or excitations. This can be incorporated by adding spatially-temporally varying body forces $\mathbf{d}(x, y, z, t)$ to obtain

$$\tilde{\mathbf{u}}_t \;=\; -\left(\bar{\mathbf{u}} \cdot \boldsymbol{\nabla}\right)\tilde{\mathbf{u}} \,-\, \left(\tilde{\mathbf{u}} \cdot \boldsymbol{\nabla}\right)\bar{\mathbf{u}} \,-\, \boldsymbol{\nabla}\tilde{p} + \frac{1}{R}\Delta\tilde{\mathbf{u}} \,+\, \mathbf{d}, \tag{2.6a}$$

$$0 \;=\; \boldsymbol{\nabla} \cdot \tilde{\mathbf{u}}. \tag{2.6b}$$

Finally, by substituting (2.2) into (2.6a), we can rewrite the externally excited LNS system (2.6) as

$$\begin{aligned} u_t \,+\, U\,\partial_x\,u \,+\, U'\,v &= \,-\,\partial_x\,p \,+\, \frac{1}{R}\Delta u \,+\, d_1, &(2.7a)\\ v_t \,+\, U\,\partial_x\,v &= \,-\,\partial_y\,p \,+\, \frac{1}{R}\Delta v \,+\, d_2, &(2.7b)\\ w_t \,+\, U\,\partial_x\,w &= \,-\,\partial_z\,p \,+\, \frac{1}{R}\Delta w \,+\, d_3, &(2.7c)\\ \partial_x\,u \,+\, \partial_y\,v \,+\, \partial_z\,w &= \,0, &(2.7d)\end{aligned}$$

where $\tilde{\mathbf{u}} = \begin{bmatrix} u & v & w \end{bmatrix}^T$, $\mathbf{d} = \begin{bmatrix} d_1 & d_2 & d_3 \end{bmatrix}^T$, and $U' = \mathrm{d}U/\mathrm{d}y$.

2.1.2 Evolution model

We first note that the LNS equations (2.7) are not in an evolution form because this form does not allow the static-in-time relationship (2.7d). Instead, we can obtain the evolution equations by expressing the velocity fields in terms of the wall-normal velocity (v) and vorticity ($\eta = \partial_z u - \partial_x w$) fluctuations. This is achieved by first taking the divergence of (2.7a) – (2.7c) and using (2.7d) to get an expression for the Laplacian of the pressure

$$\Delta p \;=\; -2U'\partial_x v \,+\, \partial_x\,d_1 \,+\, \partial_y\,d_2 \,+\, \partial_z\,d_3. \tag{2.8}$$

We can obtain an expression for the wall-normal velocity by eliminating pressure from (2.7b), which yields

$$\Delta v_t \;=\; \left(-U\,\partial_x\,\Delta \,+\, U''\partial_x \,+\, \frac{1}{R}\Delta^2\right) v \,-\, \partial_{xy}\,d_1 \,+\, (\partial_{xx} + \partial_{zz})\,d_2 \,-\, \partial_{yz}\,d_3. \tag{2.9}$$

Then, the equation for η can be obtained by taking the curl of (2.7),

$$\eta_t \;=\; \left(-U\,\partial_x \,+\, \frac{1}{R}\Delta^2\right) \eta \,-\, U'\,\partial_z\,v \,+\, \partial_z\,d_1 \,-\, \partial_x\,d_3. \tag{2.10}$$

Finally, by rearranging the wall-normal velocity and vorticity as the state variables, $\boldsymbol{\psi} = \begin{bmatrix} v & \eta \end{bmatrix}^T$, we arrive at the following evolution equation [39, 40]

$$\boldsymbol{\psi}_t \;=\; \mathcal{A}\,\boldsymbol{\psi} \,+\, \mathcal{B}\,\mathbf{d}, \tag{2.11}$$

where

$$\mathcal{A} \;=\; \begin{bmatrix} \mathcal{A}_{os} & 0 \\ \mathcal{A}_{cp} & \mathcal{A}_{sq} \end{bmatrix} \;=\; \begin{bmatrix} -\Delta^{-1} U\,\partial_x\,\Delta \,+\, \Delta^{-1} U'' \partial_x \,+\, \dfrac{1}{R}\Delta^{-1}\Delta^2 & 0 \\ -\,U'\,\partial_z & -U\,\partial_x \,+\, \dfrac{1}{R}\Delta^2 \end{bmatrix},$$

$$\mathcal{B} \;=\; \begin{bmatrix} \mathcal{B}_1 & \mathcal{B}_2 & \mathcal{B}_3 \end{bmatrix} \;=\; \begin{bmatrix} -\Delta^{-1}\partial_{xy} & \Delta^{-1}\left(\partial_{xx} + \partial_{zz}\right) & -\Delta^{-1}\partial_{yz} \\ \partial_z & 0 & -\partial_x \end{bmatrix}.$$

We note that $\mathcal{A}_{os}$, $\mathcal{A}_{cp}$, and $\mathcal{A}_{sq}$ are respectively referred to as the Orr-Sommerfeld, coupling, and Squire operators. These operators represent integro-differential operators in spatial directions. Furthermore, since $\mathcal{A}$ and $\mathcal{B}$ are translationally invariant in the horizontal directions (x,z), equation (2.11) can be transformed into a parameterized family of one-dimensional operators in the wall-normal direction

$$\hat{\boldsymbol{\psi}}_t \;=\; \hat{\mathcal{A}}\,\hat{\boldsymbol{\psi}} \,+\, \hat{\mathcal{B}}\,\hat{\mathbf{d}}, \tag{2.12}$$

with

$$\hat{\mathcal{A}} \;=\; \begin{bmatrix} \hat{\mathcal{A}}_{os} & 0 \\ \hat{\mathcal{A}}_{cp} & \hat{\mathcal{A}}_{sq} \end{bmatrix} \;=\; \begin{bmatrix} -\mathrm{i}k_x \hat{\Delta}^{-1} U\,\hat{\Delta} \,+\, \mathrm{i}k_x \hat{\Delta}^{-1} U'' \,+\, \dfrac{1}{R}\hat{\Delta}^{-1}\hat{\Delta}^2 & 0 \\ -\mathrm{i}k_z U' & -\mathrm{i}k_x U \,+\, \dfrac{1}{R}\hat{\Delta} \end{bmatrix},$$

$$\hat{\mathcal{B}} \;=\; \begin{bmatrix} \hat{\mathcal{B}}_1 & \hat{\mathcal{B}}_2 & \hat{\mathcal{B}}_3 \end{bmatrix} \;=\; \begin{bmatrix} -\mathrm{i}k_x \hat{\Delta}^{-1}\partial_y & -\left(k_x^2 + k_z^2\right)\hat{\Delta}^{-1} & -\mathrm{i}k_z \hat{\Delta}^{-1}\partial_y \\ \mathrm{i}k_z & 0 & -\mathrm{i}k_x \end{bmatrix}.$$

Here, $\mathrm{i} = \sqrt{-1}$ and $\hat{\Delta} = \partial_{yy} \,-\, \left(k_x^2 \,+\, k_z^2\right)$. For any wavenumber pair (k_x, k_z), $\hat{\mathcal{A}}$ and $\hat{\mathcal{B}}$ are one-dimensional operators in the wall-normal direction.

The boundary conditions on $\hat{v}$ and $\hat{\eta}$ are derived from the no-slip no-penetration boundary conditions

$$\hat{v}(k_x, y = \pm 1, k_z, t) \;=\; \hat{v}'(k_x, y = \pm 1, k_z, t) \;=\; \hat{\eta}(k_x, y = \pm 1, k_z, t) \;=\; 0.$$

Furthermore, the streamwise and spanwise velocity fluctuations can be determined from $\hat{v}$ and $\hat{\eta}$

$$\hat{u} \;=\; \frac{\mathrm{i}}{k_x^2 + k_z^2}\left(k_x\,\partial_y\,\hat{v} \,-\, k_z\,\hat{\eta}\right), \qquad \hat{w} \;=\; \frac{\mathrm{i}}{k_x^2 + k_z^2}\left(k_z\,\partial_y\,\hat{v} \,+\, k_x\,\hat{\eta}\right).$$

2.2 Direct numerical simulations

High-fidelity (or direct numerical) simulations have been extensively used to study fully developed channel flow. Such tools have helped physicists, engineers, and applied mathematicians gain valuable insight into the mechanics of wall-bounded turbulent flows, see [41] for a comprehensive review. In this section, since we utilize direct numerical simulations as a tool for verification of flow control strategies, we provide a discussion of the mathematics behind the spectral method for conducting high-fidelity simulations of transitional and turbulent flows. We note that the mathematical details presented here follow a similar procedure presented in [38]; for full details on spectral methods used in fluid dynamics, consult [32, 42, 43]. The algorithm presented here is utilized to simulate incompressible channel flows of Newtonian fluids and is a fundamental part of the work in Chapters 3 and 4.

We begin by considering an incompressible wall-bounded shear flow of Newtonian fluids in a rectangular domain $L_x \times [-1, 1] \times L_z$. The fluid flow is governed by the Navier-Stokes and continuity equations (2.1). The boundary conditions in the x and z directions are periodic:

$$\mathbf{u}(x + L_x, y, z, t) \;=\; \mathbf{u}(x, y, z, t), \quad \mathbf{u}(x, y, z + L_z, t) \;=\; \mathbf{u}(x, y, z, t).$$

For brevity, we consider the no-slip no-penetration boundary conditions on the velocity fields:

$$\mathbf{u}(x, -1, z, t) \;=\; \mathbf{u}(x, 1, z, t) \;=\; 0.$$

In Section 2.2.4, we describe the procedure for incorporating control actuations on the channel walls by imposing appropriate boundary conditions on the velocity fields.

2.2.1 Base-fluctuation decomposition

We first decompose the total velocity and pressure fields into their respective base and fluctuating parts,

$$\mathbf{u} \;=\; U(y)\,\mathbf{e}_x \,+\, \tilde{\mathbf{u}}, \quad p \;=\; \Pi_x(t)\,x \,+\, \tilde{p}. \tag{2.13}$$

where $U(y)$ denotes the base streamwise velocity, $\mathbf{e}_x$ represents the unit coordinate vector in the streamwise direction, $\tilde{\mathbf{u}}$ is the fluctuating velocity vector, $\Pi_x(t)$ is the time-dependent base pressure gradient, and $\tilde{p}$ denotes the fluctuating pressure field. We note that the decomposition (2.13) for the base flow and pressure gradient are general enough to represent cases like Poisseuille, Couette, and turbulent mean profiles. Substituting (2.13) into (2.1a) gives

$$\tilde{\mathbf{u}}_t \,+\, \boldsymbol{\nabla}\tilde{p} \;=\; \mathbf{L}\tilde{\mathbf{u}} \,-\, \mathbf{N}(\tilde{\mathbf{u}}) \,+\, \mathbf{C}, \tag{2.14}$$

where the linear term $\mathbf{L}\tilde{\mathbf{u}}$, the nonlinear term $\mathbf{N}(\tilde{\mathbf{u}})$, and the constant term $\mathbf{C}$ are given by

$$\begin{aligned} \mathbf{L}\tilde{\mathbf{u}} &= (1/R)\,\Delta\tilde{\mathbf{u}}, & (2.15a)\\ \mathbf{N}(\tilde{\mathbf{u}}) &= (\tilde{\mathbf{u}}\cdot\boldsymbol{\nabla})\,\tilde{\mathbf{u}}, & (2.15b)\\ \mathbf{C} &= \big((1/R)\,U'' \,-\, \Pi_x(t)\big)\,\mathbf{e}_x. & (2.15c) \end{aligned}$$

Since the flow field is periodic in the streamwise and spanwise directions, we next take the discrete spatial Fourier transform of (2.14) which yields

$$\hat{\mathbf{u}}_t \,+\, \hat{\boldsymbol{\nabla}}\hat{p} \,=\, \hat{\mathbf{L}}\hat{\mathbf{u}} \,-\, \widehat{\mathbf{N}(\mathbf{u})} \,+\, \hat{\mathbf{C}}, \tag{2.16}$$

where the Fourier transformed operators for the gradient, the Laplacian, and the linear operator $\mathbf{L}$ are given by

$$\begin{aligned} \hat{\boldsymbol{\nabla}}_{n_x n_z} &= 2\pi\mathrm{i}\,(n_x/L_x)\,\mathbf{e}_x \,+\, \partial_y\,\mathbf{e}_y \,+\, 2\pi\mathrm{i}\,(n_z/L_z)\,\mathbf{e}_z, & (2.17a)\\ \hat{\Delta}_{n_x n_z} &= \partial_{yy} \,-\, 4\pi^2\left((n_x/L_x)^2 \,+\, (n_z/L_z)^2\right), & (2.17b)\\ \hat{\mathbf{L}}_{n_x n_z} &= (1/R)\,\hat{\Delta}_{n_x n_z}, & (2.17c) \end{aligned}$$

with i denoting the imaginary unit, $\mathbf{e}_y$ and $\mathbf{e}_z$ representing the unit coordinate vectors in the wall-normal and spanwise directions and, n_x and n_z denoting the streamwise and spanwise wavenumber modes, respectively. Hereafter, the subscripts $n_x n_z$ and the hat accent will be suppressed for notational convenience.

2.2.2 Time-stepping schemes

We next discuss the time-stepping algorithms used for discrete time-integration. In particular, we present three classes of algorithms: (i) a Crank-Nicolson/Adams-Bashforth (CNAB) scheme; (ii) a 3rd-order Runge-Kutta (RK3) scheme; and (iii) a k-multistep Adams-Bashforth/Backward-Differentiation (ABBDk) scheme. All three classes treat, in (2.16), the linear term implicitly and the nonlinear term explicitly. That is, the approximation of the linear term depends on information from flow quantities at present and future time steps while the approximation of the nonlinear term requires information from flow fields at past and present time levels.

Crank-Nicolson/Adams-Bashforth

Since it is the simplest of all three algorithms, we begin by showing the procedure for the Crank-Nicolson/Adams-Bashforth time stepping scheme. We begin by discretizing the time variable into uniform intervals, $t^n = nh$, and by representing $\mathbf{u}$ at time $t = t^n$ by $\mathbf{u}^n$. Here, h denotes the discretized time step and n is a positive integer. Hence, each term in (2.16) approximated at $t^{n+1/2}$ is given by

$$\begin{aligned} \partial_t \mathbf{u}^{n+1/2} &= \frac{\mathbf{u}^{n+1} - \mathbf{u}^n}{h} + \mathcal{O}(h^2), \\ \mathbf{L}\mathbf{u}^{n+1/2} &= (1/2)\,\mathbf{L}\mathbf{u}^{n+1} + (1/2)\,\mathbf{L}\mathbf{u}^n + \mathcal{O}(h^2), \\ \boldsymbol{\nabla} p^{n+1/2} &= (1/2)\,\boldsymbol{\nabla} p^{n+1} + (1/2)\,\boldsymbol{\nabla} p^n + \mathcal{O}(h^2), \\ \mathbf{N}^{n+1/2} &= (3/2)\,\mathbf{N}^n - (1/2)\,\mathbf{N}^{n-1} + \mathcal{O}(h^2), \\ \mathbf{C}^{n+1/2} &= (1/2)\,\mathbf{C}^{n+1} + (1/2)\,\mathbf{C}^n + \mathcal{O}(h^2), \end{aligned} \tag{2.18}$$

where $\mathbf{N}^n = \widehat{\mathbf{N}(\mathbf{u}^n)}$. This numerical scheme is called Crank-Nicolson/Adams-Bashforth because the nonlinear term $\mathbf{N}$ is approximated using Crank-Nicholson method and the linear term $\mathbf{Lu}$ is approximated using Adams-Bashforth formula. Substituting (2.18) into (2.16) yields

$$\begin{aligned} &\left(\frac{1}{h} - \frac{1}{2}\mathbf{L}\right)\mathbf{u}^{n+1} + \frac{1}{2}\boldsymbol{\nabla} p^{n+1} = \\ &\left(\frac{1}{h} + \frac{1}{2}\mathbf{L}\right)\mathbf{u}^{n} - \frac{1}{2}\boldsymbol{\nabla} p^{n} - \frac{3}{2}\mathbf{N}^n + \frac{1}{2}\mathbf{N}^{n-1} + \frac{1}{2}\mathbf{C}^{n+1} + \frac{1}{2}\mathbf{C}^{n}. \end{aligned} \tag{2.19}$$

We note a few important properties of (2.19): (i) the set of equations are linear in terms of the unknown variables, $\mathbf{u}^{n+1}$ and p^{n+1}; (ii) the right-hand-side can be determined entirely from flow quantities at $t = nh$ and $t = (n-1)h$ and the external mean-pressure parameter; and (iii) it is a parameterized family of linear ordinary differential equations in y where each set of equations can be determined independently for each wavenumber pair (n_x, n_z).

Equations (2.19) can be rewritten into a differential form by expanding the linearized operator on the left-hand-side, which yields

$$\frac{1}{R}\frac{\mathrm{d}^2}{\mathrm{d}y^2}\mathbf{u}^{n+1} - \lambda\mathbf{u}^{n+1} - \boldsymbol{\nabla} p^{n+1} = -\mathbf{R}^n, \tag{2.20}$$

where

$$\begin{aligned} \lambda &= \frac{2}{h} + \frac{4\pi^2}{R}\left(\frac{n_x^2}{L_x^2} + \frac{n_z^2}{L_z^2}\right), \\ \mathbf{R}^n &= ((2/h) + \mathbf{L})\,\mathbf{u}^n + \boldsymbol{\nabla} p^n - 3\mathbf{N}^n + \mathbf{N}^{n-1} + \mathbf{C}^{n+1} + \mathbf{C}^n. \end{aligned}$$

Hence, at each time step, we need to solve (2.20) for each pair of (n_x, n_z). This set of equations is called the tau-equations and can be solved using the influence-matrix method [32, 44] presented in Section 2.2.3.

Scheme	i	α_i	β_i	γ_i	ζ_i
CNAB	0	1/2	1/2	3/2	−1/2
RK3	0	29/96	37/160	8/15	0
	1	−3/40	5/24	5/12	−17/60
	2	1/6	1/6	3/4	−5/12

Table 2.1: Time-stepping coefficients of the Crank-Nicolson/Adams-Bashforth and 3rd-order Runge-Kutta methods.

Third-order Runge-Kutta

Runge-Kutta methods represent one of the important classes of implicit/explicit iterative algorithms for the approximation of solutions to differential equations. The method is similar in principle to the Crank-Nicholson/Adams-Bashforth algorithm, however, it involves multiple subintervals for each time step of length h. That is, a three-substep algorithm follows the sequence $t^{n,0}$, $t^{n,1}$, $t^{n,2}$, $t^{n+1,0}$. By averaging over multiple subintervals within each time step, greater precision can be achieved. Here, we present an algorithm for the third-order Runge-Kutta method which has total accumulated error of $\mathcal{O}(h^3)$.

In summary, using RK3, the numerical discretization of the NS equations is given by

$$\begin{aligned} &\left(\frac{1}{h} - \beta_i\,\mathbf{L}\right)\mathbf{u}^{n,i+1} + \beta_i\,\boldsymbol{\nabla} p^{n,i+1} = \\ &\left(\frac{1}{h} + \alpha_i\,\mathbf{L}\right)\mathbf{u}^{n,i} - \alpha_i\,\boldsymbol{\nabla} p^{n,i} - \gamma_i\,\mathbf{N}^{n,i} - \zeta_i\,\mathbf{N}^{n,i-1} + \beta_i\,\mathbf{C}^{n,i+1} + \alpha_i\,\mathbf{C}^{n,i}, \end{aligned} \tag{2.21}$$

where the second superscript denotes the Runge-Kutta substeps and α_i, β_i, γ_i, and ζ_i represent the appropriate discretization weights which are presented in table 2.1. Furthermore, table 2.1 shows the time-stepping coefficients in which (2.21) simplifies to the CNAB scheme (2.19).

It is worth noting that, since $\zeta_0 = 0$, the RK3 algorithm does not depend on the nonlinear term at the previous timestep, $\mathbf{N}^{n,i-1}$ when $i = 0$. Consequently the time marching scheme can be initiated from a single instantaneous velocity field. This is in contrast to the CNAB algorithm where both $\mathbf{N}^n$ and $\mathbf{N}^{n-1}$ are required and so, two consecutive velocity fields are needed for starting the time-stepping. This makes RK3 particularly convenient for initialization.

Scheme	k	a_0	a_1	a_2	a_3	a_4	b_0	b_1	b_2	b_3
ABBDk	2	$\frac{3}{2}$	-2	$\frac{1}{2}$			2	-1		
	3	$\frac{11}{6}$	-3	$\frac{3}{2}$	$-\frac{1}{3}$		3	-3	1	
	4	$\frac{25}{12}$	-4	3	$-\frac{4}{3}$	$\frac{1}{4}$	4	-6	4	-1

Table 2.2: Time-stepping coefficients of the Adams-Bashforth/Backward-Differentiation (ABBDk) schemes.

Finally, the differential form of (2.21) is given by

$$\frac{1}{R}\frac{\mathrm{d}^2}{\mathrm{d}y^2}\mathbf{u}^{n,i+1} - \lambda_i\,\mathbf{u}^{n,i+1} - \boldsymbol{\nabla} p^{n,i+1} = -\mathbf{R}^{n,i}, \tag{2.22}$$

where

$$\begin{aligned}
\lambda_i &= \frac{1}{\beta_i h} + \frac{4\pi^2}{R}\left(\frac{n_x^2}{L_x^2} + \frac{n_z^2}{L_z^2}\right), \\
\mathbf{R}^{n,i} &= \left(\frac{1}{\beta_i h} + \frac{\alpha_i}{\beta_i}\mathbf{L}\right)\mathbf{u}^{n,i} + \frac{\alpha_i}{\beta_i}\boldsymbol{\nabla} p^{n,i} - \frac{\gamma_i}{\beta_i}\mathbf{N}^{n,i} - \frac{\zeta_i}{\beta_i}\mathbf{N}^{n,i-1} + \mathbf{C}^{n,i+1} + \frac{\alpha_i}{\beta_i}\mathbf{C}^{n,i}.
\end{aligned}$$

k-multistep Adams-Bashforth/Backward-Differentiation

We next present the k-multistep Adams-Bashforth/Backward-Differentiation formulae. Unlike the aforementioned CNAB and RK schemes, the ABBDk is a particularly convenient method because it is based on a semi-implicit multistep algorithm. In addition, the advantage of ABBDk schemes compared to other multistep methods is that ABBDk only involves the linear part at t^{n+1}. In contrast, the high-order extension of the CNAB scheme would require information (of the linear term) at several previous time steps [42]. This strongly implicit formulation produces strong damping for high-frequency modes and results in pressure field as accurate as the velocity field.

The high-order ABBDk schemes, belonging to the family of implicit-explicit multistep methods for parabolic equations introduced by [45], for the NS equations are given by

$$\frac{1}{h}\sum_{j=0}^{k} a_j\,\mathbf{u}^{n+1-j} = -\sum_{j=0}^{k-1} b_j\,\mathbf{N}^{n-j} + \mathbf{L}\mathbf{u}^{n+1} - \boldsymbol{\nabla} p^{n+1} + \mathbf{C}^{n+1}, \tag{2.23}$$

where a_j and b_j represent the appropriate discretization coefficients and they are shown in table 2.2. Note that the 2nd, 3rd, and 4th-order ABBD methods require 1, 2, and 3 initialization steps, respectively. After some algebraic manipulations, we arrive at the tau-equations

$$\frac{1}{R}\frac{\mathrm{d}^2}{\mathrm{d}y^2}\mathbf{u}^{n+1} - \lambda\mathbf{u}^{n+1} - \boldsymbol{\nabla}p^{n+1} = -\mathbf{R}^n, \tag{2.24}$$

where

$$\begin{aligned}\lambda &= \frac{a_j}{h} + \frac{4\pi^2}{R}\left(\frac{n_x^2}{L_x^2} + \frac{n_z^2}{L_z^2}\right),\\ \mathbf{R}^n &= -\sum_{j=0}^{k-1}\left(\frac{a_j}{h}\mathbf{u}^{n-j} + b_j\,\mathbf{N}^{n-j}\right) + \mathbf{C}^{n+1}.\end{aligned}$$

We note that for the NS equations, which require some degree of implicitness, the multistep schemes ABBDk are recommended [42]. In general, the ABBDk scheme requires less computing time compared to the CNAB and RK3 methods and it has a truncation error of $\mathcal{O}\left(h^k\right)$.

2.2.3 Tau-equations and influence-matrix method

In Section 2.2.2, after time-discretization of the NS-equations, we arrive at the following set of ordinary differential equations in the wall-normal y coordinate given in a compact form,

$$\nu\mathbf{u}'' - \lambda\mathbf{u} - \boldsymbol{\nabla}p = -\mathbf{R}, \tag{2.25a}$$

$$\boldsymbol{\nabla}\cdot\mathbf{u} = 0, \tag{2.25b}$$

$$\mathbf{u}(\pm 1) = 0, \tag{2.25c}$$

where $\nu = 1/R$. For notational convenience, we have omitted the time superscripts from here on. It is worthy to note that (2.25) represent a set of three coupled differential equations (2.25a) with four unknowns (u, v, w, p), with one constraint (2.25b), and six boundary conditions (2.25c). This set of equations is called the tau-equations [38]. We next present the influence-matrix method proposed by Kleiser & Schumann [44] to solve (2.25). This method is based on transforming (2.25) into a set of Helmholtz equations which can be efficiently solved using a banded-tridiagonal matrix technique [32].

The influence-matrix method begins by obtaining a system of equations in p and v; this is achieved by: taking the divergence of (2.25a) and extracting the wall-normal component of (2.25a),

$$p'' - \kappa^2 p = -\boldsymbol{\nabla}\cdot\mathbf{R}, \qquad v'(\pm 1) = 0, \tag{2.26a}$$

$$\nu\, v'' - \lambda\, v - p' = -R_y, \qquad v(\pm 1) = 0, \tag{2.26b}$$

where R_y represents the y-component of vector $\mathbf{R}$ and

$$\kappa^2 \;=\; 4\pi\left(\frac{n_x^2}{L_x^2}+\frac{n_z^2}{L_z^2}\right).$$

Equations (2.26) form a well-posed set of equations for p and v. As it stands, this set of equations is difficult to solve since p appears in the differential equation for v while v appears in the boundary conditions for p-equation. In order to solve this set of equations, we consider the following inhomogeneous problem

$$\begin{aligned} p'' - \kappa^2 p \;&=\; -\,\boldsymbol{\nabla}\cdot\mathbf{R}, \qquad p(\pm 1) \;=\; P_{\pm}, &\qquad (2.27\text{a})\\ \nu\, v'' \,-\, \lambda\, v \,-\, p' \;&=\; -\,R_y, \qquad\quad v(\pm 1) \;=\; 0. &\qquad (2.27\text{b}) \end{aligned}$$

where $P_{\pm}$ denotes the pressure value at the walls and is unknown *a priori*. However, we can determine $P_{\pm}$ from the boundary condition requirement that $v'(\pm 1) = 0$. This is achieved by solving the following three sets of equations

$$\begin{aligned} p_\star'' - \kappa^2 p_\star \;&=\; -\,\boldsymbol{\nabla}\cdot\mathbf{R}, \qquad p_\star(\pm 1) \;=\; 0, &\qquad (2.28\text{a})\\ \nu\, v_\star'' \,-\, \lambda\, v_\star \,-\, p_\star' \;&=\; -\,R_y, \qquad\quad v_\star(\pm 1) \;=\; 0, &\qquad (2.28\text{b}) \end{aligned}$$

$$\begin{aligned} p_+'' - \kappa^2 p_+ \;&=\; 0, \qquad p_+(+1) \;=\; 1, \quad p_+(-1) \;=\; 0, &\qquad (2.29\text{a})\\ \nu\, v_+'' \,-\, \lambda\, v_+ \,-\, p_+' \;&=\; 0, \qquad v_+(\pm 1) \;=\; 0, &\qquad (2.29\text{b}) \end{aligned}$$

$$\begin{aligned} p_-'' - \kappa^2 p_- \;&=\; 0, \qquad p_-(+1) \;=\; 0, \quad p_-(-1) \;=\; 1, &\qquad (2.30\text{a})\\ \nu\, v_-'' \,-\, \lambda\, v_- \,-\, p_-' \;&=\; 0, \qquad v_-(\pm 1) \;=\; 0. &\qquad (2.30\text{b}) \end{aligned}$$

The solution $(p_\star, v_\star)$ to the first set of equations (2.28) denotes the particular solution with homogeneous Dirichlet boundary conditions. On the other hand, (p_+, v_+) and (p_-, v_-) represent the solutions to the homogenous problem (2.27). Then, the solution (p, v) to problem (2.26) can be constructed by the following relation

$$\begin{bmatrix} p \\ v \end{bmatrix} \;=\; \begin{bmatrix} p_\star \\ v_\star \end{bmatrix} \,+\, \delta_+ \begin{bmatrix} p_+ \\ v_+ \end{bmatrix} \,+\, \delta_- \begin{bmatrix} p_- \\ v_- \end{bmatrix}, \qquad (2.31)$$

where δ_+ and δ_- are determined such that the boundary conditions on (p, v) for problem (2.27) are satisfied, i.e.,

$$\begin{bmatrix} v_+'\,(+1) & v_-'\,(+1) \\ v_+'\,(-1) & v_-'\,(-1) \end{bmatrix} \begin{bmatrix} \delta_+ \\ \delta_- \end{bmatrix} \;=\; -\begin{bmatrix} v_\star'\,(+1) \\ v_\star'\,(-1) \end{bmatrix}. \qquad (2.32)$$

The 2×2 coefficient matrix in (2.32) is known as the influence-matrix. Solving (2.32) for $\delta_\pm$ produces the proper boundary conditions for (2.27) (i.e., $P_\pm = \delta_\pm$) and consequently, the solution to (2.27) then satisfies the original problem (2.26). It is noteworthy that since the solution to (2.29) and (2.30) are independent of the velocity and pressure fields, their solutions can be precomputed and saved in memory. Hence, the influence-matrix is calculated only once initially for each wavenumber pair (n_x, n_z).

In summary, at each time step, the following steps are taken to find the velocity and pressure fields:

1. solve problem (2.28) for solution $(p_\star, v_\star)$;
2. determine the correct pressure boundary conditions $P_\pm$ using the influence matrix;
3. solve problem (2.27) using the correct boundary conditions for the solution (p, v);
4. with p, solve the following equations for the streamwise and spanwise velocities,

$$\begin{array}{rcll} \nu\, u'' \,-\, \lambda\, u \,-\, 2\pi \mathrm{i}\, (n_x/L_x)\, p &=& -R_x, & u\,(\pm 1) \;=\; 0, \\ \nu\, w'' \,-\, \lambda\, w \,-\, 2\pi \mathrm{i}\, (n_z/L_z)\, p &=& -R_z, & w\,(\pm 1) \;=\; 0, \end{array} \tag{2.33}$$

where R_x and R_z represent the x- and z-components of the vector $\mathbf{R}$.

It is crucial to mention that discretization of the differential operators in tau-equations (2.25) introduces additional terms that need to be taken into account when solving for the velocity and pressure fields. This requires adding a tau-correction to the solution of the tau-equations in their discretized form. Discussion of the tau-correction is beyond the scope of this dissertation; however, detailed procedure can be found in [32].

2.2.4 Boundary actuations

Up to now, we have assumed no-slip no-penetration boundary conditions on the velocity fields, i.e.,

$$\begin{array}{rcccl} v(x, \pm 1, z, t) &=& v'(x, \pm 1, z, t) &=& 0, \\ u(x, \pm 1, z, t) &=& w(x, \pm 1, z, t) &=& 0. \end{array}$$

However, in flows with control the velocity fields may inherit different boundary conditions. In this section, we demonstrate the procedure for installing nonhomogeneous boundary conditions in the numerical schemes. We present the procedure for blowing and suction along the walls in the form of a streamwise traveling wave. A similar procedure can be used to implement other boundary actuations, for example, transverse wall-oscillations or more complicated scenarios encountered when designing feedback control strategies.

Blowing and suction: streamwise traveling waves

In Chapter 3, we use blowing and suction actuation along the walls of a channel in the form of a streamwise traveling wave to control the onset of turbulence in shear flows.

This sensorless control strategy has been shown to exhibit promising drag reducing properties [2]. In flows subjected to zero-net-mass-flux surface blowing and suction in the form of a streamwise traveling wave, the following boundary conditions are imposed on the velocity fields

$$\begin{aligned} v\,(x,\pm 1,z,t) \;&=\; \mp\, 2\,\alpha \cos\left(\omega_x\,(x-ct)\right), && \text{(2.34a)}\\ u\,(x,\pm 1,z,t) \;&=\; v'\,(x,\pm 1,z,t) \;=\; w\,(x,\pm 1,z,t) \;=\; 0, && \text{(2.34b)} \end{aligned}$$

where ω_x, c, and α denote frequency, speed, and amplitude of the streamwise traveling wave. The numerical methods discussed in the aforementioned sections are capable of handling the boundary conditions (2.34). This is done by appropriately changing the boundary conditions for the velocity fields in (2.28). To illustrate this, we first rewrite (2.34a) using the Euler's formula,

$$v\,(x,\pm 1,z,t) \;=\; \mp\,\alpha\left(\mathrm{e}^{\mathrm{i}\omega_x x}\mathrm{e}^{-\mathrm{i}\omega_x ct} \,+\, \mathrm{e}^{-\mathrm{i}\omega_x x}\mathrm{e}^{\mathrm{i}\omega_x ct}\right), \tag{2.35}$$

where e denotes the base of the natural logarithm. Furthermore, taking the discrete spatial Fourier transform of (2.35) in the horizontal directions yields

$$\hat{v}_{n_x n_z}\,(y=\pm 1,t) \;=\; \begin{cases} \mp\alpha\,\mathrm{e}^{-\mathrm{i}\omega_x ct}, & n_x \;=\; \bar{n}_x, \quad n_z \;=\; 0,\\ \mp\alpha\,\mathrm{e}^{\mathrm{i}\omega_x ct}, & n_x \;=\; -\bar{n}_x, \quad n_z \;=\; 0,\\ 0, & \text{otherwise}, \end{cases} \tag{2.36}$$

where

$$\bar{n}_x \;=\; \frac{\omega_x L_x}{2\pi}.$$

Here, we let $\bar{n}_x$ be called the fundamental streamwise wavenumber for obvious reason. This indicates that for streamwise traveling waves, the wall-normal velocity assumes non-zero boundary conditions at the fundamental wavenumber and homogeneous boundary conditions at all other wavenumber pairs. We note that, since the fundamental wavenumber $\bar{n}_x$ is an integer by definition, the length of the channel walls in the streamwise direction L_x need to be selected such that $\bar{n}_x$ is an integer for a given frequency of the traveling wave ω_x.

Finally, the boundary conditions for $v_\star$ in the problem (2.28) are given by

$$v_\star\,(y=\pm 1,t) \;=\; \begin{cases} \mp\alpha\,\mathrm{e}^{-\mathrm{i}\omega_x ct}, & n_x \;=\; \bar{n}_x, \quad n_z \;=\; 0,\\ \mp\alpha\,\mathrm{e}^{\mathrm{i}\omega_x ct}, & n_x \;=\; -\bar{n}_x, \quad n_z \;=\; 0,\\ 0, & \text{otherwise}. \end{cases} \tag{2.37}$$

Chapter 3

Controlling the onset of turbulence by streamwise traveling waves: direct numerical simulations

This chapter builds on and confirms the theoretical findings of Moarref & Jovanović [3]. Here, we use direct numerical simulations of the Navier-Stokes equations to assess the efficacy of blowing and suction in the form of streamwise traveling waves for controlling the onset of turbulence in a channel flow. We highlight the effects of the modified base flow on the dynamics of velocity fluctuations and net power balance. Our simulations verify the theoretical predictions of [3] that the upstream traveling waves promote turbulence even when the uncontrolled flow stays laminar. On the other hand, the downstream traveling waves with parameters selected in [3] are capable of reducing the fluctuations' kinetic energy, thereby maintaining the laminar flow. In flows driven by a fixed pressure gradient, a positive net efficiency as large as 25 % relative to the uncontrolled turbulent flow can be achieved with downstream waves. Furthermore, we show that these waves can also relaminarize fully developed turbulent flows at low Reynolds numbers. We conclude that the theory developed in [3] for the linearized flow equations with uncertainty has considerable ability to predict full-scale phenomena.

3.1 Introduction

The problem of controlling channel flows using strategies that do not require measurement of the flow quantities and disturbances has recently received significant attention. Examples of these sensorless approaches to flow control include wall geometry deformation such as riblets, transverse wall oscillations, and control of conductive fluids using the Lorentz force, to name only a few. Min *et al.* [2] used direct numerical simulations (DNS) to show that surface blowing and suction in the form of an upstream traveling wave (UTW) leads to a sustained sub-laminar drag in a fully developed turbulent channel flow. This motivated Marusic, Joseph & Mahesh [46] to derive a criterion for achieving sub-laminar drag and to compare laminar and turbulent channel flows with and without control. Furthermore, Hœpffner & Fukagata [47] characterized the mechanism behind UTWs as a *pumping* rather than as a drag reduction; this is because the UTWs increase flux relative to the uncontrolled flow. Finally, Bewley [48] and Fukagata, Sugiyama & Kasagi [49] independently established that for any blowing and suction boundary actuation, the power exerted at the walls is always larger than the power saved by reducing drag to sub-laminar levels. This leads one to conclude that the optimal control solution is to relaminarize the flow.

Heretofore, sensorless flow control strategies have been designed by combining physical intuition with extensive numerical and experimental studies. For example, a number of simulations on turbulent drag reduction by means of spanwise wall oscillation was conducted by [50] where 37 cases of different control parameters were considered. Compared to the turbulent uncontrolled flow, a maximum drag reduction of 44.7 % was reported. However, analysis of the power spent by the movement of the walls shows that a maximum net power gain of only 7.3 % can be achieved. Even though DNS and experiments offer valuable insight into sensorless strategies, their utility can be significantly enhanced by developing a model-based framework for sensorless flow control design.

This chapter builds directly on the theoretical findings of [3], which we refer to as Part 1 from hence forward, where receptivity analysis was used to show that the downstream traveling waves (DTWs) are capable of reducing energy amplification of velocity fluctuations in a transitional channel flow. The effectiveness of DTWs and UTWs in preventing or enhancing transition is examined in this work. In contrast to the current practice, we do not use DNS as a design tool; rather, we utilize them as a means for verification and validation of theoretical predictions offered in Part 1 of this study. Namely, we use DNS to confirm that the DTWs with parameters selected in Part 1 can control the onset of turbulence and achieve positive net efficiency relative to the uncontrolled flow that becomes turbulent. On the contrary, the UTWs enhance transient growth and induce turbulence even when the uncontrolled flow stays laminar. In spite of promoting turbulence, the UTWs with large amplitudes can provide sub-laminar drag coefficient. However, we show that this comes at the expense of poor net power balance in flows driven by a fixed pressure gradient. This is in agreement with [47], where it was shown that it costs more to achieve the same amount of pumping using wall-transpiration than pressure gradient type of actuation. Our numerical simulations show the predictive power of the theoretical framework developed in Part 1 and suggest that the linearized Navier-Stokes (NS) equations with uncertainty represent an effective control-oriented model for maintaining the laminar flow.

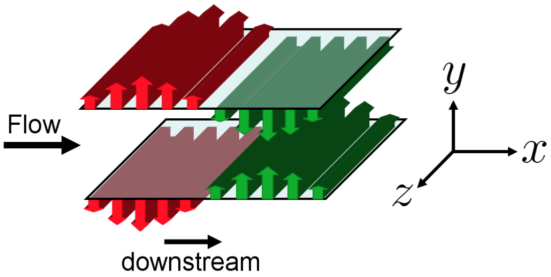

Figure 3.1: A channel flow with blowing and suction along the walls.

This chapter is organized as follows: in Section 3.2, we present the governing equations, describe the numerical method used in our simulations, and outline the influence of traveling waves on control net efficiency. The evolution of three dimensional (3D) fluctuations around base flows induced by surface blowing and suction is studied in Section 3.3. We further emphasize how velocity fluctuations affect skin-friction drag coefficient and net power balance. The energy amplification mechanisms are discussed in Section 3.3.4, where we show that the DTWs improve transient behavior relative to the uncontrolled flow by reducing the production of kinetic energy. In addition, the effect of traveling waves on coherent flow structures in transitional flows is visualized in Section 3.3.5, where it is shown that the DTWs control the onset of turbulence by weakening the intensity of the streamwise streaks. In Section 3.4, we show that the downstream waves designed in Part 1 can also relaminarize fully developed turbulent flows at low Reynolds numbers. A summary of the chapter and an outlook for future research directions is given in Section 3.5.

3.2 Problem formulation and numerical method

3.2.1 Governing equations

We consider a 3D incompressible flow of a viscous Newtonian fluid in a straight channel; see figure 3.1 for geometry. The spatial coordinates (x, y, z) are scaled with the channel half height, δ, and they denote the streamwise, wall-normal, and spanwise directions, respectively; the velocities are scaled with the centerline velocity of the laminar parabolic profile, U_c; the pressure is scaled with ρU_c^2, where ρ denotes the fluid density; and the time is scaled with the convective time scale, δ / U_c. The flow is driven by a streamwise pressure gradient and it satisfies the non-dimensional NS and continuity equations

$$\mathbf{u}_t \;=\; -\left(\mathbf{u} \cdot \boldsymbol{\nabla}\right) \mathbf{u} \;-\; \boldsymbol{\nabla} P \;+\; (1/R_c) \Delta \mathbf{u}, \quad 0 \;=\; \boldsymbol{\nabla} \cdot \mathbf{u}. \tag{3.1}$$

Here, R_c denotes the Reynolds number, $R_c = U_c \delta / \nu$, ν is the kinematic viscosity, $\mathbf{u}$ is the velocity vector, P is the pressure, $\boldsymbol{\nabla}$ is the gradient, and Δ is the Laplacian,

$\Delta = \boldsymbol{\nabla} \cdot \boldsymbol{\nabla}$.

In addition to the constant pressure gradient, $P_x = -2/R_c$, let the flow be subject to a zero-net-mass-flux surface blowing and suction in the form of a streamwise traveling wave [2]. The base velocity, $\mathbf{u}_b = (U, V, W = 0)$, represents the steady-state solution to (3.1) in the presence of the following boundary conditions

$$V(y = \pm 1) \;=\; \mp 2\,\alpha\,\cos\left(\omega_x(x \,-\, c\,t)\right), \;\; U(\pm 1) \;=\; V_y(\pm 1) \;=\; W(\pm 1) \;=\; 0, \qquad (3.2)$$

where ω_x, c, and α denote frequency, speed, and amplitude of the streamwise traveling wave. Positive values of c identify a DTW, while negative values of c identify a UTW. In the presence of velocity fluctuations, $\mathbf{u}$ represents the sum of base velocity, $\mathbf{u}_b$, and velocity fluctuations, $\mathbf{v} = (u, v, w)$, where u, v, and w denote the fluctuations in the streamwise, wall-normal, and spanwise directions, respectively.

3.2.2 Numerical method

The streamwise traveling waves, considered theoretically in Part 1, are tested in DNS of a 3D transitional Poiseuille flow in this work. All DNS calculations are obtained using the code developed by [38]. A multistep semi-implicit Adams-Bashforth/Backward-Differentiation (AB/BDE) scheme described in Chapter 2 is used for time discretization. The AB/BDE treats the linear terms implicitly and the nonlinear terms explicitly. A spectral method [32] is used for the spatial derivatives with Chebyshev polynomial expansion in the wall-normal direction and Fourier series expansion in the streamwise and spanwise directions. Aliasing errors from the evaluation of the nonlinear terms are removed by the 3/2-rule when the horizontal FFTs are computed. We modified the code to account for the streamwise traveling wave boundary conditions (3.2) according to the procedure described in Chapter 2.

The NS equations are integrated in time with the objective of computing fluctuations' kinetic energy, skin-friction drag coefficient, and net power balance, Section 3.3. The velocity field is first initialized with the laminar parabolic profile in the absence of 3D fluctuations, Section 3.2.3; this yields the 2D base flow which is induced by the fixed pressure gradient, $P_x = -2/R_c$, and the boundary conditions (3.2). In simulations of the full 3D flows (cf. Section 3.3), an initial 3D perturbation is superimposed to the base velocity, $\mathbf{u}_b$. As the initial perturbation, we consider a random velocity field developed by [38] which has the ability to trigger turbulence by exciting all the relevant Fourier and Chebyshev modes. This divergence-free initial condition is composed of random spectral coefficients that decay exponentially and satisfy homogenous Dirichlet boundary conditions at the walls. The flux and energy of the velocity fluctuations are computed at each time step.

A *fixed pressure gradient* is enforced in all simulations which are initiated at $R_c = 2000$; this value corresponds to the Reynolds number $R_\tau = 63.25$ based on the friction velocity, u_τ. Owing to the fixed pressure gradient, the steady-state value of R_τ is

Case	Symbol	c	ω_x	α	L_x/δ	L_z/δ	N_y	N_x	N_z
0	×	–	–	–	2π	$4\pi/3$	65	50	50
1	□	5	2	0.035	2π	$4\pi/3$	65	50	50
2	○	5	2	0.050	2π	$4\pi/3$	65	50	50
3	◇	5	2	0.125	2π	$4\pi/3$	65	50	50
4	◁	−2	0.5	0.015	8π	$4\pi/3$	65	200	50
5	▽	−2	0.5	0.050	8π	$4\pi/3$	65	200	50
6	△	−2	0.5	0.125	8π	$4\pi/3$	65	200	50

Table 3.1: The computational domain and spatial discretization considered in simulations of the uncontrolled flow, DTWs with ($c = 5$, $\omega_x = 2$, $\alpha = \{0.035,\, 0.050, 0.125\}$), and UTWs with ($c = -2$, $\omega_x = 0.5$, $\alpha = \{0.015, 0.050, 0.125\}$). Symbols identify the corresponding flow in figures that follow. The box sizes in the streamwise and spanwise directions are denoted by L_x and L_z, respectively. The number of grid points in the streamwise, wall-normal, and spanwise directions are represented by N_i, $i = \{x, y, z\}$, respectively.

the same for all simulations, $R_\tau = 63.25$. In addition, we consider a streamwise box length, $L_x = 4\pi/\omega_x$, for all controlled flow simulations. This box length captures the streamwise modes $k_x = \{0,\, \pm\,\omega_x/2,\, \pm\,\omega_x,\, \pm\,3\omega_x/2, \ldots\}$; relative to Part 1, these modes correspond to the union of the fundamental ($k_x = \{0,\, \pm\,\omega_x,\, \pm 2\,\omega_x,\, \ldots\}$) and subharmonic ($k_x = \{\pm\,\omega_x/2,\, \pm\,3\omega_x/2,\, \ldots\}$) modes. In addition to the uncontrolled flow, we consider three DTWs with ($c = 5$, $\omega_x = 2$, $\alpha = \{0.035, 0.050, 0.125\}$), and three UTWs with ($c = -2$, $\omega_x = 0.5$, $\alpha = \{0.015, 0.050, 0.125\}$). The complete list of the parameters along with the computational domain sizes and the number of spatial grid points is shown in table 3.1. The total integration time is $t_{\text{tot}} = 1000\,\delta/U_c$. We have verified our simulations by making sure that the changes in results are negligible by increasing the number of wall-normal grid points to $N_y = 97$.

3.2.3 Base flow and nominal net efficiency

Base velocity, $\mathbf{u}_b = (U(x, y, t), V(x, y, t), 0)$, is computed using DNS of 2D Poiseuille flow with $R_\tau = 63.25$ in the presence of streamwise traveling wave boundary control (3.2). Figure 3.2 shows the mean velocity profiles, $\overline{U}(y)$ (with overline denoting the average over horizontal directions), in uncontrolled flow and in flows subject to selected DTWs and UTWs; these results agree with the results obtained using Newton's method in Part 1. The nominal bulk flux, which quantifies the area under $\overline{U}(y)$,

$$U_{B,N} \;=\; \frac{1}{2}\int_{-1}^{1} \overline{U}(y)\,\mathrm{d}y,$$

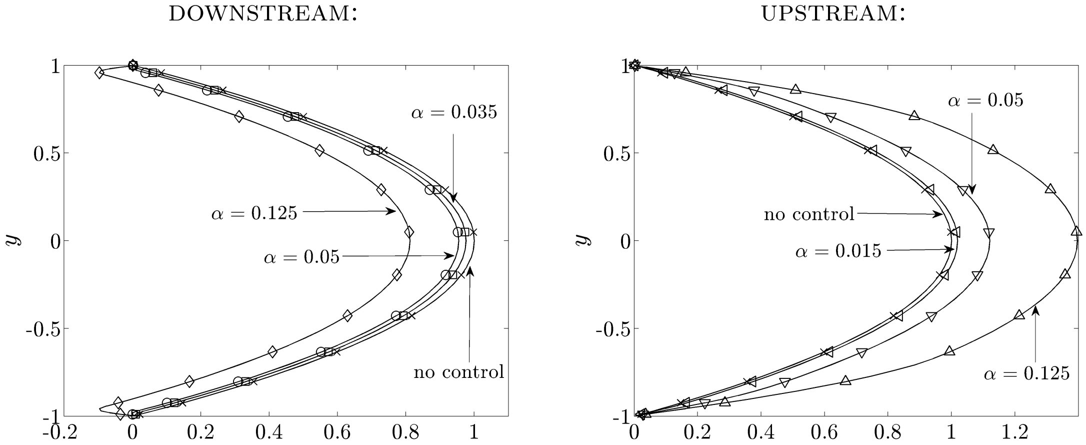

(a)

(b)

Figure 3.2: Mean streamwise base velocity, $\overline{U}(y)$, obtained in 2D simulations of the uncontrolled Poiseuille flow with $R_\tau = 63.25$, $\times$, and controlled flows subject to: (a) DTWs with $\square$, ($c = 5$, $\omega_x = 2$, $\alpha = 0.035$); $\circ$, ($c = 5$, $\omega_x = 2$, $\alpha = 0.05$); $\Diamond$, ($c = 5$, $\omega_x = 2$, $\alpha = 0.125$); and (b) UTWs with $\triangleleft$, ($c = -2$, $\omega_x = 0.5$, $\alpha = 0.015$); $\triangledown$, ($c = -2$, $\omega_x = 0.5$, $\alpha = 0.05$); $\triangle$, ($c = -2$, $\omega_x = 0.5$, $\alpha = 0.125$).

and the nominal skin-friction drag coefficient for three UTWs and three DTWs are reported in table 3.2. For fixed pressure gradient, $P_x = -2/R_c$, the nominal skin-friction drag coefficient is inversely proportional to square of the nominal flux, i.e.,

$$C_{f,N} \;=\; -2\,P_x/U_{B,N}^2. \tag{3.3}$$

As shown by [47], compared to the uncontrolled laminar flow, the nominal flux is reduced (increased) by DTWs (UTWs); according to (3.3), this results in larger (smaller) nominal drag coefficients, respectively.

The above results suggest that properly chosen traveling waves can exhibit increased flux compared to the uncontrolled flow. For fixed pressure gradient, this results in production of a driving power

$$\Pi_{prod} \;=\; -P_x\,(U_{B,c} \,-\, U_{B,u})\,(2L_xL_z),$$

where $U_{B,c}$ and $U_{B,u}$ denote the flux of the controlled and uncontrolled flows. The normalized produced power $\%\Pi_{prod}$ is expressed as a percentage of the power spent to drive the uncontrolled flow, $\Pi_u = -P_x\,U_{B,u}\,(2L_xL_z)$,

$$\%\Pi_{prod} \;=\; 100\,(U_{B,c} \,-\, U_{B,u})\,/U_{B,u}.$$

Case	c	ω_x	α	$U_{B,N}$	$10^3\ C_{f,N}$	$\%\Pi_{prod}$	$\%\Pi_{req}$	$\%\Pi_{net}$
0	–	–	–	0.6667	4.5000	0	0	0
1	5	2	0.035	0.6428	4.8404	−3.58	16.64	−20.22
2	5	2	0.050	0.6215	5.1778	−6.77	31.74	−38.51
3	5	2	0.125	0.4821	8.6050	−27.69	136.50	−164.19
4	−2	0.5	0.015	0.6703	4.4513	2.70	5.46	−2.76
5	−2	0.5	0.050	0.7791	3.2949	16.86	37.69	−20.83
6	−2	0.5	0.125	1.0133	1.9478	51.99	145.05	−93.06

Table 3.2: Nominal results in Poiseuille flow with $R_\tau = 63.25$. The nominal flux, $U_{B,N}$, and skin-friction drag coefficient, $C_{f,N}$, are computed using the base flow described in Section 3.2.3. The produced power, $\%\Pi_{prod}$, required power, $\%\Pi_{req}$, and net power, $\%\Pi_{net}$, are normalized by the power required to drive the uncontrolled flow. The produced and net powers are computed with respect to the laminar uncontrolled flow.

On the other hand, the input power required for maintaining the traveling waves is obtained from [51]

$$\Pi_{req} \;=\; \left(\overline{VP}\big|_{y=-1} \;-\; \overline{VP}\big|_{y=1} \right) L_x L_z,$$

and the normalized required power $\%\Pi_{req}$ is expressed as

$$\%\Pi_{req} \;=\; 100\, \frac{\overline{VP}\big|_{y=-1} \;-\; \overline{VP}\big|_{y=1}}{-2\, P_x\, U_{B,u}}.$$

In order to assess the efficacy of traveling waves for controlling transitional flows, the control net power is defined as the difference between the produced and required powers [50]

$$\%\Pi_{net} \;=\; \%\Pi_{prod} \;-\; \%\Pi_{req},$$

where $\%\Pi_{net}$ signifies how much net power is gained (positive $\%\Pi_{net}$) or lost (negative $\%\Pi_{net}$) in the controlled flow as a percentage of the power spent to drive the uncontrolled flow.

The nominal efficiency of the selected streamwise traveling waves in 2D flows, i.e. in the absence of velocity fluctuations, is shown in table 3.2. Note that the nominal net power is negative for all controlled 2D simulations. This is in agreement with a recent study of [47] where it was shown that the net power required to drive a flow with wall transpiration is always larger than in the standard pressure gradient type of actuation.

3.3 Avoidance/promotion of turbulence by streamwise traveling waves

In Part 1 it was shown that a positive net efficiency can be achieved in a situation where the controlled flow stays laminar but the uncontrolled flow becomes turbulent. Whether the controlled flow can remain laminar depends on velocity fluctuations around the modified base flow. In this section, we study the influence of streamwise traveling waves on the dynamics and the control net efficiency. This problem is addressed by simulating a 3D channel flow with initial perturbations which are superimposed on the base velocity induced by the wall actuation. Depending on the kinetic energy of the initial condition, we distinguish three cases: (i) both the uncontrolled and properly designed controlled flows remain laminar (*small* initial energy); (ii) the uncontrolled flow becomes turbulent, while the controlled flow stays laminar for the appropriate choice of traveling wave parameters (*moderate* initial energy); and (iii) both the uncontrolled and controlled flows become turbulent for selected traveling wave parameters (*large* initial energy). Our simulations indicate, however, that *poorly* designed traveling waves can promote turbulence even for initial conditions for which the uncontrolled flow stays laminar. It was demonstrated in Part 1 that properly designed DTWs are capable of significantly reducing receptivity of velocity fluctuations which makes them well-suited for preventing transition; on the other hand, compared to the uncontrolled flow, the velocity fluctuations around the UTWs at best exhibit similar receptivity to background disturbances. Following Part 1, we present our main results for DTWs with ($c = 5$, $\omega_x = 2$); these results are compared to UTWs with ($c = -2$, $\omega_x = 0.5$) (as selected in [2]). In both cases, three wave amplitudes are selected (cf. table 3.1).

The 3D simulations, which are summarized in table 3.3, confirm and complement the theoretical predictions of Part 1 at two levels. At the level of controlling the onset of turbulence, we illustrate in Section 3.3.1 that the UTWs increase receptivity of velocity fluctuations and promote turbulence even for initial perturbations for which the uncontrolled flow stays laminar. In contrast, the DTWs can prevent transition even in the presence of initial conditions with moderate and large energy (cf. Section 3.3.2 and Section 3.3.3). At the level of net power efficiency, it is first shown in Section 3.3.1 that the net power is negative when the uncontrolled flow stays laminar. However, for the uncontrolled flow that becomes turbulent, we demonstrate that the DTWs can result in a positive net efficiency. As discussed in Section 3.3.2 and Section 3.3.3, the positive net efficiency is achieved if the required power for maintaining the laminar DTW is less than the produced power. In addition, in Section 3.3.3, we highlight an important trade-off that limits the advantages of DTWs in controlling the onset of turbulence in flows subject to large initial conditions. Namely, we show that in this case preventing transition by DTWs requires a large input power that results in a negative efficiency. Our simulations in Section 3.3.2 reveal that although UTWs become turbulent, a positive net efficiency can be achieved for small enough wave amplitudes. For the initial

Initial Energy	Case	c	ω_x	α	$10^3\ C_f$	$\%\Pi_{prod}$	$\%\Pi_{req}$	$\%\Pi_{net}$
Small	0	–	–	–	4.5002	0	0	0
	2	5	2	0.050	5.1778	−6.77	31.77	−38.54
	4	−2	0.5	0.015	4.3204	−1.54	5.14	−3.60
	5	−2	0.5	0.050	5.9426	−16.52	23.22	−39.74
	6	−2	0.5	0.125	3.6853	12.20	108.41	−96.21
Moderate	0	–	–	–	10.3000	0	0	0
	1	5	2	0.035	4.9244	52.07	26.44	25.63
	2	5	2	0.050	5.2273	47.35	50.40	−3.05
	4	−2	0.5	0.015	8.7866	11.36	4.53	6.83
	5	−2	0.5	0.050	6.7406	31.15	41.96	−10.81
	6	−2	0.5	0.125	3.9264	77.03	155.80	−78.77
Large	0	–	–	–	11.2000	0	0	0
	2	5	2	0.050	11.9000	−3.37	47.90	−51.27
	3	5	2	0.125	12.1000	−11.31	196.89	−208.20
	5	−2	0.5	0.050	7.4438	13.68	34.19	−20.51
	6	−2	0.5	0.125	3.9872	57.75	142.92	−85.17

Table 3.3: Results of 3D simulations in Poiseuille flow with $R_\tau = 63.25$ for initial conditions of small, moderate, and large energy (respectively, $E(0) = 2.25 \times 10^{-6}$, $E(0) = 5.0625 \times 10^{-4}$, and $E(0) = 2.5 \times 10^{-3}$). The values of C_f, $\%\Pi_{prod}$, $\%\Pi_{req}$, and $\%\Pi_{net}$ correspond to $t = 1000$. For small initial energy, the produced and net powers are computed with respect to laminar uncontrolled flow; for moderate and large initial energies, they are computed with respect to turbulent uncontrolled flow.

conditions with moderate energy, we further point out that the achievable positive net efficiency for UTWs is much smaller than for the DTWs that sustain the laminar flow (cf. Section 3.3.2).

3.3.1 Small initial energy

We first consider the initial perturbations with small kinetic energy, $E(0) = 2.25 \times 10^{-6}$, which cannot trigger turbulence in flow with no control. Our simulations show that the DTWs selected in Part 1 of this study improve transient response of the velocity fluctuations; on the contrary, the UTWs considered in [2] lead to deterioration of the transient response and, consequently, promote turbulence. Since the uncontrolled flow stays laminar, both DTWs and UTWs lead to the negative net efficiency.

The energy of velocity fluctuations is given by

$$E(t) \;=\; \frac{1}{\Omega} \int_{\Omega} (u^2 + v^2 + w^2)\,\mathrm{d}\Omega,$$

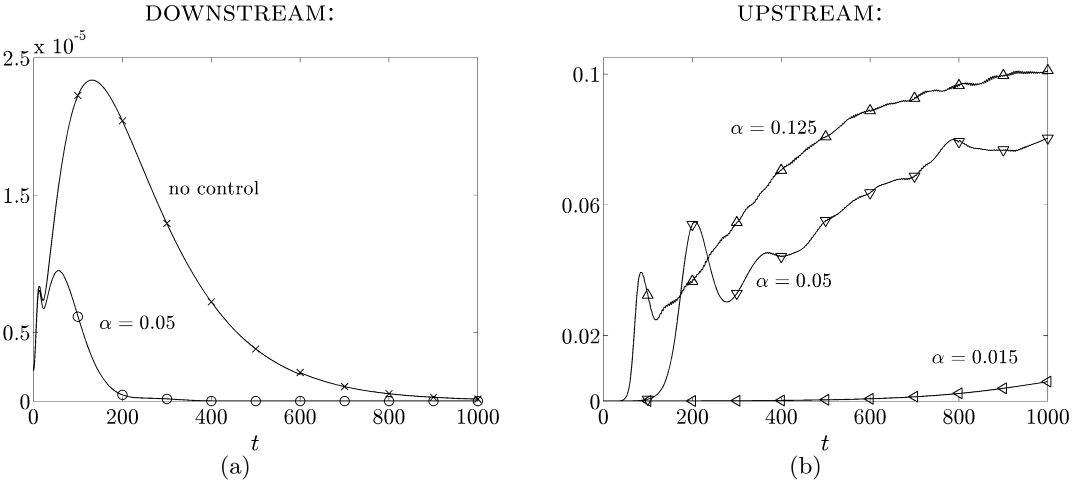

Figure 3.3: Energy of the velocity fluctuations, $E(t)$, for the initial condition with small energy: (a) $\times$, uncontrolled; $\circ$, a DTW with ($c = 5$, $\omega_x = 2$, $\alpha = 0.05$); and (b) UTWs with $\triangleleft$, ($c = -2$, $\omega_x = 0.5$, $\alpha = 0.015$); $\triangledown$, ($c = -2$, $\omega_x = 0.5$, $\alpha = 0.05$); $\triangle$, ($c = -2$, $\omega_x = 0.5$, $\alpha = 0.125$).

where $\Omega = 2L_xL_z$ is the volume of the computational box. Figure 3.3 shows the fluctuations' kinetic energy as a function of time for the uncontrolled flow and controlled flows subject to a DTW with ($c = 5$, $\omega_x = 2$, $\alpha = 0.05$) and three UTWs with ($c = -2$, $\omega_x = 0.5$, $\alpha = \{0.015, 0.05, 0.125\}$). As evident from figure 3.3(a), the energy of the uncontrolled flow exhibits a transient growth followed by an exponential decay to zero (i.e., to the laminar flow). We see that a DTW moves the transient response peak to a smaller time, which is about half the time at which peak of $E(t)$ in the uncontrolled flow takes place. Furthermore, maximal transient growth of the uncontrolled flow is reduced by approximately 2.5 times, and a much faster disappearance of the velocity fluctuations is achieved. On the other hand, figure 3.3(b) clearly exhibits the negative influence of the UTWs on a transient response. In particular, the two UTWs with larger amplitudes significantly increase the energy of velocity fluctuations. We note that the fluctuations' kinetic energy in a flow subject to a UTW with an amplitude as small as $\alpha = 0.015$ at $t = 1000$ is already about two orders of magnitude larger than the maximal transient growth of the flow with no control.

Figure 3.4(a) shows the skin-friction drag coefficient,

$$C_f(t) \;=\; \frac{2\overline{\tau}_w}{U_B^2} \;=\; \frac{1}{R_c\,U_B^2}\left[\left(\frac{\mathrm{d}\overline{U}}{\mathrm{d}y} + \frac{\mathrm{d}\overline{u}}{\mathrm{d}y}\right)\bigg|_{y\,=\,-1} - \left(\frac{\mathrm{d}\overline{U}}{\mathrm{d}y} + \frac{\mathrm{d}\overline{u}}{\mathrm{d}y}\right)\bigg|_{y\,=\,1}\right],$$

as a function of time for the traveling waves considered in figure 3.3. Here, $\overline{\tau}_w$ denotes the non-dimensional average wall-shear stress and

$$U_B(t) \;=\; \frac{1}{2}\int_{-1}^{1} \left(\overline{U}(y) \,+\, \overline{u}(y,t)\right)\,\mathrm{d}y,$$

is the total bulk flux. Since both the uncontrolled flow and the flow subject to a DTW stay laminar, their steady-state drag coefficients agree with the nominal values computed in the absence of velocity fluctuations (cf. tables 3.2 and 3.3). On the other hand, the drag coefficients of the UTWs that become turbulent are about twice the values predicted using the base flow analysis. The large amplification of velocity fluctuations by UTWs is responsible for this increase. The velocity fluctuations in the UTW with $\alpha = 0.015$ are not amplified enough to have a pronounced effect on the drag coefficient. Furthermore, the drag coefficients for the UTWs with ($c = -2$, $\omega_x = 0.5$, $\alpha = \{0.05, 0.125\}$) at $t = 1000$ agree with the results of [2] computed for the fully developed turbulent channel flow. This indicates that the UTWs with larger amplitudes in our simulations have transitioned to turbulence. The above results confirm the theoretical prediction of Part 1 where it is shown that the UTWs are poor candidates for controlling the onset of turbulence for they increase receptivity relative to the uncontrolled flow.

The normalized required, produced, and net powers for the initial conditions with small kinetic energy are shown in figures 3.4(b) - 3.4(d). Note that the normalized net power for all traveling waves is negative (cf. figure 3.4(d)). This confirms the prediction of Part 1 that the net power is negative whenever the uncontrolled flow stays laminar. It is noteworthy that the UTW with $\alpha = 0.125$ has a negative net power despite its significantly smaller drag coefficient compared to the laminar uncontrolled flow. As evident from figures 3.4(b) and 3.4(c), this is because the required power for maintaining this UTW is much larger than the power produced by reducing drag. The above results agree with the studies of [48] and [49] where it was established that the net cost to drive a flow by any transpiration-based strategy is larger than in the uncontrolled laminar flow. Therefore, aiming for sub-laminar drag may not be advantageous from efficiency point of view. Instead, one can design control strategies that yield smaller drag than the uncontrolled turbulent flow and provide positive net power balance (cf. Section 3.3.2).

3.3.2 Moderate initial energy

We next consider the velocity fluctuations with moderate initial energy, $E(0) = 5.0625 \times 10^{-4}$. This selection illustrates a situation where the initial conditions are large enough to trigger turbulence in the uncontrolled flow but small enough to allow the properly chosen DTWs to maintain the laminar flow and achieve positive net power balance. As shown in Section 3.3.1, the UTWs trigger turbulence even for the initial conditions whose kinetic energy is about 200 times smaller than the value considered here.

The energy of the velocity fluctuations and drag coefficients as a function of time for

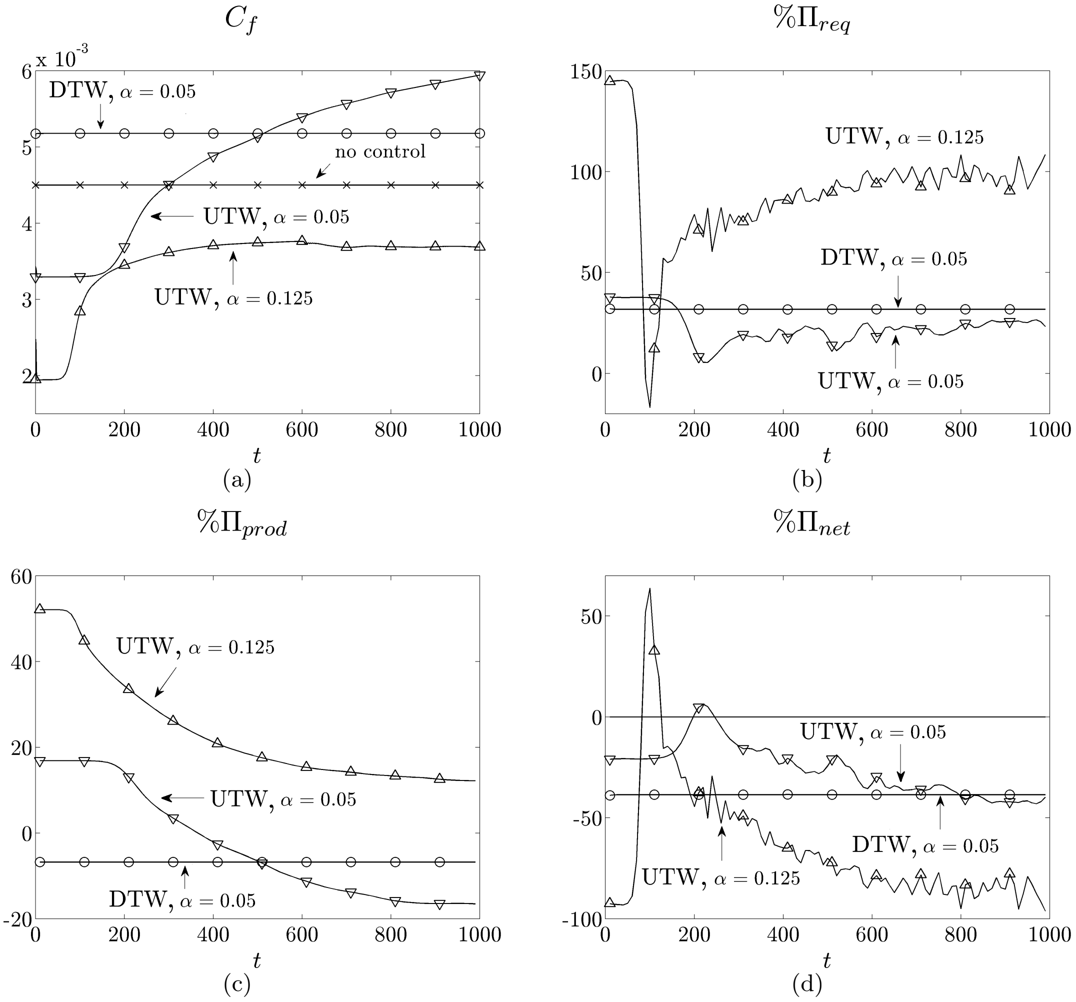

Figure 3.4: (a) Skin-friction drag coefficient, C_f; (b) normalized required power, $\%\Pi_{req}$; (c) normalized produced power, $\%\Pi_{prod}$; and (d) normalized net power, $\%\Pi_{net}$, for the initial condition with small energy: $\times$, uncontrolled flow; $\circ$, DTW with ($c = 5$, $\omega_x = 2$, $\alpha = 0.05$); and UTWs with $\triangleleft$, ($c = -2$, $\omega_x = 0.5$, $\alpha = 0.015$); $\triangledown$, ($c = -2$, $\omega_x = 0.5$, $\alpha = 0.05$); $\triangle$, ($c = -2$, $\omega_x = 0.5$, $\alpha = 0.125$).

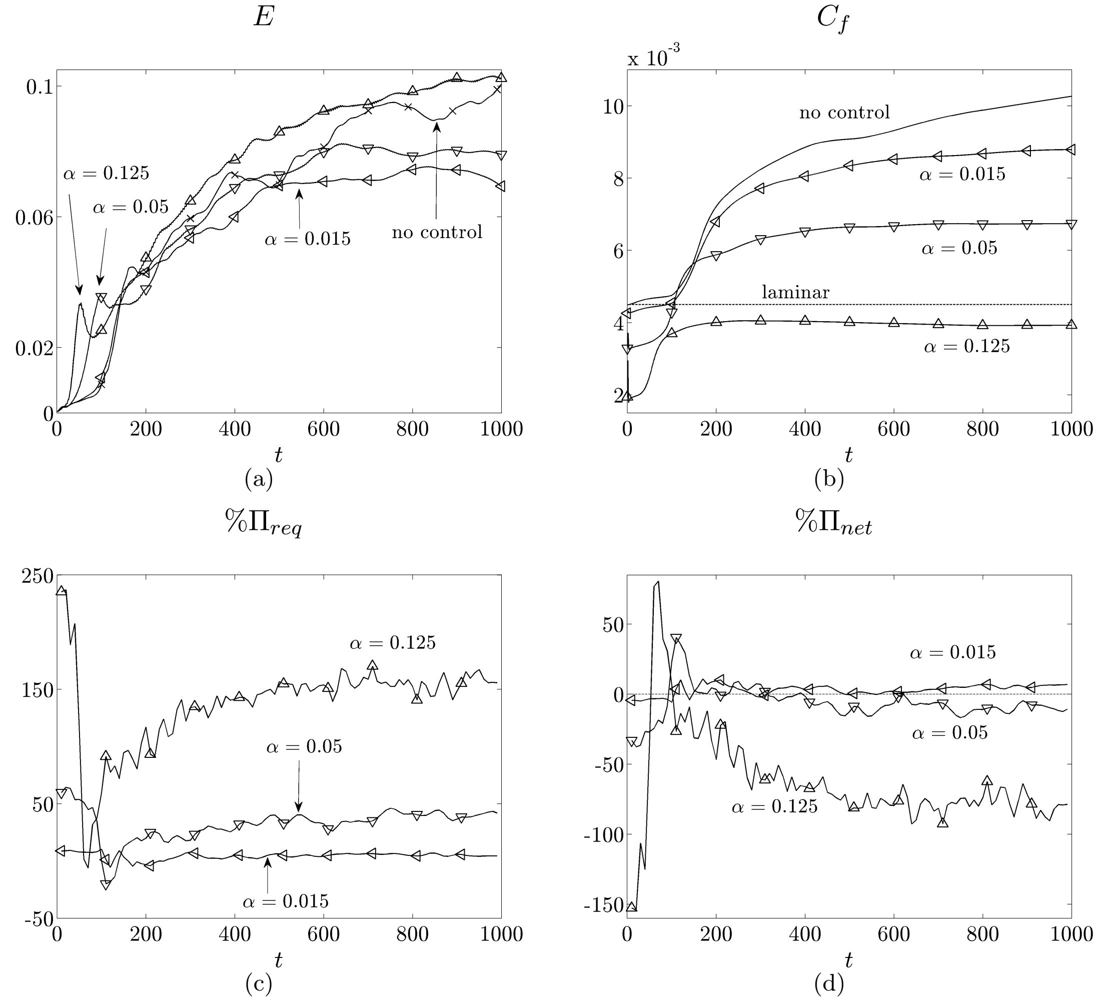

Figure 3.5: (a) Energy of the velocity fluctuations, $E(t)$; (b) skin-friction drag coefficient, $C_f(t)$; (c) normalized required power, $\%\Pi_{req}$; and (d) normalized net power, $\%\Pi_{net}$, for the initial condition with moderate energy: $\times$, uncontrolled; and UTWs with $\triangleleft$, $(c = -2, \omega_x = 0.5, \alpha = 0.015)$; $\triangledown$, $(c = -2, \omega_x = 0.5, \alpha = 0.05)$; $\vartriangle$, $(c = -2, \omega_x = 0.5, \alpha = 0.125)$.

the uncontrolled flow and UTWs are shown in figures 3.5(a) and 3.5(b). Figure 3.5(a) indicates that the kinetic energy of the uncontrolled flow and the flow subject to UTWs with ($c = -2$, $\omega_x = 0.5$, $\alpha = \{0.015, 0.05, 0.125\}$) is increased by orders of magnitude which eventually results in transition to turbulence. This large energy amplification of UTWs is captured by the linear analysis around the laminar base flows in Part 1. As evident from figure 3.5(b), the large fluctuations' energy in both the uncontrolled flow and in UTWs yields much larger drag coefficients compared to the nominal values reported in table 3.2. In addition, figure 3.5(b) is in agreement with [2] where it was shown that the skin-friction drag coefficients of the UTWs are smaller than in the uncontrolled flow that becomes turbulent, and that the UTW with ($c = -2$, $\omega_x = 0.5$, $\alpha = 0.125$) achieves a sub-laminar drag. The normalized required and net powers for the UTWs are shown in figures 3.5(c) and 3.5(d). Note that the required power for maintaining the UTW with $\alpha = 0.125$ (which yields sub-laminar drag) is so large that it results in a negative net power balance (cf. figure 3.5(d)). On the other hand, the UTW with $\alpha = 0.015$ is capable of producing a small positive net power for two main reasons: (i) it has a smaller drag coefficient than the uncontrolled turbulent flow (although it becomes turbulent itself); and (ii) it requires a much smaller power compared to the UTW with $\alpha = 0.125$.

The fluctuations' kinetic energy and skin-friction drag coefficient for the DTWs are shown in figures 3.6(a) and 3.6(b). Figure 3.6(a) shows that the DTWs with ($c = 5$, $\omega_x = 2$, $\alpha = \{0.035, 0.05\}$) significantly weaken intensity of the velocity fluctuations, thereby facilitating maintenance of the laminar flow. From figure 3.6(b) we also see that the small transient growth of fluctuations' kinetic energy results in a small transient increase in the drag coefficients which eventually decay to their nominal values reported in table 3.2. Even though these drag coefficients are larger than in the uncontrolled laminar flow, they are still approximately two times smaller than in the uncontrolled flow that becomes turbulent (cf. table 3.3).

The normalized produced, required, and net powers for DTWs are shown in figures 3.6(c) and 3.6(d). As can be seen from figure 3.6(c), the normalized produced power for the DTWs is positive by virtue of the fact that the uncontrolled flow becomes turbulent while the controlled flows stay laminar. Figure 3.6(d) shows that the DTW with $\alpha = 0.035$ (respectively, $\alpha = 0.05$) has a positive (respectively, negative) net power balance. The reason for this is twofold: first, as evident from figure 3.6(c), the DTW with larger α results in a smaller produced power since it induces a larger negative nominal bulk flux than the DTW with smaller α; and second, the required power to maintain the DTW with larger α is bigger than in the DTW with smaller α. Furthermore, at $t = 1000$, the DTW with $\alpha = 0.035$ has a larger net power than the UTW with $\alpha = 0.015$ ($\%\Pi_{net} = 25.63$ vs. $\%\Pi_{net} = 6.83$; cf. table 3.3). This is because the DTW with $\alpha = 0.035$, in contrast to the UTW with $\alpha = 0.015$, remains laminar and produces a much larger power than it requires.

In summary, the results of this section highlight an important trade-off that needs

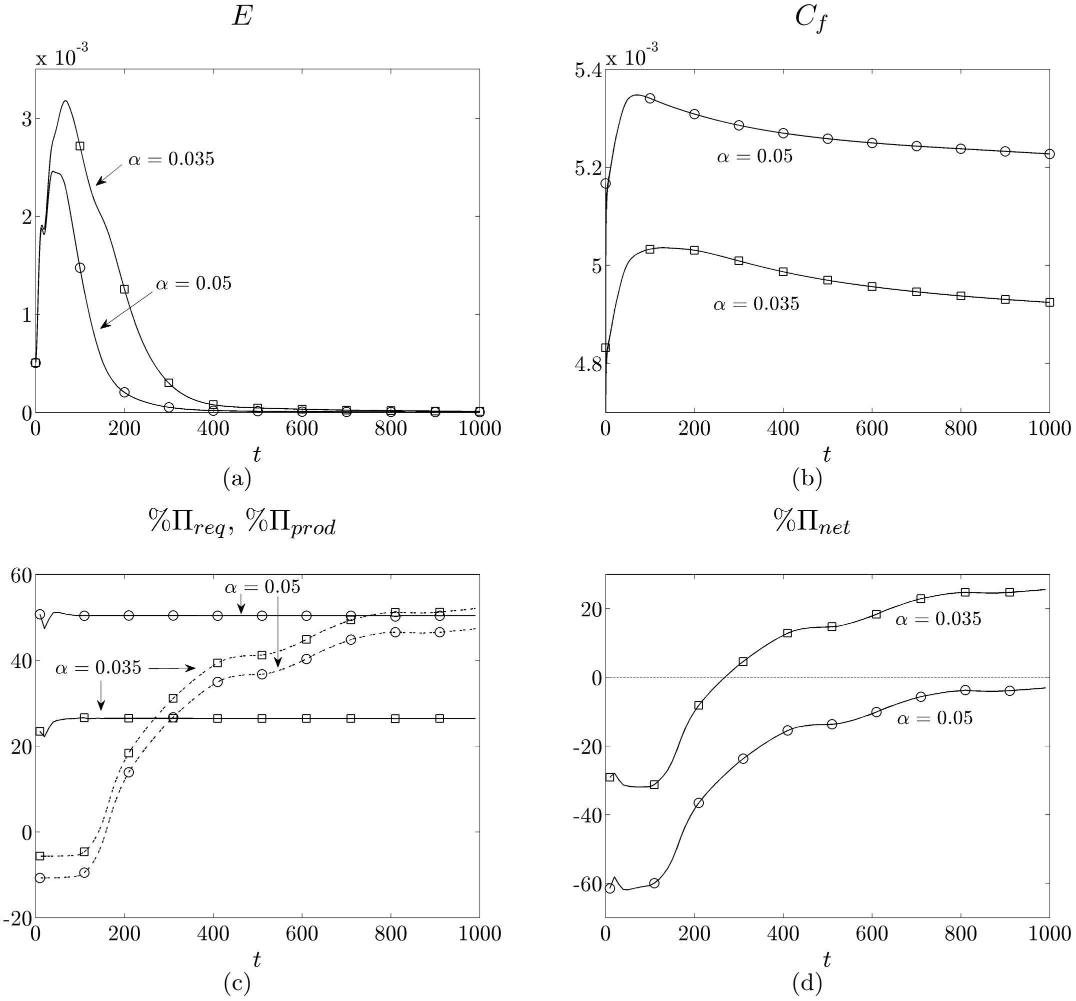

Figure 3.6: (a) Energy of the velocity fluctuations, $E(t)$; (b) skin-friction drag coefficient, $C_f(t)$; (c) normalized required power, $\%\Pi_{req}$ (solid), normalized produced power, $\%\Pi_{prod}$ (dashed); and (d) normalized net power, $\%\Pi_{net}$, for the initial condition with moderate energy: DTWs with $\square$, $(c = 5, \omega_x = 2, \alpha = 0.035)$; $\circ$, $(c = 5, \omega_x = 2, \alpha = 0.05)$.

to be taken into account when designing the traveling waves. Large amplitudes of properly designed downstream waves yield larger receptivity reduction which is desirable for controlling the onset of turbulence. However, this is accompanied by an increase in drag coefficient and required control power. Thus, to maximize net efficiency, it is advantageous to select the smallest possible amplitude of wall-actuation that can maintain the laminar flow.

3.3.3 Large initial energy

Section 3.3.2 illustrates capability of properly designed DTWs to maintain the laminar flow in the presence of initial conditions that induce transition in the uncontrolled flow. In this section, we demonstrate that, as the energy of the initial perturbation increases, a DTW with larger amplitude is needed to prevent transition. Our results confirm the prediction made in Part 1 that maintaining a laminar flow with a larger DTW amplitude comes at the expense of introducing a negative net power balance.

Simulations in this section are done for the initial condition with large kinetic energy, $E(0) = 2.5 \times 10^{-3}$. The time evolution of the fluctuations' energy for a pair of DTWs with ($c = 5$, $\omega_x = 2$, $\alpha = \{0.05, 0.125\}$) is shown in figure 3.7(a). The uncontrolled flow becomes turbulent and exhibits similar trends in the evolution of $E(t)$ as the corresponding flow initiated with moderate energy perturbations (cf. figures 3.5(a) and 3.7(a)). On the other hand, figure 3.7(a) shows that the DTW with $\alpha = 0.05$ is not capable of maintaining the laminar flow; in comparison, the same set of control parameters prevented transition for the perturbations of moderate initial energy (cf. figures 3.6(a) and 3.7(a)). Conversely, the DTW with $\alpha = 0.125$ remains laminar even though $E(t)$ transiently reaches about half the energy of the turbulent uncontrolled flow. Therefore, the DTWs with frequency and speed selected in Part 1 and sufficiently large amplitudes are capable of maintaining the laminar flow even in the presence of large initial perturbations.

Figure 3.7(b) shows the skin-friction drag coefficients for the flows considered in figure 3.7(a). For the DTW with $\alpha = 0.05$ the steady-state value of C_f is given by $C_f = 11.9 \times 10^{-3}$, which is a slightly larger value than in the turbulent uncontrolled flow, $C_f = 11.2 \times 10^{-3}$ (cf. table 3.3). We note that the drag coefficient of the DTW that stays laminar initially reaches values that are about 50 % larger than in the uncontrolled flow; after this initial increase, $C_f(t)$ then gradually decays to the value predicted using the base flow analysis, $C_f = 8.6 \times 10^{-3}$ (cf. table 3.2). Figures 3.7(c) and 3.7(d) show the normalized required, produced, and net powers for the initial condition with large kinetic energy. As evident from figure 3.7(d), the net power balance is negative for all considered flows. The DTW with $\alpha = 0.05$ becomes turbulent, and it has a larger drag coefficient than the uncontrolled flow which consequently leads to negative produced and net powers. Moreover, even though the DTW with $\alpha = 0.125$ can sustain laminar flow, its net power balance is very poor. There are two main reasons for the lack of efficiency of this control strategy: first, its nominal drag coefficient is significantly larger

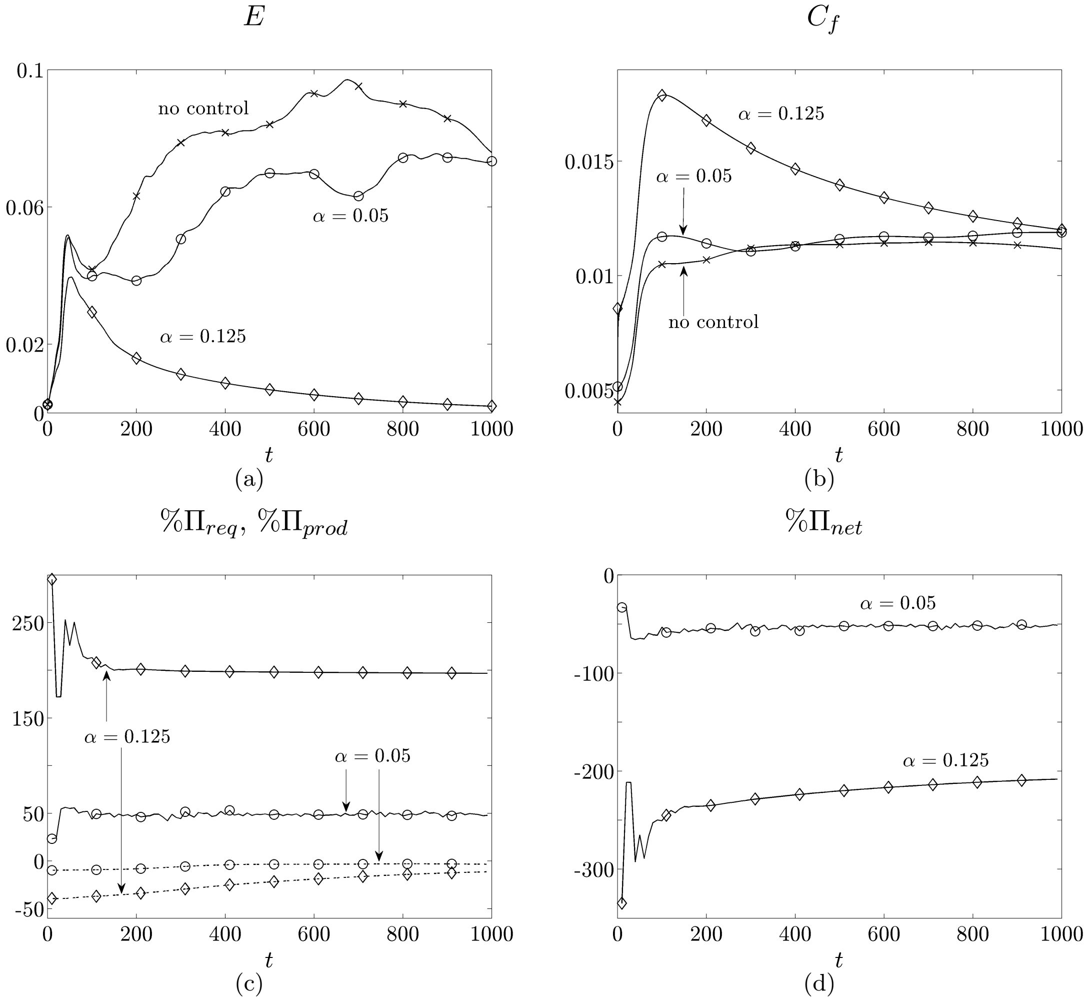

Figure 3.7: (a) Energy of the velocity fluctuations, $E(t)$; (b) skin-friction drag coefficient, $C_f(t)$; (c) normalized required power, $\%\Pi_{req}$ (solid), normalized produced power, $\%\Pi_{prod}$ (dashed); and (d) normalized net power, $\%\Pi_{net}$, for the initial condition with large energy: $\times$, uncontrolled; DTWs with $\circ$, $(c = 5, \omega_x = 2, \alpha = 0.05)$; and $\lozenge$, $(c = 5,$ $\omega_x = 2$, $\alpha = 0.125)$.

than in a DTW with smaller amplitudes which consequently yields very small produced power (at larger times not shown in figure 3.7(c)); and second, a prohibitively large power is required to maintain this large amplitude DTW.

The results of this section show that preventing transition by DTWs in the presence of large initial conditions comes at the expense of large negative net power balance. We also highlight that in the presence of large initial perturbations (or, equivalently, at large Reynolds numbers), transition to turbulence may be inevitable. Furthermore, the results of Section 3.3.2 show that the UTWs may reduce the turbulent skin-friction drag and achieve positive net efficiency. The approach used in Part 1 considers dynamics of fluctuations around laminar flows and, thus, it cannot be used for explaining the positive efficiency of the UTWs that become turbulent.

3.3.4 Energy amplification mechanisms

The Reynolds-Orr equation can be used to quantify the evolution of fluctuations' kinetic energy around a given base flow [52]. In this section, we use this equation to examine mechanisms that contribute to production and dissipation of kinetic energy in flows subject to traveling waves. For base velocity, $\mathbf{u}_b = (U(x,y,t), V(x,y,t), 0)$, the evolution of the energy of velocity fluctuations, $E(t)$, is determined by

$$\begin{aligned} \frac{1}{2}\,\frac{\mathrm{d}E}{\mathrm{d}t} &= P_E(t) \,+\, D_E(t), \\ P_E(t) &= -\frac{1}{\Omega}\int_{\Omega}\big(uvU_y \,+\, uvV_x \,+\, v^2V_y \,+\, u^2U_x\big)\,\mathrm{d}\Omega, \\ D_E(t) &= \frac{1}{R_c\Omega}\int_{\Omega}\mathbf{v}\cdot\Delta\mathbf{v}\,\mathrm{d}\Omega. \end{aligned} \tag{3.4}$$

Here, P_E represents the production of kinetic energy and is associated with the work of the Reynolds stresses on the base shear, whereas D_E accounts for viscous dissipation.

We confine our attention to the simulations for initial conditions with small energy. This situation is convenient for explaining why the DTWs exhibit improved transient behavior compared to the laminar uncontrolled flow while the UTWs promote transition to turbulence. Figure 3.8(a) shows production and dissipation terms for the uncontrolled flow and for the flow subject to a DTW with ($c = 5$, $\omega_x = 2$, $\alpha = 0.05$). For the uncontrolled flow, P_E is always positive, D_E is always negative, and they both decay to zero at large times. On the contrary, the production term for the DTW becomes negative for $80 \lesssim t \lesssim 220$. We see that, at early times, P_E and D_E for the DTW follow their uncontrolled flow counterparts. However, after this initial period, they decay more rapidly to zero. These results confirm the prediction of Part 1 that the DTWs reduce the production of kinetic energy. In contrast, figure 3.8(b) shows that the UTWs with ($c = -2$, $\omega_x = 0.5$, $\alpha = \{0.05, 0.125\}$) increase both P_E and D_E by about four orders of magnitude compared to the values reported in figure 3.8(a). This verifies the theoretical

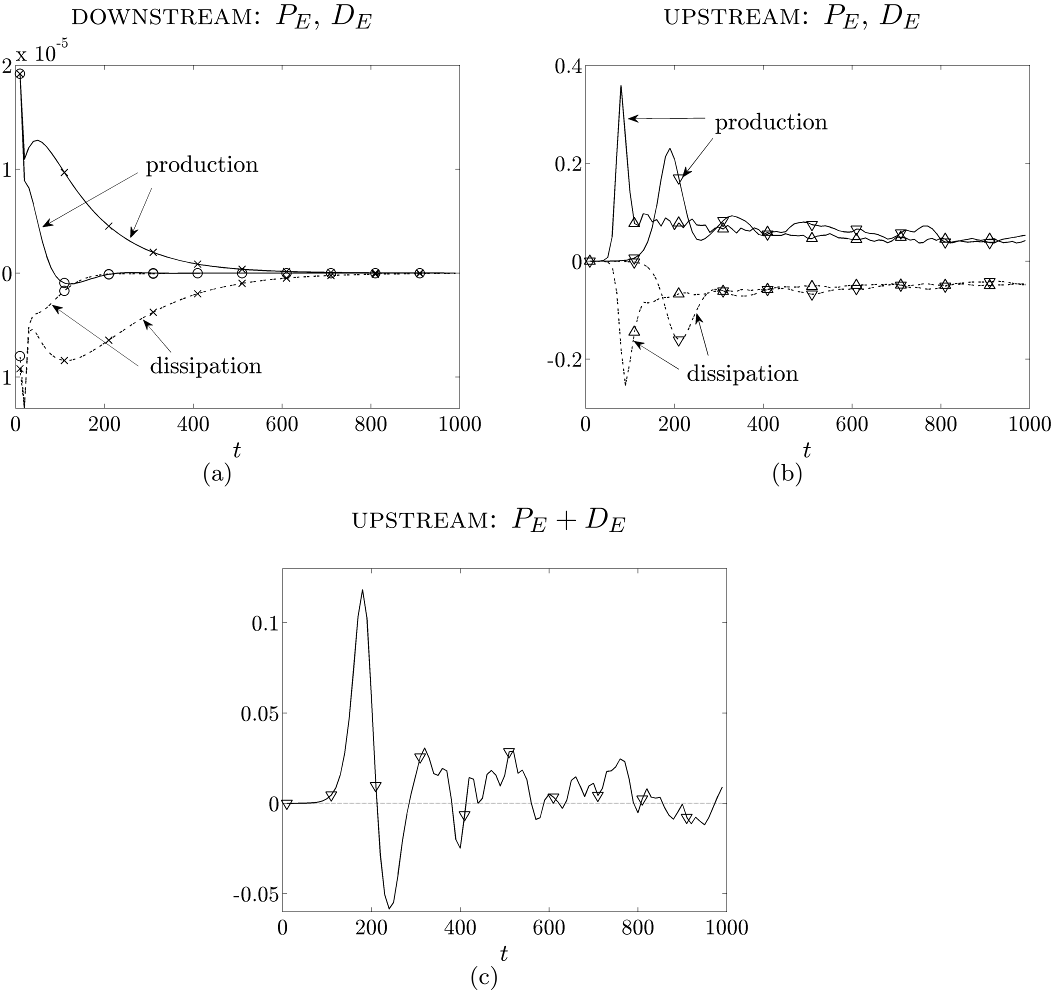

DOWNSTREAM: P_E, D_E

UPSTREAM: P_E, D_E

UPSTREAM: $P_E + D_E$

Figure 3.8: (a) and (b) Production, $P_E(t)$ (solid), and dissipation, $D_E(t)$ (dashed), of kinetic energy in Poiseuille flow with $R_\tau = 63.25$ for the initial condition with small energy: (a) $\times$, uncontrolled; $\circ$, DTW with ($c = 5$, $\omega_x = 2$, $\alpha = 0.05$); and (b) $\triangledown$, UTW with ($c = -2$, $\omega_x = 0.5$, $\alpha = 0.05$); $\triangle$, UTW with $\alpha = 0.125$. (c) $P_E(t) + D_E(t)$ for the UTW with ($c = -2$, $\omega_x = 0.5$, $\alpha = 0.05$).

prediction of Part 1 that the UTWs increase the production of kinetic energy. Moreover, production dominates dissipation transiently, thereby inducing large growth of kinetic energy observed in figure 3.3(b). For the UTW with $\alpha = 0.05$, this is further illustrated in figure 3.8(c) by showing that P_E accumulates more energy than D_E dissipates (i.e., the area under the curve in figure 3.8(c) is positive). We also note that, in the above simulations, the work of Reynolds stress uv on the base shear U_y dominates the other energy production terms. Furthermore, our results show that the wall-normal diffusion of u is responsible for the largest viscous energy dissipation.

3.3.5 Flow visualization

In sections 3.3.1 - 3.3.3, transition was identified by examining fluctuations' kinetic energy and skin-friction drag coefficients. Large levels of sustained kinetic energy and substantial increase in drag coefficients (compared to base flows) were used as indicators of transition. Here, we use flow visualization to identify coherent structures in both the uncontrolled and controlled flows.

The onset of turbulence in a bypass transition is usually characterized by formation of streamwise streaks and their subsequent break-down. For the initial condition with moderate energy, figure 3.9 shows the streamwise velocity fluctuations at $y = -0.5557$ ($y^+ = 28.11$ in wall units) for the uncontrolled flow and flows subject to a UTW with ($c = -2$, $\omega_x = 0.5$, $\alpha = 0.05$) and a DTW with ($c = 5$, $\omega_x = 2$, $\alpha = 0.05$). Clearly, the initial perturbations evolve into streamwise streaks in all three flows (cf. figures 3.9(a) - 3.9(e) for $t = 50$). At $t = 120$, the growth of velocity fluctuations results in a break-down of the streaks both in the flow with no control and in the flow subject to UTWs (cf. figures 3.9(b) and 3.9(d)). We see that the streaks evolve into complex flow patterns much faster in the latter case. For the UTWs, the streak distortion occurs as early as $t = 50$ and a broad range of spatial scales is observed at $t = 120$. On the contrary, figure 3.9(f) shows that, at $t = 120$, the DTWs have reduced the magnitude of velocity fluctuations to about half the value at $t = 50$, thereby weakening intensity of the streaks and maintaining the laminar flow.

We next examine the flow to look for regions that exhibit *vortex-like* motion [53]. We illustrate that, relative to the uncontrolled flow that becomes turbulent, the DTWs eliminate the formation of strong vortical motions. We also compare the transient and steady-state features of the uncontrolled flow with the flow subject to the UTWs. Flow visualization has been used extensively to understand the nature of transitional and turbulent flows, see, for example [54–57]. The utility of critical point analysis in quantifying vortical motions in complex flows is discussed in [53, 58, 59]. In particular, Chong, Perry & Cantwell [53] showed that discriminant, $D(x, y, z, t)$, of the velocity gradient tensor provides information about focal regions in the flow. The vortex cores are characterized by $D > 0$, and they are associated with the regions where the rate of rotation tensor dominates the rate of strain tensor [53]. Therefore, 3D visualization of D is a useful technique for recognizing vortex motions in the flow. The discriminant is

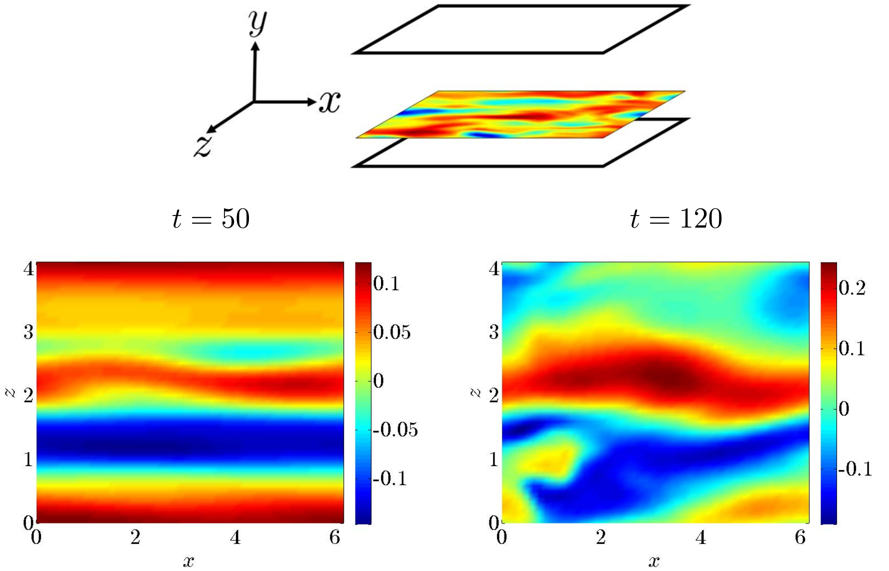

(a) UNCONTROLLED (b) UNCONTROLLED

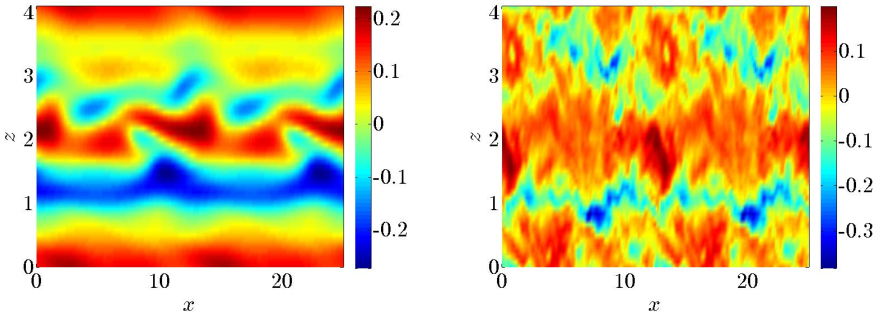

(c) UPSTREAM (d) UPSTREAM

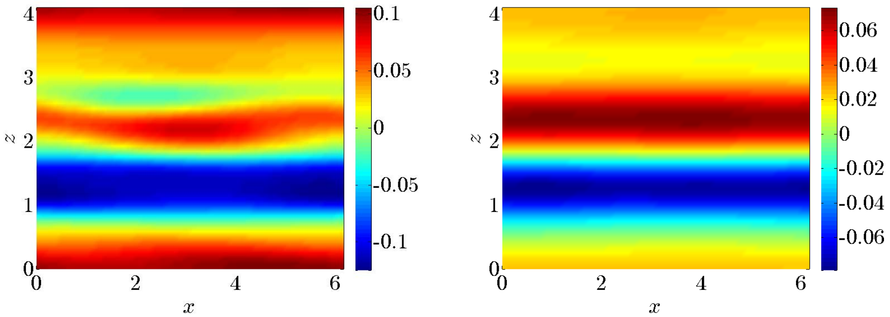

(e) DOWNSTREAM (f) DOWNSTREAM

Figure 3.9: Streamwise velocity fluctuations, $u(x,z)$, at $y = -0.5557$ ($y^+ = 28.11$), (a), (c), (e) $t = 50$, and (b), (d), (f) $t = 120$ for initial condition with moderate energy: uncontrolled flow; UTW with ($c = -2$, $\omega_x = 0.5$, $\alpha = 0.05$); and DTW with ($c = 5$, $\omega_x = 2$, $\alpha = 0.05$).

obtained from $D = (27/4)R^2 + Q^3$, where $Q = \left(\mathrm{tr}\,(\mathbf{A})^2 - \mathrm{tr}\,(\mathbf{A}^2)\right)/2$ and $R = -\det(\mathbf{A})$ are the second and third invariants of the velocity gradient tensor, $\mathbf{A}$, defined as $\mathbf{A}_{ij} = \partial u_i/\partial x_j$.

In order to visualize the effect of traveling waves on transition, an initial condition of moderate energy is considered. The isosurfaces of D, greater than a threshold value, for the uncontrolled flow and the flows subject to a DTW with ($c = 5$, $\omega_x = 2$, $\alpha = 0.05$) and a UTW with ($c = -2$, $\omega_x = 0.5$, $\alpha = 0.05$) are shown in figures 3.10, 3.11, and 3.12, respectively. The cross-flow velocity vectors in the (y, z)-plane and the x-average of the streamwise vorticity are also plotted for comparison. We see that the regions of strong vorticity are correctly captured by the discriminant of the velocity gradient tensor. Figures 3.10(a) and 3.11(a) show that, at $t = 30$, the uncontrolled flow and the DTW have similar vortical structures. However, at $t = 50$ and $t = 70$, the uncontrolled flow exhibits large vortical motions close to the upper channel wall; these motions are considerably suppressed by the DTW. In addition, at $t = 70$, the magnitude of the streamwise vorticity for the DTW is about two times smaller than in the uncontrolled flow. In contrast, figure 3.12 shows build-up of vorticity by the UTW of approximately two times larger magnitude than in the uncontrolled flow. Note that, in the early stages of transition, the vortical structures with $D > 10^{-6}$ are significantly more abundant in flows subject to the UTW than in the uncontrolled flow (cf. figures 3.12(c) and 3.10(c)).

For $t \gtrsim 100$, the mixing of the lower and upper channel halves breaks the aforementioned elongated structures into smaller ones which leads to formation of new vortices throughout the channel (see [54] for the uncontrolled flow discussion). Figure 3.13 illustrates this behavior both in the uncontrolled flow and in the flow subject to the UTW. In the uncontrolled flow, the strong vortical motions in the upper half of the channel at $t = 100$ spread to the lower half at $t \approx 200$ (cf. figures 3.13(a) and 3.13(c)). We see that the isosurfaces of the discriminant are in the form of tubes that extend from the lower wall to the channel centerplane (cf. figure 3.13(g)); similar structures were reported in turbulent wall-bounded shear flows by [56, 59]. We note that transition occurs much faster in the UTW with ($c = -2$, $\omega_x = 0.5$, $\alpha = 0.05$) than in the uncontrolled flow. For example, at $t = 100$, the UTW populates the entire channel with strong vortical motions. In the uncontrolled flow, however, these structures appear only in certain portions of the upper half of the channel. This is in agreement with figure 3.5(a) where deterioration of the transient response of the uncontrolled flow by this UTW was observed. Our results also show that, for $t > 100$, in the DTW with ($c = 5$, $\omega_x = 2$, $\alpha = 0.05$) the discriminant is nowhere larger than 10^{-8}. This indicates that the DTWs are effective in suppressing the vortical motions that may arise naturally as a result of flow disturbances.

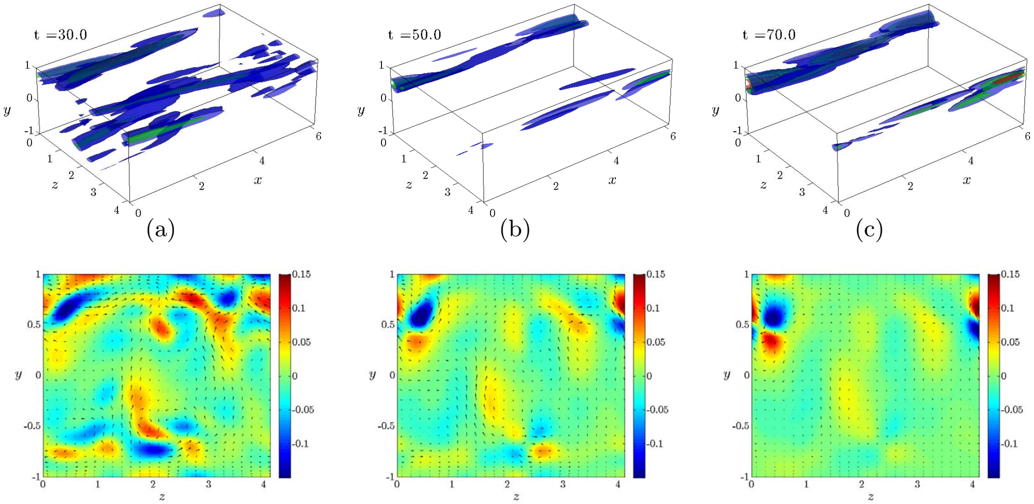

(a) (b) (c)

(d) (e) (f)

Figure 3.10: Simulation of the uncontrolled flow for the initial condition with moderate energy. (a) - (c) 3D visualizations of the isosurfaces of the discriminant, $D > 10^{-6}$ (blue), $D > 10^{-5}$ (green), and $D > 10^{-4}$ (red). (d) - (f) 2D visualizations of the crossflow velocity vectors (arrows) and the x-averaged streamwise vorticity (color plots).

3.4 Relaminarization by downstream waves

Thus far we have shown that properly designed DTWs represent an effective means for controlling the onset of turbulence. In this section, we demonstrate that the DTWs designed in Part 1 can also relaminarize fully developed turbulent flows. Since the lifetime of turbulence depends on the Reynolds number [60–63], we examine turbulent flows with $R_c = 2000$ (i.e., $R_\tau \approx 63.25$) and $R_c = 4300$ (i.e., $R_\tau \approx 92.80$).

The numerical scheme described in Section 3.2.2 is used to simulate the turbulent flows. For $R_c = 4300$, the number of grid points in the streamwise, wall-normal, and spanwise directions is increased to $80 \times 97 \times 80$. The velocity field is initialized with a fully developed turbulent flow obtained in the absence of control. The surface blowing and suction that generates DTWs is then introduced (at $t = 0$), and the kinetic energy and drag coefficients are computed at each time step.

The fluctuations' kinetic energy for the uncontrolled flow and for the flows subject to DTWs with ($c = 5$, $\omega_x = 2$, $\alpha = \{0.035, 0.05, 0.125\}$) at $R_c = 2000$ are shown in figure 3.14. The energy of velocity fluctuations around base flows $\mathbf{u}_b$ of Section 3.2.1 (parabola for flow with no control; traveling waves for flow with control) are shown; relaminarization occurs when the energy of velocity fluctuations converges to zero. Clearly, large levels of fluctuations in the flow with no control are maintained up until $t \approx 1100$. After this time instant, however, velocity fluctuations exhibit gradual decay. On the

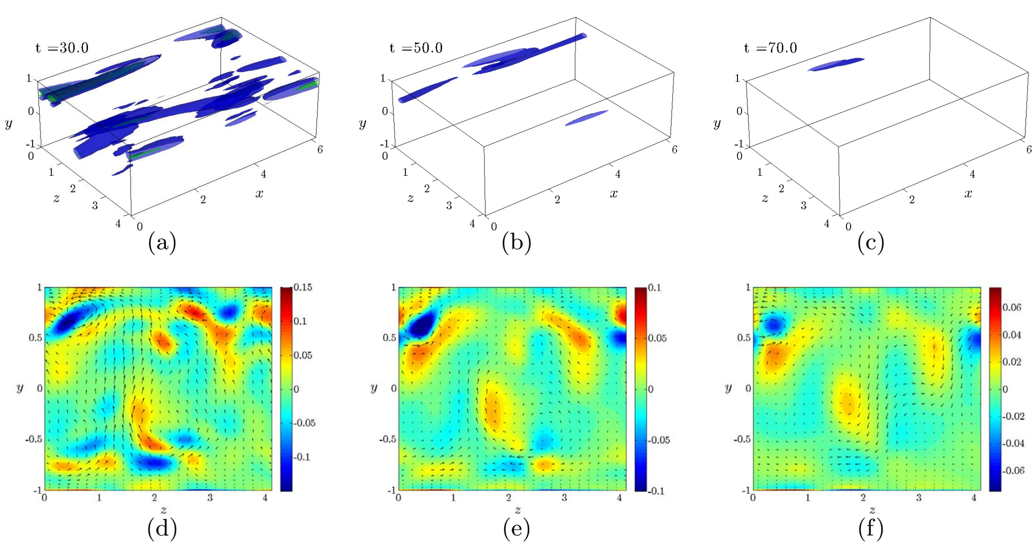

(a) (b) (c)

(d) (e) (f)

Figure 3.11: Simulation of the DTW with ($c = 5$, $\omega_x = 2$, $\alpha = 0.05$) for the initial conditions with moderate energy. (a) - (c) 3D visualizations of the isosurfaces of the discriminant, $D > 10^{-6}$ (blue), $D > 10^{-5}$ (green), and $D > 10^{-4}$ (red). (d) - (f) 2D visualizations of the crossflow velocity vectors (arrows) and the x- averaged streamwise vorticity (color plots).

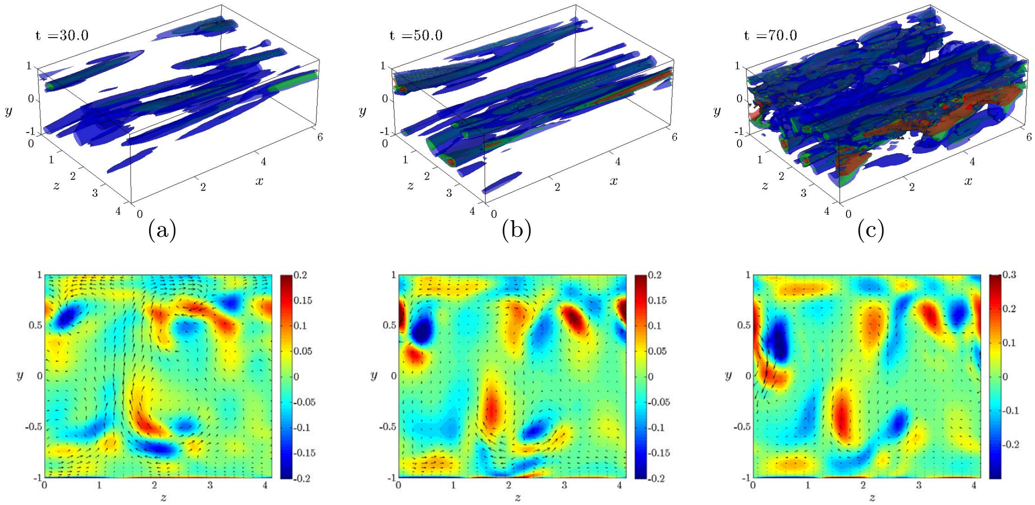

(a) (b) (c)

(d) (e) (f)

Figure 3.12: Simulation of the UTW with ($c = -2$, $\omega_x = 0.5$, $\alpha = 0.05$) for the initial condition with moderate energy. (a) - (c) 3D visualizations of the isosurfaces of the discriminant, $D > 10^{-6}$ (blue), $D > 10^{-5}$ (green), and $D > 10^{-4}$ (red). (d) - (f) 2D visualizations of the crossflow velocity vectors (arrows) and the x-averaged streamwise vorticity (color plots). Only one quarter of the channel ($x \in [0, 2\pi]$) is shown.

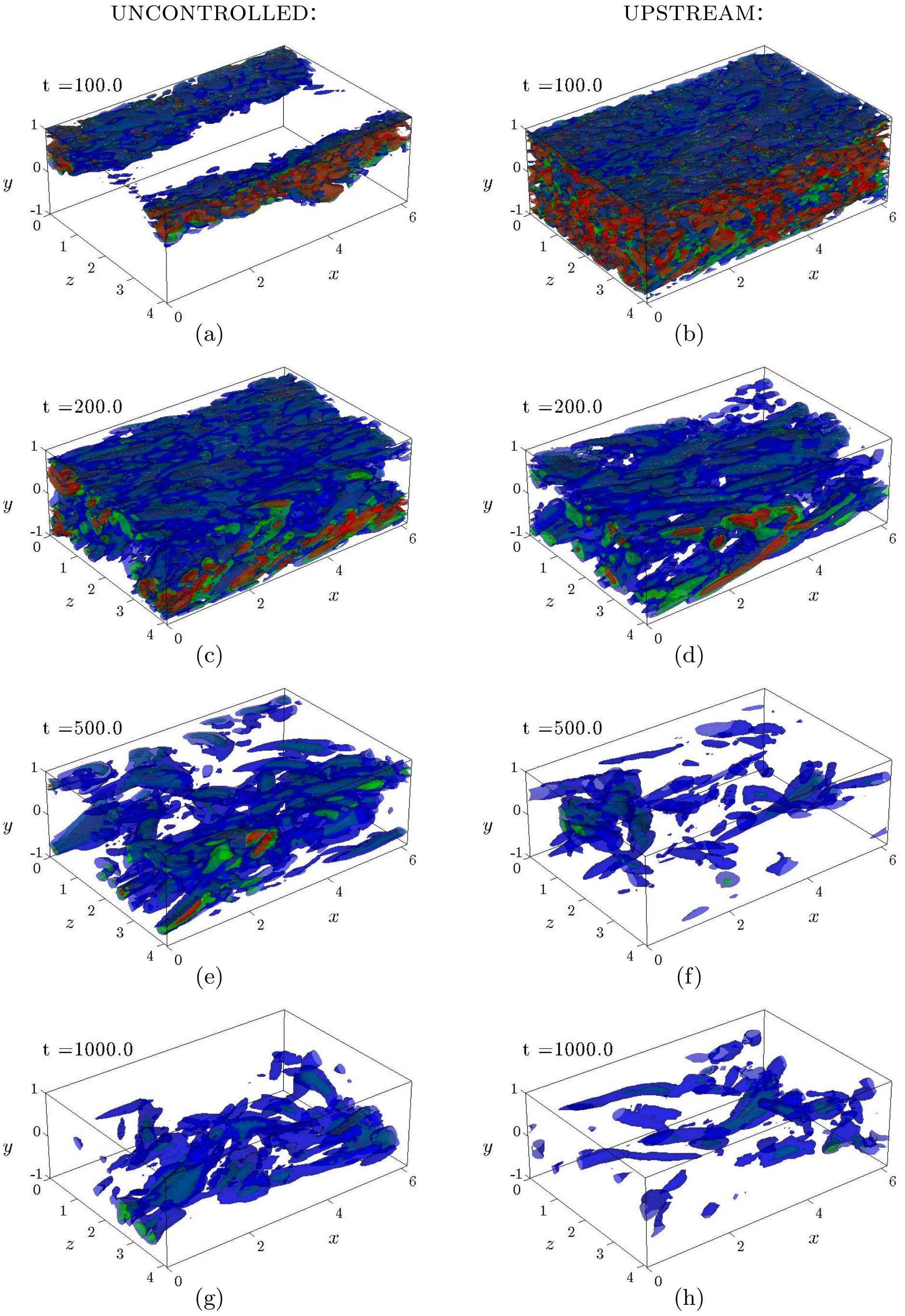
UNCONTROLLED:
UPSTREAM:
t =100.0
t =100.0
(a)
(b)
t =200.0
t =200.0
(c)
(d)
t =500.0
t =500.0
(e)
(f)
t =1000.0
t =1000.0
(g)
(h)
y
1
0
-1
z
0
1
2
3
4
x
0
2
4
6

Figure 3.13: 3D visualizations of the isosurfaces of the discriminant, $D > 10^{-5}$ (blue), $D > 10^{-4}$ (green), and $D > 10^{-3}$ (red) for the uncontrolled flow (left figures) and the UTW with ($c = -2$, $\omega_x = 0.5$, $\alpha = 0.05$) (right figures) for the initial condition with moderate energy. Only one quarter of the channel ($x \in [0, 2\pi]$) is shown for the UTW.

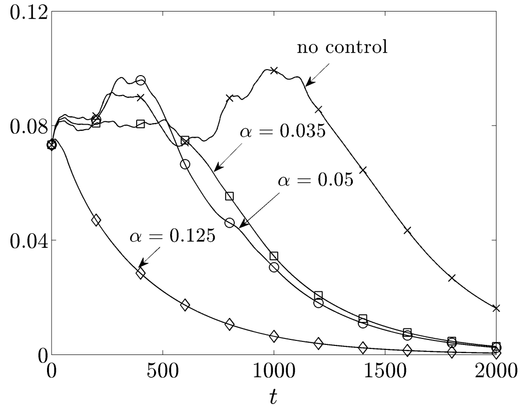

Figure 3.14: Energy of velocity fluctuations around base flows of Section 3.2.1. Simulations are initiated by a fully developed turbulent flow with $R_c = 2000$: $\times$, uncontrolled; DTWs with $\square$, $(c = 5, \omega_x = 2, \alpha = 0.035)$; $\circ$, $(c = 5, \omega_x = 2, \alpha = 0.05)$; and $\diamondsuit$, $(c = 5, \omega_x = 2, \alpha = 0.125)$.

other hand, fluctuations in flows subject to DTWs start decaying much earlier, thereby indicating that the lifetime of turbulence is reduced by surface blowing and suction. Relative to the uncontrolled flow, the fluctuations' kinetic energy for the DTWs considered here converge much faster to zero. We also see that the rate of decay increases as the wave amplitude gets larger.

We next consider a turbulent flow with $R_c = 4300$. The energy of velocity fluctuations around base flows $\mathbf{u}_b$ of Section 3.2.1 is shown in figure 3.15(a). In both the uncontrolled flow and the flows subject to the DTWs with $(c = 5,\ \omega_x = 2,\ \alpha = \{0.035, 0.05\})$ the energy oscillates around large values that identify turbulent flow. This indicates that the DTWs with smaller amplitudes cannot eliminate turbulence. On the contrary, the DTW with $\alpha = 0.125$ reduces the energy of velocity fluctuations, thereby relaminarizing the flow. Figure 3.15(b) shows that the skin-friction drag coefficient for the uncontrolled flow and for the DTWs with smaller amplitudes is approximately constant throughout the simulation. On the other hand, owing to relaminarization, the drag coefficient for the DTW with $\alpha = 0.125$ is smaller than that of the uncontrolled turbulent flow. However, relaminarization comes at the expense of poor net efficiency. This is because of the large required power (i.e., high cost of control), which reduces the appeal of using DTWs for control of turbulent flows.

Figure 3.16 shows the mean velocity, $\overline{U}(y)$, at three time instants in the flow subject to the DTW with $(c = 5,\ \omega_x = 2,\ \alpha = 0.125)$. The instantaneous values of streamwise velocity in the (x, z)-plane at $y = -0.7518$ are also shown. As time advances, the initial turbulent mean velocity at $R_c = 4300$ moves towards the laminar mean velocity induced

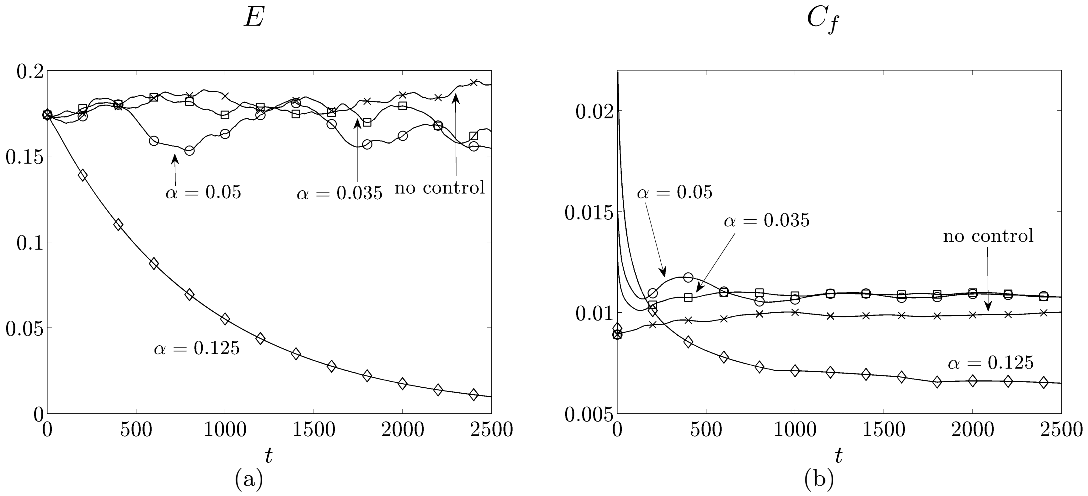

(a) (b)

Figure 3.15: (a) Energy of velocity fluctuations around base flows of Section 3.2.1, $E(t)$; and (b) skin-friction drag coefficient, $C_f(t)$. Simulations are initiated by a fully developed turbulent flow with $R_c = 4300$: ×, uncontrolled; DTWs with □, $(c = 5, \omega_x = 2, \alpha = 0.035)$; ○, $(c = 5, \omega_x = 2, \alpha = 0.05)$; and ◇, $(c = 5,\ \omega_x = 2,\ \alpha = 0.125)$.

by the surface blowing and suction (dashed line). The shaded plots illustrate how the initial turbulent flow evolves into the DTW laminar base flow. We conjecture that receptivity reduction is important not only for controlling the onset of turbulence but also for relaminarization of fully developed flows. As outlined in Part 1, explaining the effect of traveling waves on turbulent flows requires additional control-oriented modeling and further scrutiny.

3.5 Concluding remarks

This work, along with a companion paper [3], represents a continuation of recent efforts [64, 65] to develop a *model-based* paradigm for design of sensorless flow control strategies in wall-bounded shear flows. Direct numerical simulations are used to complement and verify theoretical predictions of [3], where receptivity analysis of the linearized NS equations was used to design small amplitude traveling waves. We have shown that perturbation analysis (in the wave amplitude) represents a powerful simulation-free method for predicting full-scale phenomena and controlling the onset of turbulence.

Simulations of nonlinear flow dynamics have demonstrated that the DTWs, designed in Part 1, can maintain laminar flow and achieve positive net efficiency. In contrast, the UTWs promote turbulence even with the initial conditions for which the uncontrolled flow remains laminar. Our analysis of the Reynolds-Orr equation shows that, compared

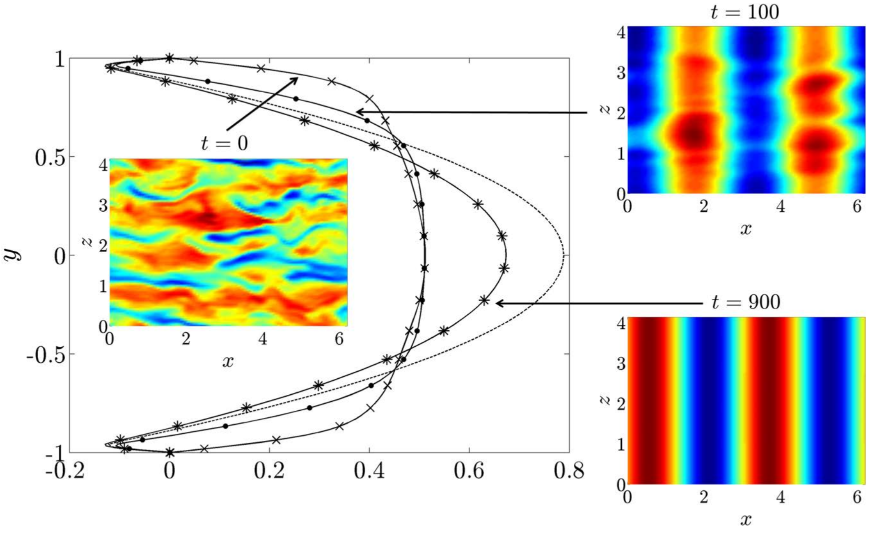

Figure 3.16: Mean velocity, $\overline{U}(y)$, and streamwise velocity (shaded plots) at $y = -0.7518$. Simulations are initiated by a fully developed turbulent flow with $R_c = 4300$: $\times$, $t = 0$; $\bullet$, $t = 100$; $*$, $t = 900$. The dashed line identifies the laminar mean velocity induced by the DTW with ($c = 5$, $\omega_x = 2$, $\alpha = 0.125$).

to the uncontrolled flow, the DTWs (UTWs) reduce (increase) the production of kinetic energy.

We have also examined the effects of DTWs on fully developed turbulent flows at low Reynolds numbers. It turns out that the DTWs with speed and frequency selected in Part 1 and large enough amplitudes can eliminate turbulence (i.e., relaminarize the flow). We also note that, in spite of promoting turbulence, the UTWs may still achieve smaller drag coefficients compared to the uncontrolled flow. By increasing the UTW amplitude, even sub-laminar drag can be attained [2]. It is to be noted, however, that large wave amplitudes introduce poor net efficiency in flows subject to a fixed pressure gradient. Nevertheless, these traveling waves may still be utilized when the primal interest is to eliminate turbulence (with DTWs) or reduce the skin-friction drag (with UTWs) irrespective of the cost of control.

All simulations in the present study are enforced by a fixed pressure gradient, as opposed to the constant mass flux simulations of [2]. This is consistent with Part 1 where receptivity analysis was done for flows driven by a fixed pressure gradient. Even though these setups are equivalent in steady flows [66], they can exhibit fundamentally different behavior in unsteady flows. For example, the two simulations may possess different stability characteristics and yield structurally different solutions for near-wall turbulence [67,68]. Moreover, Jiménez *et al.* [68] remarked that the dynamical properties of the two simulations can significantly differ in small computational domains. Also, Kerswell [69] suggested that specifying the simulation type comes next to defining the boundary conditions.

In order to examine the effect of simulation type on transition, skin-friction drag coefficient, and control net efficiency, we have repeated some of the simulations by adjusting the pressure gradient to maintain a constant mass flux. Our results reveal that regardless of the simulation type, the DTWs designed in Part 1 are effective in preventing transition while the UTWs promote turbulence. Moreover, the steady-state skin-friction drag coefficients are almost identical in both cases. However, the control net efficiency depends significantly on the simulation type. This is because of the difference in the definition of the produced power: in the fixed pressure gradient setup, the produced power is captured by the difference between the bulk fluxes in the uncontrolled and controlled flows; in the constant mass flux setup, the produced power is determined by the difference between the driving pressure gradients in the uncontrolled and controlled flows. It turns out that the produced power is larger in the constant mass flux simulation than in the fixed pressure gradient simulation, whereas the required power remains almost unchanged. Consequently, both DTWs and UTWs have larger efficiency in constant mass flux simulations. For example, in fixed pressure gradient setup of the present study, the UTWs with ($c = -2$, $\omega_x = 0.05$ $\alpha = \{0.05, 0.125\}$) have negative efficiency. The efficiency of these UTWs is positive, however, in constant mass flux simulations [2]. Our ongoing effort is directed towards understanding the reason behind this disagreement which may be ultimately related to the fundamental difference between these two types of simulations.

Chapter 4

Optimal localized control of transitional channel flow

In this chapter, we study the design of optimal localized state-feedback controllers for the problem of controlling the onset of turbulence in a channel flow. The actuation is generated by blowing and suction at the walls and the actuators are placed along a two-dimensional lattice of equally spaced points with each actuator using information from only a limited number of nearby neighbors. We utilize recently developed tools for designing structured optimal feedback gains to reduce receptivity of velocity fluctuations to flow disturbances in the presence of control. Our preliminary direct numerical simulation result, conducted at a low Reynolds number, show that this approach can indeed maintain the laminar flow. This is in contrast to the localized strategies obtained by spatial truncation of optimal centralized controllers, which may introduce instability and promote transition even in the situations where the uncontrolled flow stays laminar.

4.1 Introduction

Feedback strategies for control of fluid flows involve individual system components that are capable of sensing, computation, and actuation. Therefore, an important question in design of flow controllers is related to the interconnection structure between these components. A centralized controller yields best performance at the expense of excessive communication and computation. A fully decentralized controller, while advantageous from a communications perspective, may sacrifice performance. A reasonable compromise between these competing approaches is offered by localized strategies where each component exchanges information with a limited number of nearby components.

Early flow control efforts have focused on drag reduction in turbulent flows. These include the opposition control [70] and gradient-based strategies where the optimal control problem is solved over infinitesimal [71, 72] or finite [56] time horizons. During the last decade, the emphasis has shifted to model-based techniques from linear control theory which represent an efficient means for design of optimal flow controllers, see [73] for an overview of recent developments. In this paper, we study the problem of controlling the onset of turbulence. Since the early stages of transition are initiated by high flow receptivity [74–77], we formulate an optimal control problem aimed at reducing this receptivity. For transition control at low Reynolds numbers, this strategy has proven successful in both vibrational sensor-less [3, 78] and centralized feedback [79] setups. These references show that, by substantially reducing high flow receptivity, transition to turbulence can be prevented and even relaminarization of a fully-developed turbulent flow can be achieved.

The main difference between the problem addressed here and by [79] is that we consider control designs that are localized in space. Namely, the actuation at a certain location depends only on local flow information. The localized controller is obtained using recently developed tools for optimal design of feedback gains subject to structural constraints [80, 81]. We compare the performance of the optimal localized controller with that of the optimal centralized controller and the controller that is obtained by spatial truncation of the centralized feedback gain. When the actuators use information from only the nearest neighbor components, we demonstrate the danger of enforcing the constraint by spatial truncation. On the other hand, we show that the optimal localized controller achieves performance comparable to that of the optimal centralized controller.

The chapter is organized as follows. In § 4.2, the evolution model for channel flow subject to body force disturbances and boundary actuation is derived. The problem of optimal state-feedback design in the presence of structural constraints is formulated in § 4.3. In addition, a gradient descent method for solving necessary conditions for optimality is briefly described. In § 4.4, the effectiveness of the designed feedback gains for controlling the onset of turbulence is examined by comparing the receptivity of the controlled flows and the flow with no control. Our design is further verified using direct numerical simulations of the nonlinear flow dynamics. We conclude the paper in § 4.5.

4.2 Problem formulation

4.2.1 Governing equations

We consider an incompressible channel flow, driven by a fixed pressure gradient and subject to a control actuation in the form of blowing and suction along the walls. The evolution of infinitesimal fluctuations around the laminar parabolic profile $U(y)$ is governed by the linearized Navier-Stokes (NS) equations

$$\mathbf{v}_t \;=\; -U\,\mathbf{v}_x - U'\,v_2\,\mathbf{i} \;-\; \boldsymbol{\nabla} p \;+\; (1/R_c)\Delta\mathbf{v} \;+\; \mathbf{d}, \;\; 0 \;=\; \boldsymbol{\nabla}\cdot\mathbf{v}, \tag{4.1}$$

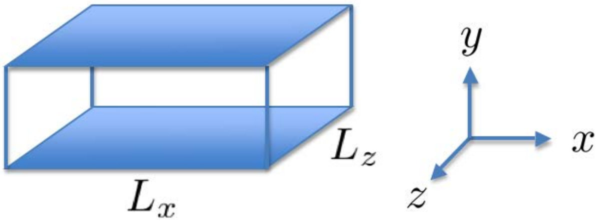

Figure 4.1: A periodic channel with size $L_x \times 2 \times L_z$.

where $\mathbf{i}$ denotes the unit vector in the streamwise direction, and $R_c = U_c\,\delta/\nu$ is the Reynolds number defined in terms of the centerline velocity of the parabolic laminar profile U_c and channel half-height δ. The spatial coordinates and time are denoted by (x, y, z) and t, respectively. The kinematic viscosity is denoted by ν, p is the pressure, the velocity fluctuations are given by $\mathbf{v} = (v_1, v_2, v_3)$, and $\mathbf{d} = (d_1, d_2, d_3)$ represents the body force disturbance. Here, the indices 1, 2, and 3 correspond to x, y, and z coordinates, respectively, $\boldsymbol{\nabla}$ is the gradient, $\Delta = \boldsymbol{\nabla} \cdot \boldsymbol{\nabla}$ is the Laplacian, and $U'(y) = \mathrm{d}U(y)/\mathrm{d}y$. Actuation along the walls imposes the following boundary conditions on the wall-normal velocity

$$v_2(x, y = -1, z, t) \;=\; v_{2,l}(x, z, t), \quad v_2(x, y = 1, z, t) \;=\; v_{2,u}(x, z, t), \tag{4.2}$$

where $v_{2,l}$ and $v_{2,u}$ denote actuations at the lower and upper walls. The horizontal velocity components satisfy Dirichlet boundary conditions

$$v_1(x, y = \pm 1, z, t) \;=\; v_3(x, y = \pm 1, z, t) \;=\; 0.$$

To obtain the standard control formulation, the actuation must enter as an explicit input into the evolution equation [82]. The following change of variables

$$v_2(x, y, z, t) \;=\; \bar{v}_2(x, y, z, t) \,+\, f_l(y)\, v_{2,l}(x, z, t) \,+\, f_u(y)\, v_{2,u}(x, z, t), \tag{4.3}$$

can be used to achieve this objective, where f_l and f_u are specified by the requirement that $\bar{v}_2$ satisfies Dirichlet and Neumann boundary conditions at the walls,

$$f_l(y) \;=\; \left(y^3 - 3y + 2\right)/4, \quad f_u(y) \;=\; -\left(y^3 - 3y - 2\right)/4.$$

The evolution model is obtained from the linearized NS equations (4.1) by eliminating pressure via a standard choice of wall-normal velocity and vorticity (v, η) as the flow variables. By incorporating the change of variables (4.3) and augmenting the flow variables by the boundary actuation, we obtain the state vector $\boldsymbol{\phi} = [\,\boldsymbol{\phi}_1^T \;\; \boldsymbol{\phi}_2^T\,]^T$ with $\boldsymbol{\phi}_1 = [\,\bar{v}_2 \;\; \eta\,]^T$ and $\boldsymbol{\phi}_2 = [\,v_{2,l} \;\; v_{2,u}\,]^T$. This choice brings the time-derivative of the boundary actuation $\mathbf{u} = \boldsymbol{\phi}_{2t}$ as an explicit input to the evolution model. This procedure yields the following evolution model for the controlled flow

$$\boldsymbol{\phi}_t \;=\; \mathcal{A}\,\boldsymbol{\phi} \,+\, \mathcal{B}_1\,\mathbf{d} \,+\, \mathcal{B}_2\,\mathbf{u}, \quad \mathbf{v} \;=\; \mathcal{C}_1\,\boldsymbol{\phi}, \tag{4.4}$$

where

$$\mathcal{A} = \begin{bmatrix} \mathcal{A}_{11} & \mathcal{A}_{12} \\ 0 & 0 \end{bmatrix}, \; \mathcal{B}_1 = \begin{bmatrix} \mathcal{B}_{11} \\ 0 \end{bmatrix}, \; \mathcal{B}_2 = \begin{bmatrix} \mathcal{B}_{21} \\ \mathcal{B}_{22} \end{bmatrix}, \; \mathcal{C}_1 = \begin{bmatrix} \mathcal{C}_{11} & \mathcal{C}_{12} \end{bmatrix},$$

$$\mathcal{A}_{11} = \begin{bmatrix} \Delta^{-1}\left((1/R_c)\Delta^2 - (U_0\Delta - U_0'')\,\partial_x\right) & 0 \\ -U_0'\,\partial_z & (1/R_c)\Delta - U_0\,\partial_x \end{bmatrix},$$

$$\mathcal{A}_{12} = \begin{bmatrix} \mathcal{A}_{12,1} & \mathcal{A}_{12,2} \\ -U_0' f_l\,\partial_z & -U_0' f_u \partial_z \end{bmatrix},$$

$$\mathcal{A}_{12,1} = \Delta^{-1}((2\,f_l''(\partial_x^2 + \partial_z^2) + f_l(\partial_x^2 + \partial_z^2)^2)/R_c - (U_0 f_l'' + U_0 f_l(\partial_x^2 + \partial_z^2) - U_0'' f_l)\,\partial_x),$$
$$\mathcal{A}_{12,2} = \Delta^{-1}((2\,f_u''(\partial_x^2 + \partial_z^2) + f_u(\partial_x^2 + \partial_z^2)^2)/R_c - (U_0 f_u'' + U_0 f_u(\partial_x^2 + \partial_z^2) - U_0'' f_u)\,\partial_x),$$

$$\mathcal{B}_{11} = \begin{bmatrix} \Delta^{-1}(-\partial_{xy}) & \Delta^{-1}(\partial_x^2 + \partial_z^2) & \Delta^{-1}(-\partial_{yz}) \\ \partial_z & 0 & -\partial_x \end{bmatrix},$$

$$\mathcal{B}_{21} = \begin{bmatrix} \Delta^{-1}(-f_l'' - f_l(\partial_x^2 + \partial_z^2)) & \Delta^{-1}(-f_u'' - f_u(\partial_x^2 + \partial_z^2)) \\ 0 & 0 \end{bmatrix}, \; \mathcal{B}_{22} = \begin{bmatrix} 1 & 0 \\ 0 & 1 \end{bmatrix},$$

$$\mathcal{C}_{11} = \begin{bmatrix} -\partial_{xy}\,(\partial_x^2 + \partial_z^2)^{-1} & \partial_z\,(\partial_x^2 + \partial_z^2)^{-1} \\ I & 0 \\ -\partial_{yz}\,(\partial_x^2 + \partial_z^2)^{-1} & -\partial_x\,(\partial_x^2 + \partial_z^2)^{-1} \end{bmatrix},$$

$$\mathcal{C}_{12} = \begin{bmatrix} -f_l'\,\partial_x\,(\partial_x^2 + \partial_z^2)^{-1} & -f_u'\,\partial_x\,(\partial_x^2 + \partial_z^2)^{-1} \\ f_l & f_u \\ -f_l'\,\partial_z\,(\partial_x^2 + \partial_z^2)^{-1} & -f_u'\,\partial_z\,(\partial_x^2 + \partial_z^2)^{-1} \end{bmatrix},$$

with $\Delta = \partial_x^2 + \partial_y^2 + \partial_z^2$ denoting the three-dimensional Laplacian.

The operator $\mathcal{A}$ represents the dynamical generator of (4.4), $\mathcal{B}_1$ and $\mathcal{B}_2$ determine how disturbances and control enter into (4.4), and $\mathcal{C}_1$ specifies kinematic relation between velocity fluctuations $\mathbf{v}$ and state $\boldsymbol{\phi}$.

4.2.2 Actuation along the discrete lattice

In what follows, we impose periodic boundary conditions in the horizontal directions; see figure 4.1 for geometry. The size of the computational domain is given by $L_x \times 2 \times L_z$, where L_x and L_z denote the channel lengths in x and z. We use N_x and N_z Fourier modes to represent differential operators in the streamwise and spanwise directions, respectively. In physical space, this yields a two-dimensional lattice of equally-spaced points $(x_r = rh_x,\; z_s = sh_z)$, with $r \in \mathbb{N}_x = \{0, 1, \ldots, N_x - 1\}$ and $s \in \mathbb{N}_z = \{0, 1, \ldots, N_z - 1\}$.

The horizontal spacings between two adjacent points are determined by $h_x = L_x/N_x$ and $h_z = L_z/N_z$. For simplicity, we use the same symbol to denote variables in physical and frequency domains; for example, $v_2(m,n;y,t)$ denotes the frequency representation of $v_2(r,s;y,t) = v_2(x_r,y,z_s,t)$, where $m \in \mathbb{Z}_x = \{-N_x/2, -N_x/2+1, \ldots, N_x/2-1\}$ and $n \in \mathbb{Z}_z = \{-N_z/2, -N_z/2+1, \ldots, N_z/2-1\}$. The corresponding spatial wavenumbers are determined by $k_m = m\,2\pi/L_x$ and $k_n = n\,2\pi/L_z$.

We consider the design problem with wall-actuation taking place along the aforementioned two-dimensional lattice. Furthermore, we assume that the states are available for measurement, implying that the control input at (x_r, z_s) is obtained from

$$\begin{aligned}\mathbf{u}(r,s;t) \;=\; -\sum_{\tilde r\,\in\,\mathbb{N}_x,\,\tilde s\,\in\,\mathbb{N}_z} \Bigg(\int_{-1}^{1} &\mathcal{K}_1(r-\tilde r, s-\tilde s; y)\,\boldsymbol{\phi}_1(\tilde r,\tilde s; y,t)\,\mathrm{d}y \;+ \\ &\mathcal{K}_2(r-\tilde r, s-\tilde s)\,\boldsymbol{\phi}_2(\tilde r,\tilde s;t)\Bigg),\end{aligned} \tag{4.5}$$

where $\mathcal{K}_1$ and $\mathcal{K}_2$ are the corresponding state-feedback gains. The frequency representation of (4.5), for each $m \in \mathbb{Z}_x$ and $n \in \mathbb{Z}_z$, is given by

$$\mathbf{u}(m,n;t) \;=\; -\int_{-1}^{1} \mathcal{K}_1(m,n;y)\,\boldsymbol{\phi}_1(m,n;y,t)\,\mathrm{d}y \;-\; \mathcal{K}_2(m,n)\,\boldsymbol{\phi}_2(m,n;t). \tag{4.6}$$

For computational purposes, the wall-normal operators in (4.4) and (4.6) are approximated using pseudospectral method with N_y Chebyshev collocation points [83]. This yields the discretized evolution model

$$\begin{aligned}\dot{\boldsymbol{\phi}}_{m,n}(t) &= A_{m,n}\,\boldsymbol{\phi}_{m,n}(t) \,+\, B_{1m,n}\,\mathbf{d}_{m,n}(t) \,+\, B_{2m,n}\,\mathbf{u}_{m,n}(t), \\ \mathbf{v}_{m,n}(t) &= C_{1m,n}\,\boldsymbol{\phi}_{m,n}(t),\end{aligned} \tag{4.7}$$

parameterized by $m \in \mathbb{Z}_x$ and $n \in \mathbb{Z}_z$. Here, $\boldsymbol{\phi}_{m,n}(t)$ and $\mathbf{u}_{m,n}(t)$ are column-vectors with $(2N_y+2)$ and 2 components, respectively, and the dot is the derivative with respect to time. Furthermore, the control action is determined by

$$\mathbf{u}_{m,n}(t) \;=\; -K_{m,n}\,\boldsymbol{\phi}_{m,n}(t) \;=\; -\left[\begin{array}{cc} K_{1m,n} & K_{2m,n}\end{array}\right]\left[\begin{array}{c}\boldsymbol{\phi}_{1m,n}(t) \\ \boldsymbol{\phi}_{2m,n}(t)\end{array}\right]. \tag{4.8}$$

where the $2 \times (2N_y+2)$ matrix $K_{m,n}$ denotes the discretized form of the state-feedback gain in the frequency domain.

4.3 Design of optimal localized feedback gains

We consider the problem of designing structured optimal feedback gains for controlling the onset of turbulence. To this end, we determine the stabilizing gains that minimize a performance index J obtained by penalizing flow receptivity and control effort. These are, respectively, quantified by the variance amplification of velocity fluctuations $\mathbf{v}$ in the presence of zero-mean white stochastic disturbance $\mathbf{d}$, and by the kinetic energy of the blowing and suction along the walls. In addition, to obtain the well-posed optimal control formulation, the penalty on $\mathbf{u}$ is introduced in the performance index as well.

The above described optimal control problem amounts to finding the stabilizing gains that minimize the variance amplification of the performance output

$$\boldsymbol{\zeta}_{m,n}(t) \;=\; \left[\begin{array}{c} W^{1/2}\,C_{1m,n} \\ 0 \end{array}\right] \boldsymbol{\phi}_{m,n}(t) \;+\; \left[\begin{array}{c} 0 \\ R^{1/2} \end{array}\right] \mathbf{u}_{m,n}(t). \tag{4.9}$$

Here, R is the positive definite matrix, and W denotes a $3N_y \times 3N_y$ diagonal matrix with $\{\mathbf{w}, \mathbf{w}, \mathbf{w}\}$ on its main diagonal where the vector $\mathbf{w}$ contains the integration weights at the Chebyshev collocation points [84]. Substitution of (4.8) into (4.7) and (4.9) yields the following evolution model of the closed-loop system

$$\begin{aligned} \dot{\boldsymbol{\phi}}_{m,n}(t) \;&=\; \big(A_{m,n} \,-\, B_{2m,n}\,K_{m,n}\big)\,\boldsymbol{\phi}_{m,n}(t) \;+\; B_{1m,n}\,\mathbf{d}_{m,n}(t), \\ \boldsymbol{\zeta}_{m,n}(t) \;&=\; \left[\begin{array}{c} W^{1/2}\,C_{1m,n} \\ -R^{1/2}\,K_{m,n} \end{array}\right] \boldsymbol{\phi}_{m,n}(t). \end{aligned} \tag{4.10}$$

Mathematically, the problem of steady-state variance (i.e., the $\mathcal{H}_2$ norm) minimization for system (4.10) can be formulated as [82]

$$\text{minimize}: \;\; J(K) \;=\; \sum_{m\in\mathbb{Z}_x, n\in\mathbb{Z}_z} \text{trace}\,\left(X_{m,n}\,Q_{Bm,n}\right), \tag{4.11a}$$

$$\text{subject to}: \;\; A^*_{\mathrm{cl}m,n}\,X_{m,n} + X_{m,n}\,A_{\mathrm{cl}m,n} \;=\; -\big(Q_{Cm,n} \,+\, K^*_{m,n}\,R\,K_{m,n}\big), \tag{4.11b}$$

where * denotes the complex conjugate transpose, $A_{\mathrm{cl}m,n} = A_{m,n} - B_{2m,n}K_{m,n}$, $Q_{Bm,n} = B_{1m,n}W^{-1}B^*_{1m,n}$, and $Q_{Cm,n} = C^*_{1m,n}WC_{1m,n}$. The solution to (4.11) in the absence of structural constraints is given by

$$K_{m,n} \;=\; R^{-1}\,B^*_{2m,n}\,X_{m,n}, \tag{4.12}$$

where $X_{m,n}$ is determined from the algebraic Riccati equation

$$A^*_{m,n}\,X_{m,n} \,+\, X_{m,n}\,A_{m,n} \,-\, X_{m,n}\,B_{2m,n}\,R^{-1}\,B^*_{2m,n}\,X_{m,n} \,+\, Q_{Cm,n} \;=\; 0.$$

In general, actuation based on the optimal solution (4.12) necessitates centralized implementation which requires knowledge of the entire flow field. The problem of designing optimal centralized feedback gains for controlling transition is considered by [79]. As shown by [85], the magnitude of the centralized feedback gains decays exponentially in space, implying that they can be spatially truncated. Although this suggests a way for obtaining localized controllers, the problem of designing optimal localized feedback

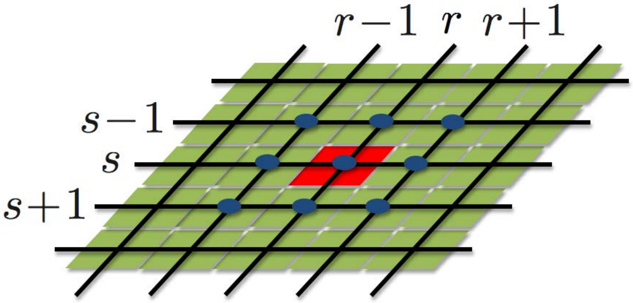

Figure 4.2: Sketch of a localized control strategy where the actuator placed at (r, s) uses information from only the nearest neighbors on the two-dimensional lattice.

gains is more challenging. The main difference between the problem considered here and in [79] is that we ask the following question: Can actuation based on local flow information prevent transition to turbulence? To answer this question, we *a priori* impose structural constraints on the feedback gains. It is assumed that each actuator uses information only from the points that are located within a small relative distance. The set of all such relative distances in units of h_x and h_z is denoted by S. In other words, only the feedback gains that correspond to the points in S are allowed to be nonzero. For example, when information from only the nearest neighbors is used, we have (see figure 4.2 for an illustration)

$$S \;=\; \big\{(r,s) \;\big|\; r = \{-1,0,1\}, s = \{-1,0,1\}\big\}\,.$$

Furthermore, by $F(r, s)$ we denote the corresponding structured feedback gains.

For spatially invariant systems, the structured optimal state-feedback problem can be formulated as [80]

$$\text{minimize}: \;\; J(F) \;=\; \sum_{m\in\mathbb{Z}_x, n\in\mathbb{Z}_z} \text{trace}\,\left(X_{m,n}\, Q_{Bm,n}\right), \tag{P1}$$

$$\text{subject to}: \;\; A^*_{\text{cl}m,n}\, X_{m,n} + X_{m,n}\, A_{\text{cl}m,n} \;=\; -\big(Q_{Cm,n} \,+\, C^*_{2m,n}\, F^*\, R\, F\, C_{2m,n}\big), \tag{P2}$$

where F denotes the block-row matrix which is independent of m and n and contains the structured feedback gain $F(r, s)$,

$$F \;=\; \text{row}\,\{F(r,s)\}_{(r,s)\in S}\,, \tag{P3}$$

and $C_{2m,n}$ is given by the block-column matrix

$$C_{2m,n} \;=\; \text{col}\left\{ \text{e}^{-\text{i}\,2\pi\,(r\,m/N_x \,+\, s\,n/N_z)}\; I \right\}_{(r,s)\in S}. \tag{P4}$$

Here, I is the identity matrix of size $2N_y + 2$, and $A_{\mathrm{cl}m,n} = A_{m,n} - B_{2m,n}\, F\, C_{2m,n}$ denotes the dynamical generator of the closed-loop system.

Note that in the absence of structural constraints (i.e., $S = \mathbb{N}_x \times \mathbb{N}_z = \{(r,s) \big| \ r \in \mathbb{N}_x, s \in \mathbb{N}_z\}$), the structured optimal control problem (P1)-(P4) reduces to the unstructured problem (4.11).

4.3.1 Computation of the structured optimal feedback gains

We briefly describe the method that is used to solve the optimal control problem (P1)-(P4) with specified S. This method is adopted from the developments of [81] where efficient descent methods for structured optimal design are introduced.

The necessary conditions for optimality of the stabilizing feedback gain F with $R = rI_{2\times 2}$ in (P2), $r > 0$, are given by [81]

$$\begin{aligned} A_{\mathrm{cl}m,n}^{*}\, X_{m,n} \,+\, X_{m,n}\, A_{\mathrm{cl}m,n} \;&=\; -\left(Q_{Cm,n} \,+\, r\, C_{2m,n}^{*}\, F^{*}\, F\, C_{2m,n}\right), \\ A_{\mathrm{cl}m,n}\, Y_{m,n} \,+\, Y_{m,n}\, A_{\mathrm{cl}m,n}^{*} \;&=\; -\, Q_{Bm,n}, \\ F \;=\; \frac{1}{r}\left(\sum_{m\,\in\,\mathbb{Z}_x,\, n\,\in\,\mathbb{Z}_z} B_{2m,n}^{*}\, X_{m,n}\, Y_{m,n}\, C_{2m,n}^{*} \right) &\left(\sum_{m\,\in\,\mathbb{Z}_x,\, n\,\in\,\mathbb{Z}_z} C_{2m,n}\, Y_{m,n}\, C_{2m,n}^{*} \right)^{-1}. \end{aligned} \tag{4.13}$$

This system of equations is nonlinear in the unknown matrices $X_{m,n}$, $Y_{m,n}$, and F. Moreover, as seen from the last condition in (4.13) the structural constraints on F introduce coupling between all wavenumbers; this is in contrast to the unstructured optimal control problem (4.11).

Next, we describe the algorithm that is employed for solving (4.13) [81]:

Descent method for solving (4.13):

```
given stabilizing $F^0$ that satisfies the structural constraints imposed by $S$,
for $i = 0, 1, 2, \ldots$, do:
    (1) compute descent direction $\tilde{F}^i$;
    (2) determine step-size $q^i$;
    (3) update $F^{i+1} = F^i + q^i\, \tilde{F}^i$;
until: the stopping criterion $||\nabla J(F^i)||_F < \epsilon$ is achieved, where $||\cdot||_F$ denotes the Frobenius norm and $\epsilon$ is the convergence tolerance.
```

We consider the gradient descent direction that provides linear rate of convergence to the local minimum. More sophisticated descent directions, such as Newton or quasi-Newton directions, provide faster convergence at the expense of increased computational cost (for example, see [81]). The gradient direction is given by $\tilde{F}^i = -\nabla J(F^i)$ where $\nabla J(F^i)$ is determined from [81]

$$\nabla J(F^i) \;=\; \frac{2}{N_x\, N_z} \sum_{m\,\in\,\mathbb{Z}_x,\, n\,\in\,\mathbb{Z}_z} \left(r\, F\, C_{2m,n} \,-\, B_{2m,n}^{*}\, X_{m,n}\right) Y_{m,n}\, C_{2m,n}^{*}.$$

For the step-size rule, the backtracking line search [86] is used where in addition to guaranteeing descent of the performance index, we also guarantee the stability of the updated closed-loop system. Namely, we repeat $q^i = \beta q^i$ $(0 < \beta < 1)$ until both of the following conditions are satisfied:

(a) descent: $J(F^i + q^i \tilde{F}^i) < J(F^i) + \alpha q^i \sum_{m,n} (\nabla J(F^i)^T \tilde{F}^i)$ with $0 < \alpha < 0.5$;

(b) closed-loop stability: $A_{m,n} - B_{2m,n} \, F \, C_{2m,n}$ is stable for all $m \in \mathbb{Z}_x$ and $n \in \mathbb{Z}_z$.

4.4 Localized control of transition

As discussed in § 4.1, the problem of controlling the onset of turbulence is formulated as the receptivity (i.e., the $\mathcal{H}_2$ norm) reduction problem. Therefore, to assess the effectiveness of feedback controllers, we compare the receptivity of controlled flows to the receptivity of flow with no control. We consider the stochastically forced linearized NS equations in the subcritical regime where the flow with no control is linearly stable. The energy density of fluctuations in the presence of stochastic forcing is used to quantify the flow receptivity. The zero-mean stochastic forcing which is white in time and y and purely harmonic in horizontal directions yields a nonzero steady-state variance of velocity fluctuations $E(k_m, k_n)$ [87]. For any $m \in \mathbb{Z}_x$ and $n \in \mathbb{Z}_z$, this quantity can be obtained from

$$\begin{aligned} E(k_m, k_n) \; &= \; \text{trace} \, (Z_{m,n} \, Q_{Bm,n}) \, , \\ (A_{m,n} - B_{2m,n} \, F \, C_{2m,n})^* \, Z_{m,n} \; + \; Z_{m,n} \, (A_{m,n} - B_{2m,n} \, F \, C_{2m,n}) \; &= \; -Q_{Cm,n}. \end{aligned} \tag{4.14}$$

For the flow with no control (i.e., for $F = 0$), the streamwise-constant fluctuations are the most amplified by the linearized dynamics [76, 77, 87]. These fluctuations correspond to the streamwise streaks that are ubiquitous in wall-bounded shear flows. The large amplification of streaks is physically associated with the vortex-tilting (lift-up) mechanism which arises from the non-normal coupling between dynamics of the wall-normal velocity and vorticity fluctuations [74, 88]. This non-normal coupling is also responsible for the pseudo-resonance phenomenon [75, 89] where large amplification of harmonic disturbances that are not associated with eigenvalues of the linearized model is obtained. On the other hand, the least stable modes of the uncontrolled flow (i.e., the Tollmien-Schlichting (TS) waves) are much less amplified than the streamwise streaks. This highlights the importance of amplification of the streamwise constant fluctuations in the early stages of transition. Therefore, a control strategy that is capable of reducing the receptivity of streamwise streaks to stochastic disturbances represents a viable approach for controlling the onset of turbulence.

4.4.1 Receptivity of the controlled flows

For the controlled flows, we consider three state-feedback gains: (a) the centralized gains determined by (4.12); (b) the truncated gains obtained by enforcing the structural constraints by spatial truncation of the centralized feedback gains; and (c) the optimal localized gain F that is designed using the method presented in § 4.3.1. For the truncated and localized controllers, we consider the case where each actuator uses information from only its nearest neighbors (for an illustration, see figure 4.2).

Figure 4.3 compares the energy amplification of the controlled flows with $R_c = 2000$ and the flow with no control for different horizontal wavenumbers. The optimal centralized controller significantly reduces flow receptivity for all wavenumbers. Compared to the flow with no control, 89% reduction in amplification of the most energetic structures (i.e., streaks) is achieved (cf. peak values in figure 4.3(a)).

Next, we look at the flows that are controlled by the truncated centralized and optimal localized feedback gains. Figures 4.3(b) and 4.3(c) illustrate that truncated centralized gains introduce instability at small streamwise wavenumbers. The numerical simulations of § 4.4.2 confirm that the flow controlled with these gains diverges from the laminar profile and becomes turbulent. In addition, for the stable wavenumbers, figure 4.3 shows that the variance amplification of the truncated centralized controller is much larger than that of the centralized controller. This justifies the need for designing optimal localized controllers that satisfy the structural constraints and exhibit similar performance to that of the centralized controller.

In order to obtain the optimal localized gains, we have used the truncated centralized gains to initialize the iterative scheme described in § 4.3.1. Although the truncated gains are not stabilizing, it turns out that the initial gradient direction can be used to obtain stabilizing structured gains. We are currently also developing algorithms based on the augmented Lagrangian method [81] that does not require stabilizing gains for the initial iteration.

Figure 4.3 shows that the optimal localized gains maintain stability for all wavenumbers. In addition, the variance amplification of the localized controller is similar to that of the centralized controller. In particular, figure 4.3(a) shows that amplification of the most energetic modes is almost the same for optimal localized and centralized controllers. Therefore, the properly designed localized controller is a good candidate for controlling the onset of turbulence, as verified in direct numerical simulations of § 4.4.2.

4.4.2 Direct numerical simulations

Using the numerical method described in Chapter 2, we simulate a channel flow with $R_c = 2000$ that is driven by a constant pressure gradient and is subject to actuation in the form of blowing and suction at the walls. This value of R_c is smaller than the Reynolds number at which linear instability occurs ($R_c = 5772$) and larger than the value for which transition usually takes place in experiments and DNS ($R_c \approx 1000$).

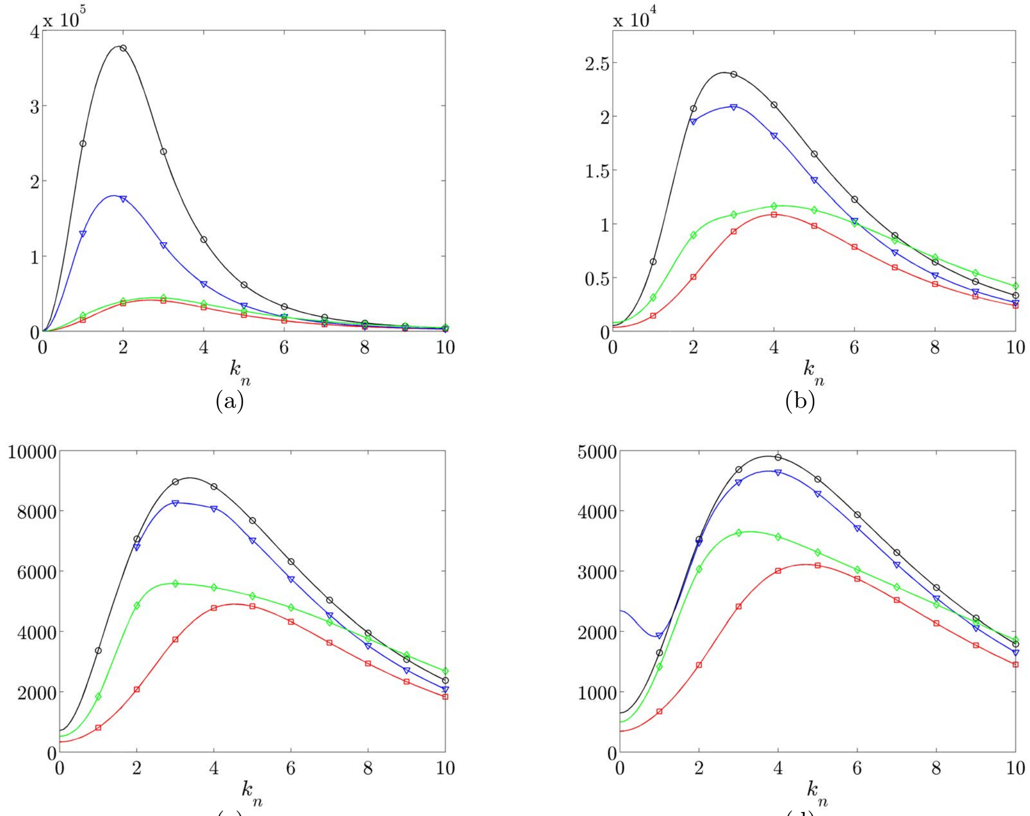

(a) (b) (c) (d)

Figure 4.3: Energy density of the velocity fluctuations $E(k_n)$ for the uncontrolled flow with $R_c = 2000$ ($\circ$), optimal centralized ($\Box$), truncated centralized ($\triangledown$), and optimal localized ($\diamond$) controllers for (a) $k_m = 0$; (b) $k_m = 0.5$; (c) $k_m = 1$; and (d) $k_m = 1.5$. The truncated controller is unstable for $k_m = \{0.5, 1\}$ and $k_n = \{0, 1\}$ and the energy density is not defined for any combination of these wavenumbers. Note: The energy density is computed at the discrete set of wavenumbers k_n and k_m (symbols) and the lines are plotted for visual aid.

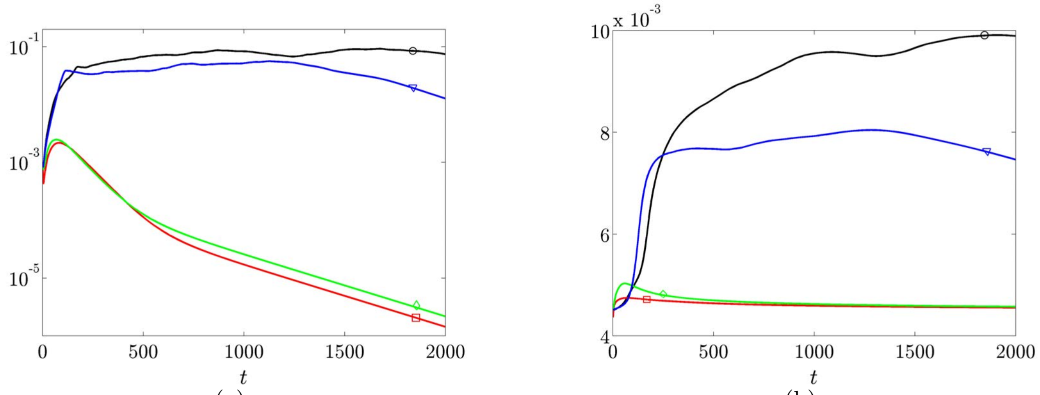

(a) (b)

Figure 4.4: (a) Energy of the velocity fluctuations $E(t)$; and (b) skin-friction drag coefficient $C_f(t)$ for the flow with no control (○) and optimal centralized (□), truncated centralized (▽), and optimal localized (◇) controllers. The results are obtained using DNS with $R_c = 2000$.

The fully nonlinear NS equations are discretized with spectral accuracy using Fourier modes in horizontal directions and Chebyshev polynomials in y, as described in § 4.2.2. The lengths of the computational box in units of the channel half height δ are $L_x = 4\pi$ and $L_z = 2\pi$, with $N_x \times N_y \times N_z = 52 \times 97 \times 42$ points in x, y, and z directions (after dealiasing in x and z). In our study, 42 collocation points in y were enough for computing convergent feedback gains. These gains are then interpolated and scaled to determine the feedback gains for 97 Chebyshev collocation points.

The flow is initialized with a perturbation that is capable of driving the uncontrolled flow to turbulence. For the optimal centralized, truncated optimal centralized, and optimal localized feedback gains, we evaluate the energy of velocity fluctuations $E(t)$ around the laminar parabolic profile and the skin-friction drag coefficient $C_f(t)$.

Figure 4.4(a) shows $E(t)$ for the controlled flows and the flow with no control. Compared to its initial value, the energy of 3D fluctuations in the uncontrolled flow is increased by approximately two orders of magnitude, resulting in divergence from the laminar parabolic profile. On the other hand, the optimal centralized controller provides decay of fluctuations' energy to zero after a small transient growth. Our results agree with the study of [79] where it was shown that the optimal centralized controller is capable of preventing transition. The truncated centralized controller introduces faster growth of $E(t)$ relative to the flow with no control, thereby promoting divergence from the laminar flow. On the other hand, figure 4.4(a) shows that the optimal localized controller is capable of maintaining the laminar flow by providing performance comparable to that of the optimal centralized controller.

Figure 4.4(b) shows the skin-friction drag coefficient $C_f(t)$. We see that the drag coefficients of the optimal centralized and localized controllers are equal to 4.5×10^{-3} which corresponds to the drag coefficient of the laminar flow. On the other hand, the drag coefficient of the uncontrolled flow is 10^{-2} which is a clear indicator of a fully developed turbulent flow. The drag coefficient of the truncated centralized controller is approximately 7.5×10^{-3}. This suggests that although the truncated gains cannot maintain the laminar flow, they achieve 16% reduction in drag relative to the uncontrolled turbulent flow.

4.5 Concluding remarks

We consider design of optimal localized flow controllers for preventing transition to turbulence. We formulate an optimal control problem for minimizing the flow receptivity and control effort. In addition, structural constraints are imposed on the feedback gains such that only the gains that are associated with the nearest neighbors are nonzero. This problem is solved using recently developed techniques for optimal design of state-feedback controllers with structural constraints. We show that spatial truncation of the optimal centralized gains can introduce flow instability. Therefore, the truncated feedback gains may not be suitable for controlling transition and they may even promote turbulence in the situations where the uncontrolled flow stays laminar. On the other hand, we demonstrate that the optimal localized controller can exhibit receptivity reduction similar to that of the optimal centralized controller. Furthermore, our simulations of the nonlinear flow dynamics show that transition can be prevented using optimal localized gains.

Chapter 5

Dynamics of the roll and streak structure in transition and turbulence

The prominence of streamwise elongated structures in wall-bounded shear flow turbulence previously motivated turbulence investigations using streamwise constant (2D/3C) and streamwise averaged (SSST) models. Results obtained using these models imply that the statistical mean turbulent state is in large part determined by streamwise constant structures, particularly the well studied roll and streak. In this work the role of streamwise structures in transition and turbulence is further examined by comparing theoretical predictions of roll/streak dynamics made using 2D/3C and SSST models with direct numerical simulations (DNS). The results confirm that the 2D/3C model accurately obtains the turbulent mean velocity profile despite the fact that it only includes one-way coupling from the cross-stream perturbations to the mean flow. The SSST system augments the 2D/3C model through the addition of feedback from this streamwise constant mean flow to the dynamics of streamwise varying perturbations. With this additional feedback, the SSST system supports a perturbation/mean flow interaction instability leading to a bifurcation from the laminar mean flow to a self-sustaining turbulent state. Once in this self-sustaining state the SSST collapses to a minimal representation of turbulence in which a single streamwise perturbation interacts with the mean flow. Comparisons of DNS data with simulations of this self-sustaining state demonstrate that this minimal representation of turbulence produces accurate statistics for both the mean flow and the perturbations. These results suggest that SSST captures fundamental aspects of the mechanisms underlying transition to and maintenance of turbulence in wall-bounded shear flows.

5.1 Introduction

The dynamical significance of streamwise elongated structures in wall-turbulence is supported by a growing body of work pointing to their central role in both transition to turbulence [77,90,91] and maintenance of a turbulent flow [92–94]. Streamwise coherent "roll cells" associated with streamwise elongated regions of low and high streamwise momentum have been observed in both Direct Numerical Simulations (DNS) of turbulent channel flow [11] as well as in boundary layer and pipe flow experiments [95–98]. These so-called streak structures are of great interest because they account for a substantial portion of the turbulent kinetic energy [96,98,99] and have been shown to modulate the activity of near-wall structures [99, 100].

The importance of these streamwise coherent structures previously motivated the use of a streamwise constant (so-called 2D/3C) model for plane Couette flow, which was shown to accurately simulate the mean turbulent velocity profile [101]. A more comprehensive model can be obtained by including feedback from the streamwise constant mean flow to the dynamics of the perturbation field. A recent parameterization of this feedback was incorporated in a Stochastic Structural Stability Theory (SSST) model using a second order closure [102].

In both the 2D/3C and SSST models the flow field is decomposed into a streamwise constant mean flow and a streamwise varying perturbation field but they differ in their parameterizations of the perturbations. In the 2D/3C model, stochastically forced streamwise roll structures produce Reynolds stresses that drive the mean flow. The SSST model uses a three dimensional stochastic turbulence model (STM) along with an ensembling assumption to parameterize the perturbation dynamics. The associated Reynolds stresses force the streamwise roll structures and drive the mean flow, which is then used in the STM to evolve a consistent perturbation field. With these additions to the basic 2D/3C system, the SSST model produces both the mean turbulent velocity profile and the quadratic turbulence statistics. In addition, the inclusion of streamwise varying components and the feedback mechanisms associated with them enables the SSST system to capture both transition to turbulence and the self-sustaining process (SSP) that maintains the turbulent state [102].

The success of these models in simulating turbulence statistics has implications for understanding the dynamics of turbulent flows. The 2D/3C model suggests that turbulence statistics are fundamentally determined by the streamwise invariant dynamics of the roll structure. The SSST model supports this notion and also implies that transition is instigated through an interaction instability. It further suggests that turbulence is maintained by an essentially non-normal, parametric, quasi-linear interaction instability regulated by a quasi-linear feedback process that determines the statistical mean state. In the current work, we test the validity of the mechanisms suggested by these models by comparing 2D/3C and SSST based simulations to DNS data. We begin by deriving a so-called quasi-linear (QL) numerical approximation of the SSST model from the Navier Stokes equations. The 2D/3C model is shown to be a simplification of the

QL. We then discuss the underlying theory of these models and derive the full SSST dynamics. Finally, we compare results predicted by SSST (obtained from simulations of QL) and 2D/3C simulations to DNS data.

5.2 Modeling framework

Consider an incompressible unit density fluid in a channel and decompose the velocity fields as $\vec{u}_{tot} = \vec{u}+\vec{U}$, where the streamwise constant mean flow variables are denoted by uppercase letters and variables associated with perturbations from this mean flow are denoted by lowercase letters. Throughout this paper, streamwise averaged, spanwise averaged and ensemble averaged quantities are respectively denoted by an overbar, $\bar{\cdot}$, square brackets, $[\cdot]$ and angled brackets, $\langle\cdot\rangle$. Using these notations, the equations governing the mean flow and the perturbation fields are

$$\vec{u}_t \,+\, \vec{U}\cdot\nabla\vec{u} \,+\, \vec{u}\cdot\nabla\vec{U} \,+\, \nabla p \,-\, \Delta\vec{u}/R \;=\; -\left(\vec{u}\cdot\nabla\vec{u} \,-\, \overline{\vec{u}\cdot\nabla\vec{u}}\right) \,+\, \vec{\epsilon} \tag{5.1a}$$

$$\vec{U}_t \,+\, \vec{U}\cdot\nabla\vec{U} \,+\, \nabla P \,-\, \Delta\vec{U}/R \;=\; -\overline{\vec{u}\cdot\nabla\vec{u}}, \tag{5.1b}$$

$$\nabla\cdot\vec{u} \;=\; 0, \quad \nabla\cdot\vec{U} = 0, \tag{5.1c}$$

where the Reynolds number, R, is the only explicit parameter. The term $\vec{\epsilon}$ in (5.1a) represents an externally imposed stochastic forcing. In a DNS this $\vec{\epsilon}$ typically represents the initial condition required to instigate transition to turbulence. In the current work it represents a small finite time stochastic disturbance that is used in a similar manner. In what follows, we refer to the system (5.1) as the NL system.

We first simplify (5.1) by stochastically parameterizing both the perturbation – perturbation nonlinearity $(\vec{u}\cdot\nabla\vec{u} \,-\, \overline{\vec{u}\cdot\nabla\vec{u}})$ and the external excitation in equation (5.1a) to obtain

$$\vec{u}_t \,+\, \vec{U}\cdot\nabla\vec{u} \,+\, \vec{u}\cdot\nabla\vec{U} \,+\, \nabla p \,-\, \Delta\vec{u}/R \;=\; \vec{e} \tag{5.2a}$$

$$\vec{U}_t \,+\, \vec{U}\cdot\nabla\vec{U} \,+\, \nabla P \,-\, \Delta\vec{U}/R \;=\; -\overline{\vec{u}\cdot\nabla\vec{u}}, \tag{5.2b}$$

where $\vec{e}$ is a stochastic forcing to be specified. This is a nonlinear system where the first equation (5.2a) captures interactions between the streamwise constant mean flow $\vec{U}$ and the streamwise varying perturbations $\vec{u}$. The mean flow equation (5.2b) is driven by the streamwise constant component of the Reynolds stresses, $\overline{\vec{u}\cdot\nabla\vec{u}}$. Hereafter, the equations (5.2) will be referred to as the QL system.

The mean flow considered here consists of streamwise, U, wall-normal, V, and spanwise, W, velocity components. The nondivergence of this velocity field can be enforced by defining a stream function Ψ that satisfies $V = -\Psi_z$, $W = \Psi_y$. For non-zero V and W the mean flow has a roll structure, with mean streamwise vorticity $\Omega_x = \Delta_1\Psi$, where $\Delta_1 \equiv \partial^2_{xx} + \partial^2_{zz}$. The deviation of the streamwise velocity $U(y,z,t)$ from its spanwise average $[U](y,t)$ defines the streak velocity $U_s(y,z,t)$. In terms of the streamwise mean velocity U and the stream function Ψ the mean equation (5.2b) takes the form

$$U_t - U_y\Psi_z + U_z\Psi_y - \Delta_1 U/R = F_x, \tag{5.3a}$$

$$\Delta_1\Psi_t - (\partial_{yy} - \partial_{zz})\,\Psi_y\Psi_z + \partial_{yz}\left(\Psi_y^2 - \Psi_z^2\right) - \Delta_1\Delta_1\Psi/R = F_{yz}, \tag{5.3b}$$

$$F_x = -\partial_y\overline{uv} - \partial_z\overline{uw}, \quad F_{yz} = -(\partial_{yy} - \partial_{zz})\,\overline{vw} - \partial_{yz}\left(\overline{w^2} - \overline{v^2}\right). \tag{5.3c}$$

The streamwise mean velocity, U, in (5.3a) is forced by the Reynolds stress divergence F^x, which is obtained from (5.2a) and by $U_y\Psi_z - U_z\Psi_y$, the first part of which is the familiar lift-up mechanism. The Reynolds stress term in (5.3b), F^{yz}, provides the streamwise roll forcing by generating streamwise mean vorticity, $\Omega_x = \Delta_1\Psi$. The mean velocities can only advect Ω_x, via the term $-(\partial_{yy} - \partial_{zz})\Psi_y\Psi_z + \partial_{yz}(\Psi_y^2 - \Psi_z^2)$.

A minimal 2D/3C representation of (5.3) is obtained by setting $F^x = 0$ in (5.3a) and parameterizing F^{yz} in (5.3b) as a stochastic excitation as follows:

$$U_t - U_y\Psi_z + U_z\Psi_y - \Delta_1 U/R = 0, \tag{5.4a}$$

$$\Delta_1\Psi_t - (\partial_{yy} - \partial_{zz})\,\Psi_y\Psi_z + \partial_{yz}\left(\Psi_y^2 - \Psi_z^2\right) - \Delta_1\Delta_1\Psi/R = F_L(y,z,t). \tag{5.4b}$$

In the simulations described in Section 5.6, the stochastic excitation $F_L(y,z,t)$ in (5.4b) is generated by the Reynolds stresses obtained by stochastically forcing the perturbation dynamics linearized about a laminar Couette flow. A similar stochastic forcing is used to force the perturbation field in the QL simulations, except that the Reynolds stresses arise from linearizing about the time dependent mean flow $\vec{U}$.

Figure 5.1 illustrates the nonlinear interactions between the mean flow and perturbation dynamics that is captured by the 2D/3C and QL models. Both of these models include pathway (1) in which the perturbations ($\vec{u}$) influence the dynamics of the mean flow ($\vec{U}$). However, the QL (and its associated ensemble mean SSST model) also includes the feedback pathway (2), from the mean flow to the perturbation dynamics.

5.3 Relation of 2D/3C and QL to SSST

The QL and the 2D/3C models are stochastic dynamical systems. Theoretical understanding of the behavior of these systems is facilitated by considering the dynamics of the associated ensemble mean systems. The ensemble mean dynamical system associated with QL is the SSST system, which is given explicitly by equation (5.7) below. The SSST system comprises the streamwise mean flow dynamics coupled to the second order covariances of the flow fields obtained using a stochastic turbulence model. The SSST is preferred for theoretical investigations because it is a second order closure in which quadratic perturbation quantities are directly computed in terms of the perturbation covariance, which is the perturbation variable in SSST.

An analytically and computationally powerful simplification used in the derivation of

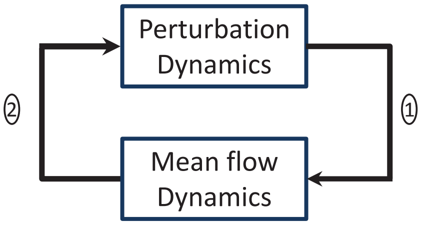

Figure 5.1: In both the 2D/3C (5.4) and QL (5.2) (and its associated ensemble mean SSST model) the perturbations ($\vec{u}$) influence the dynamics of the mean flow ($\vec{U}$). This coupling is denoted pathway (1) in the block diagram. The SSST model augments the 2D/3C formulation with feedback from the mean flow to the perturbation dynamics, which is illustrated through pathway (2).

the SSST system is to equate the ensemble means of second order perturbation statistics with the streamwise average of these quantities. In this way, the ensemble mean of a Reynolds stress can be assumed to be equal to the streamwise mean of that Reynolds stress.

We write the stochastically forced perturbation equation (5.2a) concisely as

$$\partial_t \phi \;=\; \mathsf{A}\phi \,+\, e, \tag{5.5}$$

is the dynamical operator linearized about the instantaneous mean flow $\vec{U}$. The operator A governs the evolution of the perturbation state ϕ. If we define the covariance of the perturbation fields between coordinate point a and b as $C(a,b) =< \phi(a)\phi(b) >$ where $\phi(a)$ is any perturbation state at point a (similarly for b), and multiply the perturbation equations (5.5) at locations a and b with $\phi(b)$ and $\phi(a)$ respectively we obtain the following ensemble mean covariance equation

$$\partial_t \mathsf{C}(a,b) \;=\; \left(\mathsf{A}(a) \,+\, \mathsf{A}(b)\right) \mathsf{C}(a,b) \,+\, \mathsf{Q}(a,b), \tag{5.6}$$

Here, $\mathsf{Q}(a,b)$ is the spatial covariance of the forcing, defined as: $< e(a,t_1)e(b,t_2) >:= \delta\left(t_1 - t_2\right) \mathsf{Q}(a,b)$. The spatial covariance of this forcing will be assumed to be homogeneous. The operator $\mathsf{A}(a)$ acts only on the $\phi(a)$ component of $\mathsf{C}(a,b)$ and similarly $\mathsf{A}(b)$ acts only on the $\phi(b)$ component.

With this notation, all of the Reynolds stress terms in (5.3c) can be expressed in terms of C. For example,

$$\partial_y < uv > = \; \partial_y \left. \langle u(a)v(b) \rangle \right|_{a=b} \;=\; \left. \left(\partial_{y(a)} \,+\, \partial_{y(b)}\right) \mathsf{C}_{uv}(a,b) \right|_{a=b},$$

where $\mathsf{C}_{uv}(a,b) =< u(a)v(b) >$. In this way we obtain the autonomous and deterministic

SSST system that governs the evolution of the mean flow (U, Ψ) and the perturbation field expressed in terms of its covariance field C. The SSST system is then

$$\begin{aligned} \partial_t \mathsf{C}(a,b) \;&=\; (\mathsf{A}(a) \,+\, \mathsf{A}(b))\, \mathsf{C}(a,b) \,+\, \mathsf{Q}(a,b) && \text{(5.7a)} \\ U_t \,-\, U_y \Psi_z \,+\, U_z \Psi_y \,-\, \Delta_1 U/R \;&=\; \langle F_x \rangle && \text{(5.7b)} \\ \Delta_1 \Psi_t \,-\, (\partial_{yy} \,-\, \partial_{zz})\, \Psi_y \Psi_z \,+\, \partial_{yz} \left(\Psi_y^2 \,-\, \Psi_z^2\right) \,-\, \Delta_1 \Delta_1 \Psi/R \;&=\; \langle F_{yz} \rangle \,. && \text{(5.7c)} \end{aligned}$$

The corresponding ensemble mean Reynolds stress divergences are obtained from the perturbation covariance as

$$\begin{aligned} \langle F_x \rangle \;&=\; -\left[\left(\partial_{y(a)} \,+\, \partial_{y(b)}\right) \mathsf{C}_{uv}(a,b) \,+\, \left(\partial_{z(a)} \,+\, \partial_{z(b)}\right) \mathsf{C}_{uw}(a,b)\right]_{a=b} && \text{(5.8a)} \\ \langle F_{yz} \rangle \;&=\; -\left[\left(\left(\partial_{y(a)} \,+\, \partial_{y(b)}\right)^2 \,-\, \left(\partial_{z(a)} \,+\, \partial_{z(b)}\right)^2\right) \mathsf{C}_{vw}(a,b)\right]_{a,b} && \\ &\quad -\left[\left(\partial_{y(a)} \,+\, \partial_{y(b)}\right) \left(\partial_{z(a)} \,+\, \partial_{z(b)}\right) \left(\mathsf{C}_{ww}(a,b) \,-\, \mathsf{C}_{vv}(a,b)\right)\right]_{a=b} && \text{(5.8b)} \end{aligned}$$

The counterpart of the SSST system in this work is the QL model (5.3). The QL also employs a stochastic parameterization of perturbation-perturbation interaction and exploits the streamwise mean flow and perturbation decomposition to obtain quasi-linear dynamics. However, in QL the perturbation covariance is not solved for directly and no large ensemble approximation is made.

The advantage of QL is that it can be directly simulated in a manner that is computationally feasible for large systems, through a restriction of a DNS code to the QL dynamics of (5.3). The SSST model, which has the perturbation covariance as a variable, has dimension $\mathrm{O}(N^2)$ for a system of dimension $\mathrm{O}(N)$ and is only directly integrable for low order systems. In this work we compare predictions based on previous low order simulations of the SSST [102] to a higher order QL simulation, a 2D/3C model and DNS data.

5.4 Analysis of the models and prior results

We study Couette flow and define the Reynolds number R based on the wall velocities $\pm U_c$ and the channel half width h. In the absence of forcing both the 2D/3C model (5.4) and the SSST model (5.7) admit the laminar Couette flow as an equilibrium. This solution is globally stable for the unforced 2D/3C model [103], which implies that this system will return to the laminar Couette flow if the forcing is removed. A stochastically forced 2D/3C model captures the turbulent mean flow profile, as shown in Figure 5.2. The mechanisms underlying maintenance of this mean flow profile are further described in [103]. Although the 2D/3C model captures the basic dynamics of the interaction between rolls and the mean turbulent velocity profile, it does not include the feedback from the mean flow to the perturbation dynamics (as seen in Figure 5.1). As described below, this feedback is critical for capturing the mechanism of transition

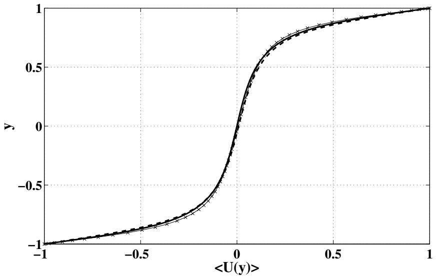

Figure 5.2: Turbulent mean velocity profiles (based on a streamwise, spanwise and time averages) obtained from DNS with the $L_x = 4\pi$ channel (solid line), the QL model (line with an x marker) and the 2D/3C model (dashed line), all at R=1000. The forcing f in the 2D/3C model is 0.065. There is no forcing applied to the DNS or QL during the time interval used to generate the profile, (i.e. the QL is in the self-sustaining state).

and the establishment of the self-sustaining process that maintains the turbulent state.

At fixed R and with sufficiently small values of forcing, the SSST model has a globally stable equilibrium state with a streamwise mean component that varies only in the wall-normal direction (i.e. there is no roll or streak). As the forcing increases, this equilibrium bifurcates and at sufficiently high forcing a saddle-node bifurcation occurs. At this point the SSST flow becomes time dependent and has the mean structure and perturbation statistics of fully turbulent Couette flow. As described in [102], transition to turbulence in SSST is associated with this perturbation/mean flow interaction instability. During transition to the time-dependent SSST state, evolution under SSST produces the familiar overshoot of flow quantities that occurs before the flow settles onto the turbulent attractor. After transition to turbulence the forcing can be removed and the turbulence self-sustains, with little change in the turbulence statistics. In the absence of forcing the SSST perturbation covariance in minimal channel flow collapses to rank 1 with the perturbation field becoming asymptotically confined to a single streamwise component. The SSST framework therefore suggests that the interaction of a perturbation field at a single streamwise wave number with the mean flow provides a minimal representation of turbulent Couette flow [102].

5.5 Numerical Approach

The numerical simulations in this paper are based on a spectral code developed by [104]. The time integration uses a third order multistep semi-implicit Adams-Bashforth/backward-differentiation scheme that is detailed in [105]. The spatial derivatives employ Chebyshev polynomials in the wall-normal (y) direction and Fourier series expansions in the streamwise (x) and spanwise (z) directions [106]. No-slip boundary conditions in the wall-normal direction and periodic boundary conditions in the streamwise (x) and spanwise (z) directions are imposed on the velocity fields. Aliasing errors from the evaluation of the nonlinear terms are removed by the 3/2-rule when the horizontal FFTS are computed, as detailed in [107]. A zero constant pressure gradient was imposed in all simulations.

We employ two different computational boxes for the DNS. The lengths of the first computational box in units of channel half height h are $L_x = 4\pi$, $y \in [-1, 1]$ and $L_z = 4\pi$ with $N_x \times N_y \times N_z = 128 \times 65 \times 128$ grid points in the x, y and z directions. The second DNS box represents a minimal channel in the streamwise direction [92] with $L_x = 1.2\pi$ and $N_x = 64$. In order to perform the QL and $2D/3C$ computations the DNS code was respectively restricted to the dynamics of (5.2) and (5.4).

The stochastic forcing for all of the models was constructed by first creating independent random excitations of the streamwise and wall-normal velocities. These were used to derive the spanwise excitation that produces a divergence free flow. For the $L_x = 1.2\pi$ simulations the stochastic forcing was designed to only excite the streamwise mode with a wave number of $k_x = 1.67$, which is the largest streamwise harmonic perturbation in the $L_x = 1.2\pi$ channel. The structure of the random excitations of the streamwise and wall-normal momentum equations are given by

$$\Xi(x, y, z) \;=\; 2W(\alpha, y) \sum_{n=-M_z/2}^{M_z/2} \sum_{m=0}^{M_y} \mathrm{Re}\left(a_{mn}\, e^{2\pi \mathrm{i}(x/L_x + nz/L_z)}\right) T_m(y), \tag{5.9}$$

where $T_m(y)$ is the mth Chebyshev polynomial. The number of modes excited in y and z are $M_y = (1/2)N_y$ and $M_z = (2/3)N_z$. We use a Tukey window function $W(\alpha, y)$ with $\alpha = 0.4$ in order to obtain smooth forcing realizations close to the walls. The coefficients a_{mn} are complex random numbers that are normally distributed with zero mean and variance 2. These numbers are regenerated every $\Delta T = 0.05$. Within this time interval the models are advanced using an adjustable step 4th order Runge-Kutta algorithm that keeps the Courant-Friedrichs-Lewy (CFL) condition number between 0.05 and 0.2. If the normalized forcing obtained from the random Ξ that satisfies $\|\vec{\mathcal{F}}\|_2^2 = 1$ (i.e. has a unit energy norm) is denoted by $\vec{\mathcal{F}}$, then the body force introduced every ΔT is $\vec{F} = f/\sqrt{\Delta T}\ \vec{\mathcal{F}}$. We divide this forcing by $\sqrt{\Delta T}$ so that its variance is independent of ΔT. The parameter f controls the amplitude of the forcing and is an adjustable parameter in the simulations.

5.6 Results

In this section, we compare 2D/3C and QL simulations to DNS. Figure 5.2 demonstrates a close correspondence between the mean velocity profiles resulting from 2D/3C, QL, and DNS simulations. Further results obtained using the SSST and 2D/3C model were previously reported in [101, 102]. Here we focus on the roll and streak structure and the dynamical properties of the flow field. All simulations in this section were conducted at $R = 1000$.

Figure 5.3 compares QL, 2D/3C and DNS RMS streak, $\sqrt{U_s^2}$, roll, $\sqrt{V^2 + W^2}$, and perturbation, $\sqrt{u^2 + v^2 + w^2}$, velocities along with the square root of the change in their energy from that of the laminar flow. Figure 5.3(d) shows that the RMS of the change from the laminar velocity obtained in the QL simulation and the DNS are very similar, whereas the 2D/3C produces slightly more energy. This additional energy is primarily a result of the larger RMS streak velocity seen in figure 5.3(a). However, the RMS perturbation velocity ($\sqrt{u^2 + v^2 + w^2}$) in the 2D/3C simulation is less than that of both the QL and DNS, as shown in figure 5.3(c). This result is consistent with the fact that in the 2D/3C the streak is not regulated by feedback from the mean flow to the perturbation field (pathway (2) in figure 5.1). This regulation corrects the streak in the QL model to a value similar to that of the DNS.

The forcing in the QL simulation shown in figure 5.3 was stopped at $t = 500$, which indicates that the behavior of the QL for $t > 500$, which is similar to that of the DNS, is a result of the self-sustaining process (SSP) described in [102]. This behavior is further explored in figure 5.4, which shows the time evolution of turbulent statistics obtained by continuing the QL beyond $t = 500$ with the following three different levels of forcing: $f = 0$, $f = 0.04$ and $f = 0.1$. The fact that the amount of forcing applied to the QL after $t = 500$ had minimal effect on the turbulence seen in figure 5.4 indicates that the turbulent state in the self-sustaining regime is tightly regulated by the two-way coupling in the QL.

Figures 5.5(a) and 5.5(b) show details of roll and streak development during transition and establishment of the turbulent state for DNS, QL and 2D/3C. Here, the effect of feedback from the mean flow to the perturbations (pathway (2) in figure 5.1) is quite evident. Lack of this feedback in 2D/3C results in the streak continuing to grow after the transient growth phase. In QL and DNS, the magnitude of the streak is reduced through a combination of perturbation Reynolds stress induced dissipation and modification to the roll forcing based on feedback from the mean flow. Another feature of figure 5.5 is the prominent initial overshoot of roll and streak energy that occurs just prior to the establishment of a statistically steady turbulent state in the QL and DNS. This overshoot is associated with the perturbation/mean flow structural instability described in [102]. The exponential growth of this instability is intercepted by nonlinear feedback dynamics that regulate the unstable growth and establishes the statistically steady turbulent state. This agrees with the dynamics predicted by the low order minimal channel simulation of SSST shown in figure 24 of [102] and serves to validate the SSST theory first introduced in that work.

Figure 5.6 shows contour plots of the U velocity field superimposed with the V, W vector fields at a single time snapshot for the $k_x = 0$ (zero streamwise wave number) mode of the DNS (with a minimal streamwise channel $L_x = 1.2\pi$), the QL and the 2D/3C. A minimal channel was used in order to minimize any smoothing effects resulting

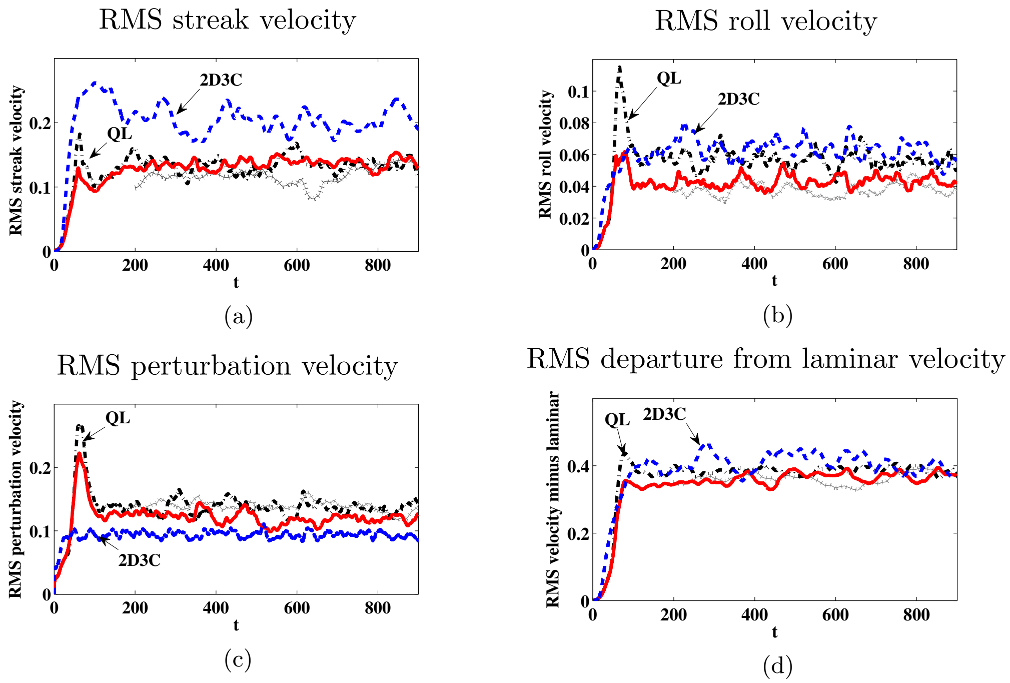

(a)

(b)

(c)

(d)

Figure 5.3: Roll, streak and perturbation development during transition and turbulence at $R = 1000$.Shown are (a) RMS streak velocity $\sqrt{U_s^2}$, (b) RMS roll velocity $\sqrt{V^2 + W^2}$,(c) RMS perturbation velocity $\sqrt{u^2 + v^2 + w^2}$, and (d) RMS velocity departure from the laminar flow. All figures show DNS for boxes with $L_x = 1.2\pi$ (solid line) and $L_x = 4\pi$ (cross-marker with line), QL forced with $f = 0.04$ at $k_x = 1.67$ (dash-dot line) and the 2D/3C with $f = 0.04$ (dashed line). The perturbation forcing of the QL simulation was stopped at $t = 500$ demonstrating that after transition, the QL self-sustains.

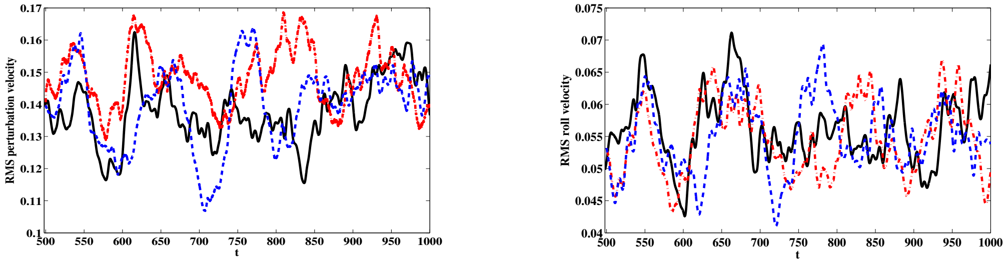

(a) (b)

Figure 5.4: The self sustaining state in the QL simulation. In all plots the QL was forced with amplitude $f = 0.04$ until $t = 500$. At $t = 500$ the same QL was was evolved under no forcing $f = 0$ (solid), with $f = 0.04$ (dashed) and with $f = 0.1$ (dashed-dot). Shown are: the RMS perturbation velocity $\sqrt{u^2 + v^2 + w^2}$ (left) and the RMS roll velocity $\sqrt{V^2 + W^2}$ (right). This shows that after the QL enters the self sustaining state, the statistics are independent of f. When the QL is on this turbulent attractor the dynamics are strongly regulated by the interaction between the perturbations and the roll/streak structure.

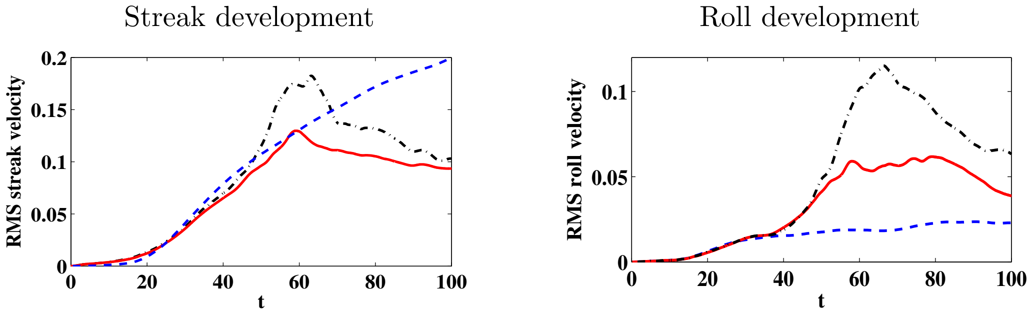

(a) (b)

Figure 5.5: Initial development of the roll and streak structure during transition to turbulence at $R = 1000$. Shown are the RMS values of (a) the streak velocity $\sqrt{U_s^2}$ and (b) the roll velocity $\sqrt{(V^2 + W^2)}$ for DNS (solid line), QL (dashed-dot), 2D/3C (dashed line). All simulations were initialized from a laminar state. A stochastic perturbation forcing with amplitude $f = 0.04$ was introduced to instigate transition. This figure shows that the QL and DNS exhibit exponential growth of the roll/streak structure in accordance with the roll/streak instability predicted by SSST with the predicted overshoot and subsequent establishment of the feedback regulated turbulent state. The 2D/3C produces continued algebraic growth of the roll/streak structure because of the lack of feedback from the mean flow to the perturbations, pathway (2) in figure 5.1.

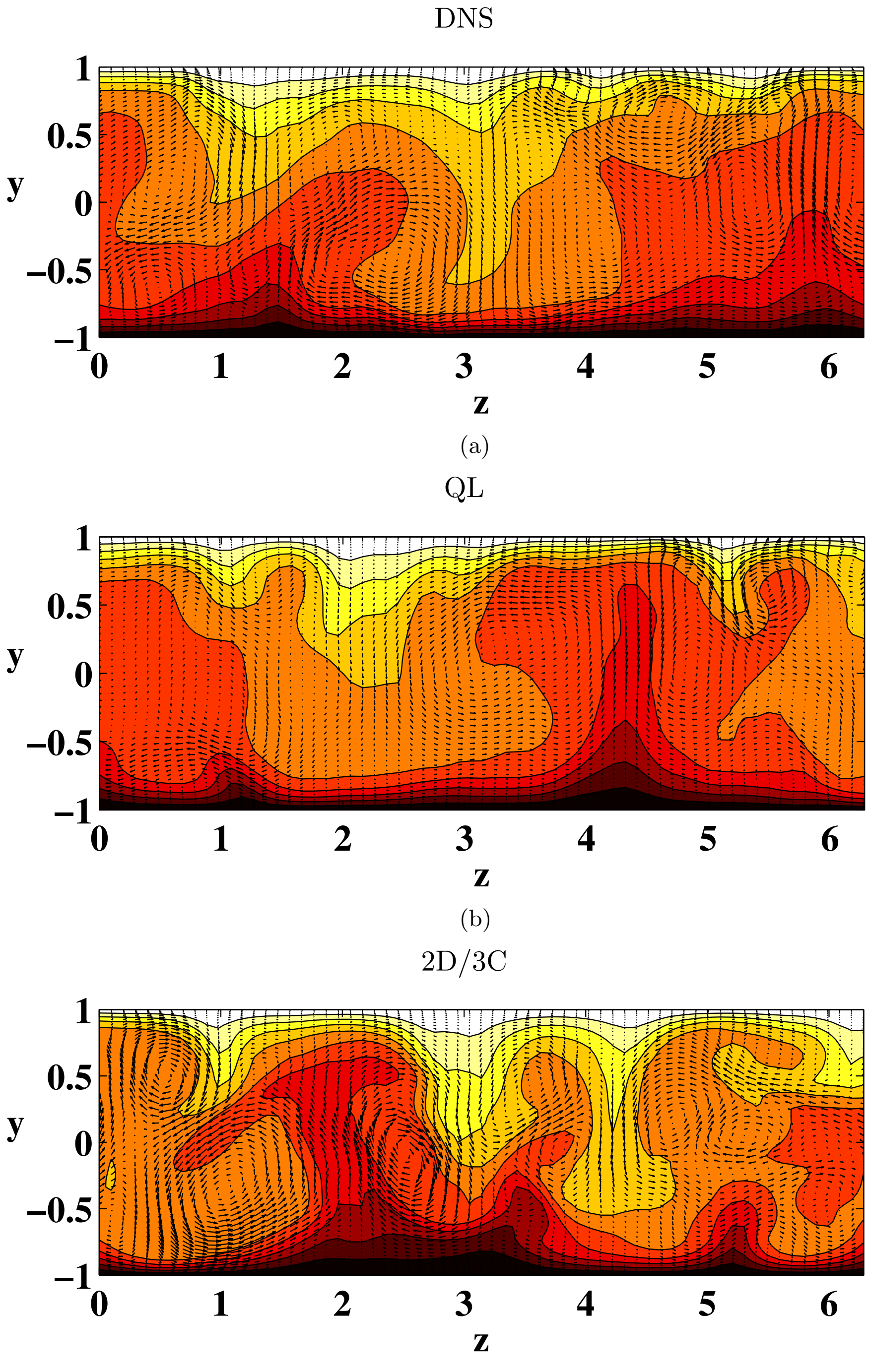

DNS

(a)

QL

(b)

2D/3C

(c)

Figure 5.6: A y-z plane cross-section of the flow at a single snapshot in time (a) the $k_x = 0$ mode of the DNS, (b) the QL, and (c) the 2D/3C simulations, all at $R = 1000$. All panels show contours of the streamwise component of the mean flow U with the velocity vectors of (V, W) superimposed. The QL is self-sustaining ($f = 0$), and the 2D3C is forced with an amplitude $f = 0.065$.

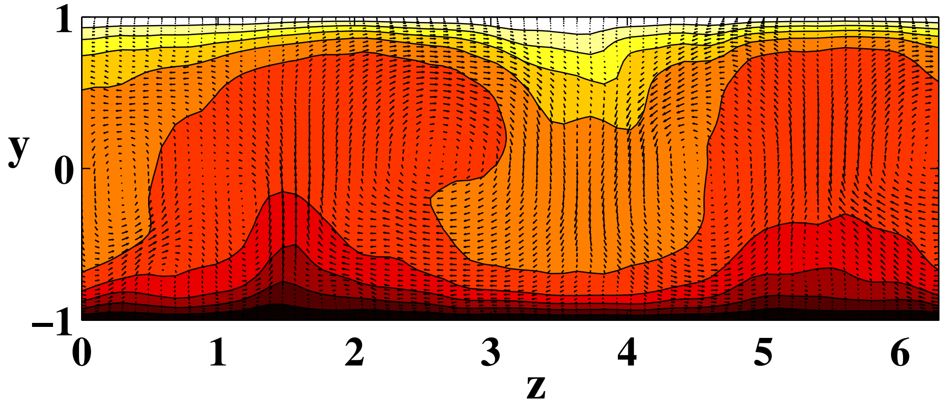

Figure 5.7: A $k_x = 0$ snapshot of the DNS with the longer ($L_x = 4\pi$) channel showing contours of the streamwise velocity field U with the velocity vectors of (V, W) superimposed. The averaging effect caused by the longer channel is clearly evident in the more regularized features versus the plots in figure 5.6

from the implied streamwise averaging associated with the $k_x = 0$ mode of the DNS. For comparison, figure 5.7 shows the same plot obtained from a DNS run in the longer channel (with $L_x = 4\pi$), where the affects of this averaging are much more evident. The qualitative features of the roll and streak structures depicted in figures 5.6 and 5.7 are remarkably similar for all of the models discussed.

5.7 Concluding remarks

The 2D/3C model captures the dynamics of the interactions between the roll structures and the mean flow. It provides accurate statistics for the turbulent mean flow when stochastically forced at the appropriate amplitude. This result implies that the primary mechanism determining the structure of the turbulent mean flow is streamwise constant. One implication of this conclusion is that the mechanism producing the mean flow can be isolated from the mechanism maintaining the turbulent state and analyzed separately. However, understanding how the roll and streak structure is maintained in a statistical steady state requires a model that also includes feedback from the streamwise constant mean flow to the streamwise varying perturbation dynamics. The addition of this feedback is accomplished in the SSST formulation by means of a second order closure. The additional feedback mechanism in the SSST model allows it to capture the dynamics of transition to turbulence as well as the self sustaining process that maintains the turbulent state. In this work we tested the predictions of both the 2D/3C and the SSST model by comparing them to DNS data. The SSST was simulated by imposing the dynamical restrictions of SSST on a DNS code to emulate the SSST dynamics via a

QL model. The results demonstrated good agreement between the 2D/3C, QL and DNS in the structure of the mean flow and mean perturbation statistics. The SSST based predictions for the behavior of the roll and streak structures during transition and the development of a self sustaining state was also verified by comparing the QL to DNS. These results imply that fundamental aspects of the dynamics of turbulence in plane Couette flow are streamwise constant (i.e. captured by the 2D/3C model). Also, further aspects, including transition and mechanisms associated with the self-sustaining process maintaining turbulence are contained in the extension to SSST. Moreover, because these dynamics are accurately captured by a maximally simple model that is dominated by one streamwise wave number interacting with the time-dependent streamwise mean flow, the results suggest that SSST provides a computationally tractable model system for further study of the dynamics of shear flow turbulence.

Part II

Dynamics of transitional and turbulent channel flows of viscoelastic fluids

Chapter 6

Worst-case amplification of disturbances in inertialess Couette flows of viscoelastic fluids

In this chapter, amplification of deterministic disturbances in inertialess shear-driven channel flows of viscoelastic fluids is examined by analyzing the frequency responses from spatio-temporal body forces to the velocity and polymer stress fluctuations. In strongly elastic flows, we show that disturbances with large streamwise length scales may be significantly amplified even in the absence of inertia. For fluctuations without streamwise variations, we derive explicit analytical expressions for the dependence of the worst-case amplification (from different forcing to different velocity and polymer stress components) on the Weissenberg number (We), the maximum extensibility of the polymer chains (L), the viscosity ratio, and the spanwise wavenumber. For the Oldroyd-B model, the amplification of the most energetic components of velocity and polymer stress fields scales as We^2 and We^4. On the other hand, finite extensibility of polymer molecules limits the largest achievable amplification even in flows with infinitely large Weissenberg numbers: in the presence of wall-normal and spanwise forces the amplification of the streamwise velocity and polymer stress fluctuations is bounded by quadratic and quartic functions of L. This high amplification signals low robustness to modeling imperfections of inertialess channel flows of viscoelastic fluids. The underlying physical mechanism involves interactions of polymer stress fluctuations with a base shear, and it represents a close analog of the lift-up mechanism that initiates a bypass transition in inertial flows of Newtonian fluids.

6.1 Introduction

Newtonian fluids transition to turbulence under the influence of inertia. In stark contrast, recent experiments have shown that flows of viscoelastic fluids may undergo a transition to a time-dependent disordered flow state and become turbulent even when inertial forces are considerably weaker than viscous forces [5, 9, 18, 108]. Since viscoelastic fluid flows are often encountered in commercially important settings, understanding transition to *elastic turbulence* in such flows is important from both fundamental and technological standpoints. In polymer processing, for example, elastic turbulence is not desirable because it compromises quality of the final product [10]. But in microfluidic devices elastic turbulence can help promote transport, thereby improving the quality of mixing [6, 109].

Transition in the experiments of Groisman & Steinberg [5, 18] is thought to be initiated by the occurrence of a linear instability that arises from the presence of curved streamlines [10, 110]. However, the question of whether and how transition can occur in channel flows of viscoelastic fluids with straight streamlines remains wide open. Standard modal stability analysis of the upper convected Maxwell and Oldroyd-B constitutive equations shows that these flows are linearly stable when inertial effects are negligible; yet, they exhibit complex dynamical responses in strongly elastic regimes [19–21, 111]. Thus, if an inertialess transition can indeed be described using such basic constitutive models, it would likely involve finite-amplitude disturbances that would trigger nonlinear effects [112, 113]. However, the lack of a modal instability does not rule out the possibility that the early stages of transition can be described by the linearized equations. If non-modal growth is present, initially small-amplitude disturbances could grow to a finite amplitude at intermediate times before decaying at long times. For sufficiently large disturbance amplitudes the flow could enter a regime where nonlinear interactions are no longer negligible. This can induce secondary amplification and instability of the flow structures that are selected by the linearized dynamics and promote eventual transition to elastic turbulence.

Hoda, Jovanović & Kumar [114, 115] recently employed tools from linear systems theory to study the amplification of stochastic spatio-temporal body forces in plane Couette and Poiseuille flows of viscoelastic fluids with nonzero Reynolds numbers. In strongly elastic flows, the results of Hoda *et al.* [114, 115] indicate that significant amplification of streamwise-constant velocity fluctuations can occur even when inertial forces are weak. As in Newtonian fluids, this amplification is caused by non-normality of the underlying operators and it cannot be predicted via standard linear stability analysis. Furthermore, recent work of Jovanović & Kumar [116, 117] shows that this large amplification arises from the interactions between the polymer stress fluctuations in the wall-normal/spanwise plane with the base shear. Through these interactions weak streamwise vortices induce a viscoelastic analogue of the lift-up mechanism which is responsible for the creation of alternating regions of high and low streamwise velocities (relative to the mean flow). Jovanović & Kumar [116, 117] demonstrated significant conceptual similarities between this purely elastic mechanism and the well-known inertial vortex tilting mechanism that initiates a bypass transition in shear flows of Newtonian fluids.

Despite this recent progress, analytical results that quantify influence of finite extensibility of polymer molecules on the amplification of disturbances in channel flows of viscoelastic fluids without inertia are still lacking. Such results may provide physical insight into the early stages of transition and help benchmark direct numerical simulations. Analogous results have been extremely helpful in understanding the early stages of transition to turbulence in wall-bounded shear flows of Newtonian fluids [75,77,87,89].

It is worth noting that the problem of determining the amplification of white-in-time stochastic forcing is ill-posed when inertia is completely absent. This restricts the results of Hoda *et al.* [114, 115] to cases where the flow has finite inertia. Jovanović & Kumar [117] used singular perturbation methods to identify the spatial structure of velocity and polymer stress fluctuations that exhibit the highest amplification in stochastically forced weakly inertial channel flows of viscoelastic fluids. As the influence of inertial forces vanishes, it was demonstrated that the velocity fluctuations become white-in-time, thereby exhibiting infinite variance. Furthermore, Hoda *et al.* [114, 115] and Jovanović & Kumar [116,117] employed the Oldroyd-B constitutive model to investigate energy amplification of velocity and polymer stress fluctuations. However, since the Oldroyd-B model allows the polymers to stretch indefinitely, examining the role of finite extensibility of polymer molecules on the amplification of disturbances remains an open question.

In the present work, we address these issues by examining the worst-case amplification of deterministic disturbances in inertialess (i.e., creeping) shear-driven channel flows of viscoelastic fluids. We consider spatially distributed and temporally varying forcing that is purely harmonic in the horizontal directions and time, and deterministic in the wall-normal direction. The motivation for studying creeping flows arises from the observation that viscoelastic fluids can become turbulent even in low inertial regimes, i.e., at small Reynolds number [5,10]. Furthermore, the present analysis uses the finitely extensible nonlinear elastic Chilcott-Rallison (FENE-CR) model [118], which captures the finite extensibility of the polymer molecules. It is well-known that, for infinitely extensible polymers, the FENE-CR model simplifies to the Oldroyd-B model.

With our approach, we show that velocity and polymer stress fluctuations can exhibit significant amplification and that the most energetic flow structures have large streamwise length scales. In the absence of streamwise variations, we derive explicit expressions for the worst-case amplification from different components of the forcing field to different components of velocity and polymer stress fluctuations. For the Oldroyd-B model, the wall-normal and spanwise forces induce amplification of the streamwise components of velocity and polymer stress fields that scales quadratically and quarticly with the Weissenberg number. On the other hand, we demonstrate that finite extensibility of the polymer molecules saturates the largest achievable amplification even for flows with infinitely large Weissenberg numbers. The functions that bound the worst-case amplification of the velocity and polymer stress fluctuations scale quadratically and quarticly with the largest extensibility of the polymer molecules. We also identify the viscoelastic analogue of the well-known inertial lift-up mechanism as the primary driving force for high flow sensitivity; the underlying mechanism arises from interactions of polymer stress fluctuations with a base shear and it is facilitated by spanwise variations in flow fluctuations [117]. This non-modal amplification may provide a route by which infinitesimal disturbances can grow to finite amplitude and perhaps trigger a transition to elastic turbulence in channel flows of viscoelastic fluids.

To facilitate development of explicit analytical expressions for worst-case amplification of velocity and polymer stress fluctuations, we restrict our study to an inertialess shear-driven channel (Couette) flow of FENE-CR fluids. Even though the current analysis can be readily applied to the FENE-P model and to a pressure-driven channel (Poiseuille) flow, more complicated base state removes algebraic convenience encountered in Couette flow of FENE-CR fluids. We note that all physical mechanisms identified here remain at play in inertialess Poiseuille flow of both FENE-CR and FENE-P fluids.

The rest of this chapter is organized as follows: in Section 6.2, we use a simple example to illustrate how techniques from control theory can be used to quantify amplification of disturbances and robustness to modeling imperfections. In Section 6.3, we describe the governing equations for inertialess channel flows of FENE-CR fluids, provide the evolution model, and briefly discuss the essential features of the frequency response analysis. In Section 6.4, we examine the frequency responses of three-dimensional velocity fluctuations in inertialess Couette of FENE-CR fluids. In Section 6.5, we provide analytical expressions for the worst-case amplification from the forcing to velocity fluctuations using a streamwise-constant linearized model. We also identify the spatial structures of the dominant forcing and velocity components and demonstrate the importance of the viscoelastic lift-up mechanism. In Section 6.6, we study the dynamics of streamwise-constant polymer stress fluctuations. Finally, in Section 6.7, we summarize the major contributions of this work and discuss future research directions.

6.2 The role of uncertainty: an illustrative example

In the course of addressing the issue of disturbance amplification, the present chapter provides insight into the robustness of viscoelastic flow models. In this section, we briefly summarize how the tools from control theory facilitate quantification of sensitivity and robustness of a system to modeling imperfections via frequency response analysis. The approach taken here is closely related to classical frequency response studies of systems arising in physics and engineering. For example, in the design of operational amplifiers it is well-known that caution must be exercised with models that show a low degree of robustness because small modeling errors could cause otherwise stable dynamics to become unstable. Similar ideas have found use in fluid mechanics, including the analysis of the early stages of transition in shear flows of Newtonian fluids [89].

To fix ideas, let us begin with a simple system of two coupled first-order differential

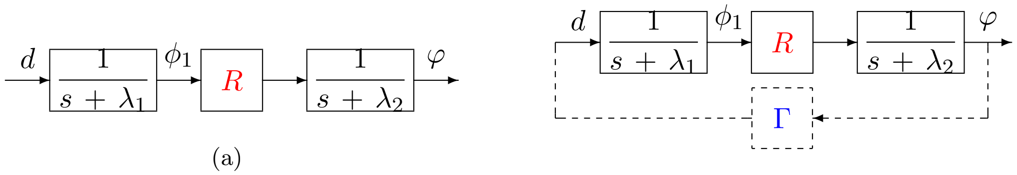

(a)

(b)

Figure 6.1: Block diagrams of (a) system (6.1); and (b) system (6.1) connected in feedback with norm-bounded unstructured uncertainty Γ. Here, $s \in \mathbb{C}$ denotes the temporal Laplace transform variable, and the transfer function, from d to φ, is determined by $H(s) = R/\big((s+\lambda_1)(s+\lambda_2)\big)$.

equations

$$\begin{aligned} \begin{bmatrix} \dot{\phi}_1 \\ \dot{\phi}_2 \end{bmatrix} &= \begin{bmatrix} -\lambda_1 & 0 \\ R & -\lambda_2 \end{bmatrix} \begin{bmatrix} \phi_1 \\ \phi_2 \end{bmatrix} + \begin{bmatrix} 1 \\ 0 \end{bmatrix} d, \\ \varphi &= \begin{bmatrix} 0 & 1 \end{bmatrix} \begin{bmatrix} \phi_1 \\ \phi_2 \end{bmatrix}, \end{aligned} \tag{6.1}$$

where ϕ_1 and ϕ_2 are the states, d is the disturbance, and φ is the output. We assume positivity of scalars λ_1 and λ_2, which guarantees modal stability of (6.1). Equivalently, this system can be represented via its block-diagram in figure 6.1(a). Clearly, we have a cascade connection of two stable first-order systems with parameter R determining the strength of coupling between the two subsystems. For $\lambda_1 \neq \lambda_2$ the solution of the unforced problem, i.e. with $d \equiv 0$, is determined by

$$\begin{aligned} \phi_1(t) &= \mathrm{e}^{-\lambda_1 t}\phi_1(0), \\ \phi_2(t) &= \mathrm{e}^{-\lambda_2 t}\phi_2(0) + \frac{R}{\lambda_2 - \lambda_1}\left(\mathrm{e}^{-\lambda_1 t} - \mathrm{e}^{-\lambda_2 t}\right)\phi_1(0). \end{aligned} \tag{6.2}$$

Thus, the initial conditions in ϕ_i create monotonically decaying responses of ϕ_i, with a rate of decay determined by λ_i. In contrast, the response of ϕ_2 arising from the initial condition in ϕ_1 is characterized by two competing exponentials, and it vanishes both for $t = 0$ and for asymptotically large times. For finite times, however, transient growth, directly proportional to the coupling coefficient R, is exhibited with the largest value of transient response taking place at $t = (1/(\lambda_1 - \lambda_2)) \log(\lambda_1/\lambda_2)$. This transient growth does not require the presence of near resonances (i.e., $\lambda_1 \approx \lambda_2$) or modes with algebraic growth (i.e., $\lambda_1 = \lambda_2$); it is instead caused by the non-normality of the dynamical generator in (6.1).

We note that transient growth represents one particular manifestation of the non-normality of the dynamical generator in the above example (see [61] for a comprehensive treatment). Additional features can be observed by analyzing (6.1) in the frequency domain. The frequency response is obtained by evaluating the transfer function $H(s)$

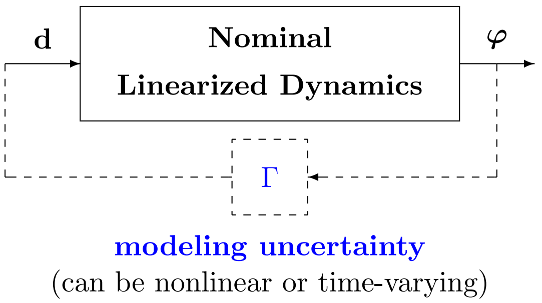

Figure 6.2: Block diagram of a system connected in feedback with norm-bounded unstructured uncertainty Γ.

(from input d to output φ, $\varphi(s) = H(s)d(s)$) on the iω axis, where $\omega \in \mathbb{R}$ is the temporal frequency and $\mathrm{i} = \sqrt{-1}$. The largest value of $|H(\mathrm{i}\omega)|$ determines the so-called H_∞ norm. This measure of input-output amplification has an appealing physical interpretation: it quantifies the worst-case amplification of finite-energy disturbances [82]. In the above example, $\|H\|_\infty = |R|/(\lambda_1\lambda_2)$ indicates the existence of a unit energy disturbance that generates output whose energy is given by $|R|^2/(\lambda_1\lambda_2)^2$.

Furthermore, the H_∞ norm has an interesting robustness interpretation which is closely related to the analysis of pseudospectra of linear operators [31]. Namely, $\|H\|_\infty$ determines the size of modeling uncertainty, $d(s) = \Gamma(s)\varphi(s)$, that can destabilize the system; see figure 6.2 for an illustration. This uncertainty may arise from the inevitable imperfections in the laboratory environment or from the approximate nature of the governing equations (caused by, e.g., high-frequency unmodeled dynamics, parametric variations, neglected nonlinearities, or crude physical assumptions made in modeling). In particular, system (6.1) with $d(s) = \Gamma(s)\varphi(s)$ can be represented by a feedback interconnection in figure 6.1(b). If, apart from being norm-bounded, there are *no structural restrictions* on uncertainty Γ, then the *necessary and sufficient condition* for stability of a feedback interconnection in figure 6.1(b) is given by the so-called small-gain theorem, $\|\Gamma\|_\infty < 1/\|H\|_\infty$. In the above example, this condition simplifies to $\|\Gamma\|_\infty < \lambda_1\lambda_2/|R|$. In particular, it is easy to establish the existence of a constant gain uncertainty, $\Gamma(s) = \gamma = \text{const.}$, of magnitude larger than $\lambda_1\lambda_2/|R|$ that makes the system in figure 6.1(b) unstable.

The above example illustrates that, in systems with non-normal generators, the eigenvalues may represent misleading measures of both transient growth and input-output amplification. While they successfully predict system's behavior for asymptotically large times, they may fail to capture important aspects of short-time behavior, disturbance propagation, and robustness. In particular, the coupling R between subsystems in (6.1) plays a crucial role in determining transient and input-output features of the system's response: large values of R signal large transient responses, poor stability margins, and large amplification of disturbances. In the absence of the coupling, i.e., for $R = 0$, the stability margins of subsystems in (6.1) are determined by λ_1 and λ_2. In contrast, for non-zero R this margin is determined by $\lambda_1 \lambda_2 / |R|$, thereby indicating that, even for subsystems with large stability margins, small uncertainties can have a destabilizing effect on the overall system if the coupling between the subsystems is large enough.

The main ideas from the above example extend to multivariable and infinite dimensional systems. For these problems, the *singular values* of the frequency response operator can be used to determine input-output amplification in the presence of disturbances. Furthermore, the analysis of spatio-temporal frequency responses for spatially distributed systems can be used to identify prevalent spatial length scales and spatio-temporal patterns that are most amplified by the system's dynamics. For example, if instead of being constant scalars, parameters λ_i and R in (6.1) are given by $\{\lambda_i = a_i + b_i \kappa^2,\, R = c\,\mathrm{i}\kappa\}$, then (6.1) can be interpreted as an equivalent of the following system

$$\begin{aligned}
\phi_{1t}(x,t) &= b_1\, \phi_{1xx}(x,t) \,-\, a_1\, \phi_1(x,t) \,+\, d(x,t),\\
\phi_{2t}(x,t) &= c\, \phi_{1x}(x,t) \,+\, b_2\, \phi_{2xx}(x,t) \,-\, a_2\, \phi_2(x,t),\\
\varphi(x,t) &= \phi_2(x,t), \quad x \in \mathbb{R},
\end{aligned}$$

in the spatial frequency domain after applying the spatial Fourier transform to the above system. Here, $\kappa \in \mathbb{R}$ denotes the spatial wavenumber, and (a_i, b_i, c) denote positive reaction, diffusion, and convection coefficients. The κ-parameterized H_∞ norm, $c|\kappa|/((a_1 + b_1\kappa^2)(a_2 + b_2\kappa^2))$, disappears for $\kappa = 0$ and as $\kappa \to \infty$, thereby achieving its peak for non-zero κ, $\bar{\kappa}$. This value of κ identifies the spatial length scale, $2\pi/\bar{\kappa}$, that has the smallest stability margin and that is most amplified by deterministic disturbances. Thus, convective coupling in reaction-diffusion systems can provide dynamical responses that cannot be inferred by analyzing subsystems in isolation.

We finally note that this simple example captures the essential features of non-modal amplification in wall-bounded shear flows of both Newtonian and viscoelastic fluids. In Newtonian fluids the subsystems in figure 6.1(a) would correspond to the Orr-Sommerfeld and Squire equations and the coupling between them would represent the vortex tilting term whose strength is directly proportional to the Reynolds number [77]. In a study focusing on transient growth in inertialess channel flows of viscoelastic fluids, [116] showed that polymer stretching and the Weissenberg number effectively take the role that vortex tilting and the Reynolds number play in inertial flows of Newtonian fluids.

6.3 Problem formulation

In this section, we present the governing equations for inertialess shear-driven channel flow of viscoelastic fluids. We show how the linearized equations can be cast into an evolution form that is amenable to both analytical and computational developments. We then provide a brief description of frequency responses and input-output norms, along with the numerical tools for computing them.

6.3.1 Governing equations

The non-dimensional momentum, continuity, and constitutive equations for an incompressible shear-driven channel flow of viscoelastic fluids, with geometry shown in figure 6.3, are given by [16, 17]

$$\begin{aligned} Re\,\dot{\mathbf{V}} &= We\left((1-\beta)\,\boldsymbol{\nabla}\cdot\mathbf{T} + \beta\,\boldsymbol{\nabla}^2\mathbf{V} - \boldsymbol{\nabla}P - Re\,\mathbf{V}\cdot\boldsymbol{\nabla}\mathbf{V}\right), & (6.3\text{a}) \\ 0 &= \nabla\cdot\mathbf{V}, & (6.3\text{b}) \\ \dot{\mathbf{R}} &= We\Big(\mathbf{R}\cdot\boldsymbol{\nabla}\mathbf{V} + (\mathbf{R}\cdot\boldsymbol{\nabla}\mathbf{V})^T - \mathbf{V}\cdot\boldsymbol{\nabla}\mathbf{R} - \mathbf{T}\Big). & (6.3\text{c}) \end{aligned}$$

Here, the overdot denotes a partial derivative with respect to time t, $\mathbf{V}$ is the velocity vector, P is the pressure, $\mathbf{T}$ is the polymer stress tensor, $\mathbf{R}$ is the conformation tensor, $\boldsymbol{\nabla}$ is the gradient, and $\boldsymbol{\nabla}^2$ is the Laplacian. System (6.3) governs the behavior of dilute polymer solutions with fluid density ρ, and it has been obtained by scaling length with the channel half-height h, time with the fluid relaxation time λ, velocity with the largest base flow velocity U_0, polymer stresses with $\eta_p U_0/h$, and pressure with $(\eta_s + \eta_p)\,U_0/h$, where η_s and η_p are the solvent and polymer viscosities. This scaling leads to three parameters that characterize the properties of (6.3): the viscosity ratio, $\beta = \eta_s/\,(\eta_s + \eta_p)$; the Weissenberg number, $We = \lambda U_0/h$; and the Reynolds number, $Re = \rho U_0 h/(\eta_s + \eta_p)$. While the Reynolds number quantifies the ratio of inertial to viscous forces, the Weissenberg number determines the ratio of the fluid relaxation time λ to the characteristic flow time h/U_0.

The momentum (6.3a) and continuity (6.3b) equations describe the motion of an incompressible viscoelastic fluid. For given $\mathbf{T}$, the pressure adjusts itself so that the velocity satisfies the continuity equation (6.3b). In our previous work [114–117], we used the Oldroyd-B model, which is based on a linear bead-spring dumbbell, to relate the polymeric stress tensor to the conformation tensor. However, it is well-known that the Oldroyd-B model does not account for the finite extensibility of the polymer chains. In this work, we address this issue by using the FENE-CR model, which utilizes a nonlinear relationship between the polymeric stress tensor $\mathbf{T}$ and the conformation tensor $\mathbf{R}$ [16],

$$\mathbf{T} = \frac{f}{We}\,(\mathbf{R} - \mathbf{I})\,. \tag{6.4}$$

Here, $\mathbf{I}$ is the unit tensor, and the function f (that quantifies the influence of the nonlinear spring) is determined by the trace of the conformation tensor, trace$\,(\mathbf{R})$, and the square of the maximum extensibility of polymer chains,

$$f = \frac{L^2 - 3}{L^2 - \text{trace}\,(\mathbf{R})}. \tag{6.5}$$

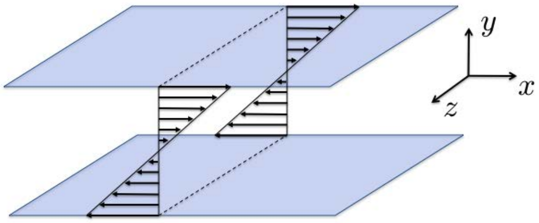

Figure 6.3: Geometry of a three-dimensional shear-driven channel flow.

Note that $\mathbf{R}$ and L^2 are made dimensionless with respect to kT/c, where k, T, and c denote the Boltzmann constant, the absolute temperature, and the spring constant of the Hookean dumbbell, respectively. In the limiting case $L \to \infty$, we have $f \to 1$; consequently, the nonlinear spring becomes linear and the FENE-CR model simplifies to the Oldroyd-B model.

In a shear-driven channel flow, system of equations (6.3) – (6.4) exhibits the following steady-state solution

$$\begin{aligned}\bar{\mathbf{v}} &= \begin{bmatrix} U(y) & 0 & 0 \end{bmatrix}^T,\\ \bar{\mathbf{R}} &= \begin{bmatrix} \bar{R}_{11} & \bar{R}_{21} & \bar{R}_{13} \\ \bar{R}_{12} & \bar{R}_{22} & \bar{R}_{23} \\ \bar{R}_{13} & \bar{R}_{23} & \bar{R}_{33} \end{bmatrix} = \begin{bmatrix} 1 + 2We^2/\bar{f}^2 & We/\bar{f} & 0 \\ We/\bar{f} & 1 & 0 \\ 0 & 0 & 1 \end{bmatrix},\end{aligned}$$

where

$$U(y) \, = \, y, \quad \bar{f} \, = \, \frac{1}{2}\left(1 \, + \, \sqrt{1 \, + \, \frac{8\,We^2}{\bar{L}^2}}\right), \quad \bar{L}^2 \, = \, L^2 \, - \, 3.$$

We also note that the first normal stress difference in Couette flow is determined by

$$\bar{N}_1 \, = \, \bar{R}_{11} \, - \, \bar{R}_{22} \, = \, 2\left(We/\bar{f}\right)^2.$$

In Section 6.5 and Section 6.6 we will show that this parameter, that can take values between 0 and $\bar{L}^2$, plays a key role in the dynamics of velocity and polymer stress fluctuations.

In the absence of inertia, i.e. in flows with $Re = 0$, the dynamics of infinitesimal velocity, $\mathbf{v}$, pressure, p, and conformation tensor, $\mathbf{r}$, fluctuations around the base flow

$\big(\bar{\mathbf{v}}, \bar{\mathbf{R}}\big)$ are governed by

$$\begin{aligned} 0 \;&=\; -\,\boldsymbol{\nabla} p \,+\, (1\,-\,\beta)\,\boldsymbol{\nabla}\cdot\boldsymbol{\tau} \,+\, \beta\,\boldsymbol{\nabla}^2\mathbf{v} \,+\, \mathbf{d}, && \text{(6.6a)}\\ 0 \;&=\; \boldsymbol{\nabla}\cdot\mathbf{v}, && \text{(6.6b)}\\ \dot{\mathbf{r}} \;&=\; \mathit{We}\Big(\mathbf{r}\cdot\boldsymbol{\nabla}\bar{\mathbf{v}} \,+\, \bar{\mathbf{R}}\cdot\boldsymbol{\nabla}\mathbf{v} \,+\, (\mathbf{r}\cdot\boldsymbol{\nabla}\bar{\mathbf{v}})^T \,+ \\ &\qquad \big(\bar{\mathbf{R}}\cdot\boldsymbol{\nabla}\mathbf{v}\big)^T \,-\, \mathbf{v}\cdot\boldsymbol{\nabla}\bar{\mathbf{R}} \,-\, \bar{\mathbf{v}}\cdot\boldsymbol{\nabla}\mathbf{r} \,-\, \boldsymbol{\tau}\Big), && \text{(6.6c)}\\ \boldsymbol{\tau} \;&=\; \frac{\bar{f}}{\mathit{We}}\left(\mathbf{r} \,+\, \frac{\bar{f}\,(\bar{\mathbf{R}}\,-\,\mathbf{I})}{\bar{L}^2}\,\mathrm{trace}(\mathbf{r})\right). && \text{(6.6d)} \end{aligned}$$

Here, (6.6d) establishes a relation between polymer stress and conformation tensor fluctuations. Furthermore, u, v, and w are the components of the velocity fluctuation vector $\mathbf{v} = \left[\begin{array}{ccc} u & v & w \end{array}\right]^T$ in the streamwise (x), wall-normal (y), and spanwise (z) directions, respectively. The momentum equation (6.6a) is driven by a spatially distributed and temporally varying body forcing, $\mathbf{d} = \left[\begin{array}{ccc} d_1 & d_2 & d_3 \end{array}\right]^T$, where d_1, d_2, and d_3 are the forcing fluctuations in the streamwise, wall-normal, and spanwise directions, respectively. In prior work using the Oldroyd-B constitutive equations [114, 115, 117], the three-dimensional body forcing varies harmonically in the horizontal directions and stochastically in the wall-normal direction and in time. However, given the static-in-time momentum equation (6.6a), white-in-time stochastic disturbances $\mathbf{d}$ induce white-in-time velocity fluctuations $\mathbf{v}$, and the problem of variance amplification (in the absence of inertia) becomes ill-posed [117]. Hence, in this work, we consider the body forcing $\mathbf{d}$ to be purely harmonic in the horizontal directions and time, and deterministic in the wall-normal direction, and we study the worst-case amplification of deterministic disturbances.

6.3.2 Model in the evolution form

We note that (6.6a) and (6.6b) can be simplified by expressing the velocity fields in terms of the wall-normal velocity (v) and vorticity ($\eta = \partial_z u - \partial_x w$) fluctuations. This is done by first taking the divergence of (6.6a) and using (6.6b) to get an expression for p. The equation for v is then obtained by eliminating p from (6.6a). The equation for η can be obtained by taking the curl of (6.6a). Finally, by rearranging the components of the conformation tensor into the vector

$$\boldsymbol{\phi} \;=\; \left[\begin{array}{cc} \boldsymbol{\phi}_1^T & \boldsymbol{\phi}_2^T \end{array}\right]^T,$$

with

$$\boldsymbol{\phi}_1 \;=\; \left[\begin{array}{ccc} r_{22} & r_{23} & r_{33} \end{array}\right]^T, \quad \boldsymbol{\phi}_2 \;=\; \left[\begin{array}{ccc} r_{13} & r_{12} & r_{11} \end{array}\right]^T,$$

and by applying the Fourier transform in the x- and z-directions, we arrive at the following static-in-time expressions for v and η in terms of the conformation tensor and body-forcing fluctuations

$$\begin{array}{rcl} v & = & \mathbf{C}_v \, \boldsymbol{\phi} \, + \, \mathbf{D}_v \, \mathbf{d}, \\ \eta & = & \mathbf{C}_\eta \, \boldsymbol{\phi} \, + \, \mathbf{D}_\eta \, \mathbf{d}. \end{array} \tag{6.7}$$

In addition, equation (6.6c) can be brought to the following form

$$\begin{array}{rcl} \dot{\boldsymbol{\phi}}_1 & = & \mathbf{F}_{11} \, \boldsymbol{\phi}_1 \, + \, \mathbf{F}_{1v} \, v \, + \, \mathbf{F}_{1\eta} \, \eta, \\ \dot{\boldsymbol{\phi}}_2 & = & \mathbf{F}_{21} \, \boldsymbol{\phi}_1 \, + \, \mathbf{F}_{22} \, \boldsymbol{\phi}_2 \, + \, \mathbf{F}_{2v} \, v \, + \, \mathbf{F}_{2\eta} \, \eta. \end{array} \tag{6.8}$$

The operators in (6.7) and (6.8) are defined in Appendix 6.8. For notational convenience, we have suppressed the dependence of $\{v, \eta, \boldsymbol{\phi}_i, \mathbf{d}\}$ on $(\boldsymbol{\kappa}, y, t; \beta, We, L)$, where $\boldsymbol{\kappa} = (k_x, k_z)$ with k_x and k_z denoting the horizontal wavenumbers.

The boundary conditions on the wall-normal velocity and vorticity are dictated by the no-slip and no-penetration requirements

$$v\,(\boldsymbol{\kappa}, y = \pm 1, t) \; = \; \partial_y v\,(\boldsymbol{\kappa}, y = \pm 1, t) \; = \; \eta\,(\boldsymbol{\kappa}, y = \pm 1, t) \; = \; 0.$$

We note that there are no boundary conditions on the components of $\mathbf{R}$.

An evolution model for (6.6) can be obtained by substituting (6.7) into (6.8) which yields

$$\dot{\boldsymbol{\phi}}\,(\boldsymbol{\kappa}, y, t) \; = \; \mathbf{A}\,(\boldsymbol{\kappa}) \; \boldsymbol{\phi}\,(\boldsymbol{\kappa}, y, t) \; + \; \mathbf{B}\,(\boldsymbol{\kappa}) \; \mathbf{d}\,(\boldsymbol{\kappa}, y, t)\,, \tag{6.9a}$$

$$\mathbf{v}\,(\boldsymbol{\kappa}, y, t) \; = \; \mathbf{C}\,(\boldsymbol{\kappa}) \; \boldsymbol{\phi}\,(\boldsymbol{\kappa}, y, t) \; + \; \mathbf{D}\,(\boldsymbol{\kappa}) \; \mathbf{d}\,(\boldsymbol{\kappa}, y, t)\,, \tag{6.9b}$$

where the operators $\mathbf{A}$, $\mathbf{B}$, $\mathbf{C}$, and $\mathbf{D}$ are defined in Appendix 6.8.

6.3.3 Spatio-temporal frequency responses

Application of the temporal Fourier transform yields the frequency response operator for system (6.9)

$$\mathbf{H}\,(\boldsymbol{\kappa}, \omega; \beta, We, L) \; = \; \mathbf{C}\,(\boldsymbol{\kappa})\,(\mathrm{i}\,\omega\,\mathbf{I} \, - \, \mathbf{A}\,(\boldsymbol{\kappa}))^{-1} \, \mathbf{B}\,(\boldsymbol{\kappa}) \, + \, \mathbf{D}\,(\boldsymbol{\kappa})\,, \tag{6.10}$$

where ω is the temporal frequency, and $\mathbf{I}$ is the identity operator. For a stable system (6.9), (6.10) can be used to characterize the steady-state response to harmonic input signals across spatial wavenumbers $\boldsymbol{\kappa}$ and temporal frequency ω. Namely, if the input $\mathbf{d}$ is harmonic in x, z, and t, i.e.,

$$\mathbf{d}(x, y, z, t) \; = \; \bar{\mathbf{d}}(y)\,\mathrm{e}^{\mathrm{i}\left(\bar{k}_x\,x + \,\bar{k}_z\,z + \bar{\omega}\,t\right)},$$

with $\bar{\mathbf{d}}(y)$ denoting some spatial distribution in the wall-normal direction, then the output $\mathbf{v}$ is also harmonic in x, z, and t with the same frequencies but with a modified amplitude and phase

$$\mathbf{v}(x,y,z,t) \;=\; \left(\left[\mathbf{H}\left(\bar{k}_x,\bar{k}_z,\bar{\omega}\right)\bar{\mathbf{d}}\right](y)\right)\mathrm{e}^{\mathrm{i}\left(\bar{k}_x\,x\,+\,\bar{k}_z\,z\,+\,\bar{\omega}t\right)},$$

where the amplitude and phase are precisely determined by the frequency response at the input frequencies $(\bar{k}_x,\bar{k}_z,\bar{\omega})$. Note that we have dropped the dependence of the frequency response operator on We, β, and L for notational convenience.

The nth singular value of the frequency response operator $\mathbf{H}$ is determined by

$$\sigma_n^2\left(\mathbf{H}\right) \;=\; \lambda_n\left(\mathbf{H}^\star\,\mathbf{H}\right),$$

where $\lambda_n(\cdot)$ denotes the nth eigenvalue of a given self-adjoint operator and $\mathbf{H}^\star$ is the adjoint of $\mathbf{H}$. For any (k_x,k_z,ω), $\sigma_{\max}(\mathbf{H}) = \max_n \sigma_n(\mathbf{H})$ determines the largest amplification from $\mathbf{d}$ to $\mathbf{v}$. Furthermore, the temporal supremum of the maximal singular value of $\mathbf{H}$ determines the H_∞ norm of system (6.9) [82]

$$G\left(\boldsymbol{\kappa};\beta,We,L\right) \;=\; \sup_{\omega}\,\sigma_{\max}^2\left(\mathbf{H}\left(\boldsymbol{\kappa},\omega;\beta,We,L\right)\right).$$

This measure of input-output amplification has several appealing interpretations:

(a) for any (k_x,k_z), the H_∞ norm represents the worst-case amplification of purely harmonic (in x, z, and t) deterministic (in y) disturbances. This worst-case input-output gain is obtained by maximizing over input temporal frequencies (sup over ω) and wall-normal shapes (maximal singular value of $\mathbf{H}$);

(b) in the temporal domain, the H_∞ norm represents the energy gain from forcing to velocity fluctuations

$$G(\boldsymbol{\kappa}) \;=\; \sup_{E_{\mathbf{d}}(\boldsymbol{\kappa})\,\leq\,1}\frac{E_{\mathbf{v}}(\boldsymbol{\kappa})}{E_{\mathbf{d}}(\boldsymbol{\kappa})},$$

where $E_{\mathbf{v}}(\boldsymbol{\kappa})$ denotes the $\boldsymbol{\kappa}$-parameterized energy of velocity fluctuations, i.e.,

$$E_{\mathbf{v}}(\boldsymbol{\kappa}) \;=\; \int_0^\infty\int_{-1}^1 \mathbf{v}^*(\boldsymbol{\kappa},y,t)\,\mathbf{v}(\boldsymbol{\kappa},y,t)\,\mathrm{d}y\,\mathrm{d}t.$$

In other words, for a unit-energy forcing, $G(\boldsymbol{\kappa})$ captures the largest possible energy of velocity fluctuations across wavenumbers $\boldsymbol{\kappa}$; and

(c) at any (k_x,k_z), the inverse of the H_∞ norm quantifies the size of an additive unstructured modeling uncertainty $\mathbf{\Gamma}$ that can destabilize generator $\mathbf{A}$ in (6.9). As described in Section 6.2, large H_∞ norm indicates small stability margins (i.e., low robustness to modeling imperfections). For systems with poor robustness properties, even small modeling uncertainties (captured by operator $\mathbf{\Gamma}$) can lead to instability of operator $\mathbf{A} + \mathbf{\Gamma}$.

We also note that the frequency response of system (6.9) can be further decomposed into 3×3 block-operator form

$$\begin{bmatrix} u \\ v \\ w \end{bmatrix} = \begin{bmatrix} \mathbf{H}_{u1} & \mathbf{H}_{u2} & \mathbf{H}_{u3} \\ \mathbf{H}_{v1} & \mathbf{H}_{v2} & \mathbf{H}_{v3} \\ \mathbf{H}_{w1} & \mathbf{H}_{w2} & \mathbf{H}_{w3} \end{bmatrix} \begin{bmatrix} d_1 \\ d_2 \\ d_3 \end{bmatrix}. \tag{6.11}$$

This form is suitable for identifying forcing components that introduce the largest amplification of velocity fluctuations. In (6.11), $\mathbf{H}_{sj}$ maps d_j to s, and

$$G_{sj}(\boldsymbol{\kappa}; \beta, We, L) \;=\; \sup_{\omega} \sigma_{\max}^2 \left(\mathbf{H}_{sj} \left(\boldsymbol{\kappa}, \omega; \beta, We, L \right) \right), \quad s \;=\; \{u, v, w\}, \quad j \;=\; \{1, 2, 3\}.$$

The finite-dimensional approximations of the underlying operators are obtained using MATLAB Differentiation Matrix Suite [83], which utilizes pseudospectral methods to approximate differential operators. After discretization in the wall-normal direction, each component in (6.11) becomes an $N \times N$ matrix, where N denotes the number of Chebyshev collocation points in y. All computations are performed in MATLAB and grid-point convergence is confirmed by running additional computations with larger number of grid points in y.

After discretization in y, the H_∞ norm of the frequency response matrix can, in principle, be computed by determining $\sigma_{\max}(\mathbf{H}(\omega))$ for many values of ω and by choosing the resulting maximum value. However, there are two obvious problems associated with such a method: difficulty in determining the range and spacing of the temporal frequencies, and the large number of computations. To avoid these issues, Boyd, Balakrishnan & Kabamba [119] devised a bisection method that can efficiently compute the H_∞ norm. Furthermore, Bruinsma & Steinbuch [120] introduced a fast algorithm that utilizes an efficient method of choosing the temporal frequency for computing the H_∞ norm. This fast algorithm is utilized in our computations and it is based on the relation between the singular values of the frequency response matrix and the eigenvalues of a related Hamiltonian matrix.

All of our results are confirmed by additional frequency response computations that utilize the integral formulation of (6.9). This is accomplished by rewriting the evolution equations (6.9) into an equivalent two-point boundary value problem and then reformulating it into a system of integral equations. The procedure for achieving this along with easy-to-use MATLAB source codes is provided in [121]. This new paradigm for computing frequency responses utilizes the CHEBFUN computing environment [37] and it exhibits superior numerical accuracy compared to conventional numerical schemes.

6.4 Frequency responses of 3D velocity fluctuations

In this section, we study the dynamics of three-dimensional velocity fluctuations in an inertialess shear-driven channel flow. In particular, we examine the worst-case amplification of deterministic disturbances and identify the corresponding wavenumbers that contain most energy. Our analysis shows that velocity fluctuations with large streamwise and $\mathcal{O}(1)$ spanwise length scales display the highest sensitivity to disturbances (and consequently the lowest robustness to modeling imperfections). We further utilize the component-wise frequency responses [77] to identify forcing components that have the strongest influence on the velocity fluctuations. In strongly elastic flows, we demonstrate that the wall-normal and spanwise forces have the highest impact, and that the streamwise velocity is most amplified by the system's dynamics.

In the remainder of this section, we set the viscosity ratio to $\beta = 0.5$ and study the effect of the Weissenberg number, We, and the maximum dumbbell extensibility, L, on the kinetic energy density. Figure 6.4 shows the worst-case amplification of velocity fluctuations triggered by all three body forces in flows with $We = \{10, 50, 100\}$ and $L = \{10, 50, 100\}$. For $L = 10$, the spatial frequency responses display low-pass filter features commonly seen in flows governed by viscous dissipation, with the peak amplification taking place at low wavenumbers. Furthermore, this spatial distribution remains almost unchanged as We increases from 10 to 100 (cf. figures 6.4(a), 6.4(d), and 6.4(g)). However, as L increases to 50, the velocity fluctuations become more amplified with Weissenberg number and a dominant peak starts to appear in an isolated region around $k_x \approx \mathcal{O}(10^{-2})$ and $k_z \approx \mathcal{O}(1)$; see figures 6.4(e) and 6.4(h). As L increases to 100, amplification with We increases even further. This indicates that in flows with large enough L and We, streamwise-elongated and spanwise-periodic flow fluctuations are the most amplified by deterministic body forces. Thus, in strongly elastic channel flows without inertia, streamwise-constant and nearly streamwise-constant fluctuations with a preferential spanwise length scale are most sensitive to external disturbances.

We next study the component-wise frequency responses that quantify amplification from different forcing to different velocity components. This analysis facilitates identification of forcing components that are most effective in amplifying velocity fluctuations. In Couette flow with $We = 50$ and $L = 50$, figure 6.5 shows the worst-case amplification of the 9 frequency response components in (6.11). We see that the streamwise and spanwise velocity fluctuations are the most amplified. Furthermore, the maximum amplification of the streamwise velocity fluctuations triggered by d_2 and d_3 occurs around $k_x \approx \mathcal{O}(10^{-2})$ and $k_z \approx \mathcal{O}(1)$, respectively. This illustrates that streamwise velocity fluctuations are responsible for the most amplified region ($k_x \approx 10^{-2}$, $k_z \approx 2$) in figure 6.4(e). In contrast, the square region around $k_x \approx 0$ and $k_z \approx 0$ in figure 6.4(e) arises from the responses of streamwise and spanwise velocity fluctuations to d_1 and d_3, respectively. We note that the wall-normal velocity experiences negligible amplification compared to that of the other two velocity components and hence, does not contribute to the large energy amplification in inertialess flows.

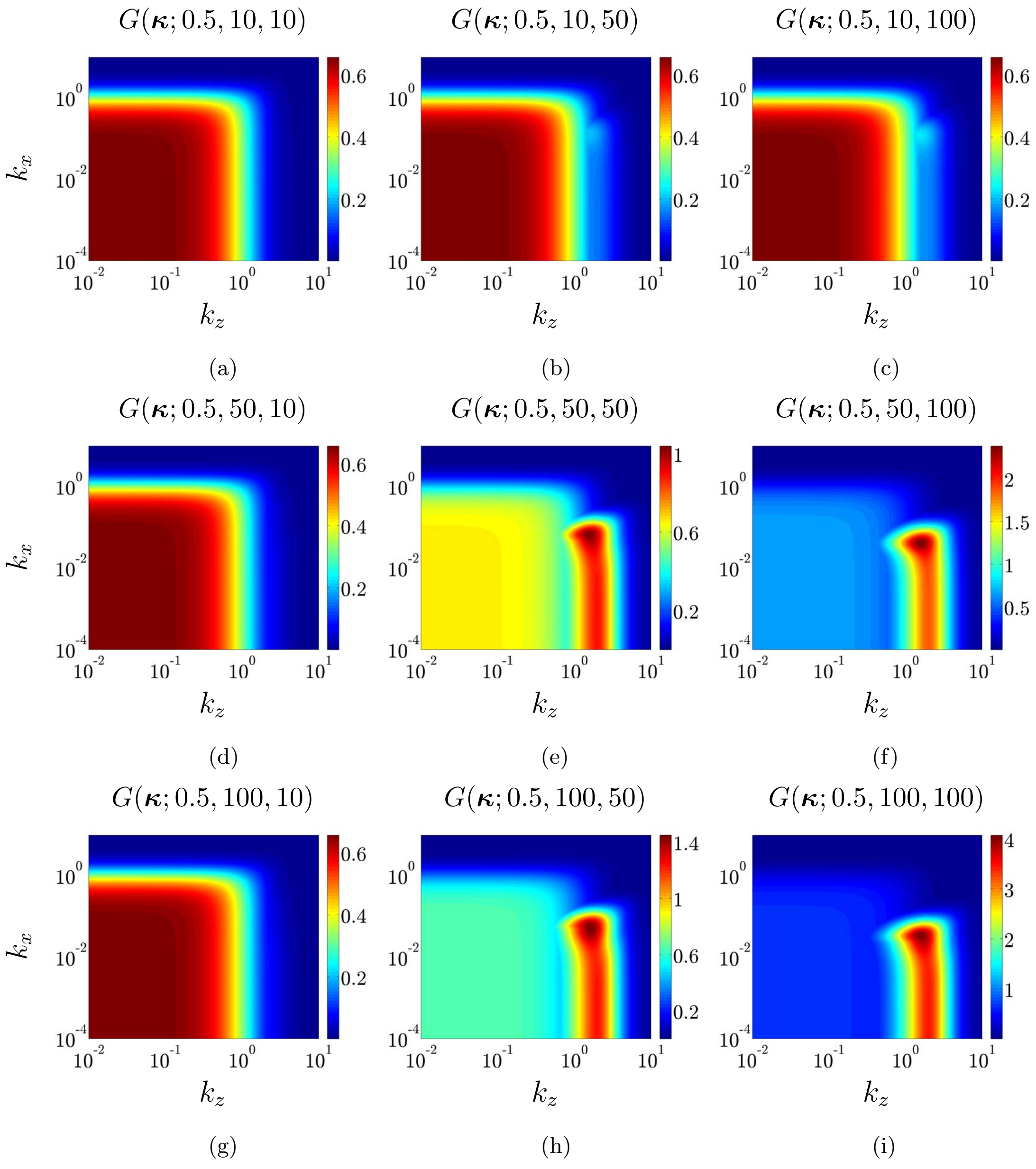

(a) (b) (c)

(d) (e) (f)

(g) (h) (i)

Figure 6.4: Worst-case amplification from $\mathbf{d}$ to $\mathbf{v}$ in Couette flow with $\beta = 0.5$, $We = \{10, 50, 100\}$, and $L = \{10, 50, 100\}$: first row, $We = 10$; second row, $We = 50$; and third row, $We = 100$.

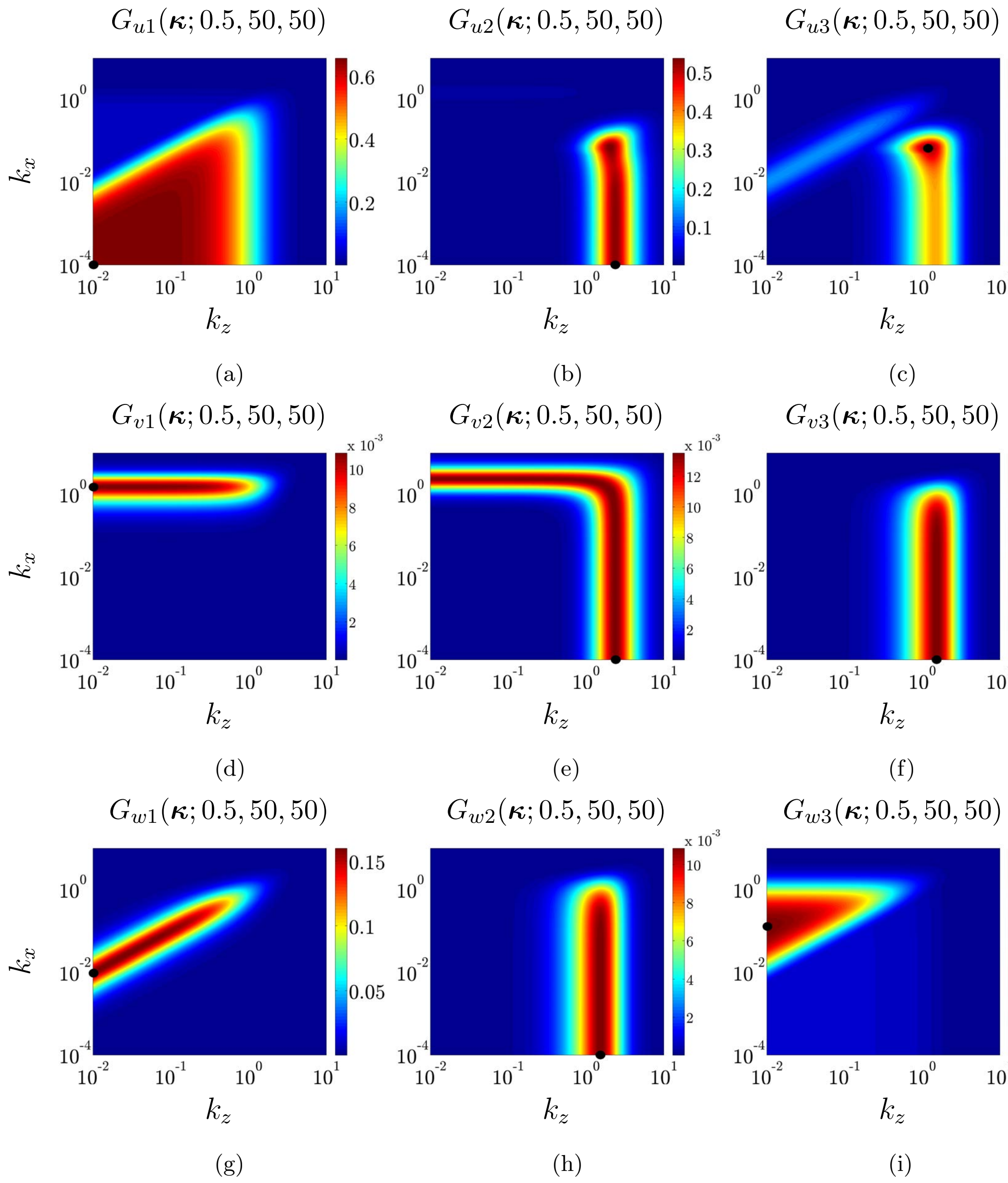

Figure 6.5: Component-wise worst-case amplification from d_j to s in Couette flow with $s = \{u, v, w\}$, $j = \{1, 2, 3\}$, $\beta = 0.5$, $We = 50$, and $L = 50$. The symbol ($\bullet$) identifies the largest value of the corresponding plot.

The above results clearly illustrate the dominance of streamwise-constant and nearly streamwise-constant velocity fluctuations in strongly elastic Couette flow without inertia. The streamwise velocity is most amplified by disturbances, and this large response is caused by the wall-normal and spanwise body forces. Even though this section provides useful insight into the dynamics of inertialess channel flows of viscoelastic fluids, the scaling of energy amplification with We and L cannot be deducted from our computations. For streamwise-constant velocity fluctuations, this issue is addressed in Section 6.5 by developing explicit analytical expressions that quantify the dependence of the worst-case amplification on We, L, β, and k_z.

6.5 Dynamics of streamwise-constant velocity fluctuations

Motivated by the observation that in strongly elastic flows the most amplified velocity fluctuations have large streamwise length-scales, we next examine the linearized model for fluctuations without streamwise variations, i.e., at $k_x = 0$. We use this model to establish an explicit scaling of the components of the frequency response operator with We and L, and to explain the observations made in Section 6.4. Since the largest amplification takes place at low temporal frequencies, we use analytical developments to show that in flows without temporal variations the worst-case amplification from d_2 and d_3 to u scales linearly with the first normal stress difference $\bar{N}_1$ of the nominal flow. Consequently, this worst-case amplification scales quadratically with We as $L \to \infty$ and quadratically with L as $We \to \infty$. Therefore, even in flows with infinitely large polymer relaxation times finite extensibility of polymer molecules limits the largest achievable amplification. Furthermore, the worst-case amplification from all other forcing to all other velocity components is both We- and L-independent. We also present the spatial structures of the forcing and velocity fluctuation components that contribute to the above mentioned unfavorable scaling with $\bar{N}_1$, and demonstrate that the key physical mechanism involves interactions of polymer stress fluctuations in the (y, z)-plane with base shear.

6.5.1 Dependence of worst-case amplification on We and L

For fluctuations without streamwise variations, i.e. at $k_x = 0$, equations (6.8) and (6.7) simplify to

$$\dot{\boldsymbol{\phi}}_1 = -\mathbf{F}_{11}\,\boldsymbol{\phi}_1 + \mathbf{F}_{1v}\,v, \tag{6.12a}$$

$$\dot{\boldsymbol{\phi}}_2 = -\mathbf{F}_{22}\,\boldsymbol{\phi}_2 + \mathbf{F}_{21}\,\boldsymbol{\phi}_1 + \mathbf{F}_{2v}\,v + \mathbf{F}_{2\eta}\,\eta, \tag{6.12b}$$

$$v = \frac{1-\beta}{\beta}\,\mathbf{C}_{v1}\,\boldsymbol{\phi}_1 + \frac{1}{\beta}\,\mathbf{D}_{v2}\,d_2 + \frac{1}{\beta}\,\mathbf{D}_{v3}\,d_3, \tag{6.12c}$$

$$\eta = \frac{1-\beta}{\beta}\,\mathbf{C}_{\eta 2}\,\boldsymbol{\phi}_2 + \frac{1}{\beta}\,\mathbf{D}_{\eta 1}\,d_1, \tag{6.12d}$$

$$\begin{bmatrix} u \\ v \\ w \end{bmatrix} = \begin{bmatrix} 0 & \mathbf{C}_{u\eta} \\ \mathbf{I} & 0 \\ \mathbf{C}_{wv} & 0 \end{bmatrix} \begin{bmatrix} v \\ \eta \end{bmatrix}, \tag{6.12e}$$

where $\boldsymbol{\phi}_1 = \begin{bmatrix} r_{22} & r_{23} & r_{33} \end{bmatrix}^T$, $\boldsymbol{\phi}_2 = \begin{bmatrix} r_{13} & r_{12} & r_{11} \end{bmatrix}^T$, v is the wall-normal velocity, and η is the wall-normal vorticity. On the other hand, the operators in (6.12) are given by

$$\begin{aligned}
\mathbf{F}_{11} &= \begin{bmatrix} \bar{f} & 0 & 0 \\ 0 & \bar{f} & 0 \\ 0 & 0 & \bar{f} \end{bmatrix}, \quad \mathbf{F}_{22} = \begin{bmatrix} \bar{f} & 0 & 0 \\ 0 & \bar{f} & We\,\bar{f}/\bar{L}^2 \\ 0 & -2\,We & \bar{f} + 2We^2/\bar{L}^2 \end{bmatrix}, \\
\mathbf{F}_{1v} &= We \begin{bmatrix} 2\,\partial_y \\ (\mathrm{i}/k_z)\left(\partial_{yy} + k_z^2\right) \\ -2\,\partial_y \end{bmatrix}, \quad \mathbf{F}_{21} = We \begin{bmatrix} 0 & 1 & 0 \\ 1 - \bar{f}/\bar{L}^2 & 0 & -\bar{f}/\bar{L}^2 \\ -2\,We/\bar{L}^2 & 0 & -2\,We/\bar{L}^2 \end{bmatrix}, \\
\mathbf{F}_{2v} &= \frac{We^2}{\bar{f}} \begin{bmatrix} (\mathrm{i}/k_z)\,\partial_{yy} \\ \partial_y \\ 0 \end{bmatrix}, \quad \mathbf{F}_{2\eta} = \begin{bmatrix} 1 \\ -We\,(\mathrm{i}/k_z)\,\partial_y \\ -2\left(We^2/\bar{f}\right)(\mathrm{i}/k_z)\,\partial_y \end{bmatrix}, \\
\mathbf{C}_{v1} &= \left(\bar{f}/We\right)\Delta^{-2} \begin{bmatrix} k_z^2\,\partial_y & \mathrm{i}\,k_z\left(\partial_{yy} + k_z^2\right) & -k_z^2\,\partial_y \end{bmatrix}, \\
\mathbf{C}_{\eta 2} &= \left(\bar{f}/We\right)\Delta^{-1} \begin{bmatrix} k_z^2 & -\mathrm{i}\,k_z\,\partial_y & -\left(We/\bar{L}^2\right)\mathrm{i}\,k_z\,\partial_y \end{bmatrix}, \\
\mathbf{D}_{v2} &= k_z^2\Delta^{-2}, \;\; \mathbf{D}_{v3} = \mathrm{i}\,k_z\,\Delta^{-2}\,\partial_y, \;\; \mathbf{D}_{\eta 1} = -\mathrm{i}\,k_z\,\Delta^{-1}, \;\; \Delta = \partial_{yy} - k_z^2, \\
\mathbf{C}_{u\eta} &= -\mathrm{i}/k_z, \;\; \mathbf{C}_{wv} = (\mathrm{i}/k_z)\,\partial_y, \;\; \Delta^2 = \partial_{yyyy} - 2\,k_z^2\,\partial_{yy} + k_z^4.
\end{aligned}$$

An evolution representation of the streamwise-constant model (6.12) can be obtained by eliminating the components of the conformation tensor from the equations. This is achieved by substituting the temporal Fourier transforms of (6.12a) and (6.12b) into (6.12c) and (6.12d) and taking the inverse temporal Fourier transform of the resulting equations. We will show that this representation leads to convenient analytical expressions for the frequency response operator.

For streamwise-constant fluctuations the frequency response operator $\mathbf{H}$ in (6.11) simplifies to

$$\begin{bmatrix} u \\ v \\ w \end{bmatrix} = \begin{bmatrix} \mathbf{H}_{u1} & \mathbf{H}_{u2} & \mathbf{H}_{u3} \\ 0 & \mathbf{H}_{v2} & \mathbf{H}_{v3} \\ 0 & \mathbf{H}_{w2} & \mathbf{H}_{w3} \end{bmatrix} \begin{bmatrix} d_1 \\ d_2 \\ d_3 \end{bmatrix}, \tag{6.13}$$

where the operators $\mathbf{H}_{sj}$ are given by

$$\begin{aligned}
\mathbf{H}_{v2}(k_z,\omega;\beta,We,L) &= \frac{\mathrm{i}\omega+\bar{f}}{\mathrm{i}\omega\beta+\bar{f}}\,\mathbf{D}_{v2}, \quad \mathbf{H}_{w2}(k_z,\omega;\beta,We,L) \;=\; \frac{\mathrm{i}\omega+\bar{f}}{\mathrm{i}\omega\beta+\bar{f}}\,\mathbf{C}_{wv}\,\mathbf{D}_{v2}, \\
\mathbf{H}_{v3}(k_z,\omega;\beta,We,L) &= \frac{\mathrm{i}\omega+\bar{f}}{\mathrm{i}\omega\beta+\bar{f}}\,\mathbf{D}_{v3}, \quad \mathbf{H}_{w3}(k_z,\omega;\beta,We,L) \;=\; \frac{\mathrm{i}\omega+\bar{f}}{\mathrm{i}\omega\beta+\bar{f}}\,\bar{\mathbf{C}}_{wv}\,\mathbf{D}_{v3}, \\
\mathbf{H}_{u1}(k_z,\omega;\beta,We,L) &= \frac{\mathrm{i}\omega+\bar{f}}{\mathrm{i}\omega\beta+\bar{f}}\,\mathbf{E}_{uu}^{-1}\mathbf{C}_{u\eta}\,\mathbf{D}_{\eta 1}, \\
\mathbf{H}_{u2}(k_z,\omega;\beta,We,L) &= \mathbf{E}_{uu}^{-1}\,\mathbf{E}_{uv}\,\mathbf{D}_{v2}, \quad \mathbf{H}_{u3}(k_z,\omega;\beta) \;=\; \mathbf{E}_{uu}^{-1}\,\mathbf{E}_{uv}\,\mathbf{D}_{v3},
\end{aligned} \tag{6.14}$$

with

$$\mathbf{E}_{uu} \;=\; \mathbf{I} - \frac{2\,We^2\,(\beta-1)}{\bar{L}^2}\,\frac{2\mathrm{i}\omega\bar{f}-\omega^2}{\left(\mathrm{i}\omega\beta\,+\,\bar{f}\right)(\zeta_0\,-\,\omega^2\,+\,\mathrm{i}\omega\zeta_1)}\,\Delta^{-1}\,\partial_{yy}, \tag{6.15a}$$

$$\mathbf{E}_{uv} \;=\; \frac{We\bar{f}\,(\beta-1)}{\left(\mathrm{i}\omega\beta+\bar{f}\right)^2} + \frac{2\,We^3\,(\beta-1)}{\bar{L}^2}\,\frac{3\mathrm{i}\omega\bar{f}-\omega^2}{\left(\mathrm{i}\omega\beta\,+\,\bar{f}\right)^2(\zeta_0\,-\,\omega^2\,+\,\mathrm{i}\omega\zeta_1)}\,\Delta^{-1}\,\partial_{yy}, \tag{6.15b}$$

$$\zeta_0 \;=\; \bar{f}^2 + \frac{4We^2\bar{f}}{\bar{L}^2}, \quad \zeta_1 \;=\; 2\bar{f} + \frac{2We}{\bar{L}^2}. \tag{6.15c}$$

In (6.14), we have successfully separated the temporal and spatial parts of the frequency response operators from d_2 and d_3 to v and w. The absence of inertia induces simple temporal dependence of $\mathbf{H}_{sj}$ with $\{s = v, w;\; j = 2, 3\}$ and facilitates analytical determination of the temporal frequency ω at which the largest worst-case amplification takes place. These four frequency response operators exhibit high-pass temporal characteristics, with the peak amplification taking place at infinite frequency, $\omega = \infty$. The addition of a small amount of inertia would introduce roll-off at high temporal frequencies, thereby shifting the peak amplification to finite temporal frequency [117].

These observations allow us to obtain explicit expressions for the worst-case amplification from d_2 and d_3 to v and w. For example, the worst-case amplification from d_2

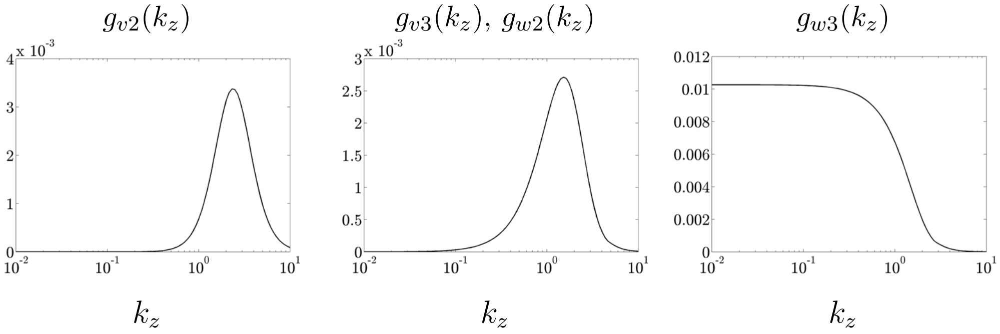

(a) (b) (c)

Figure 6.6: Functions characterizing worst-case amplification from d_2 and d_3 to v and w at $k_x = 0$; $g_{sj}(k_z)$ with $\{s = v, w;\ j = 2, 3\}$.

to v is given by

$$\begin{aligned} G_{v2}(k_z;\beta) &= \sup_{\omega} \sigma^2_{\max}\left(\mathbf{H}_{v2}(k_z,\omega; We, \beta, L)\right) \\ &= \left(1/\beta^2\right)\sigma^2_{\max}\left(\mathbf{D}_{v2}\right) \\ &= \left(1/\beta^2\right) g_{v2}(k_z), \end{aligned}$$

where the function g_{v2}, which is independent of We, β, and L, captures the spanwise frequency response (from d_2 to v). A similar procedure yields the following expressions for the worst-case amplification from d_2 and d_3 to v and w

$$\begin{bmatrix} G_{v2}(k_z;\beta) & G_{v3}(k_z;\beta) \\ G_{w2}(k_z;\beta) & G_{w3}(k_z;\beta) \end{bmatrix} = \begin{bmatrix} g_{v2}(k_z)/\beta^2 & g_{v3}(k_z)/\beta^2 \\ g_{w2}(k_z)/\beta^2 & g_{w3}(k_z)/\beta^2 \end{bmatrix}, \tag{6.16}$$

where the functions g represent the β-, We-, and L-independent spanwise frequency responses. We note that, in Couette flow without inertia, the worst-case amplification of the four components in (6.16) is equivalent for Oldroyd-B and FENE-CR fluids.

The functions $g_{sj}(k_z)$ with $\{s = v, w;\ j = 2, 3\}$, are shown in figure 6.6. We see that g_{v2} and g_{v3} exhibit similar trends with peaks at $k_z \approx \mathcal{O}(1)$; we also note that $g_{w2} = g_{v3}$. In contrast, g_{w3} has a low-pass shape with maximum occurring at $k_z = 0$. The peak value of this function is about four times larger than the peak values of g_{v2} and g_{v3}.

We next examine responses of streamwise velocity to different forcing components. We first analyze the temporal characteristics of the frequency response operators $\mathbf{H}_{uj}$ with $j = \{1, 2, 3\}$. Since the largest amplification of u arising from $\mathbf{d}$ takes place at $k_z \approx \mathcal{O}(1)$, in figure 6.7 we show the temporal frequency dependence of $\sigma_{\max}(\mathbf{H}_{uj})$ for $k_z = 1.5$, $\beta = 0.5$ and $L = 10$. Figure 6.7(a) shows high-pass temporal features of

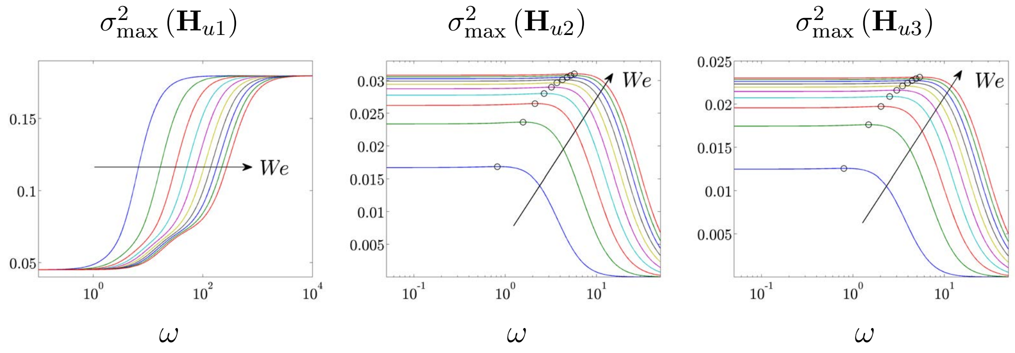

(a) (b) (c)

Figure 6.7: Maximum singular values of the frequency response operators from d_j to u as a function of ω in streamwise-constant Couette flow with $j = \{1, 2, 3\}$, $k_z = 1.5$, $\beta = 0.5$, $L = 10$, and $We = [10, 100]$. The symbol ($\circ$) identifies the peak values of the corresponding curves.

$\sigma_{\max}(\mathbf{H}_{u1})$ with its maximum value taking place at $\omega = \infty$; furthermore, this peak value is independent of the Weissenberg number and the maximum extensibility of the polymer molecules L. In contrast, $\sigma_{\max}(\mathbf{H}_{u2})$ and $\sigma_{\max}(\mathbf{H}_{u3})$ have low-pass characteristics and attain their largest values (which depend on both We and L) at low temporal frequencies.

Figure 6.8 shows the k_z-dependence of the functions G_{uj} that quantify the worst-case amplification from different forcing components to the streamwise velocity for $L = \{10, 100\}$ and for multiple values of the Weissenberg number. Compared to the wall-normal and spanwise velocity fluctuations, streamwise velocity is more amplified by disturbances; cf. figures 6.6 and 6.8. As evident from figures 6.8(a) and 6.8(d), G_{u1} has high values for low spanwise wavenumbers and is independent of both We and L. On the other hand, G_{u2} and G_{u3} achieve their peaks at $k_z \approx \mathcal{O}(1)$. For a fixed value of L these two functions increase with the Weissenberg number, and the largest amplification takes place in the limit of infinitely large We. In contrast to the Oldroyd-B fluids, finite extensibility of the nonlinear springs in the FENE-CR model induces finite values of G_{u2} and G_{u3} even at arbitrarily large Weissenberg numbers. Furthermore, for a fixed value of We, worst-case amplification increases with L and the largest amplification is obtained in the Oldroyd-B limit (as $L \to \infty$). Analytical explanation for these observations is provided below.

We next present explicit expressions for the worst-case amplification from different forcing components to the streamwise velocity. We summarize our major findings here and relegate derivations to Appendix 6.9. We first consider the worst-case response of the streamwise velocity in the presence of the streamwise body forcing. For all values of We and L, our computations indicate that the worst-case amplification from d_1 to u

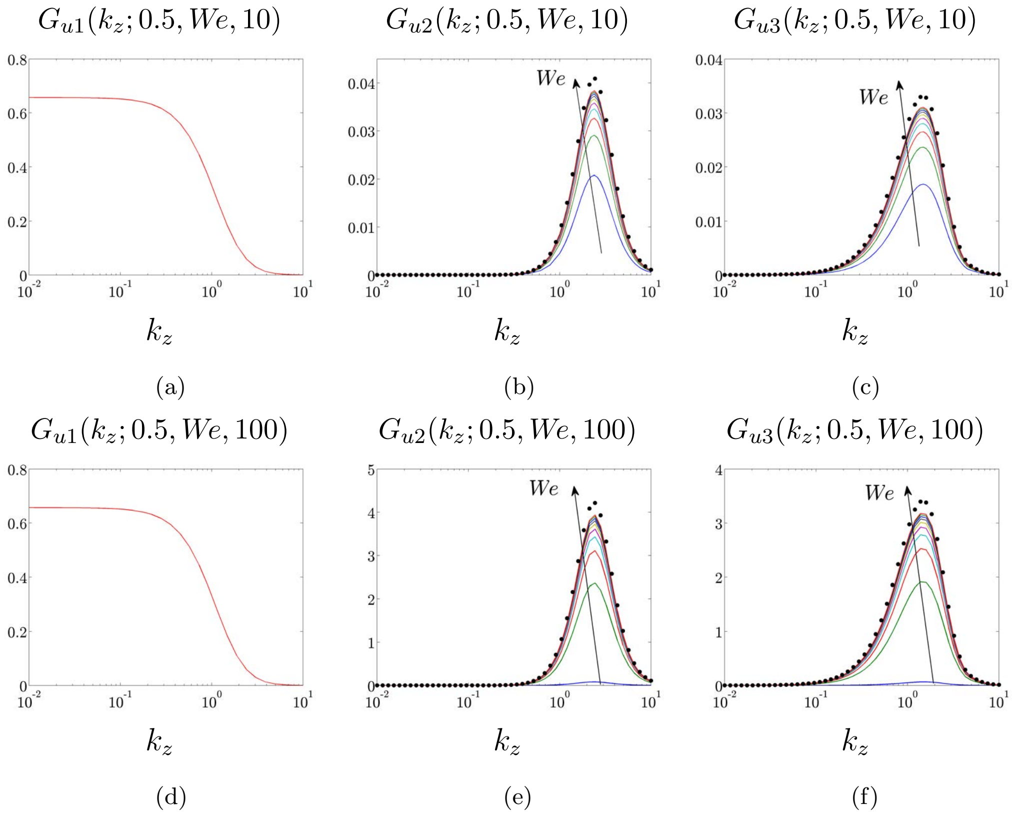

(a) (b) (c)

(d) (e) (f)

Figure 6.8: Worst-case amplification from d_j to u in streamwise-constant Couette flow: first row, $L = 10$ and $We = [10, 100]$; and second row, $L = 100$ and $We = [10, 1000]$. The symbol ($\bullet$) shows the worst-case amplification from d_j to u in the limit of infinitely large We.

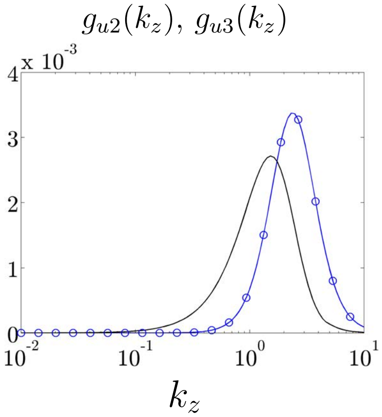

Figure 6.9: Functions characterizing worst-case amplification from d_2 and d_3 to u at $k_x = 0$ and $\omega = 0$: g_{u2} (○); and g_{u3} (solid).

	$L \longrightarrow \infty$	$We \longrightarrow \infty$
$G_{u2}\,(k_z; \beta, \cdot, \cdot)$	$We^2\,(1-\beta)^2\,g_{u2}(k_z)$	$0.5\,\bar{L}^2\,(1-\beta)^2\,g_{u2}(k_z)$
$G_{u3}\,(k_z; \beta, \cdot, \cdot)$	$We^2\,(1-\beta)^2\,g_{u3}(k_z)$	$0.5\,\bar{L}^2\,(1-\beta)^2\,g_{u3}(k_z)$

Table 6.1: Worst-case amplification of streamwise velocity fluctuations arising from the wall-normal and spanwise forces in the limit of infinitely large maximum extensibility of polymer chains L or infinitely large Weissenberg number We.

takes place at $\omega = \infty$. Consequently, in the limit of infinitely large ω we have

$$\begin{aligned} G_{u1}(k_z; \beta) &= \lim_{\omega \to \infty} \sigma^2_{\max}\left(\mathbf{H}_{u1}(k_z, \omega; \beta, We, L)\right) \\ &= \left(1/\beta^2\right) \sigma^2_{\max}\left(\mathbf{C}_{u\eta}\,\mathbf{D}_{\eta 1}\right) \;=\; \left(1/\beta^2\right) g_{u1}(k_z), \end{aligned} \tag{6.17}$$

where g_{u1} is the spanwise frequency response from d_1 to u. Note that G_{u1} is independent of both We and L which is in agreement with the observations made in figures 6.8(a) and 6.8(d).

Derivation of the analytical expressions for G_{u2} and G_{u3} is more challenging because the worst-case amplification of u arising from d_2 and d_3 depends on both We and L. However, since our computations demonstrate that the worst-case amplification from d_2 and d_3 to u takes place at low temporal frequencies, the essential features can be captured by analyzing the corresponding frequency responses at $\omega = 0$. Thus, the worst-case amplification of u caused by d_2 and d_3 can be reliably approximated by

$$\begin{aligned} G_{uj}\left(k_z;\beta,We,L\right) &\approx \sigma_{\max}^2\left(\mathbf{H}_{uj}(k_z,0;\beta,We,L)\right) \\ &= \left(We/\bar{f}\right)^2 (1-\beta)^2\, g_{uj}(k_z) \\ &= \frac{1}{2}\,\bar{N}_1\,(1-\beta)^2\, g_{uj}(k_z), \quad j \;=\; \{2,3\}, \end{aligned} \tag{6.18}$$

where the functions g_{uj} with $j = \{2,3\}$ quantify the spanwise frequency responses from d_2 and d_3 to u; see figure 6.9. Equation (6.18) shows that the worst-case amplification of the streamwise velocity fluctuations scales linearly with the first normal stress difference $\bar{N}_1$ of the nominal Couette flow. Hence, even in the absence of inertia, velocity fluctuations can experience large amplification in flows with large normal stress difference.

Furthermore, table 6.1 shows explicit expressions for G_{u2} and G_{u3} in the limit of infinitely large We (or infinitely large L). In these two cases, the first normal stress difference of the base Couette flow is given by

$$\lim_{L\,\to\,\infty} \bar{N}_1 \;=\; 2\,We^2, \quad \lim_{We\,\to\,\infty} \bar{N}_1 \;=\; \bar{L}^2.$$

For Oldroyd-B fluids polymer molecules are modeled by infinitely extensible linear springs and both G_{u2} and G_{u3} scale quadratically with the Weissenberg number. On the other hand, as $We \to \infty$, G_{u2} and G_{u3} scale quadratically with the maximum extensibility of the polymer molecules L. We conclude that – even for infinitely large polymer relaxation times – energy amplification of velocity fluctuations in inertialess Couette flow of viscoelastic fluids is bounded by the maximum extensibility of nonlinear dumbbells.

6.5.2 Dominant flow structures

In this section, we present the spatial structures of the wall-normal and spanwise body forces that induce the largest amplification in streamwise velocity. We also discuss the (y,z)-dependence of the resulting streamwise velocity fluctuations. These structures are purely harmonic in the spanwise direction with period determined by the value of k_z at which the functions g_{u2} and g_{u3} attain their maxima ($k_z \approx 2.5$ and $k_z \approx 1.5$, respectively). Furthermore, since the worst-case amplification occurs at $\omega = 0$, these structures are constant in time and their wall-normal profiles are determined by the principal singular functions of the frequency response operators that map d_2 and d_3 to u.

Fluctuations in d_2 and d_3 that lead to the largest amplification of u are shown in figures 6.10(a) and 6.10(b). The wall-normal forcing is symmetric with respect to the channel centerline with the peak value located at the center of the channel; in contrast, the spanwise forcing is antisymmetric with respect to the channel centerline.

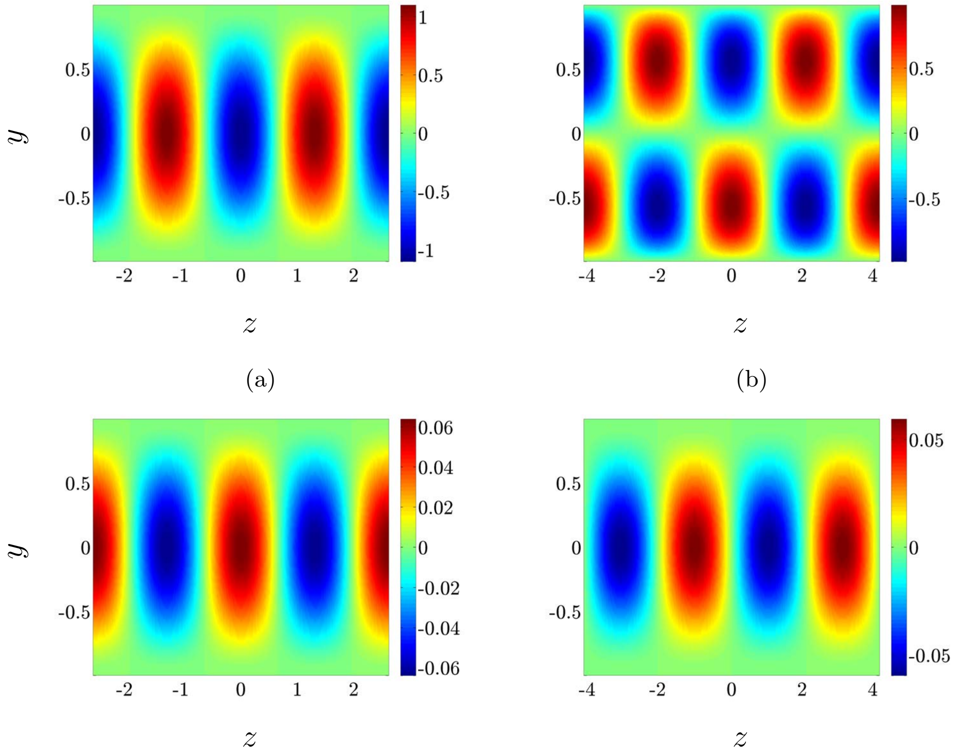

(a) (b)

(c) (d)

Figure 6.10: First row: body forcing fluctuations in d_2 and d_3 leading to the largest amplification of u. Second row: streamwise velocity fluctuations obtained by forcing the inertialess Couette flow with the body force fluctuations shown in (a) and (b), respectively.

Figures 6.10(c) and 6.10(d) illustrate the spatial structures of streamwise velocity induced by the body forcing fluctuations shown in figures 6.10(a) and 6.10(b). Both body forces yield a symmetric response in u with vortices occupying the entire channel width. We note that the dominant flow structures shown in figure 6.10 do not exhibit significant deviation with β, We, and L. Furthermore, we observe striking similarity between these flow structures and flow structures resulting from the analysis of stochastically forced Couette flow of Oldroyd-B fluids [117]. Although these spatial structures may not match the full complexity of flow patterns produced in experiments and direct numerical simulations, our analysis identifies dynamical features that are likely to play an important role in shear-driven channel flows of viscoelastic fluids.

6.5.3 Physical mechanisms

We next discuss the physical mechanisms responsible for strong influence of wall-normal and spanwise forces on streamwise velocity fluctuations in inertialess channel flows. As shown in Appendix 6.9, in the absence of streamwise forcing and streamwise variations in flow fluctuations, $u(y,z,t)$ evolves according to

$$\begin{aligned}
\Delta \dot{u} \;&=\; -\frac{\bar{f}}{\beta}\left\{ \Delta u \,+\, (1-\beta)\,\big(\partial_y\,(U' r_{22}) \,+\, \partial_z\,(U' r_{23})\big) \,+\, \frac{1-\beta}{\bar{L}^2}\,\partial_y \dot{r}_{11} \right\} \\
&=\; -\frac{\bar{f}}{\beta}\left\{ \Delta u \,+\, \sqrt{\frac{\bar{N}_1}{2}}\,(1-\beta)\,\big(\partial_y\,(U' \tau_{22}) \,+\, \partial_z\,(U' \tau_{23})\big) \,+\, \right. \\
&\qquad \left. \frac{1-\beta}{\bar{L}^2}\left(\frac{2We^2}{\bar{f}}\,\partial_{yy} u \,+\, 2We\,\partial_y\,(U' r_{12}) \,-\, \left(\bar{f} \,+\, \frac{2We^2}{\bar{L}^2}\right)\partial_y r_{11} \right) \right\}.
\end{aligned} \tag{6.19}$$

Therefore, even in the absence of inertia, the source term in the evolution equation for streamwise velocity is provided by the interactions between polymer stress fluctuations (in the wall-normal/spanwise plane) with the base shear U'. Furthermore, the finite extensibility of the polymer chains introduces additional source terms that are not present in the Oldroyd-B model; physically, these additional terms originate from: (i) the interaction between the streamwise shear component of the conformation tensor r_{12} with the base shear; and (ii) the wall-normal gradient of the streamwise component of the conformation tensor r_{11}. Relative to the terms that are already present in the Oldroyd-B model, the influence of these additional terms (that arise from temporal changes in r_{11}) is much weaker.

We have demonstrated in Section 6.5.1 that the the essential features of the worst-case amplification from d_2 and d_3 to u can be captured by analyzing the corresponding frequency responses at $\omega = 0$. At zero temporal frequency, equation (6.19) simplifies to a static-in-time relation between the streamwise velocity and the fluctuating components of the polymer stress tensor,

$$\Delta u \;=\; -\sqrt{\bar{N}_1/2}\;(1-\beta)\left(\partial_y\left(U'\tau_{22}\right)\;+\;\partial_z\left(U'\tau_{23}\right)\right). \tag{6.20}$$

Furthermore, τ_{22} and τ_{23} are proportional to the spatial gradients of the (y,z)-plane streamfunction ψ (i.e., $v=\partial_z\psi$, $w=-\partial_y\psi$),

$$\tau_{22} \;=\; 2\,\partial_{yz}\psi, \quad \tau_{23} \;=\; -\left(\partial_{yy}-\partial_{zz}\right)\psi, \tag{6.21}$$

and ψ is induced by the action of the wall-normal and spanwise forces

$$\psi \;=\; \Delta^{-2}\left[\begin{array}{cc} -\partial_z & \partial_y \end{array}\right]\left[\begin{array}{c} d_2 \\ d_3 \end{array}\right]. \tag{6.22}$$

Finally, by substituting (6.21) into (6.20) we obtain the following expression

$$\begin{aligned} \Delta u \;&=\; -\sqrt{\bar{N}_1/2}\;(1-\beta)\,\partial_z\,\Delta\psi \\ &=\; \sqrt{\bar{N}_1/2}\;(1-\beta)\,\partial_z\,\omega_x, \end{aligned} \tag{6.23}$$

that relates fluctuations in the streamwise velocity u and the streamwise vorticity ω_x in inertialess Couette flow of FENE-CR fluids without streamwise and temporal variations (i.e., at $k_x=0$ and $\omega=0$).

This demonstrates that $\mathcal{O}(1)$ fluctuations in streamwise vorticity induce $\mathcal{O}(\sqrt{\bar{N}_1})$ fluctuations in streamwise velocity through a viscoelastic equivalent of the well-known lift-up mechanism. In contrast to Newtonian fluids, where vortex tilting induces large amplification, the lift-up mechanism in viscoelastic fluids originates from interactions between polymer stress fluctuations in the (y,z)-plane with background shear [117]. In the absence of inertia, a static-in-time momentum equation relates the wall-normal and spanwise velocity fluctuations (and consequently the streamwise vorticity) to the polymer stress fluctuations τ_{22}, τ_{23}, and τ_{33}. Interactions of these polymer stress fluctuations with background shear induce the energy transfer from the mean flow to fluctuations and redistribute momentum in the (y,z)-plane through a movement of the low speed fluid (away from the wall) and the high speed fluid (towards the wall). This momentum exchange is responsible for the generation of alternating regions of high and low streamwise velocity (relative to the mean flow), and it is facilitated by large normal stress difference $\bar{N}_1$, low viscosity ratios β, strong base shear U', and strong spatial variations in streamwise vorticity fluctuations. As in streamwise-constant inertial flows of Newtonian fluids, this amplification disappears either in the absence of spanwise variations in flow fluctuations or in the absence of the background shear.

6.6 Dynamics of streamwise-constant polymer stress fluctuations

Although we have so far confined our attention to the dynamics of velocity fluctuations, it is worth noting that polymer stress fluctuations can also experience significant amplification even in the absence of inertia. Since our computations (not shown here) demonstrate that largest responses in polymer stress fluctuations are induced by streamwise-constant deterministic forcing, we next examine the responses from body forcing to polymer stress fluctuations without streamwise-variations. We use analytical developments to show that the wall-normal and spanwise forces induce the largest amplification of the polymer stress fluctuations. The worst-case amplification obtained in the presence of these two forcing components takes place at $\omega = 0$ and it is proportional to: $\bar{N}_1$ for τ_{13} and τ_{12}; and $\bar{N}_1^2/\left(1 + \bar{N}_1/\bar{L}^2\right)^2$ for τ_{11}. Furthermore, the worst-case amplification from all forcing components to τ_{22}, τ_{23}, and τ_{33} is independent of β, *We*, and L. We also illustrate that the worst-case amplification from d_2 and d_3 to τ_{11} scales

- quartically with *We* as $L \to \infty$;
- quartically with L as $We \to \infty$.

Following a sequence of straightforward algebraic manipulations, the frequency response operator $\mathbf{G}$ that maps body forcing fluctuations d_1, d_2, and d_3 to polymer stress fluctuations can be expressed as

$$\begin{bmatrix} \tau_{22} \\ \tau_{23} \\ \tau_{33} \\ \tau_{13} \\ \tau_{12} \\ \tau_{11} \end{bmatrix} = \begin{bmatrix} 0 & \mathbf{G}_{12} & \mathbf{G}_{13} \\ 0 & \mathbf{G}_{22} & \mathbf{G}_{23} \\ 0 & \mathbf{G}_{32} & \mathbf{G}_{33} \\ \mathbf{G}_{41} & \mathbf{G}_{42} & \mathbf{G}_{43} \\ \mathbf{G}_{51} & \mathbf{G}_{52} & \mathbf{G}_{53} \\ \mathbf{G}_{61} & \mathbf{G}_{62} & \mathbf{G}_{63} \end{bmatrix} \begin{bmatrix} d_1 \\ d_2 \\ d_3 \end{bmatrix}, \qquad (6.24)$$

where the streamwise-constant frequency response operators $\mathbf{G}_{\ell j}$ are given in Appendix 6.10.

We note that all components of the frequency response operator in (6.24) exhibit roll-off at high temporal frequencies, thereby indicating that the largest singular value of each component of $\mathbf{G}$ peaks at finite temporal frequency. In particular, the worst-case amplification from d_2 and d_3 to τ_{22}, τ_{23}, and τ_{33} takes place at $\omega = 0$ and is determined by the following β-, *We*-, and L-independent functions

$$\begin{bmatrix} G_{12}(k_z) & G_{13}(k_z) \\ G_{22}(k_z) & G_{23}(k_z) \\ G_{32}(k_z) & G_{33}(k_z) \end{bmatrix} = \begin{bmatrix} g_{12}(k_z) & g_{13}(k_z) \\ g_{22}(k_z) & g_{23}(k_z) \\ g_{32}(k_z) & g_{33}(k_z) \end{bmatrix}. \qquad (6.25)$$

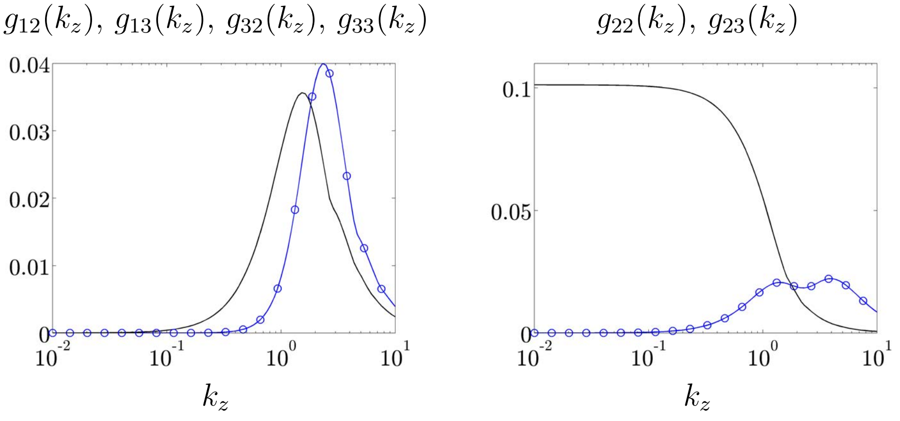

(a) (b)

Figure 6.11: Spanwise frequency responses from d_j to the polymer stress fluctuations τ_{22} (g_{1j}), τ_{23} (g_{2j}), and τ_{33} (g_{3j}) with $j = \{2, 3\}$. The function $g_{12} = g_{32}$ and the function $g_{13} = g_{33}$: (a) g_{12}, g_{32} ($\circ$) and g_{13}, g_{33} (solid); and (b) g_{22} ($\circ$) and g_{23} (solid).

Figure 6.11 shows the functions $g_{\ell j}$ with $\{\ell = 1, 2, 3; j = 2, 3\}$ that quantify the spanwise wavenumber dependence of the respective frequency response operators. We note that $g_{32} = g_{12}$ and $g_{33} = g_{13}$. From figure 6.11(a), we see that g_{12} and g_{13} decay to zero at both low and high wavenumbers with the maximum values occurring at $k_z \approx 2.3$ and $k_z \approx 1.5$, respectively. Similarly, function g_{22} decays to zero at both low and high values of k_z and it achieves two peaks at $k_z \approx 1.4$ and $k_z \approx 4.0$. On the other hand, g_{23} displays low-pass behavior and the maximum value of this frequency response is approximately three times larger than the maximum values of other responses in figure 6.11.

We next analyze the temporal frequency responses of the operators $\mathbf{G}_{\ell j}$ with $\{\ell = 4, 5, 6; j = 1, 2, 3\}$ that map different forcing components to fluctuations in τ_{13}, τ_{12}, and τ_{11}. Figure 6.12 shows ω-dependence of $\sigma_{\max}(\mathbf{G}_{\ell j})$ for $k_z = 1.5$, $\beta = 0.5$, and $L = 10$. Figures 6.12(a) – 6.12(c) show that $\sigma_{\max}(\mathbf{G}_{4j})$ with $j = \{1, 2, 3\}$ achieve their respective peaks at $\omega = 0$. Furthermore, while the peak value of $\sigma_{\max}(\mathbf{G}_{41})$ does not depend on the Weissenberg number, the peak values of $\sigma_{\max}(\mathbf{G}_{42})$ and $\sigma_{\max}(\mathbf{G}_{43})$ increase with We.

The frequency responses $\mathbf{G}_{\ell j}$ with $\{\ell = 5, 6; j = 2, 3\}$ that quantify amplification from d_2 and d_3 to τ_{12} and τ_{11} exhibit similar low-pass characteristics. On the other hand, figures 6.12(d) and 6.12(g) show that $\sigma_{\max}(\mathbf{G}_{51})$ and $\sigma_{\max}(\mathbf{G}_{61})$ achieve their peak values at non-zero temporal frequencies and that these values increase as We increases. We see that the forcing components in the wall-normal and spanwise directions induce larger amplification of polymer stress fluctuations compared to the streamwise forcing.

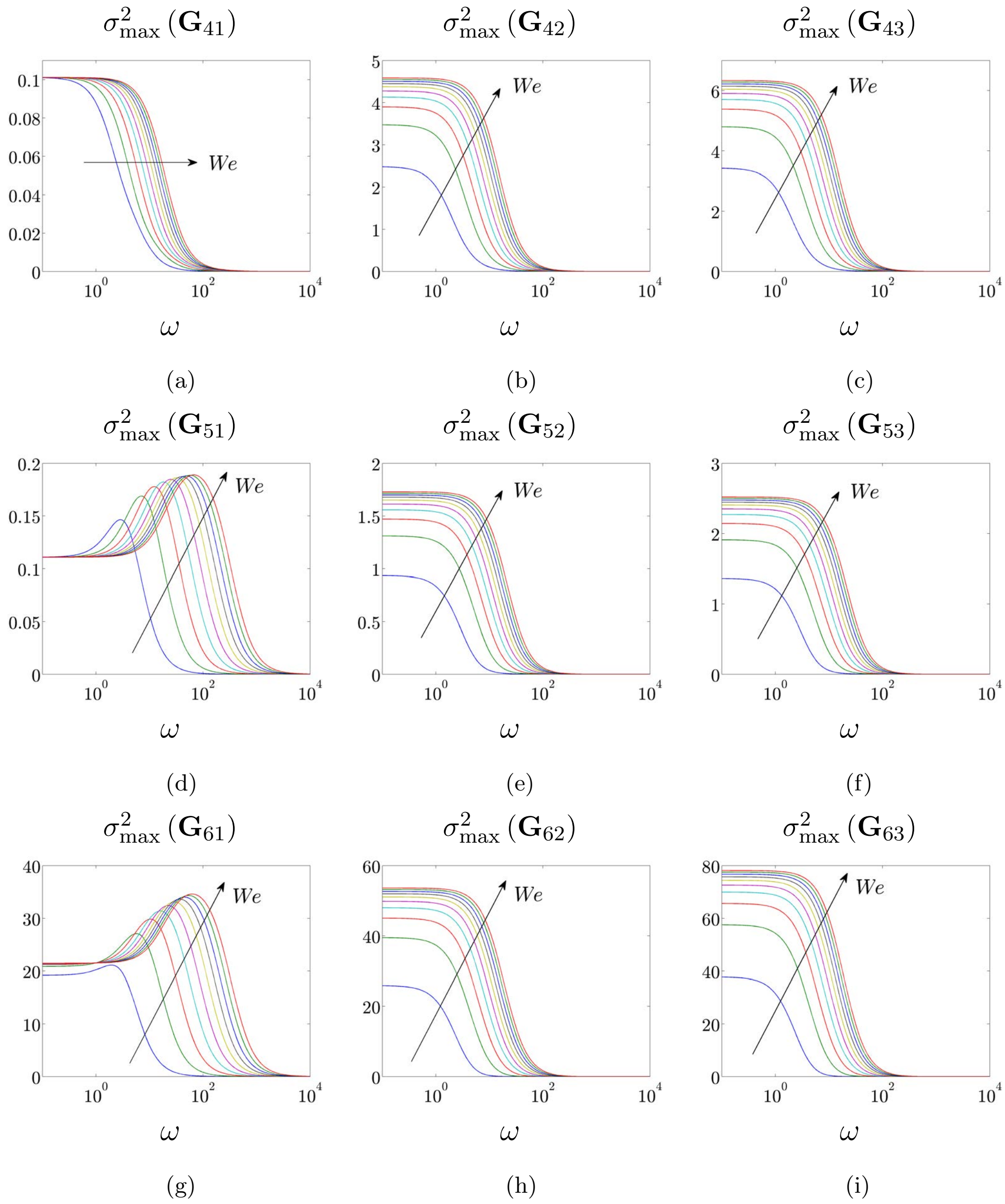

(a) (b) (c) (d) (e) (f) (g) (h) (i)

Figure 6.12: Maximum singular values of the streamwise-constant frequency responses operator from d_j to τ_{13} ($\mathbf{G}_{4j}$), τ_{12} ($\mathbf{G}_{5j}$), and τ_{11} ($\mathbf{G}_{6j}$) as a function of ω for $j = \{2, 3\}$, $k_z = 1.5$, $\beta = 0.5$, $L = 10$ and $We = [10, 100]$.

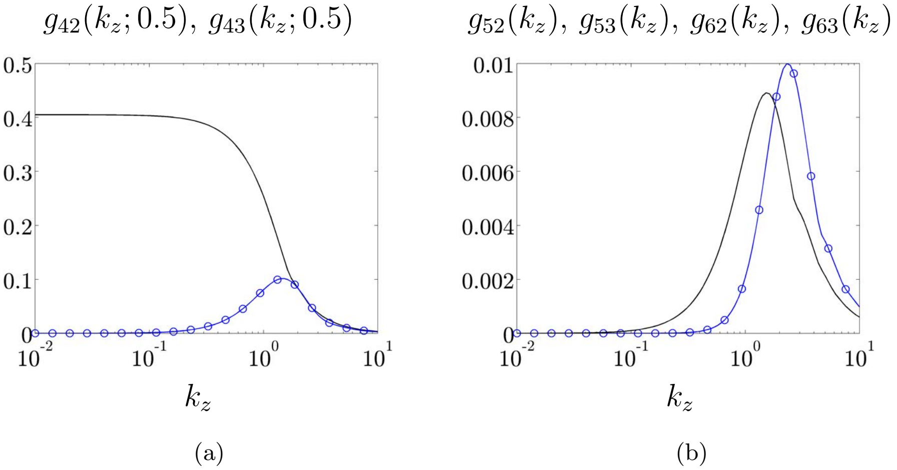

Figure 6.13: Spanwise frequency responses from d_j to the polymer stress fluctuations τ_{13} (g_{4j}), τ_{12} (g_{5j}), and τ_{11} (g_{6j}) for $j = \{2, 3\}$. The function $g_{52} = g_{62}$ and the function $g_{53} = g_{63}$: (a) g_{42} ($\circ$) and g_{43} (solid) for $\beta = 0.5$; and (b) g_{52}, g_{62} ($\circ$) and g_{53}, g_{63} (solid).

Furthermore, the streamwise component of the polymer stress tensor τ_{11} experiences the largest amplification.

Following a series of algebraic manipulations, it can be shown that the worst-case amplification from d_2 and d_3 to τ_{13}, τ_{12}, and τ_{11} takes place at $\omega = 0$ and is given by

$$\begin{aligned}
G_{4j}(k_z;\beta,We,L) &= \left(\bar{N}_1/2\right) g_{4j}(k_z;\beta),\\
G_{5j}(k_z;\beta,We,L) &= \left(\bar{N}_1/2\right)(2+\beta)^2\, g_{5j}(k_z),\\
G_{6j}(k_z;\beta,We,L) &= \frac{\bar{N}_1^2}{\left(1\,+\,\bar{N}_1/\bar{L}^2\right)^2}\,(1+2\beta)^2\, g_{6j}(k_z),\quad j=\{2,3\}.
\end{aligned} \tag{6.26}$$

The functions $g_{\ell j}$ with $\{\ell = 4, 5, 6; j = 2, 3\}$ represent the We- and L-independent spanwise frequency responses from the wall-normal and spanwise forces to τ_{13}, τ_{12}, and τ_{11}. Equation (6.26) shows that the worst-case amplification of τ_{13} and τ_{12} is proportional to $\bar{N}_1$. On the other hand, the worst-case amplification of τ_{11} scales as $\bar{N}_1^2/\left(1+\bar{N}_1/\bar{L}^2\right)^2$.

Figure 6.13 shows the k_z-dependence of the functions $g_{\ell j}$ for $\{\ell = 4, 5, 6; j = 2, 3\}$. We note that $g_{52} = g_{62}$ and $g_{53} = g_{63}$. Function g_{43} has low-pass shape and it peaks at $k_z = 0$. We also notice band-pass features of g_{52}, g_{53}, and g_{42}, with the peak values occurring at $k_z \approx 2.4$, $k_z \approx 1.6$, and $k_z \approx 1.4$, respectively.

Table 6.2 summarizes the worst-case amplification of τ_{13}, τ_{12}, and τ_{11} arising from the wall-normal and spanwise forces in the limit of infinitely large L (or infinitely large We). For Oldroyd-B fluids (i.e., as $L \to \infty$), both G_{4j} and G_{5j} scale quadratically with

$j = \{2, 3\}$	$L \longrightarrow \infty$	$We \longrightarrow \infty$
$G_{4j}\,(k_z; \beta, \cdot, \cdot)$	$We^2\, g_{4j}(k_z; \beta)$	$0.5\, \bar{L}^2\, g_{4j}(k_z; \beta)$
$G_{5j}\,(k_z; \beta, \cdot, \cdot)$	$We^2\,(2+\beta)^2\, g_{5j}(k_z)$	$0.5\, \bar{L}^2\,(2+\beta)^2\, g_{5j}(k_z)$
$G_{6j}\,(k_z; \beta, \cdot, \cdot)$	$4\, We^4\,(1+2\beta)^2\, g_{6j}(k_z)$	$0.25\, \bar{L}^4\,(1+2\beta)^2\, g_{6j}(k_z)$

Table 6.2: Worst-case amplification of τ_{13}, τ_{12}, and τ_{11} arising from d_2 and d_3 in the limit of infinitely large maximum extensibility or infinitely large Weissenberg number.

the Weissenberg number, and G_{6j} scales quarticly with We. On the other hand, as $We \to \infty$, both G_{4j} and G_{5j} scale quadratically with L and G_{6j} scales quarticly with L. This demonstrates profound influence of d_2 and d_3 on τ_{11} in strongly elastic shear flows of viscoelastic fluids. Thus, even in the absence of inertia viscoelastic shear flows with large polymer relaxation times and large extensibility of polymer molecules exhibit high sensitivity to disturbances and low robustness to modeling imperfections.

6.7 Concluding remarks

In this study, we have examined non-modal amplification of disturbances in inertialess Couette flow of viscoelastic fluids using the FENE-CR model. The amplification is quantified by the maximal singular values of the frequency response operators that map sources of excitations (body forces) to the quantities of interest (velocity and polymer stress fluctuations). Spatio-temporal body forcing fluctuations are assumed to be purely harmonic in the horizontal directions and time, and deterministic in the wall-normal direction. Our three-dimensional component-wise frequency response analysis of the FENE-CR model sets the current work apart from prior works which study the transient growth of velocity and polymer stress fluctuations in inertialess flows [116] and non-modal amplification of stochastic disturbances in elasticity-dominated flows with non-zero inertia [114, 115, 117] using the Oldroyd-B model. We have shown that streamwise-elongated flow structures are most amplified by disturbances. Furthermore, the component-wise frequency responses reveal that the wall-normal and spanwise forces have the strongest impact on the flow fluctuations, and that the influence of these forces is largest on streamwise components of velocity and polymer stress fluctuations.

For streamwise-constant fluctuations, we have established analytically that the largest amplification of the streamwise velocity and streamwise component of the polymer stress tensor is proportional to the first normal stress difference of the nominal flow $\bar{N}_1$ and to $\bar{N}_1^2 / \left(1 + \bar{N}_1/\bar{L}^2\right)^2$, respectively. This largest amplification is caused by wall-normal and spanwise forcing fluctuations and it takes place at low temporal frequencies and $\mathcal{O}(1)$ spanwise wavenumbers. Using our analytical developments we have also shown that this worst-case amplification of u and τ_{11} respectively scales as (i) $\mathcal{O}(We^2)$ and $\mathcal{O}(We^4)$ in the Oldroyd-B limit (i.e., as $L \to \infty$); and (ii) $\mathcal{O}(L^2)$ and $\mathcal{O}(L^4)$ in the limit of infinitely large Weissenberg number. We thus conclude that in the presence of large polymer relaxation times and large extensibility of the polymer molecules, the velocity and polymer stress fluctuations can experience significant amplification even when inertial effects are completely absent. The underlying physical mechanism involves interactions of polymer stress fluctuations with a background shear, which induces a viscoelastic analog of the vortex tilting mechanism that is responsible for large amplification in inertial flows of Newtonian fluids.

It is worth noting that, in the limit of infinitely large We, the worst-case amplification of both velocity and polymer stress fluctuations is bounded by the maximum extensibility of the polymer molecules. This is in contrast to Oldroyd-B fluids where infinite extensibility allows the amplification of disturbances to grow unboundedly with We [117]. Our new observations demonstrate that high sensitivity to disturbances and low robustness to modeling imperfections are reduced by finite extensibility of nonlinear dumbbells. Thus, both large polymer relaxation times and large extensibility of the polymer molecules are needed to achieve large amplification of velocity and polymer stress fluctuations in inertialess channel flows of viscoelastic fluids.

The present work extends recent efforts [114–117] that examine possible mechanisms for triggering transition to elastic turbulence in channel flows of viscoelastic fluids. In addition to providing insight into worst-case amplification of velocity and polymer stress fluctuations in inertialess flows, we also demonstrate the importance of uncertainty quantification in flows of viscoelastic fluids. Our analysis shows high sensitivity of inertialess flows of viscoelastic fluids to external disturbances. Unfavorable scaling of the worst-case amplification of flow fluctuations with We and L indicates that small-in-norm modeling imperfections can destabilize nominally stable flows. Hence, stability margins of inertialess channel flows of viscoelastic fluids decrease significantly with an increase in the Weissenberg number and the maximum extensibility of the polymer chains. This uncertainty may arise from inevitable imperfections in the laboratory environment or from the approximate nature of the constitutive equations. Our observations regarding model robustness also have important implications for numerical simulations, where numerical and/or roundoff errors may cause the simulated dynamics to differ from the actual dynamics.

The present findings suggest a plausible mechanism for transition to elastic turbulence in channel flows of viscoelastic fluids. Large amplification of disturbances induces formation of streamwise streaks whose growth can put the flow into a regime where nonlinear interactions are no longer negligible. These nonlinear interactions can then induce secondary amplification [122] or secondary instability [123] of streamwise streaks, their breakdown, and transition to a time-dependent disordered flow and elastic turbulence. To understand possible routes for the transition to elastic turbulence, it is essential to track later stages of disturbance development by considering nonlinearities in the constitutive equations and their interplay with streak development and high flow sensitivity.

Our ongoing efforts are directed toward examining sensitivity of the streaks to three-dimensional disturbances. We also intend to study the presence of a self-sustaining mechanism (proposed for Newtonian fluids by [123]) and to numerically track later stages of disturbance development in strongly elastic channel flows of viscoelastic fluids.

6.8 Appendix: Underlying operators in 3D shear-driven channel flow of FENE-CR fluids

In this appendix, we define the underlying operators appearing in (6.7)–(6.9) for a shear-driven channel flow. Operators $\{\mathbf{C}, \mathbf{D}\}$ in (6.7) are given by

$$
\begin{aligned}
\mathbf{C}_v &= \frac{(1-\beta)}{\beta} \left[\begin{array}{cc} \mathbf{C}_{v1} & \mathbf{C}_{v2} \end{array} \right], \quad \mathbf{D}_v = \frac{1}{\beta} \left[\begin{array}{ccc} \mathbf{D}_{v1} & \mathbf{D}_{v2} & \mathbf{D}_{v3} \end{array} \right], \\
\mathbf{C}_\eta &= \frac{(1-\beta)}{\beta} \left[\begin{array}{cc} \mathbf{C}_{\eta 1} & \mathbf{C}_{\eta 2} \end{array} \right], \quad \mathbf{D}_\eta = \frac{1}{\beta} \left[\begin{array}{ccc} \mathbf{D}_{\eta 1} & \mathbf{D}_{\eta 2} & \mathbf{D}_{\eta 3} \end{array} \right],
\end{aligned}
$$

where

$$
\begin{aligned}
\mathbf{C}_{v1} &= \Delta^{-2} \left[\begin{array}{ccc} \mathbf{C}_{v1,1} & \mathbf{C}_{v1,2} & \mathbf{C}_{v1,3} \end{array} \right], \quad \mathbf{C}_{v2} = \Delta^{-2} \left[\begin{array}{ccc} \mathbf{C}_{v2,1} & \mathbf{C}_{v2,2} & \mathbf{C}_{v2,3} \end{array} \right], \\
\mathbf{C}_{\eta 1} &= \Delta^{-1} \left[\begin{array}{ccc} \mathbf{C}_{\eta 1,1} & \mathbf{C}_{\eta 1,2} & \mathbf{C}_{\eta 1,3} \end{array} \right], \quad \mathbf{C}_{\eta 2} = \Delta^{-1} \left[\begin{array}{ccc} \mathbf{C}_{\eta 2,1} & \mathbf{C}_{\eta 2,2} & \mathbf{C}_{\eta 2,3} \end{array} \right], \\
\mathbf{C}_{v1,1} &= \left(\frac{k^2 \bar{f}}{We} - \frac{2\, We\, k_x^2}{\bar{L}^2} \right) \partial_y + \frac{\mathrm{i} k_x \bar{f}}{\bar{L}^2} \left(\partial_{yy} + k^2 \right), \quad \mathbf{C}_{v1,2} = \frac{\mathrm{i} k_z \bar{f}}{We} \left(\partial_{yy} + k_z^2 \right), \\
\mathbf{C}_{v1,3} &= -\left(\frac{k_z^2 \bar{f}}{We} + \frac{2\, We\, k_x^2}{\bar{L}^2} \right) \partial_y + \frac{\mathrm{i} k_x \bar{f}}{\bar{L}^2} \left(\partial_{yy} + k^2 \right), \quad \mathbf{C}_{v2,1} = -\frac{2\, k_z k_x \bar{f}}{We} \partial_y, \\
\mathbf{C}_{v2,2} &= \frac{\mathrm{i} k_x \bar{f}}{We} \left(\partial_{yy} + k^2 \right), \quad \mathbf{C}_{v2,3} = -\left(\frac{k_x^2 \bar{f}}{We} + \frac{2\, We\, k_x^2}{\bar{L}^2} \right) \partial_y + \frac{\mathrm{i} k_x \bar{f}}{\bar{L}^2} \left(\partial_{yy} + k^2 \right), \\
\mathbf{C}_{\eta 1,1} &= \left(2\, We / \bar{L}^2 \right) k_x\, k_z - \left(\mathrm{i} k_z\, \bar{f} / \bar{L}^2 \right) \partial_y, \quad \mathbf{C}_{\eta 1,2} = \left(\mathrm{i} k_x\, \bar{f} / We \right) \partial_y, \\
\mathbf{C}_{\eta 1,3} &= \left(\frac{2\, We}{\bar{L}^2} - \frac{\bar{f}}{We} \right) k_x\, k_z - \frac{\mathrm{i} k_z \bar{f}}{\bar{L}^2} \partial_y, \quad \mathbf{C}_{\eta 2,1} = \frac{\bar{f}}{We} \left(k_z^2 - k_x^2 \right), \\
\mathbf{C}_{v2,2} &= -\frac{\mathrm{i} k_z \bar{f}}{We} \partial_y, \quad \mathbf{C}_{v2,3} = \left(\frac{2\, We}{\bar{L}^2} + \frac{\bar{f}}{We} \right) k_x\, k_z - \frac{\mathrm{i} k_z \bar{f}}{\bar{L}^2} \partial_y, \\
\mathbf{D}_{v1} &= \mathrm{i} k_x \Delta^{-2} \partial_y, \ \mathbf{D}_{v2} = k^2 \Delta^{-2}, \ \mathbf{D}_{v3} = \mathrm{i} k_z \Delta^{-2} \partial_y, \\
\mathbf{D}_{\eta 1} &= -\mathrm{i} k_z \Delta^{-1}, \ \mathbf{D}_{\eta 2} = 0, \ \mathbf{D}_{\eta 3} = \mathrm{i} k_x \Delta^{-1}.
\end{aligned}
$$

Here, $k^2 = k_x^2 + k_z^2$, $\mathrm{i} = \sqrt{-1}$, $\Delta = \partial_{yy} - k^2$ with Dirichlet boundary conditions, $\Delta^2 = \partial_{yyyy} - 2k^2 \partial_{yy} + k^4$ with both Dirichlet and Neumann boundary conditions.

The **F**-operators appearing in (6.8) are determined by

$$\mathbf{F}_{11} \;=\; \begin{bmatrix} -D & 0 & 0 \\ 0 & -D & 0 \\ 0 & 0 & -D \end{bmatrix}, \; \mathbf{F}_{22} \;=\; \begin{bmatrix} -D & 0 & 0 \\ 0 & -D & -We\bar{f}/\bar{L}^2 \\ 0 & 2\,We & -\big(D \,+\, 2\,We^2/\bar{L}^2\big) \end{bmatrix},$$

$$\mathbf{F}_{21} \;=\; \begin{bmatrix} 0 & We & 0 \\ We\big(1 \,-\, \bar{f}/\bar{L}^2\big) & 0 & -We\bar{f}/\bar{L}^2 \\ -2\,We^2/\bar{L}^2 & 0 & -2\,We^2/\bar{L}^2 \end{bmatrix}, \quad D \;=\; \big(\bar{f} \,+\, We\,\mathrm{i}k_x\,U\big)\,,$$

$$\mathbf{F}_{1v} \;=\; \frac{We}{k^2}\begin{bmatrix} 2\,k^2\,\big(\partial_y \,+\, \mathrm{i}k_x\,\bar{R}_{12}\big) \\ \mathrm{i}k_z\,\big(\partial_{yy} \,+\, k^2\big) \,-\, We\,k_x\,k_z\,\bar{R}_{12}\,\partial_y \\ -2\,k_z^2\,\partial_y \end{bmatrix}, \quad \mathbf{F}_{2v} \;=\; \frac{We}{k^2}\begin{bmatrix} \mathbf{F}_{2v}^1 \\ \mathbf{F}_{2v}^2 \\ \mathbf{F}_{2v}^3 \end{bmatrix},$$

$$\mathbf{F}_{1\eta} \;=\; \frac{We}{k^2}\begin{bmatrix} 0 \\ \mathrm{i}k_x\,\partial_y \,-\, k_x^2\,\bar{R}_{12} \\ -2\,k_x\,k_z \end{bmatrix}, \; \mathbf{F}_{2\eta} \;=\; \frac{We}{k^2}\begin{bmatrix} k_z^2 + \mathrm{i}k_x\,\bar{R}_{12}\,\partial_y \,-\, k_x^2\,\bar{R}_{11} \\ k_x\,k_z\,\bar{R}_{12} \,-\, \mathrm{i}k_z\,\partial_y \\ 2\,\big(k_x\,k_z\,\bar{R}_{11} \,-\, \mathrm{i}k_z\,\bar{R}_{12}\,\partial_y\big) \end{bmatrix},$$

$$\mathbf{F}_{2v}^1 \;=\; \mathrm{i}k_z\,\bar{R}_{12}\,\partial_{yy} \,-\, k_xk_z\,\big(1 + \bar{R}_{11}\big)\,\partial_y,$$

$$\mathbf{F}_{2v}^2 \;=\; \mathrm{i}k_x\,k^2\,\bar{R}_{11} \,+\, k_z^2\,\bar{R}_{12}\,\partial_y \,+\, \mathrm{i}k_x\,\partial_{yy}, \quad \mathbf{F}_{2v}^3 \;=\; 2\,\big(\mathrm{i}k_x\,\bar{R}_{12}\,\partial_{yy} \,-\, k_x^2\,\bar{R}_{11}\,\partial_y\big)\,.$$

The operators appearing in the evolution equations (6.9) are given by

$$\mathbf{A} \;=\; \begin{bmatrix} \mathbf{F}_{11} \,+\, \mathbf{F}_{1v}\mathbf{C}_{v1} \,+\, \mathbf{F}_{1\eta}\mathbf{C}_{\eta 1} & \mathbf{F}_{1v}\mathbf{C}_{v2} \,+\, \mathbf{F}_{1\eta}\mathbf{C}_{\eta 2} \\ \mathbf{F}_{21} \,+\, \mathbf{F}_{2v}\mathbf{C}_{v1} \,+\, \mathbf{F}_{2\eta}\mathbf{C}_{\eta 1} & \mathbf{F}_{22} \,+\, \mathbf{F}_{2v}\mathbf{C}_{v2} \,+\, \mathbf{F}_{2\eta}\mathbf{C}_{\eta 2} \end{bmatrix},$$

$$\mathbf{C} \;=\; \begin{bmatrix} \mathbf{C}_{uv}\mathbf{C}_{v1} \,+\, \mathbf{C}_{u\eta}\mathbf{C}_{\eta 1} & \mathbf{C}_{uv}\mathbf{C}_{v2} \,+\, \mathbf{C}_{u\eta}\mathbf{C}_{\eta 2} \\ \mathbf{C}_{v1} & \mathbf{C}_{v2} \\ \mathbf{C}_{wv}\mathbf{C}_{v1} \,+\, \mathbf{C}_{w\eta}\mathbf{C}_{\eta 1} & \mathbf{C}_{wv}\mathbf{C}_{v2} \,+\, \mathbf{C}_{w\eta}\mathbf{C}_{\eta 2} \end{bmatrix},$$

$$\mathbf{B} \;=\; \begin{bmatrix} \mathbf{F}_{1v}\mathbf{D}_v \,+\, \mathbf{F}_{1\eta}\mathbf{D}_\eta \\ \mathbf{F}_{2v}\mathbf{D}_v \,+\, \mathbf{F}_{2\eta}\mathbf{D}_\eta \end{bmatrix}, \quad \mathbf{D} \;=\; \begin{bmatrix} \mathbf{C}_{uv}\mathbf{D}_v + \mathbf{C}_{u\eta}\mathbf{D}_\eta \\ \mathbf{D}_v \\ \mathbf{C}_{wv}\mathbf{D}_v + \mathbf{C}_{w\eta}\mathbf{D}_\eta \end{bmatrix},$$

$$\mathbf{C}_{uv} \;=\; \big(\mathrm{i}k_x/k^2\big)\,\partial_y, \;\; \mathbf{C}_{u\eta} \;=\; -\mathrm{i}k_z/k^2, \;\; \mathbf{C}_{wv} \;=\; \big(\mathrm{i}k_z/k^2\big)\,\partial_y, \;\; \mathbf{C}_{w\eta} \;=\; \mathrm{i}k_x/k^2.$$

6.9 Appendix: Explicit scaling of worst-case amplification of streamwise-constant velocity fluctuations

In this section, we discuss how to obtain explicit expressions for the worst-case amplification from the wall-normal and spanwise forces to the streamwise velocity fluctuations in the limit of infinitely large We or infinitely large L. We note that derivation of the analytical expressions for G_{u2} and G_{u3} is more challenging because the worst-case amplification of u arising from d_2 and d_3 depends on both We and L. However, since our computations presented in Section 6.5.1 demonstrate that the worst-case amplification from d_2 and d_3 to u takes place at low temporal frequencies, the essential features can be captured by analyzing the corresponding frequency responses at $\omega = 0$; see figures 6.7(b) and 6.7(c). For flows without temporal variations, we can obtain the following static-in-time expressions that relate the conformation tensor fluctuations with the streamwise velocity u and (y, z)-plane streamfunction ψ (i.e., $v = \mathrm{i}k_z\psi$, $w = -\partial_y\psi$)

$$r_{22} \;=\; \frac{2We}{\bar{f}}\,\mathrm{i}k_z\,\partial_y\psi, \quad r_{33} \;=\; -\frac{2We}{\bar{f}}\,\mathrm{i}k_z\,\partial_y\psi, \quad r_{23} \;=\; -\frac{We}{\bar{f}}\left(\partial_{yy} + k_z^2\right)\psi, \tag{6.27a}$$

$$r_{13} \;=\; \left(We/\bar{f}\right)\left(U' r_{23} \,-\, \left(We/\bar{f}\right)\partial_{yy}\psi \,+\, \mathrm{i}k_z u\right), \tag{6.27b}$$

$$r_{12} \;=\; \left(We/\bar{f}\right)\left(U' r_{22} \,-\, \left(\bar{f}/\bar{L}^2\right) r_{11} \,+\, \left(We/\bar{f}\right)\mathrm{i}k_z\,\partial_y\psi \,+\, \partial_y u\right), \tag{6.27c}$$

$$r_{11} \;=\; \left(2\,We^2/\zeta_0\right)\left(\left(3\,We/\bar{f}\right)\mathrm{i}k_z\,\partial_y\psi \,+\, 2\,\partial_y u\right). \tag{6.27d}$$

The above expression (6.27) is obtained by taking the temporal Fourier transforms of (6.12a)–(6.12b) and replacing the wall-normal velocity and vorticity with

$$v \;=\; \mathrm{i}k_z\,\psi, \quad \eta \;=\; \mathrm{i}k_z\,u.$$

In the absence of streamwise forcing and streamwise variations, the static-in-time momentum equation (in the streamwise direction) provides a relation between the streamwise velocity and the streamwise components of the conformation tensor

$$\Delta u \;=\; -\frac{1-\beta}{\beta}\left(\frac{\bar{f}}{We}\,\partial_y\,r_{12} \,+\, \frac{\bar{f}}{We}\,\mathrm{i}k_z\,r_{13} \,+\, \frac{\bar{f}}{\bar{L}^2}\,\partial_y\,r_{11}\right). \tag{6.28}$$

Substituting (6.27b) and (6.27c) into (6.28) yields a relation between streamwise velocity and the conformation tensor fluctuations in the wall-normal/spanwise plane,

$$\Delta u \;=\; -\,(1-\beta)\left(\partial_y(U'\,r_{22}) \,+\, \mathrm{i}k_z(U' r_{23})\right). \tag{6.29}$$

Furthermore, we can obtain an expression relating u and ψ by substituting (6.27a) into (6.29) which yields

$$\Delta u \;=\; -\,\left(We/\bar{f}\right)\,(1-\beta)\,\mathrm{i}k_z\,\Delta\psi. \tag{6.30}$$

It can be shown that ψ is induced by the action of the wall-normal and spanwise forcing

$$\psi \;=\; \Delta^{-2} \left[\begin{array}{cc} -\mathrm{i}k_z & \partial_y \end{array} \right] \left[\begin{array}{c} d_2 \\ d_3 \end{array} \right], \tag{6.31}$$

Finally, the frequency response from d_2 and d_3 to u at $\omega = 0$ is obtained by substituting (6.31) into (6.30) which yields

$$\mathbf{H}_{uj}(k_z, 0; \beta, We, L) \;=\; -\left(We/\bar{f}\right)(1 \,-\, \beta)\, \mathbf{D}_{vj}, \quad j \;=\; \{2, 3\},$$

where

$$\mathbf{D}_{v2} \;=\; k_z^2 \Delta^{-2}, \quad \mathbf{D}_{v3} \;=\; \mathrm{i}k_z\, \Delta^{-2} \partial_y.$$

The worst-case amplification of u caused by d_2 and d_3 can be reliably approximated by

$$\begin{aligned} G_{uj}\,(k_z; \beta, We, L) \;&\approx\; \sigma^2_{\max}\,(\mathbf{H}_{uj}(k_z, 0; \beta, We, L)) \\ &=\; \left(We/\bar{f}\right)^2\, (1 - \beta)^2\, \sigma^2_{\max}\,(\mathbf{D}_{vj}) \\ &=\; \left(\bar{N}_1/2\right)(1 - \beta)^2\, g_{uj}(k_z), \quad j \;=\; \{2, 3\}, \end{aligned}$$

where the functions g_{uj} with $j = \{2, 3\}$ quantify the spanwise frequency responses from d_2 and d_3 to u. In the Oldroyd-B limit (i.e., as $L \to \infty$), the first normal stress difference $\bar{N}_1 \to 2\, We^2$ and the function G_{uj} is given by

$$\lim_{L \to \infty} G_{uj}(k_z; \beta, We, L) \;=\; We^2\, (1 - \beta)^2\; g_{uj}(k_z).$$

On the other hand, in the limit of infinitely large We, the first normal stress difference $\bar{N}_1 \to \bar{L}^2$ and the function G_{uj} is given by

$$\lim_{We \to \infty} G_{uj}(k_z; \beta, We, L) \;=\; \left(\bar{L}^4/2\right)(1 - \beta)^2\; g_{uj}(k_z).$$

6.10 Appendix: Frequency response operators from body forces to polymer stresses in streamwise-constant Couette flow of FENE-CR fluids

The streamwise-constant frequency response operators in (6.25) that map different forcing components to the polymer stress fluctuations are given by

$$
\begin{aligned}
\mathbf{G}_{1j}(k_z,\omega;\beta,We,L) &= \frac{2\,\bar{f}}{\mathrm{i}\omega\beta+\bar{f}}\,\partial_y\,\mathbf{D}_{vj}, \quad \mathbf{G}_{3j}(k_z,\omega;\beta,We,L) \;=\; -\frac{2\,\bar{f}}{\mathrm{i}\omega\beta+\bar{f}}\,\partial_y\,\mathbf{D}_{vj},\\
\mathbf{G}_{2j}(k_z,\omega;\beta,We,L) &= \left(\bar{f}/\left(\mathrm{i}\omega\beta+\bar{f}\right)\right)(\mathrm{i}/k_z)\left(\partial_{yy}+k_z^2\right)\mathbf{D}_{vj},\\
\mathbf{G}_{41}(k_z,\omega;\beta,We,L) &= \left(\mathrm{i}k_z\bar{f}/\left(\mathrm{i}\omega\beta+\bar{f}\right)\right)\mathbf{E}_{uu}^{-1}\,\mathbf{C}_{u\eta}\,\mathbf{D}_{\eta 1},\\
\mathbf{G}_{4j}(k_z,\omega;\beta,We,L) &= \frac{We\bar{f}}{(\mathrm{i}\omega\beta+\bar{f})(\mathrm{i}\omega+\bar{f})}\,(\mathrm{i}/k_z)\left(\partial_{yy}+k_z^2\right)\mathbf{D}_{vj}\,+\\
&\quad \frac{We}{(\mathrm{i}\omega\beta+\bar{f})}\,(\mathrm{i}/k_z)\partial_{yy}\,\mathbf{D}_{vj} \;+\; \frac{\mathrm{i}k_z\bar{f}}{(\mathrm{i}\omega+\bar{f})}\,\mathbf{E}_{uu}^{-1}\,\mathbf{E}_{uv}\,\mathbf{D}_{vj},\\
\mathbf{G}_{51}(k_z,\omega;\beta,We,L) &= \frac{2We^2}{\bar{L}^2}\,\frac{2\mathrm{i}\omega\bar{f}-\omega^2}{\left(\mathrm{i}\omega\beta+\bar{f}\right)(\zeta_0\,-\,\omega^2\,+\,\mathrm{i}\omega\zeta_1)}\,\partial_y\,\mathbf{E}_{uu}^{-1}\,\mathbf{C}_{u\eta}\,\mathbf{D}_{\eta 1}\,+\\
&\quad \frac{\bar{f}}{\mathrm{i}\omega\beta+\bar{f}}\,\partial_y\,\mathbf{E}_{uu}^{-1}\,\mathbf{C}_{u\eta}\,\mathbf{D}_{\eta 1},\\
\mathbf{G}_{5j}(k_z,\omega;\beta,We,L) &= \frac{2We^2}{\bar{L}^2}\,\frac{2\mathrm{i}\omega\bar{f}-\omega^2}{\left(\mathrm{i}\omega+\bar{f}\right)(\zeta_0\,-\,\omega^2\,+\,\mathrm{i}\omega\zeta_1)}\,\partial_y\,\mathbf{E}_{uu}^{-1}\,\mathbf{E}_{uv}\,\mathbf{D}_{vj}\,+\\
&\quad \frac{2We^3}{\bar{L}^2}\,\frac{3\mathrm{i}\omega\bar{f}-\omega^2}{\left(\mathrm{i}\omega+\bar{f}\right)\left(\mathrm{i}\omega\beta+\bar{f}\right)(\zeta_0\,-\,\omega^2\,+\,\mathrm{i}\omega\zeta_1)}\,\partial_y\,\mathbf{D}_{vj}\,+\\
&\quad \frac{We\left(\mathrm{i}\omega+3\bar{f}\right)}{\left(\mathrm{i}\omega+\bar{f}\right)\left(\mathrm{i}\omega\beta+\bar{f}\right)}\,\partial_y\,\mathbf{D}_{vj} \;+\; \frac{\bar{f}}{\mathrm{i}\omega+\bar{f}}\,\partial_y\,\mathbf{E}_{uu}^{-1}\,\mathbf{E}_{uv}\,\mathbf{D}_{vj},\\
\mathbf{G}_{61}(k_z,\omega;\beta,We,L) &= \left(\frac{\bar{f}}{We}+\frac{2We}{\bar{L}^2}\right)\frac{2We^2(\mathrm{i}\omega+2\bar{f})}{\bar{f}\,(\zeta_0\,-\,\omega^2\,+\,\mathrm{i}\omega\zeta_1)}\,\frac{\mathrm{i}\omega+\bar{f}}{\mathrm{i}\omega\beta+\bar{f}}\,\partial_y\,\mathbf{E}_{uu}^{-1}\,\mathbf{C}_{u\eta}\,\mathbf{D}_{\eta 1},\\
\mathbf{G}_{6j}(k_z,\omega;\beta,We,L) &= \left(\frac{\bar{f}}{We}+\frac{2We}{\bar{L}^2}\right)\left(\frac{2We^2(\mathrm{i}\omega+2\bar{f})}{\bar{f}\,(\zeta_0\,-\,\omega^2\,+\,\mathrm{i}\omega\zeta_1)}\,\partial_y\,\mathbf{E}_{uu}^{-1}\,\mathbf{E}_{uv}\,\mathbf{D}_{vj}\,+\right.\\
&\quad \left.\frac{2We^3\left(\mathrm{i}\omega+3\bar{f}\right)}{\bar{f}\left(\mathrm{i}\omega\beta+\bar{f}\right)(\zeta_0\,-\,\omega^2\,+\,\mathrm{i}\omega\zeta_1)}\,\partial_y\mathbf{D}_{vj}\right), \quad j=\{2,3\}.
\end{aligned}
$$

Chapter 7

Slow-fast decomposition of an inertialess flow of viscoelastic fluids

In this chapter, we study frequency responses of an inertialess two-dimensional channel flow of viscoelastic fluids. By rewriting the evolution equations in terms of low-pass filtered versions of the stream function, we show that strongly-elastic flows can be brought into a standard singularly perturbed form that exhibits a slow-fast decomposition. In high-Weissenberg number regime, which is notoriously difficult to study numerically, we demonstrate that the frequency responses are reliably captured by the dynamics of the fast subsystem. We use numerical computations to validate our theoretical findings and to illustrate that our formulation does not suffer from spurious numerical instabilities.

7.1 Introduction

Viscoelastic fluids, such as polymer solutions and molten plastics, are often encountered in industrial and biological flows. Their micro-scale properties are significantly more complex than those in Newtonian fluids. Recent experiments have shown that fluids containing long polymer chains may become turbulent even at low flow rates [5, 6, 9]. This is in contrast to Newtonian fluids that become turbulent only at high speeds. Our recent work suggests that velocity and stress fluctuations in viscoelastic fluids can exhibit large amplification even in the absence of inertia [114–117, 124].

In this chapter, we consider a two-dimensional inertialess shear-driven flow of viscoelastic fluids. We identify the slow-fast system decomposition and utilize singular perturbation analysis to show that, in strongly elastic flows, the frequency responses are captured by the fast subsystem. The evolution representation that we determine facilitates reliable computation of the frequency responses in the high-Weissenberg number regime, which is known to exhibit spurious numerical instabilities [125, 126].

Our presentation for this chapter is organized as follows. In Section 7.2, we present the governing equations. In Section 7.3, we discuss the method for transforming the governing equations into an evolution representation where the states are determined by the filtered versions of the stream function. In Section 7.4, we show that the evolution model admits a standard singularly perturbed form, thereby identifying the slow-fast decomposition of the inertialess channel flow. In Section 7.5, we compute the frequency responses to validate our theoretical results. We conclude with a summary of our developments and a highlight of remaining challenges in Section 7.6.

7.2 Governing equations

The momentum, continuity, and constitutive equations for a two-dimensional incompressible channel flow of viscoelastic fluids, with geometry shown in figure 7.1, are given by

$$\begin{aligned} Re\,\dot{\mathbf{V}} &= We\Big(\beta\,\boldsymbol{\nabla}^2\mathbf{V} - \boldsymbol{\nabla}P - Re\,\mathbf{V}\cdot\boldsymbol{\nabla}\mathbf{V} + (1-\beta)\,\boldsymbol{\nabla}\cdot\mathbf{T}\Big), && (7.1\text{a}) \\ 0 &= \nabla\cdot\mathbf{V}, && (7.1\text{b}) \\ \dot{\mathbf{T}} &= \boldsymbol{\nabla}\mathbf{V} + (\boldsymbol{\nabla}\mathbf{V})^T - \mathbf{T} + We\Big(\mathbf{T}\cdot\boldsymbol{\nabla}\mathbf{V} + (\mathbf{T}\cdot\boldsymbol{\nabla}\mathbf{V})^T - \mathbf{V}\cdot\boldsymbol{\nabla}\mathbf{T}\Big). && (7.1\text{c}) \end{aligned}$$

Here, dot denotes partial derivative with respect to time t, $\mathbf{V}$ is the velocity vector, P is pressure, $\mathbf{T}$ is the polymer stress tensor, $\boldsymbol{\nabla}$ is the gradient, and $\boldsymbol{\nabla}^2$ is the Laplacian. System (7.1) has been non-dimensionalized by scaling length with the channel half-height L, time with the fluid relaxation time λ, velocity with the largest base flow velocity U_0, polymer stresses with $\eta_p U_0/L$, and pressure with $(\eta_s + \eta_p)\,U_0/L$, where η_s and η_p are the solvent and polymer viscosities. The key parameters in (7.1) are: the viscosity ratio, $\beta = \eta_s/\left(\eta_s + \eta_p\right)$; the Weissenberg number, $We = \lambda U_0/L$, which is the ratio of the fluid relaxation time to the characteristic flow time L/U_0; and the Reynolds number, $Re = \rho U_0 L/(\eta_s + \eta_p)$, which represents the ratio of inertial to viscous forces, where ρ is the fluid density.

The momentum (7.1a) and continuity (7.1b) equations describe the motion of an incompressible viscoelastic fluid. For given $\mathbf{T}$, the pressure adjusts itself so that velocity satisfies the continuity equation (7.1b). The constitutive equation (7.1c) is given for an Oldroyd-B fluid and it captures the influence of velocity gradients on the evolution of polymer stress fluctuations. This equation is obtained for dilute polymer solutions in which each polymer molecule is modeled by two spherical beads connected by a linear spring [17].

In shear driven flow, the steady-state solution of (7.1) is given by

$$\bar{\mathbf{v}} = \left[\begin{array}{c} y \\ 0 \end{array}\right], \quad \bar{\boldsymbol{\tau}} = \left[\begin{array}{cc} \bar{\tau}_{11} & \bar{\tau}_{12} \\ \bar{\tau}_{12} & \bar{\tau}_{22} \end{array}\right] = \left[\begin{array}{cc} 2We & 1 \\ 1 & 0 \end{array}\right].$$

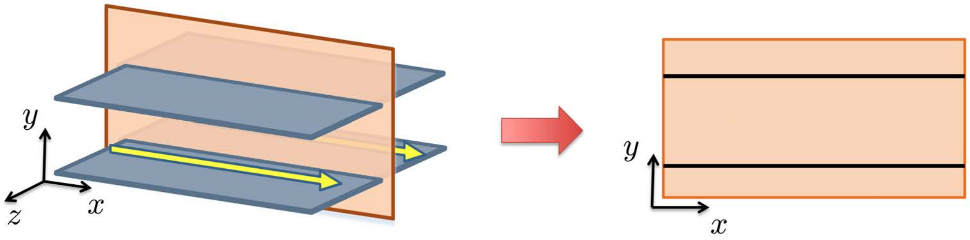

Figure 7.1: Channel flow geometry. We consider the dynamics of two-dimensional flow fluctuations in the (x, y)-plane.

Recent experiments have shown that flows of viscoelastic fluids may become turbulent (i.e., undergo a transition to a time-dependent disordered flow state) even when inertial forces are considerably weaker than viscous forces [5,6,9]. Hence, in this work, we consider flows in the absence of inertia, i.e. at $Re = 0$. In this case, the linearized equations governing the dynamics of fluctuations around the base flow $(\bar{\mathbf{v}}, \bar{\boldsymbol{\tau}})$ are given by

$$\begin{aligned}
0 &= -\boldsymbol{\nabla} p + (1-\beta)\boldsymbol{\nabla}\cdot\boldsymbol{\tau} + \beta\boldsymbol{\nabla}^2\mathbf{v} + \mathbf{d}, && (7.2a)\\
0 &= \boldsymbol{\nabla}\cdot\mathbf{v}, && (7.2b)\\
\dot{\boldsymbol{\tau}} &= \boldsymbol{\nabla}\mathbf{v} + (\boldsymbol{\nabla}\mathbf{v})^T - \boldsymbol{\tau} + We\,(\boldsymbol{\tau}\cdot\boldsymbol{\nabla}\bar{\mathbf{v}} + \bar{\boldsymbol{\tau}}\cdot\boldsymbol{\nabla}\mathbf{v} + \\
&\quad (\bar{\boldsymbol{\tau}}\cdot\boldsymbol{\nabla}\mathbf{v})^T + (\boldsymbol{\tau}\cdot\boldsymbol{\nabla}\bar{\mathbf{v}})^T - \mathbf{v}\cdot\boldsymbol{\nabla}\bar{\boldsymbol{\tau}} - \bar{\mathbf{v}}\cdot\boldsymbol{\nabla}\boldsymbol{\tau}), && (7.2c)
\end{aligned}$$

where $\mathbf{v} = \begin{bmatrix} u & v \end{bmatrix}^T$, p, and $\boldsymbol{\tau}$ are, respectively, the velocity vector, pressure, and polymer stress tensor fluctuations with u and v denoting the streamwise and wall-normal velocities. System (7.2) is driven by the spatially distributed and temporally varying body force fluctuations $\mathbf{d} = \begin{bmatrix} d_1 & d_2 \end{bmatrix}^T$ with d_1 and d_2 representing the forcing in the streamwise (x) and wall-normal (y) directions, respectively.

The pressure can be eliminated from the equations by expressing the velocity fluctuations in terms of the stream function ψ,

$$u = \partial_y \psi, \quad v = -\partial_x \psi.$$

Furthermore, by rearranging the polymer stresses

$$\boldsymbol{\phi} = \begin{bmatrix} \phi_1 & \phi_2 & \phi_3 \end{bmatrix}^T = \begin{bmatrix} \tau_{22} & \tau_{12} & \tau_{11} \end{bmatrix}^T,$$

and by applying the Fourier transform in the x-direction we arrive at a set of PDEs in

$y \in [-1, 1]$ and t parameterized by the wave-number k_x,

$$\begin{aligned}
\dot{\phi}_1 &= -\,f(y)\,\phi_1 + F_{1\psi}\,\psi, && (7.3\text{a})\\
\dot{\phi}_2 &= -\,f(y)\,\phi_2 + We\,\phi_1 + F_{2\psi}\,\psi, && (7.3\text{b})\\
\dot{\phi}_3 &= -\,f(y)\,\phi_3 + 2\,We\,\phi_2 + F_{3\psi}\,\psi, && (7.3\text{c})\\
\Delta^2\psi &= \frac{1-\beta}{\beta}\Big(\,F_{\psi 1}\,\phi_1 + F_{\psi 2}\,\phi_2 + F_{\psi 3}\,\phi_3\,\Big) + \frac{1}{\beta}\Big(-\,\partial_y\,d_1 + \mathrm{i}k_x\,d_2\Big), && (7.3\text{d})
\end{aligned}$$

where i is the imaginary unit and

$$\begin{array}{l}
F_{1\psi} = 2\left(We\,k_x^2 - \mathrm{i}k_x\partial_y\right),\; F_{2\psi} \;=\; \partial_{yy} + (1 + 2\,We^2)\,k_x^2,\\
F_{3\psi} = 2\,\mathrm{i}k_x\left(1 + 2\,We^2\right)\partial_y + 2\,We\,\partial_{yy},\\
F_{\psi 1} = \mathrm{i}k_x,\; F_{\psi 2} \;=\; -\left(\partial_{yy} + k_x^2\right),\; F_{\psi 3} \;=\; -\mathrm{i}k_x,\\
f(y) = 1 + We\,\mathrm{i}k_x\,y,\; \Delta^2 \;=\; \partial_{yyyy} - 2\,k_x^2\,\partial_{yy} + k_x^4.
\end{array} \qquad (7.4)$$

For notational convenience, we have suppressed the dependence of $\{\phi_i, \psi, d_j\}$ on $(k_x, y, t; \beta, We)$, which is a convention we adopt from now on.

The boundary conditions on the stream function are induced by the no-slip and no-penetration criteria on velocity fluctuations and they are given by

$$\psi\,(k_x, y = \pm 1, t) \;=\; \partial_y\psi\,(k_x, y = \pm 1, t) \;=\; 0.$$

Note that the kinetic energy density of the velocity fluctuations is determined by the L_2-norm of $\mathbf{v} = \left[\begin{array}{cc} u & v \end{array}\right]^T$

$$E\,(k_x, t) \;=\; \langle u, u\rangle \;+\; \langle v, v\rangle \;=\; \langle \psi, -\Delta\psi\rangle \;=\; \langle \psi, \psi\rangle_e\,, \qquad (7.5)$$

where $\Delta = \partial_{yy} - k_x^2$ and $\langle\cdot,\cdot\rangle$ denotes the standard $L_2\,[-1, 1]$ inner product

$$\langle u, u\rangle \;=\; \int_{-1}^{1} u^*(k_x, y, t)\,u(k_x, y, t)\,\mathrm{d}y.$$

The inner product $\langle\cdot,\cdot\rangle_e$ in (7.5) along with the boundary conditions on ψ determines the Hilbert space that the stream function belongs to

$$\mathbb{H} := \{\psi \in L_2[-1, 1];\; \partial_{yy}\psi \in L_2[-1, 1],\; \psi(\pm 1) = 0\}\,. \qquad (7.6)$$

On the other hand, the elastic energy of the polymer stresses is not quantified by an L_2-norm and there are no boundary conditions on the components of $\boldsymbol{\tau}$. Consequently, it is difficult to determine the appropriate Hilbert space for the polymer stress fluctuations. Furthermore, it is well known that the set of equations (7.3) exhibits spurious numerical instabilities [125, 126] which is an obstacle to conducting high-fidelity simulations of viscoelastic fluids.

In this work, we show how (7.3) can be brought into an evolution representation that is amenable to both analytical and computational developments. In addition, we demonstrate that the inertialess channel flow can be decomposed into slow and fast subsystems. At high-Weissenberg numbers, singular perturbations reveal that the system's dynamics are captured by the dynamics of the fast subsystem. Furthermore, we illustrate that the computation of the frequency responses does not exhibit any numerical instabilities upon grid refinement. This suggests that the inherent presence of two-time scales in the system's dynamics may represent one source of numerical difficulties. Full nonlinear simulations may thus not be able to capture the response of the fast subsystem correctly, and, as we show, this subsystem contributes significantly to the fluctuation's energy.

7.3 Evolution equations and low-pass versions of the stream functions

In what follows, we show how to transform (7.3) into an evolution representation where the state variables are filtered versions of the stream function. This new representation of system (7.2) has two major advantages:

- the state space is a well-defined Hilbert space;
- the evolution equations are posed in a form that is well-suited for analysis and computations.

We begin by applying the temporal Fourier transform with zero initial conditions on (7.3a) – (7.3c)

$$\phi_1 \;=\; \frac{1}{\mathrm{i}\omega + f(y)}\, F_{1\psi}\, \psi, \tag{7.7a}$$

$$\phi_2 \;=\; \frac{1}{\mathrm{i}\omega + f(y)}\, \left(We\, \phi_1 \,+\, F_{2\psi}\, \psi \right), \tag{7.7b}$$

$$\phi_3 \;=\; \frac{1}{\mathrm{i}\omega + f(y)}\, \left(2\, We\, \phi_2 \,+\, F_{3\psi}\, \psi \right), \tag{7.7c}$$

where ω is the temporal frequency. Let us introduce the following low-pass versions of the stream function,

$$\xi_1 \;=\; \frac{1}{\mathrm{i}\omega + f(y)}\,\psi, \tag{7.8a}$$

$$\xi_2 \;=\; \frac{1}{(\mathrm{i}\omega + f(y))^2}\,\psi \;=\; \frac{1}{\mathrm{i}\omega + f(y)}\,\xi_1, \tag{7.8b}$$

$$\xi_3 \;=\; \frac{1}{(\mathrm{i}\omega + f(y))^3}\,\psi \;=\; \frac{1}{\mathrm{i}\omega + f(y)}\,\xi_2, \tag{7.8c}$$

which will be used as state variables in the evolution representation. We first consider (7.7a)

$$\phi_1 = \frac{1}{\mathrm{i}\omega + f(y)}\,F_{1\psi}\,\psi \;=\; \frac{2\,We\,k_x^2}{\mathrm{i}\omega + f(y)}\,\psi \;-\; \frac{2\,\mathrm{i}k_x}{\mathrm{i}\omega + f(y)}\,\psi', \tag{7.9}$$

where $\psi'(y) = \partial\psi/\partial y$. Since

$$\begin{aligned}\frac{1}{\mathrm{i}\omega + f(y)}\,\psi' \;&=\; \partial_y\left[\frac{1}{\mathrm{i}\omega + f(y)}\,\psi\right] \;+\; \frac{f'(y)}{(\mathrm{i}\omega + f(y))^2}\,\psi\\ &=\; \partial_y\,\xi_1 \;+\; f'(y)\,\xi_2\\ &=\; \partial_y\,\xi_1 \;+\; We\,\mathrm{i}k_x\,\xi_2,\end{aligned}$$

we can rewrite (7.9) in terms of ξ_1 and ξ_2

$$\phi_1 \;=\; 2\left(We\,k_x^2 \;-\; \mathrm{i}k_x\,\partial_y\right)\xi_1 + 2\,We\,k_x^2\,\xi_2. \tag{7.10}$$

Using similar procedure, we can express ϕ_2 and ϕ_3 in terms of ξ_1, ξ_2, and ξ_3,

$$\phi_2 \;=\; \left(\partial_{yy} \;+\; \left(1 \;+\; 2\,We^2\right)k_x^2\right)\xi_1 \;+\; 2\,We^2\,k_x^2\,\xi_2 \;+\; 2\,We^2\,k_x^2\,\xi_3, \tag{7.11a}$$

$$\begin{aligned}\phi_3 \;=\; &\left(2\,We\,\partial_{yy} \;+\; 2\left(1 \;+\; 2\,We^2\right)\mathrm{i}k_x\,\partial_y\right)\xi_1\\ &+\; \left(2\,We\,\partial_{yy} \;+\; 4\,We^2\,\mathrm{i}k_x\,\partial_y\right)\xi_2 \;+\; 4\,We^2\,\mathrm{i}k_x\,\partial_y\,\xi_3.\end{aligned} \tag{7.11b}$$

We can now obtain an evolution representation of system (7.3) by letting

$$\boldsymbol{\xi} \;=\; \left[\begin{array}{ccc}\xi_1 & \xi_2 & \xi_3\end{array}\right]^T,$$

be the state and by applying the inverse temporal Fourier transform to (7.8)

$$
\begin{aligned}
\xi_1 &= \frac{1}{\mathrm{i}\omega + f(y)}\,\psi \;\;\Rightarrow\;\; \dot{\xi}_1 = -f(y)\,\xi_1 + \psi,\\
\xi_2 &= \frac{1}{\mathrm{i}\omega + f(y)}\,\xi_1 \;\;\Rightarrow\;\; \dot{\xi}_2 = -f(y)\,\xi_2 + \xi_1,\\
\xi_3 &= \frac{1}{\mathrm{i}\omega + f(y)}\,\xi_2 \;\;\Rightarrow\;\; \dot{\xi}_3 = -f(y)\,\xi_3 + \xi_2.
\end{aligned}
$$

Furthermore, substitution of (7.10) and (7.11) into (7.3d) yields an expression for the stream function in terms of $\boldsymbol{\xi}$.

In summary, the evolution model is given by

$$
\begin{aligned}
\dot{\boldsymbol{\xi}}(k_x,y,t) &= \mathcal{A}\,\boldsymbol{\xi}(k_x,y,t) \,+\, \mathcal{B}\,\psi(k_x,y,t), && (7.12a)\\
\psi(k_x,y,t) &= We^2\,\mathcal{C}_\psi\,\boldsymbol{\xi}(k_x,y,t) \,+\, \mathcal{D}\,\mathbf{d}(k_x,y,t), && (7.12b)
\end{aligned}
$$

where

$$
\begin{aligned}
\mathcal{A} &= \begin{bmatrix} -f(y) & 0 & 0\\ I & -f(y) & 0\\ 0 & I & -f(y) \end{bmatrix}, \;\; \mathcal{B} = \begin{bmatrix} I\\ 0\\ 0 \end{bmatrix},\\
\mathcal{C}_\psi &= \begin{bmatrix} \mathcal{C}_{\psi 1} & \mathcal{C}_{\psi 2} & \mathcal{C}_{\psi 3} \end{bmatrix}, \;\; \mathcal{D} = \frac{1}{\beta}\Delta^{-2}\begin{bmatrix} -\partial_y & \mathrm{i}k_x \end{bmatrix},\\
\mathcal{C}_{\psi 1} &= \frac{(1-\beta)}{\beta}\Delta^{-2}\left(2\,k_x^2\,\Delta - \frac{2}{We}\mathrm{i}k_x\,\Delta\,\partial_y - \frac{1}{We^2}\Delta^2\right),\\
\mathcal{C}_{\psi 2} &= \frac{(1-\beta)}{\beta}\Delta^{-2}\left(2\,k_x^2\,\Delta \,-\, \frac{2}{We}\mathrm{i}k_x\,\Delta\,\partial_y\right), \;\; \mathcal{C}_{\psi 3} = \frac{(1-\beta)}{\beta}2\,k_x^2\,\Delta^{-2}\,\Delta.
\end{aligned}
$$

Here, I represents the identity operator. We note that the response of the polymer stresses $\boldsymbol{\phi}$ can be determined from the dynamics of $\boldsymbol{\xi}$ using (7.10) and (7.11). The state-space representation (7.12) in conjunction with (7.10) and (7.11) completely captures the dynamics of flow fluctuations in system (7.2). We further note that the states, $\boldsymbol{\xi}$, belong to the same Hilbert space (7.6) as the stream function ψ. In the next section, we show how to transform (7.12) into a standard singularly perturbed form. We then use singular perturbation techniques to determine the slow-fast decomposition of a channel flow of viscoelastic fluids in the absence of inertia.

7.4 Singular perturbation analysis of the 2D inertialess channel flow

In this section, we show how to decompose the evolution model (7.12) into slow and fast subsystems. This is accomplished by bringing (7.12) into a standard singularly perturbed form. Furthermore, we show analytically that the fast subsystem captures the essential features of the input-output responses.

7.4.1 Singularly perturbed form of the evolution model

System (7.12) can be reformulated into a standard singularly perturbed form by multiplying $\boldsymbol{\xi}$ with We^2

$$\mathbf{x} \;=\; \begin{bmatrix} x_1 \\ x_2 \end{bmatrix} \;=\; We^2 \begin{bmatrix} \xi_2 \\ \xi_3 \end{bmatrix}, \;\; z \;=\; We^2\, \xi_1,$$

and by re-scaling time with We

$$\tau \;=\; We\, t \;\Rightarrow\; \frac{\partial}{\partial t}(\cdot) \;=\; We\,\frac{\partial}{\partial \tau}(\cdot) \;=\; \frac{1}{\epsilon}\frac{\partial}{\partial \tau}(\cdot).$$

Here, we note that τ represents the new time coordinate which should not be confused with polymer stress fluctuations τ_{ij}, which are characterized with double indices. Using state variables $(\mathbf{x}, z)$ and time τ, system (7.12) along with (7.10) and (7.11) can be represented by

$$\begin{bmatrix} \mathbf{x}_\tau \\ \epsilon\, z_\tau \end{bmatrix} \;=\; \begin{bmatrix} \mathcal{A}_{11}(\epsilon) & \mathcal{A}_{12}(\epsilon) \\ \mathcal{A}_{21}(\epsilon) & \mathcal{A}_{22}(\epsilon) \end{bmatrix} \begin{bmatrix} \mathbf{x} \\ z \end{bmatrix} + \begin{bmatrix} 0 \\ \mathcal{D} \end{bmatrix} \mathbf{d}, \tag{7.13a}$$

$$\psi \;=\; \begin{bmatrix} \mathcal{C}_{\psi \mathbf{x}}(\epsilon) & \mathcal{C}_{\psi z}(\epsilon) \end{bmatrix} \begin{bmatrix} \mathbf{x} \\ z \end{bmatrix} + \mathcal{D}\, \mathbf{d}, \tag{7.13b}$$

$$\boldsymbol{\phi} \;=\; \begin{bmatrix} \mathcal{C}_{\phi \mathbf{x}}(\epsilon) & \mathcal{C}_{\phi z}(\epsilon) \end{bmatrix} \begin{bmatrix} \mathbf{x} \\ z \end{bmatrix}. \tag{7.13c}$$

Here,

$$\epsilon \;=\; 1/We,$$

is a small positive scalar that will be used as a perturbation parameter, the τ-subscript denotes the partial derivative with respect to τ, and the operators in (7.13) are given in Appendix 7.7. Since the time derivative of z is multiplied by a small positive parameter ϵ in (7.13a) and since the operator $\mathcal{A}_{22}$ is invertible at $\epsilon = 0$, system (7.13) is in a standard singularly perturbed form [127] with homogenous Dirichlet and Neumann boundary conditions on $\mathbf{x}$, z, and ψ.

7.4.2 Block-diagonal form: slow-fast decomposition of the evolution model

In this section, we demonstrate how to decompose (7.13) into its slow and fast subsystems. This is accomplished by first introducing a change of variables

$$\eta \;=\; z \,+\, \mathcal{L}(\epsilon)\,\mathbf{x},$$

to bring (7.13a) into an upper-triangular form

$$\begin{bmatrix} \mathbf{x}_\tau \\ \epsilon\,\eta_\tau \end{bmatrix} \;=\; \begin{bmatrix} \mathcal{A}_{11} - \mathcal{A}_{12}\,\mathcal{L} & \mathcal{A}_{12} \\ 0 & \mathcal{A}_{22} + \epsilon\,\mathcal{L}\,\mathcal{A}_{12} \end{bmatrix} \begin{bmatrix} \mathbf{x} \\ \eta \end{bmatrix} \,+\, \begin{bmatrix} 0 \\ \mathcal{D} \end{bmatrix} \mathbf{d}. \tag{7.14}$$

Here, the operator $\mathcal{L}(\epsilon)$ satisfies the following *slow-manifold* condition

$$\mathcal{A}_{21} \,-\, \mathcal{A}_{22}\,\mathcal{L} \,+\, \epsilon\,\mathcal{L}\,\mathcal{A}_{11} \,-\, \epsilon\,\mathcal{L}\,\mathcal{A}_{12}\,\mathcal{L} \;=\; 0. \tag{7.15}$$

Following [127], we next introduce another change of variables

$$\boldsymbol{\varphi} \;=\; \mathbf{x} \,-\, \epsilon\,\mathcal{Q}(\epsilon)\,\eta,$$

with $\mathcal{Q}$ satisfying

$$\epsilon\,(\mathcal{A}_{11} \,-\, \mathcal{A}_{12}\,\mathcal{L})\,\mathcal{Q} \,-\, \mathcal{Q}\,(\mathcal{A}_{22} \,+\, \epsilon\,\mathcal{L}\,\mathcal{A}_{12}) \,+\, \mathcal{A}_{12} \;=\; 0. \tag{7.16}$$

This transforms (7.14) into a block-diagonal form

$$\begin{bmatrix} \boldsymbol{\varphi}_\tau \\ \epsilon\,\eta_\tau \end{bmatrix} \;=\; \begin{bmatrix} \mathcal{A}_s(\epsilon) & 0 \\ 0 & \mathcal{A}_f(\epsilon) \end{bmatrix} \begin{bmatrix} \boldsymbol{\varphi} \\ \eta \end{bmatrix} \,+\, \begin{bmatrix} \mathcal{B}_s(\epsilon) \\ \mathcal{B}_f(\epsilon) \end{bmatrix} \mathbf{d}, \tag{7.17a}$$

$$\psi \;=\; \begin{bmatrix} \mathcal{C}_{\psi s}(\epsilon) & \mathcal{C}_{\psi f}(\epsilon) \end{bmatrix} \begin{bmatrix} \boldsymbol{\varphi} \\ \eta \end{bmatrix} \,+\, \mathcal{D}\,\mathbf{d}, \tag{7.17b}$$

$$\boldsymbol{\phi} \;=\; \begin{bmatrix} \mathcal{C}_{\phi s}(\epsilon) & \mathcal{C}_{\phi f}(\epsilon) \end{bmatrix} \begin{bmatrix} \boldsymbol{\varphi} \\ \eta \end{bmatrix}, \tag{7.17c}$$

where

$$\begin{array}{rclrcl} \mathcal{A}_s &=& \mathcal{A}_{11} \,-\, \mathcal{A}_{12}\,\mathcal{L}, & \mathcal{A}_f &=& \mathcal{A}_{22} \,+\, \epsilon\,\mathcal{L}\,\mathcal{A}_{12}, \\ \mathcal{B}_s &=& -\mathcal{Q}\,\mathcal{D}, & \mathcal{B}_f &=& \mathcal{D}, \\ \mathcal{C}_{\psi s} &=& \mathcal{C}_{\psi \mathbf{x}} - \mathcal{C}_{\psi z}\,\mathcal{L}, & \mathcal{C}_{\psi f} &=& \mathcal{C}_{\psi z} + \epsilon\,(\mathcal{C}_{\psi \mathbf{x}} - \mathcal{C}_{\psi z}\,\mathcal{L})\,\mathcal{Q}, \\ \mathcal{C}_{\phi s} &=& \mathcal{C}_{\phi \mathbf{x}} - \mathcal{C}_{\phi z}\,\mathcal{L}, & \mathcal{C}_{\phi f} &=& \mathcal{C}_{\phi z} + \epsilon\,(\mathcal{C}_{\phi \mathbf{x}} - \mathcal{C}_{\phi z}\,\mathcal{L})\,\mathcal{Q}. \end{array}$$

Since the operators in (7.13) depend on the parameter ϵ, we next employ a perturbation analysis of (7.15) and (7.16) to determine the operators $\mathcal{L}$ and $\mathcal{Q}$. By substituting the following representations of the operators $\mathcal{L}$ and $\mathcal{Q}$

$$\mathcal{L}(\epsilon) \;=\; \sum_{i=0}^{\infty} \epsilon^i \, \mathcal{L}_i, \quad \mathcal{Q}(\epsilon) \;=\; \sum_{i=0}^{\infty} \epsilon^i \, \mathcal{Q}_i, \tag{7.18}$$

into (7.15) and (7.16), and by equating terms of equal order in ϵ (see Appendix 7.7) we obtain

$$\mathcal{O}(\epsilon^0): \quad \mathcal{L}_0 \;=\; \left[\begin{array}{cc} I & I \end{array} \right], \;\; \mathcal{Q}_0 \;=\; \left[\begin{array}{cc} 0 & 0 \end{array} \right]^T, \tag{7.19a}$$

$$\mathcal{O}(\epsilon^1): \left\{ \begin{array}{lcl} \mathcal{L}_1 & = & \left(\mathcal{C}_{\psi 1}^0\right)^{-1} \left[\begin{array}{cc} 0 & -\mathcal{C}_{\psi 1}^1 \end{array} \right], \\ \mathcal{Q}_1 & = & \left[\begin{array}{cc} (\mathcal{C}_{\psi 1}^0)^{-1} & 0 \end{array} \right]^T. \end{array} \right. \tag{7.19b}$$

The higher order terms in ϵ are not reported here for brevity. In the next section, we analyze the slow and fast subsystems in (7.17).

7.4.3 Analysis of slow and fast subsystems

In this section, we conduct analysis of the slow and fast subsystems of (7.17). The detailed derivations are given in Appendix 7.7. We show that, for large value of the Weissenberg number, the dynamics of flow fluctuations are captured by the response of the fast subsystem with state η.

Utilizing the expansions of $\mathcal{L}$ and $\mathcal{Q}$ in (7.18), the solutions $\boldsymbol{\varphi}$ and η are determined by applying the temporal Fourier transform to (7.17a) with zero initial conditions

$$\boldsymbol{\varphi} \;=\; \epsilon \left(\mathrm{i}\Omega I - \mathcal{A}_s(\epsilon) \right)^{-1} \left(\mathcal{B}_{s1} + \epsilon \, \mathcal{B}_{s2} + \ldots \right) \mathbf{d} \;=\; \epsilon \, \mathcal{H}_s \, \mathbf{d}, \tag{7.20a}$$

$$\eta \;=\; \left(\mathrm{i}\Omega\epsilon I - \mathcal{A}_f(\epsilon) \right)^{-1} \mathcal{B}_f \, \mathbf{d} \;=\; \mathcal{H}_f \, \mathbf{d}, \tag{7.20b}$$

where Ω is the temporal frequency corresponding to the time variable τ. Here, for a fixed temporal frequency Ω, $\mathcal{H}_s$ and $\mathcal{H}_f$ are operators in y, mapping the forcing $\mathbf{d}$ to the responses of the slow ($\boldsymbol{\varphi}$) and fast (η) subsystems. Furthermore, since

$$\begin{array}{rcl} \mathcal{C}_{\psi s}(\epsilon) & = & \epsilon^2 \, \mathcal{C}_{\psi s,2} \,+\, \epsilon^3 \, \mathcal{C}_{\psi s,3} \,+\, \mathcal{O}(\epsilon^4), \\ \mathcal{C}_{\psi f}(\epsilon) & = & \mathcal{C}_{\psi f,0} \,+\, \epsilon \, \mathcal{C}_{\psi f,1} \,+\, \mathcal{O}(\epsilon^2), \\ \mathcal{C}_{\phi s}(\epsilon) & = & \mathcal{C}_{\phi s,0} \,+\, \epsilon \, \mathcal{C}_{\phi s,1} \,+\, \mathcal{O}(\epsilon^2), \\ \mathcal{C}_{\phi f}(\epsilon) & = & \mathcal{C}_{\phi f,0} \,+\, \epsilon \, \mathcal{C}_{\phi f,1} \,+\, \mathcal{O}(\epsilon^2), \end{array}$$

the responses of the stream function ψ and polymer stresses $\boldsymbol{\phi}$ can be obtained by substituting (7.20a) and (7.20b) into the temporal Fourier transforms of (7.17b) and (7.17c)

$$
\begin{aligned}
\psi \;&=\; \epsilon^3 \left(\mathcal{C}_{\psi s,2} + \epsilon\, \mathcal{C}_{\psi s,3} + \ldots\right) \left(\mathrm{i}\Omega I - \mathcal{A}_s(\epsilon)\right)^{-1} \\
&\quad\times \left(\mathcal{B}_{s1} + \epsilon\, \mathcal{B}_{s2} + \ldots\right) \mathbf{d} \,+\, \Big\{ \left(\mathcal{C}_{\psi f,0} + \epsilon\, \mathcal{C}_{\psi f,1} + \ldots\right) \\
&\quad\times \left(\mathrm{i}\Omega\epsilon I - \mathcal{A}_f(\epsilon)\right)^{-1} \mathcal{B}_f + \mathcal{D} \Big\} \,\mathbf{d}, \qquad (7.21\text{a}) \\
&=\; \left(\epsilon^3\, \mathcal{H}_{\psi s} \,+\, \mathcal{H}_{\psi f}\right) \mathbf{d} \;=\; \mathcal{H}_{\psi} \mathbf{d}, \qquad (7.21\text{b}) \\
\boldsymbol{\phi} \;&=\; \epsilon \left(\mathcal{C}_{\phi s,0} + \epsilon\, \mathcal{C}_{\phi s,1} + \ldots\right) \left(\mathrm{i}\Omega I - \mathcal{A}_s(\epsilon)\right)^{-1} \left(\mathcal{B}_{s1} + \epsilon\, \mathcal{B}_{s2} + \ldots\right) \mathbf{d} \qquad (7.21\text{c}) \\
&\quad+\, \left(\mathcal{C}_{\phi f,0} + \epsilon\, \mathcal{C}_{\phi f,1} + \ldots\right) \left(\mathrm{i}\Omega\epsilon I - \mathcal{A}_f(\epsilon)\right)^{-1} \mathcal{B}_f \,\mathbf{d}, \\
&=\; \left(\epsilon\, \mathcal{H}_{\phi s} \,+\, \mathcal{H}_{\phi f}\right) \mathbf{d} \;=\; \mathcal{H}_{\phi} \mathbf{d}. \qquad (7.21\text{d})
\end{aligned}
$$

The frequency response operators $\{\mathcal{H}_{ij}\}$ in (7.21b) and (7.21d) map the forcing $\mathbf{d}$ to the stream function ($i = \psi$) and polymer stresses ($i = \phi$) with $\{j = s, f\}$ identifying the contributions from the slow and fast subsystems, respectively.

It is clear from (7.21) that, in high Weissenberg number regime, the response of the slow subsystem has negligible influence on the stream function and the polymer stresses. This illustrates that the fast subsystem has the largest influence on the system's response.

7.5 Frequency responses of a 2D inertialess flow of viscoelastic fluids

Here, we compute the frequency responses of the inertialess flow of viscoelastic fluids using the slow-fast decomposition (7.17). In particular, we are interested in computing the power spectral density for the 2D inertialess flow. For a fixed temporal frequency Ω, this quantity is determined by the Hilbert-Schmidt norm of the frequency response operator $\mathcal{H}_{ij}$,

$$
\Pi_{ij}(\Omega) = \|\mathcal{H}_{ij}(\Omega)\|_{HS}^2 = \operatorname{trace}\left(\mathcal{H}_{ij}(\Omega)\, \mathcal{H}_{ij}^{\star}(\Omega)\right),
$$

where $\mathcal{H}_{ij}^{\star}$ represents the adjoint of the operator $\mathcal{H}_{ij}$. All computations are done using a pseudo-spectral method [83]. Convergence of the results is tested by doubling the number of collocation points.

In view of page limitations, we will only consider the response of the velocity fluctuations. These can be determined by analyzing the frequency response operator (7.21b). Figure 7.2 shows the Hilbert-Schmidt norm of the frequency response operator from forcing to the stream function, i.e., $\Pi_{\psi f}$ and Π_{ψ}. Note that the power spectral density as a function of Ω for the stream function has a high-pass characteristic. This response is a consequence of the direct feed-through term from the forcing to the stream function. In addition, the increase in We (decrease in ϵ) moves the cut-off frequency to higher

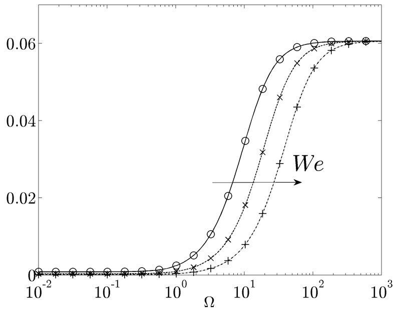

Figure 7.2: The temporal frequency dependence of $\Pi_{\psi f}$ and Π_{ψ} in flows with $k_x = 1$, $\beta = 0.5$, and $\epsilon = \{0.02, 1 \times 10^{-2}, 5 \times 10^{-3}\}$. The lines represent the results for Π_{ψ}. The symbols represent the results for $\Pi_{\psi f}$ which is the response from only the fast system.

values of Ω. We further note that $\Pi_{\psi f}$ lies on top of Π_{ψ} which indicates that at high Weissenberg numbers the fast subsystem reliably captures the response of the entire system. This thus verifies the predictions obtained using perturbation analysis.

7.6 Concluding remarks

We study the frequency responses of a two-dimensional inertialess shear-driven flow of viscoelastic fluids. In particular, we have shown that the dynamics can be decomposed into slow and fast subsystems. This is accomplished by rewriting the evolution equations in terms of low-pass filtered versions of the stream function. This state-space representation admits a standard singularly perturbed form, which is obtained by rescaling time with the Weissenberg number. We then show analytically that the dynamics of flow fluctuations can be captured by the response of the fast subsystem. This demonstrates that the inertialess shear-driven flow of strongly elastic fluids can be modeled by only a single PDE instead of the original system of three PDEs (which are determined by constitutive equation for polymer stresses). Furthermore, this new formulation does not inherit any numerical instabilities from the original model.

Our ongoing effort is devoted to studying the full nonlinear equations using singular perturbation methods. Successful analysis of the nonlinear equations may identify new methods for simulating full three-dimensional flows, thereby leading to new ways of studying the intriguing phenomenon of ‘elastic turbulence’ [5,6,9] in wall-bounded shear flows of viscoelastic fluids.

7.7 Appendix: System operators

Here, we present the system operators used in each section of the chapter. The operators $\mathcal{C}_{\psi i}$ for $\{i = 1, 2, 3\}$ in (7.12) are given by

$$\mathcal{C}_{\psi 1}(\epsilon) \;=\; \mathcal{C}_{\psi 1,0} \,+\, \epsilon\,\mathcal{C}_{\psi 1,1} \,+\, \epsilon^2\,\mathcal{C}_{\psi 1,2}, \quad \mathcal{C}_{\psi 2}(\epsilon) \;=\; \mathcal{C}_{\psi 2,0} \,+\, \epsilon\,\mathcal{C}_{\psi 2,1}, \quad \mathcal{C}_{\psi 3}(\epsilon) \;=\; \mathcal{C}_{\psi 3,0},$$

where

$$\begin{aligned} \mathcal{C}_{\psi 1,0} \;&=\; \mathcal{C}_{\psi 2,0} \;=\; \mathcal{C}_{\psi 3,0} \;=\; \frac{(1-\beta)}{\beta} 2\,k_x^2\,\Delta^{-2}\,\Delta, \\ \mathcal{C}_{\psi 1,1} \;&=\; \mathcal{C}_{\psi 2,1} \;=\; -\frac{(1-\beta)}{\beta} 2\,\mathrm{i}k_x\,\Delta^{-2}\,\Delta\,\partial_y, \quad \mathcal{C}_{\psi 1,2} \;=\; -\frac{(1-\beta)}{\beta}. \end{aligned}$$

The operators in (7.13) are given by

$$\begin{aligned} \mathcal{A}_{11} \;&=\; \begin{bmatrix} -\left(\epsilon + \mathrm{i}k_x\,y\right) & 0 \\ \epsilon & -\left(\epsilon + \mathrm{i}k_x\,y\right) \end{bmatrix}, \quad \mathcal{A}_{12} \;=\; \begin{bmatrix} \epsilon \\ 0 \end{bmatrix}, \\ \mathcal{A}_{21} \;&=\; \mathcal{C}_{\psi \mathbf{x}} \;=\; \begin{bmatrix} \mathcal{C}_{\psi 2} & \mathcal{C}_{\psi 3} \end{bmatrix}, \quad \mathcal{A}_{22} \;=\; \mathcal{C}_{\psi 1} - \left(\epsilon^2 + \epsilon\,\mathrm{i}k_x\,y\right), \quad \mathcal{C}_{\psi z} \;=\; \mathcal{C}_{\psi 1}, \\ \mathcal{C}_{\phi \mathbf{x}} \;&=\; \begin{bmatrix} \mathcal{C}_{12} & 0 \\ \mathcal{C}_{22} & \mathcal{C}_{23} \\ \mathcal{C}_{32} & \mathcal{C}_{33} \end{bmatrix}, \quad \mathcal{C}_{\phi z} \;=\; \begin{bmatrix} \mathcal{C}_{11} \\ \mathcal{C}_{21} \\ \mathcal{C}_{31} \end{bmatrix}. \end{aligned}$$

where

$$\begin{aligned} \mathcal{C}_{11} \;&=\; 2\,\epsilon\,k_x^2 \,-\, 2\,\epsilon^2\,\mathrm{i}k_x\,\partial_y \;=\; \epsilon\,\mathcal{C}_{11,1} \,+\, \epsilon^2\,\mathcal{C}_{11,2}, \quad \mathcal{C}_{12} \;=\; 2\,\epsilon\,k_x^2 \;=\; \epsilon\,\mathcal{C}_{12,1}, \\ \mathcal{C}_{21} \;&=\; 2\,k_x^2 \,+\, \epsilon^2\left(\partial_{yy} + k_x^2\right) \;=\; \mathcal{C}_{21,0} \,+\, \epsilon^2\,\mathcal{C}_{21,2}, \quad \mathcal{C}_{22} \;=\; \mathcal{C}_{23} \;=\; 2\,k_x^2 \;=\; \mathcal{C}_{22,0} \;=\; \mathcal{C}_{23,0}, \\ \mathcal{C}_{31} \;&=\; 4\,\mathrm{i}k_x\,\partial_y \,+\, 2\,\epsilon\,\partial_{yy} \,+\, 2\,\epsilon^2\,\mathrm{i}k_x\,\partial_y \;=\; \mathcal{C}_{31,0} \,+\, \epsilon\,\mathcal{C}_{31,1} \,+\, \epsilon^2\,\mathcal{C}_{31,2}, \\ \mathcal{C}_{32} \;&=\; 4\,\mathrm{i}k_x\,\partial_y \,+\, 2\,\epsilon\,\partial_{yy} \;=\; \mathcal{C}_{32,0} \,+\, \epsilon\,\mathcal{C}_{32,1}, \quad \mathcal{C}_{33} \;=\; 4\,\mathrm{i}k_x\,\partial_y \;=\; \mathcal{C}_{33,0}. \end{aligned}$$

Furthermore, we note that each operator in (7.13) can be factorized in terms of ϵ, e.g.,

$$\mathcal{A}_{11}(\epsilon) \;=\; \begin{bmatrix} -\left(\epsilon + \mathrm{i}k_x\,y\right) & 0 \\ \epsilon & -\left(\epsilon + \mathrm{i}k_x\,y\right) \end{bmatrix} \;=\; \underbrace{\begin{bmatrix} -\mathrm{i}k_x\,y & 0 \\ 0 & -\mathrm{i}k_x\,y \end{bmatrix}}_{\mathcal{A}_{11,0}} \,+\, \epsilon \underbrace{\begin{bmatrix} -I & 0 \\ I & -I \end{bmatrix}}_{\mathcal{A}_{11,1}}.$$

We employ a perturbation analysis of (7.15) and (7.16) to determine the operators $\mathcal{L}$ and $\mathcal{Q}$ with ϵ being the perturbation parameter. This is done by substituting (7.18) into (7.15) and (7.16) and equating terms of equal order in ϵ, which yields

$$\mathcal{O}(\epsilon^0): \begin{cases} \mathcal{L}_0 \;=\; \left(\mathcal{A}_{22}^0\right)^{-1} \mathcal{A}_{21}^0 \;=\; \left(\mathcal{C}_{\psi 1}^0\right)^{-1} \begin{bmatrix} \mathcal{C}_{\psi 2}^0 & \mathcal{C}_{\psi 3}^0 \end{bmatrix} \;=\; \begin{bmatrix} I & I \end{bmatrix}, \\ \mathcal{Q}_0 \;=\; \mathcal{A}_{12}^0 \left(\mathcal{A}_{22}^0\right)^{-1} \;=\; \begin{bmatrix} 0 & 0 \end{bmatrix}^T, \end{cases}$$

$$\mathcal{O}(\epsilon^1): \begin{cases} \mathcal{L}_1 \;=\; \left(\mathcal{A}_{22}^0\right)^{-1} \left(\mathcal{A}_{21}^1 - \mathcal{A}_{22}^1 \mathcal{L}_0 + \mathcal{L}_0 \mathcal{A}_{11}^0\right) \;=\; \left(\mathcal{C}_{\psi 1}^0\right)^{-1} \begin{bmatrix} 0 & -\mathcal{C}_{\psi 1}^1 \end{bmatrix}, \\ \mathcal{Q}_1 \;=\; \mathcal{A}_{12}^1 \left(\mathcal{A}_{22}^0\right)^{-1} \;=\; \begin{bmatrix} (\mathcal{C}_{\psi 1}^0)^{-1} & 0 \end{bmatrix}^T. \end{cases}$$

Using the expansions for the operators $\mathcal{L}$ and $\mathcal{Q}$, the operators in (7.17) are given by

$$\begin{aligned}
\mathcal{A}_s(\epsilon) \;&=\; \mathcal{A}_{11}(\epsilon) - \mathcal{A}_{12}(\epsilon)\, \mathcal{L}(\epsilon) \;=\; \mathcal{A}_{11,0} \;+\; \epsilon \,(\mathcal{A}_{11,1} - \mathcal{A}_{12,1}\, \mathcal{L}_0) - \epsilon^2\, \mathcal{A}_{12,1}\, \mathcal{L}_1 \;+\; \mathcal{O}(\epsilon^3) \\
&=\; \mathcal{A}_{s0} + \epsilon\, \mathcal{A}_{s1} + \epsilon^2\, \mathcal{A}_{s2} \;+\; \mathcal{O}(\epsilon^3), \\
\mathcal{A}_f(\epsilon) \;&=\; \mathcal{A}_{22}(\epsilon) + \epsilon\, \mathcal{L}(\epsilon)\, \mathcal{A}_{12}(\epsilon) \;=\; \mathcal{A}_{22,0} + \epsilon \mathcal{A}_{22,1} \;+\; \epsilon^2 \,(\mathcal{A}_{22,2} + \mathcal{L}_0\, \mathcal{A}_{12,1}) + \;\mathcal{O}(\epsilon^3) \\
&=\; \mathcal{A}_{f0} + \epsilon\, \mathcal{A}_{f1} + \epsilon^2\, \mathcal{A}_{f2} \;+\; \mathcal{O}(\epsilon^3), \\
\mathcal{B}_s(\epsilon) \;&=\; -\mathcal{Q}(\epsilon)\mathcal{D} \;=\; -\,(\mathcal{Q}_0 + \epsilon \mathcal{Q}_1)\, \mathcal{D} + \mathcal{O}(\epsilon^3) \;=\; -\epsilon\, \mathcal{Q}_1\, \mathcal{D} + \mathcal{O}(\epsilon^3) \;=\; \mathcal{B}_{s1} + \mathcal{O}(\epsilon^3), \\
\mathcal{B}_f(\epsilon) \;&=\; \mathcal{D} \;=\; \mathcal{B}_{f0}, \\
\mathcal{C}_{\psi s}(\epsilon) \;&=\; \mathcal{C}_{\psi \mathbf{x}}(\epsilon) - \mathcal{C}_{\psi z}(\epsilon)\, \mathcal{L}(\epsilon) \\
&=\; (\mathcal{C}_{\psi \mathbf{x},0} - \mathcal{C}_{\psi 1,0} \mathcal{L}_0) \;+\; \epsilon\, (\mathcal{C}_{\psi \mathbf{x},1} - \mathcal{C}_{\psi 1,0}\, \mathcal{L}_1 - \mathcal{C}_{\psi 1,1}\, \mathcal{L}_0) \\
&\quad -\epsilon^2\, (\mathcal{C}_{\psi 1,0}\, \mathcal{L}_2 + \mathcal{C}_{\psi 1,1}\, \mathcal{L}_1 + \mathcal{C}_{\psi 2,1}\, \mathcal{L}_0) \;+\; \mathcal{O}(\epsilon^3) \\
&=\; \mathcal{C}_{\psi s,0} + \epsilon\, \mathcal{C}_{\psi s,1} + \epsilon^2\, \mathcal{C}_{\psi s,2} \;+\; \mathcal{O}(\epsilon^3), \\
\mathcal{C}_{\psi f}(\epsilon) \;&=\; \mathcal{C}_{\psi z}(\epsilon) + \epsilon\, (\mathcal{C}_{\psi \mathbf{x}}(\epsilon) - \mathcal{C}_{\psi z}(\epsilon)\, \mathcal{L}(\epsilon))\, \mathcal{Q}(\epsilon) \\
&=\; \mathcal{C}_{\psi 1,0} + \epsilon\, \mathcal{C}_{\psi 1,1} \;+\; \epsilon^2\, (\mathcal{C}_{\psi \mathbf{x},0} - \mathcal{C}_{\psi 1,0}\, \mathcal{L}_0)\, \mathcal{Q}_1 \;+\; \mathcal{O}(\epsilon^3) \\
&=\; \mathcal{C}_{\psi f,0} + \epsilon\, \mathcal{C}_{\psi f,1} + \epsilon^2\, \mathcal{C}_{\psi f,2} \;+\; \mathcal{O}(\epsilon^3).
\end{aligned}$$

Since

$$\mathcal{C}_{\psi \mathbf{x},0} - \mathcal{C}_{\psi 1,0}\, \mathcal{L}_0 \;=\; \begin{bmatrix} \mathcal{C}_{\psi 2,0} & \mathcal{C}_{\psi 3,0} \end{bmatrix} \;-\; \mathcal{C}_{\psi 1,0} \begin{bmatrix} I & I \end{bmatrix} \;=\; \begin{bmatrix} 0 & 0 \end{bmatrix},$$

and

$$\begin{aligned}
\mathcal{C}_{\psi \mathbf{x},1} \;-\; \mathcal{C}_{\psi 1,1} \;-\mathcal{C}_{\psi 1,0}\, \mathcal{L}_1 \mathcal{L}_0 \;&=\; \begin{bmatrix} \mathcal{C}_{\psi 2,1} & 0 \end{bmatrix} \;-\; \mathcal{C}_{\psi 1,1} \begin{bmatrix} I & I \end{bmatrix} \\
&\quad -\mathcal{C}_{\psi 1,0}\; (\mathcal{C}_{\psi 1,0})^{-1} \begin{bmatrix} 0 & -\mathcal{C}_{\psi 1,1} \end{bmatrix} \\
&=\; \begin{bmatrix} 0 & 0 \end{bmatrix},
\end{aligned}$$

operator $\mathcal{C}_{\psi s}$ can be simplified to

$$\mathcal{C}_{\psi s}(\epsilon) \;=\; \epsilon^2\, \mathcal{C}_{\psi s,2} \;+\; \mathcal{O}(\epsilon^3).$$

Chapter 8

Model-based analysis of polymer-induced drag reduction in turbulent channel flow

Friction drag in turbulent flows of dilute polymer solutions has been shown to be reduced by as much as 80% compared to Newtonian flows alone. In this chapter, we propose a model-based approach for studying the influence of polymers on drag reduction in a turbulent channel flow. Our simulation-free method utilizes turbulence modeling in conjunction with the analysis of stochastically forced linearized equations to capture the effect of velocity and polymer stress fluctuations on the turbulent viscosity and drag. Compared to traditional methods, that relies on numerical simulations, we determine the turbulent mean velocity from the second-order statistics of the linearized model driven by white-in-time stochastic forcing. The spatial power spectrum of the forcing is selected to ensure that the linearized model for the flow without polymers reproduces the turbulent energy spectrum. We show that the essential drag-reducing trends and turbulent mean velocity observed in direct numerical simulations are captured by our approach. This demonstrates that our model-based approach has the potential for capturing underlying physical mechanisms responsible for polymer induced drag reduction. Furthermore, the proposed model is expected to pave the way for future analysis of polymer induced turbulent channel flow at higher Weissenberg number and finite-extensibility of the polymer chains than currently possible.

8.1 Introduction

Turbulent flows of non-Newtonian fluids are ubiquitous in many engineering applications such as turbulent drag reduction, oil pipeline system, fire fighting, and marine vehicles. By modifying the fluid rheology, the addition of small amount of polymer additives to Newtonian solvents in turbulent flows is an effective means for reducing skin-friction losses. In particular, it has been observed experimentally that dissolving parts-per-million quantities of polymer concentration into a turbulent flow can reduce drag by as much as 80% compared with that of solvent alone [128]. This observation has generated tremendous research effort in the past 50 years. Early reviews by [128–131] provide comprehensive explanations on the physical mechanisms of polymer drag reduction. Later review by [23] gives an overview on the history of polymer additives for turbulent drag reduction with emphasis on newer discoveries.

Study of polymer drag reduction is of both practical and fundamental importance. From applied point of view, the injection of high-molecular weight polymers to flowing liquids in pipe flows and marine vessels can have tremendous benefits. Polymer drag-reducing additives have been used in the Trans-Alaska Pipeline System to increase throughput and to maintain throughput with off-line pumping stations [22]; polymer ejection has been used in US Navy submarine testings to reduce hull drag and increase speed by 10%–15% [23]. From fundamental point of view, understanding mechanisms of polymer drag reduction may shed light into the essential turbulent flow physics and open new ways of controlling turbulence via active or passive means.

Most of our understanding of the onset of drag reduction and the interaction of polymers with turbulence comes from numerical and experimental studies. In experiments, laser-based optical techniques are the enabling technology that allowed scientists to obtain detailed turbulence measurements in flow of diluted polymer solutions [132]. The advancement in laser velocimetry measurements have improved the accuracy and precision of measuring the mean polymer shear stress profile [133–137]. The experimental data collected in these studies have provided valuable insights into the physical mechanisms of polymer drag reduction and benchmark data for the validation of numerical models.

On the other hand, although the use of numerically simulated flow of viscoelastic fluids is relatively new, their techniques have offered tremendous insight on drag reduction mechanisms [138,139], maximum drag reduction [7,26], and coherent structures [28–30]. In spite of this success, there is a need for the development of computationally attractive models that are suitable for analysis and identification of key physical mechanisms.

In this paper, we combine turbulence modeling with analysis of stochastically forced linearized flow equations to quantify the polymer-induced drag reduction in a simulation-free manner. Our approach builds on recent efforts to develop model-based techniques for controlling the onset of turbulence [3, 78] and fully developed turbulent flows [140]. In contrast to the traditional approach that relies on numerical simulations, we use eddy-viscosity-enhanced linearization to determine the influence of polymer additives on drag reduction. The difficulty in having control-oriented turbulence models is the complexity of the flow physics that arises from the interaction between the turbulent fluctuations and the mean flow. Despite this difficulty, recent advancements [89,141–143] in turbulence modeling showed that the equations linearized around turbulent mean velocity with the molecular viscosity augmented by the turbulent viscosity, qualitatively capture features of turbulent flows of Newtonian fluids. Here, for flows with polymers, we use the turbulent viscosity augmented linearization of the finitely extensible nonlinear elastic - Paterlin (FENE-P) model around a turbulent mean flow to determine the influence of polymer additives on turbulent drag. In addition, we imposed white-in-time stochastic forcing with selected second-order spatial statistics on the resulting linearized equations. Linear systems theory then allows us to determine the second-order covariance matrix of the velocity and polymer stress fluctuations by solving the corresponding Lyapunov equations. This valuable information enables us to determine the influence of flow fluctuations on the turbulent drag.

With our approach, we show that polymer additives is capable of reducing turbulent drag at the levels comparable to those observed in experiments and simulations. Furthermore, our new model can capture the essential drag-reducing trends produced by high-fidelity numerical simulations. Given a drag reduction level, our analysis is capable of producing a mean turbulent velocity that matches with that generated from direct numerical methods. In addition, we numerically show that the interactions between the fluctuating velocity gradient and the conformation tensors are the driving forces for drag reduction. Finally, our results demonstrate the potential of our model-based approach in capturing full-scale turbulent behaviors of polymer-induced turbulent channel flows.

This chapter is organized as follows. In Section 8.2, we formulate the problem and briefly discuss the governing equations and turbulence modeling. We then determine an approximation of the turbulent mean flow with polymers using an turbulent eddy-viscosity enhanced FENE-P model. We demonstrate the ability of this simple model in capturing positive turbulent drag reduction but not at the level comparable to experiments/simulations. In Section 8.3, we examine influence of fluctuations on the turbulent viscosity and drag using a stochastically forced and eddy-viscosity enhanced FENE-P model linearized around the aforementioned turbulent mean profile. We also present an efficient method for computing the second-order statistics of velocity and polymer stress fluctuations. In Section 8.4, we demonstrate that our model-based method is capable of predicting the essential drag-reducing trends. We conclude the paper with a brief summary of our developments and outlook for future research in Section 8.5.

8.2 Problem formulation

In this section, we present the governing equations for a pressure-driven channel flow of FENE-P fluids. We show how to obtain an approximation of the mean turbulent velocity in the presence of polymers using a standard model of the turbulent viscosity. We demonstrate that polymers are capable of reducing drag forces even in a simple scenario. We will utilize this mean turbulent velocity in our model-based framework presented in Section 8.3 to analyze the influence of fluctuations on the turbulent drag.

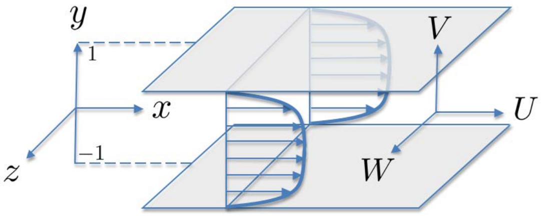

Figure 8.1: Channel flow geometry.

8.2.1 Governing equations

We study a pressure-driven turbulent channel flow of a viscoelastic fluid in a Cartesian coordinate system (x, y, z) where x is the streamwise, y the wall-normal, and z the spanwise direction; see figure 8.1 for geometry. The dimensionless equations for the conservation of momentum and mass are given by [16, 17]

$$\begin{aligned} \mathcal{U}_t &= -(\mathcal{U} \cdot \boldsymbol{\nabla})\mathcal{U} - \boldsymbol{\nabla}\mathcal{P} + \frac{\beta}{R_\tau}\Delta\mathcal{U} + \frac{(1-\beta)}{R_\tau}\boldsymbol{\nabla}\cdot\mathcal{T}, & \text{(8.1a)} \\ 0 &= \boldsymbol{\nabla}\cdot\mathcal{U}, & \text{(8.1b)} \end{aligned}$$

where $\mathcal{U}$ is the velocity vector, $\mathcal{P}$ is the pressure, $\mathcal{T}$ is the polymer stress tensor, $\boldsymbol{\nabla}$ is the gradient, and $\Delta = \boldsymbol{\nabla}\cdot\boldsymbol{\nabla}$ is the Laplacian. System (8.1) governs the behavior of dilute polymer solutions with fluid density ρ, and it has been obtained by scaling length with the channel half-height h, pressure with the wall-shear stress τ_w, velocity with the friction velocity $u_\tau = \sqrt{(\tau_w/\rho)}$, time with h/u_τ, and polymer stresses with $\eta_p u_\tau/h$ where η_p is the polymer viscosity. The two parameters appearing in (8.1) are the viscosity ratio, $\beta = \eta_s/\nu_0$, and the friction Reynolds number, $R_\tau = u_\tau h/\nu_0$. Here, η_s represents the solvent viscosity and $\nu_0 = (\eta_s + \eta_p)/\rho$ denotes the zero shear rate kinematic viscosity.

The momentum (8.1a) and continuity (8.1b) equations describe the motion of an incompressible viscoelastic fluid. For given $\mathcal{T}$, the pressure adjusts itself so that the velocity satisfies the continuity equation (8.1b). In our previous work [144], we used the Oldroyd-B model, which is based on a linear bead-spring dumbbell, to relate the polymeric stress tensor to the conformation tensor. Since the Oldroyd-B model does not account for the finite extensibility of the polymer chains, in this paper we examine the FENE-P model which utilizes a nonlinear relation between the polymeric stress tensor $\mathcal{T}$ and the conformation tensor $\mathcal{R}$ [16],

$$\mathcal{T} = \frac{(f\,\mathcal{R} - \mathbf{I})}{We}. \tag{8.2}$$

Here, $\mathbf{I}$ is the unit tensor, and the function f (that quantifies the influence of the nonlinear spring) is determined by the trace of the conformation tensor, $\mathrm{trace}\,(\mathcal{R})$, and the maximum extensibility of polymer chains, L,

$$f \;=\; \frac{L^2 \,-\, 3}{L^2 \,-\, \mathrm{trace}\,(\mathcal{R})}. \tag{8.3}$$

Note that $\mathcal{R}$ and L^2 are made dimensionless with respect to $k_\beta T/c$, where k_β, T, and c denote the Boltzmann constant, the absolute temperature, and the spring constant of the Hookean dumbbell, respectively. In the limiting case $L \to \infty$, we have $f \to 1$; consequently, the nonlinear spring becomes linear and the FENE-P model simplifies to the Oldroyd-B model. The parameter appearing in (8.2) is the Weissenberg number, $We \,=\, \lambda u_\tau/h$. While the Reynolds number quantifies the ratio of inertial to viscous forces, the Weissenberg number determines the ratio of the fluid relaxation time λ to the characteristic flow time h/u_τ. We note that, in turbulent flows, the friction Weissenberg number $We_\tau \,=\, \lambda u_\tau^2/\nu_0$ is typically used and the relationship between We and We_τ is given by [145]

$$We \;=\; We_\tau/R_\tau.$$

Finally, the dynamics of the conformation tensor $\mathcal{R}$ are governed by the following constitutive equation,

$$\mathcal{R}_t \;=\; \mathcal{R}\cdot\boldsymbol{\nabla}\mathcal{U} \,+\, (\mathcal{R}\cdot\boldsymbol{\nabla}\mathcal{U})^T \,-\, \mathcal{U}\cdot\boldsymbol{\nabla}\mathcal{R} \,-\, \mathcal{T} \,+\, \frac{D_0}{R_\tau}\,\Delta\mathcal{R}. \tag{8.4}$$

The last term in (8.4) represents an artificial stress diffusive term. The numerical diffusivity is denoted by $D_0 \,=\, \kappa/\nu_0$ where κ is the isotropic numerical diffusivity. The addition of this term helps alleviate numerical instabilities associated with the constitutive model. For small D_0, it has been shown that artificial stress diffusivity has weak influence on the flow dynamics [146]. In direct numerical simulations of turbulent channel flows, D_0 is typically chosen to have the smallest value that provides numerically stable computations.

8.2.2 Mean flow equations

Here, we present a method for computing an approximation of the mean turbulent velocity and polymer stresses. Even though this steady-state analysis shows that polymers reduce drag, it does not capture the essential drag-reducing trends observed in DNS. In Section 8.3, we show that analysis of the dynamics of flow fluctuations around this approximate mean flow improves predictive capability of our model-based approach.

We proceed by splitting the flow quantities into their mean and fluctuating components

$$\mathcal{U} \;=\; \mathbf{U} + \mathbf{u}, \quad \mathcal{R} \;=\; \mathbf{R} + \mathbf{r}, \quad \mathcal{P} \;=\; P + p, \tag{8.5}$$

where $\mathbf{U} = \overline{\mathcal{U}}$, $\overline{\mathbf{u}} = 0$, with the bar denoting averaging in time and horizontal directions. Substituting (8.5) into (8.1) and (8.4) and taking the average in time and horizontal directions yields the steady-state equations for $\mathbf{U}$ and $\mathbf{T}$ [147, 148]

$$\begin{aligned} 0 &= -(\mathbf{U}\cdot\boldsymbol{\nabla})\,\mathbf{U} - \nabla P + \frac{\beta}{R_\tau}\,\Delta\mathbf{U} + \frac{(1-\beta)}{R_\tau}\,\boldsymbol{\nabla}\cdot\mathbf{T} - \boldsymbol{\nabla}\cdot\left(\overline{\mathbf{u}\mathbf{u}^T}\right), & (8.6\text{a})\\ 0 &= \boldsymbol{\nabla}\cdot\mathbf{U}, & (8.6\text{b})\\ 0 &= \mathbf{R}\cdot\boldsymbol{\nabla}\mathbf{U} + (\boldsymbol{\nabla}\mathbf{U})^T\cdot\mathbf{R} - (\mathbf{U}\cdot\boldsymbol{\nabla})\,\mathbf{R} + \frac{D_0}{R_\tau}\,\Delta\mathbf{R} & \\ &\quad - \frac{\overline{f\,\mathcal{R}} + \mathbf{I}}{We} - \overline{(\mathbf{u}\cdot\boldsymbol{\nabla})\,\mathbf{r}} + \overline{\mathbf{r}\cdot\boldsymbol{\nabla}\mathbf{u} + (\boldsymbol{\nabla}\mathbf{u})^T\cdot\mathbf{r}}, & (8.6\text{c}) \end{aligned}$$

where

$$\mathbf{T} = \frac{\overline{f\,\mathcal{R}} + \mathbf{I}}{We}.$$

Since the second-order statistics of the fluctuations depend on higher-order moment, we face a closure problem in (8.6). The first unknown term is the Reynolds stress tensor, $\overline{\mathbf{u}\mathbf{u}^T}$, which quantifies the transport of momentum arising from turbulent fluctuations [147]. The last three terms in the mean constitutive equation (8.6c),

$$\Gamma = -\overline{(\mathbf{u}\cdot\boldsymbol{\nabla})\,\mathbf{r}}, \quad \Lambda = \overline{\mathbf{r}\cdot(\boldsymbol{\nabla}\mathbf{u}) + (\boldsymbol{\nabla}\mathbf{u})^T\cdot\mathbf{r}}, \quad \Omega = \left(\overline{f\,\mathcal{R}} + \mathbf{I}\right)/We, \qquad (8.7)$$

account for the contribution to the transport of the conformation tensor arising from the fluctuating advective terms ($\Gamma = -\overline{(\mathbf{u}\cdot\boldsymbol{\nabla})\,\mathbf{r}}$), the interactions between the fluctuating components of the conformation tensor and the velocity gradient tensor ($\Lambda = \overline{\mathbf{r}\cdot(\boldsymbol{\nabla}\mathbf{u}) + (\boldsymbol{\nabla}\mathbf{u})^T\cdot\mathbf{r}}$), and the conformation relaxation ($\Omega = \left(\overline{f\,\mathcal{R}} + \mathbf{I}\right)/We$). Several recent references [7, 149–151] have attempted to provide accurate and robust models for the second-order statistics of velocity and polymer stress fluctuations appearing in (8.6). We next describe a procedure that utilizes the turbulent eddy viscosity to obtain an approximation to the turbulent mean velocity in the presence of polymers.

8.2.3 Mean flow analysis

In this section, we discuss a procedure for determining an approximation of the mean turbulent profiles.

1. Model for the second-order statistics of velocity fluctuations

We first consider a model for the second-order statistics of velocity fluctuations. One of the most commonly used models for the second-order statistics of velocity fluctuations is the Boussinesq approximation [147]

$$\overline{\mathbf{u}\mathbf{u}^T} = \frac{2}{3}\,k\,\mathbf{I} - \frac{\beta\,\nu_T}{R_\tau}\left(\boldsymbol{\nabla}\mathbf{U} + (\boldsymbol{\nabla}\mathbf{U})^T\right), \qquad (8.8)$$

where k is the turbulent kinetic energy and ν_T is the turbulent eddy viscosity. In turbulent flows of viscoelastic fluids, ν_T is determined from statistics of flow fluctuations and it is not known *a priori*. Hence, in order to accurately capture influence of velocity fluctuations on the turbulent mean velocity and conformation tensor we need an accurate model of ν_T. For a turbulent channel flow of Newtonian fluids, [152] proposed the following model for the turbulent eddy viscosity

$$\nu_{T0}(y) \;=\; \frac{1}{2}\left(\left(1 \,+\, \left(\frac{c_2}{3}\, R_\tau\,(1-y^2)\,(1+2y^2)\,(1-e^{-(1-|y|)\,R_\tau/c_1})\right)^2\right)^{1/2} - 1\right), \tag{8.9}$$

where c_1 and c_2 are modeling parameters selected to minimize least squares deviation between the mean streamwise velocity obtained with turbulent viscosity (8.9), and the mean streamwise velocity obtained in experiments and simulations. For example, using DNS data of turbulent channel flow at $R_\tau = 186$ from [8] and [153], $c_1 = 0.61$ and $c_2 = 46.2$.

2. Second-order statistics of fluctuations in constitutive equations

We next consider the second-order statistics of fluctuations in the constitutive equations (8.7). First, the product $\overline{f\mathcal{R}}$ is approximated as the product of the mean values: $\bar{f}\mathbf{R}$, the leading term in the Taylor expansion. Here, $\bar{f}$ denotes the mean Peterlin function, i.e.,

$$\bar{f} \;=\; \frac{L^2 \,-\, 3}{L^2 \,-\, \mathrm{trace}(\mathbf{R})}.$$

The employment of this approximation has been verified by high-fidelity simulations [151] where a satisfactory agreement between $\overline{f\mathcal{R}}$ and $\bar{f}\mathbf{R}$ has been shown in turbulent channel flows of FENE-P fluids.

We note there are several approximations and models [7, 149–151] for the other two fluctuating terms, Γ and Λ, in the mean equations governing the conformation tensor. However, all of these models are based on data obtained through numerical simulations of polymer induced turbulent flows and are not easily reproduced. Hence, we have neglected these two terms in the mean flow analysis and consider their influence when we study the effects of fluctuations on the turbulent drag in Section 8.3.

Using the aforementioned approximations, for flow subject to a constant pressure gradient $P_x = -1$, we determine a mean turbulent profile,

$$\mathbf{U} \;=\; \begin{bmatrix} U(y) \\ 0 \\ 0 \end{bmatrix}, \quad \mathbf{R} \;=\; \begin{bmatrix} R_{11}(y) & R_{12}(y) & 0 \\ R_{21}(y) & R_{22}(y) & 0 \\ 0 & 0 & R_{33}(y) \end{bmatrix},$$

by solving the following set of equations:

$$0 \;=\; -\,P_x \,+\, \frac{\beta}{R_\tau}\big(\nu_{T0}'\,U' \,+\, (1+\nu_{T0})\,U''\big) \,+\, \frac{(1-\beta)}{R_\tau}\,T_{12}', \tag{8.10a}$$

$$0 \;=\; -\,\frac{1}{We}\,\bar{f}R_{12} \,+\, R_{22}\,U' \,+\, \frac{D_0}{R_\tau}R_{12}'', \tag{8.10b}$$

$$0 \;=\; -\,\frac{1}{We}\big(\bar{f}R_{22} \,-\, 1\big) \,+\, \frac{D_0}{R_\tau}R_{22}'', \tag{8.10c}$$

$$0 \;=\; -\,\frac{1}{We}\big(\bar{f}R_{33} \,-\, 1\big) \,+\, \frac{D_0}{R_\tau}R_{33}'', \tag{8.10d}$$

$$0 \;=\; -\,\frac{1}{We}\big(\bar{f}R_{11} \,-\, 1\big) \,+\, 2\,R_{12}\,U' \,+\, \frac{D_0}{R_\tau}R_{11}''. \tag{8.10e}$$

Here, prime denotes differentiation with respect to y and

$$T_{12} \;=\; \frac{\bar{f}R_{12}}{We}.$$

Homogeneous Dirichlet boundary conditions are imposed on U, and the boundary conditions for the components of the conformation tensor are obtained using the procedure described in [146]. In particular, this procedure solves for the solution of the mean equations without the additive diffusivity and uses the boundary values of the solution as the boundary conditions for the conformation tensor. Finally, we use Newton's method to determine the approximate turbulent mean velocity and conformation tensor. Furthermore, all computations are obtained using CHEBFUN computing environment [37] which is a MATLAB toolbox for solving boundary value problems. Grid-point convergence of our solution is guaranteed by CHEBFUN's automatic Chebyshev collocation method.

Figure 8.2 shows the turbulent mean velocity profiles for the flow with no polymers U_0 and for the flow with polymers U as a function of the distance from the wall,

$$y^+ \;=\; R_\tau\,(y+1)\,.$$

For Newtonian fluids, the turbulent mean velocity profile U_0 is obtained for flows with $R_\tau = 186$ and $\beta = 1$. As shown in figure 8.2(a), the linear relationship $U = y^+$ is satisfied in the viscous sublayer close to the wall ($y^+ < 2$). In the inertial sublayer far away from the wall ($y^+ > 50$), the Newtonian turbulent mean velocity is approximated by the logarithmic profile $U = 2.5\ln(y^+) + 6.5$. This indicates that the turbulent mean profile computed using turbulent viscosity (8.9) captures the essential trends in turbulent flows with no polymers.

For flows with polymers, we fix $R_\tau = 186$, $\beta = 0.9$, and $D_0 = 3.25$ to study the influence of L and We_τ on the turbulent mean velocity and consequently, drag reduction.

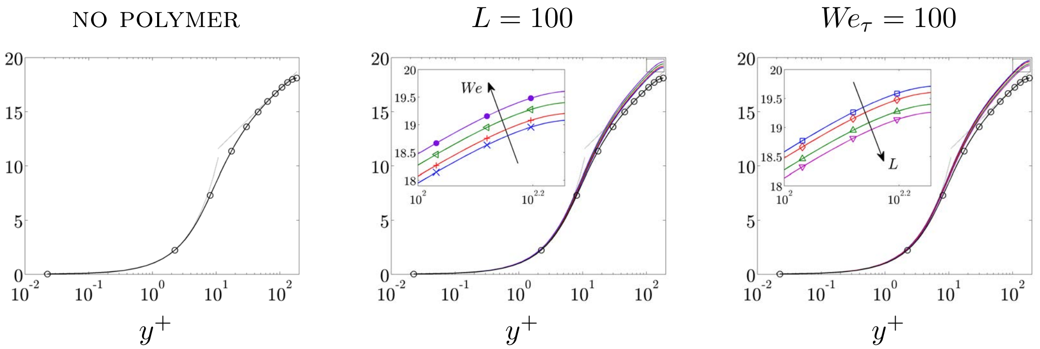

(a) (b) (c)

Figure 8.2: Mean velocity as a function of the distance from the wall in flows with (a) no polymers $U_0(y^+)$; and with polymers $U(y^+)$ for: (b) $L = 100$ and $We_\tau = 25$ ($\times$), $We_\tau = 50$ ($+$), $We_\tau = 100$ ($\triangleleft$), $We_\tau = 200$ ($\bullet$); and (c) $We = 100$ and $L = 25$ ($\square$), $L = 50$ ($\diamond$), $L = 100$ ($\triangle$), $L = 200$ ($\bigtriangledown$). For Newtonian fluids, the result is obtained for flows with $R_\tau = 186$ and $\beta = 1$. In addition, we also show the linear wall asymptote, $U = y^+$, and the logarithmic inertial sublayer asymptote, $U = 2.5\ln(y^+){+}5.5$. For flows with polymers, results are obtained for flows with $R_\tau = 186$, $\beta = 0.9$, and $D_0 = 3.25$ using the assumption that turbulent viscosity ν_{T0} captures the behavior of fluctuations.

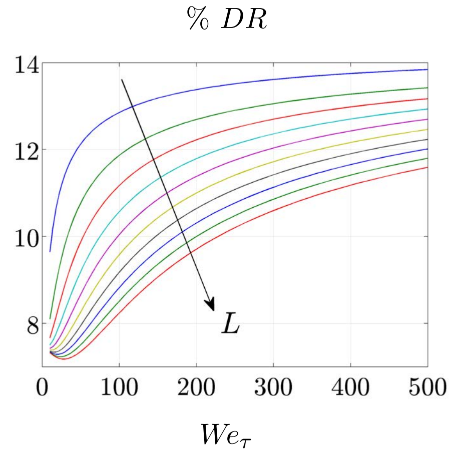

Figure 8.3: Percent drag reduction as a function of the friction Weissenberg number. Results are obtained using the turbulent mean velocity U for flows with $R_\tau = 186$, $\beta = 0.9$, $D_0 = 3.25$, and $L = [10, 1000]$ with the assumption that turbulent viscosity ν_{T0} captures the behavior of fluctuations.

For fixed $L = 100$, figure 8.2(b) demonstrates that the turbulent mean velocity U is increased in the inertial sublayer compared to U_0 and the amount of increase gets larger as We_τ increases. On the other hand, for fixed $We_\tau = 100$, the amount of increase of U in the inertial sublayer is decreased as L increases (cf. figure 8.2(c)). We next illustrate that the increase of U in the inertial sublayer directly relates to the increase in drag reduction.

In flows with polymers, [145] defined drag reduction as,

$$DR \;=\; 1 \;-\; \mu_w^{2(1-n)/n} \left(\frac{U_B}{U_{B,0}} \right)^{-2/n}, \tag{8.11}$$

where U_B and $U_{B,0}$ denote bulk velocities of flows with and without polymers,

$$U_B \;=\; \int_{-1}^{1} U(y)\,\mathrm{d}y.$$

Here, μ_w represents the effective wall viscosity and it is given by

$$\mu_w \;=\; \frac{\beta}{1 + (1-\beta)\,/\,(2R_\tau)}\,\Delta(\bar{\tau}_{xy})\,,$$

where $\Delta(\bar{\tau}_{xy})$ is the average wall shear stress at the two walls.

Figure 8.3 shows the drag reduction as a function of We_τ and L computed using the turbulent mean velocity U for flows with $R_\tau = 186$, $\beta = 0.9$, and $D_0 = 3.25$. Similar to the trend observed in figure 8.2, the amount of drag reduction increases with the increase in Weissenberg number (for fixed L) and decreases with the increase in L (for fixed We). Figure 8.3 illustrates that polymers are capable of reducing drag forces even in this simple scenario. However, we note that the decrease in drag reduction with L contradicts the DNS trends [24]. Furthermore, the amount of drag reduction at large values of L and We_τ is not correctly predicted by the above mean flow analysis. We next present a model-based framework that utilizes the mean turbulent velocity resulting from this analysis to study the influence of fluctuations on the turbulent drag.

8.3 Stochastically forced flow with polymers: fluctuation dynamics

In this section, we examine the dynamics of infinitesimal velocity and conformation tensor fluctuations $(\mathbf{u}, \mathbf{r})$ around the mean flow $(\mathbf{U}, \mathbf{R})$ described in Section 8.2.3. Our model-based approach builds on the method that [140] recently used to design drag-reducing transverse wall-oscillations. The linearization of the governing equations around the turbulent mean flow of Section 8.2.3 is given by

$$\begin{aligned}
\mathbf{u}_t \;&=\; -\left(\mathbf{U}\cdot\boldsymbol{\nabla}\right)\mathbf{u} \,-\, \left(\mathbf{u}\cdot\boldsymbol{\nabla}\right)\mathbf{U} \,-\, \nabla p \,+ \\
&\quad\; \frac{\beta}{R_\tau}\,\boldsymbol{\nabla}\cdot\big((1+\nu_{T0})\left(\boldsymbol{\nabla}\mathbf{u} \,+\, (\boldsymbol{\nabla}\mathbf{u})^T\right)\big) \,+\, \frac{1-\beta}{R_\tau}\,\boldsymbol{\nabla}\cdot\boldsymbol{\tau}, && \text{(8.12a)}\\
0 \;&=\; \boldsymbol{\nabla}\cdot\mathbf{u}, && \text{(8.12b)}\\
\mathbf{r}_t \;&=\; \mathbf{r}\cdot\boldsymbol{\nabla}\mathbf{U} \,+\, (\mathbf{r}\cdot\boldsymbol{\nabla}\mathbf{U})^T \,+\, \mathbf{R}\cdot\boldsymbol{\nabla}\mathbf{u} \,+\, (\mathbf{R}\cdot\boldsymbol{\nabla}\mathbf{u})^T \,- \\
&\quad\; \left(\mathbf{u}\cdot\boldsymbol{\nabla}\right)\mathbf{R} \,-\, \left(\mathbf{U}\cdot\boldsymbol{\nabla}\right)\mathbf{r} \,-\, \boldsymbol{\tau} \,+\, \frac{D_0}{R_\tau}\,\Delta\mathbf{r}, && \text{(8.12c)}\\
\boldsymbol{\tau} \;&=\; \frac{\bar{f}}{We}\left(\mathbf{r} \,+\, \frac{\bar{f}}{\bar{L}^2}\,\mathrm{trace}(\mathbf{r})\,\mathbf{R}\right). && \text{(8.12d)}
\end{aligned}$$

where $\bar{L}^2 = L^2 - 3$, and

$$\mathbf{u} \;=\; \begin{bmatrix} u \\ v \\ w \end{bmatrix}, \quad \mathbf{r} \;=\; \begin{bmatrix} r_{11} & r_{12} & r_{13} \\ r_{21} & r_{22} & r_{23} \\ r_{31} & r_{32} & r_{33} \end{bmatrix}.$$

The evolution form of (8.12) is obtained by eliminating the pressure from the equations, and by expressing the velocity fluctuations in terms of the wall-normal velocity v and vorticity $\eta = \partial_z u - \partial_x w$. Furthermore, by rearranging the components of $\mathbf{r}$ and by applying the Fourier transforms in the x and z-directions, we arrive at a set of partial differential equations in y and t parameterized by the vector of horizontal wave-numbers, $\boldsymbol{\kappa} = (k_x, k_z)$,

$$\begin{aligned}
\boldsymbol{\psi}_t\,(y,\boldsymbol{\kappa},t) \;&=\; \mathbf{A}(\boldsymbol{\kappa})\,\boldsymbol{\psi}\,(y,\boldsymbol{\kappa},t) \,+\, \mathbf{B}(\boldsymbol{\kappa})\,\mathbf{f}\,(y,\boldsymbol{\kappa},t)\,,\\
\boldsymbol{\phi}\,(y,\boldsymbol{\kappa},t) \;&=\; \mathbf{C}(\boldsymbol{\kappa})\,\boldsymbol{\psi}\,(y,\boldsymbol{\kappa},t)\,.
\end{aligned} \tag{8.13}$$

Here, $\boldsymbol{\psi} = \begin{bmatrix} \boldsymbol{\psi}_1^T & \boldsymbol{\psi}_2^T \end{bmatrix}^T$ is the state vector with

$$\boldsymbol{\psi}_1 \;=\; \begin{bmatrix} v & \eta \end{bmatrix}^T, \quad \boldsymbol{\psi}_2 \;=\; \begin{bmatrix} r_{22} & r_{23} & r_{33} & r_{13} & r_{12} & r_{11} \end{bmatrix}^T.$$

The output vector $\boldsymbol{\phi}$ contains fluctuations in the velocity and conformation tensor fields. The dynamical generator $\mathbf{A}$ in (8.13) can be partitioned conformably with the partition of ψ,

$$\mathbf{A} \;=\; \begin{bmatrix} \mathbf{A}_{11} & \mathbf{A}_{12} \\ \mathbf{A}_{21} & \mathbf{A}_{22} \end{bmatrix}, \tag{8.14}$$

where the operator blocks in (8.14) are given in Appendix 8.6.

In Newtonian fluids, there is only one block, $\mathbf{A}_{11}$, and in the limit $\beta \to 1$, $\mathbf{A}_{11}$

in (8.14) simplifies to the generator in the modified Orr–Sommerfeld and Squire equations of Newtonian fluids where the kinematic viscosity is augmented with turbulent eddy viscosity [140]. The operator $\mathbf{A}_{12}$ describes how the components of the conformation tensor enter into the equations for the wall-normal velocity and vorticity. On the other hand, the operators $\mathbf{A}_{21}$ and $\mathbf{A}_{22}$ appear in the constitutive equation, where $\mathbf{A}_{21}$ acts on the wall-normal velocity/vorticity and $\mathbf{A}_{22}$ acts on the components of the conformation tensor. Furthermore, $\mathbf{B}$ is an 8×2 matrix of operators through which forcing enters the evolution model. Since we only introduce forcing into the momentum equation, $\mathbf{B} = \left[\begin{array}{cc} \mathbf{I}_{2\times 2}^T & \mathbf{O}_{6\times 2}^T \end{array}\right]^T$, where $\mathbf{I}_{2\times 2}$ is the 2×2 block-identity-operator and $\mathbf{O}_{6\times 2}$ is a 6×2 null matrix. We note that the output operator in (8.13) is given by $\mathbf{C} = \left[\begin{array}{cc} \mathbf{C}_v^T & \mathbf{C}_r^T \end{array}\right]^T$ where $\mathbf{C}_v$ captures a kinematic relationship between the wall-normal velocity/vorticity vector $\boldsymbol{\psi}_1$ and velocity fluctuation vector $\mathbf{u}$, and $\mathbf{C}_r$ relates the components of the conformation tensor with the state vector $\boldsymbol{\psi}_2$. The definitions of these two operators are also provided in Appendix 8.6.

System (8.13) is forced with a zero-mean temporally white stochastic process $\mathbf{f}$,

$$\mathcal{E}\left(\mathbf{f}\left(\cdot,\boldsymbol{\kappa},t_1\right)\otimes\mathbf{f}\left(\cdot,\boldsymbol{\kappa},t_2\right)\right) \;=\; \mathbf{M}(\boldsymbol{\kappa})\,\delta(t_1\,-\,t_2), \tag{8.15}$$

where δ is the Dirac delta function, $\mathbf{f} \otimes \mathbf{f}$ is the tensor product of $\mathbf{f}$ with itself, and $\mathbf{M}(\boldsymbol{\kappa})$ is the spatial spectral-density of the forcing. Jovanović and Georgiou [154] showed that the steady-state statistics of velocity fluctuations in homogeneous isotropic turbulence can be reproduced by driving linearized NS equations with white-in-time forcing and properly selected spatial spectral-density. Inspired by this observation, [140] determined $\mathbf{M}(\boldsymbol{\kappa})$ to match the DNS-generated energy spectrum in Newtonian turbulent channel flows. In what follows, we adopt the model for spatial spectral-density of forcing developed by [140].

For the linearized system (8.13), the steady-state autocorrelation tensor of flow fluctuations is obtained by solving the Lyapunov equation [77, 155]

$$\mathbf{A}(\boldsymbol{\kappa})\,\bar{X}(\boldsymbol{\kappa}) \,+\, \bar{X}(\boldsymbol{\kappa})\,\mathbf{A}^*(\boldsymbol{\kappa}) \;=\; -\mathbf{B}(\boldsymbol{\kappa})\,\mathbf{M}(\boldsymbol{\kappa})\,\mathbf{B}^*(\boldsymbol{\kappa}), \tag{8.16}$$

where the asterisk denotes the adjoint of the corresponding operator. The operator $\bar{X}$ represents the autocorrelation operator of $\boldsymbol{\psi}$ and it contains all second-order statistics of velocity fluctuations and the fluctuating components of the conformation tensor. Furthermore, by decomposing the operator $\bar{X}$ into the block form,

$$\bar{X} \;=\; \left[\begin{array}{cc} \bar{X}_{11} & \bar{X}_{12} \\ \bar{X}_{12}^* & \bar{X}_{22} \end{array}\right],$$

we can isolate the components of the second-order statistics of vectors $\boldsymbol{\psi}_1$ and $\boldsymbol{\psi}_2$. The $(1,1)$-block operator $\bar{X}_{11}$ contains information about the second-order statistics of velocity fluctuations, and the $(2,2)$-block operator $\bar{X}_{22}$ contains information about the statistics of fluctuating components of the conformation tensor. The off-diagonal block $\bar{X}_{12}$ is the cross-correlation operator between the velocity fluctuations and fluctuating conformation tensor.

Our model-based approach to the analysis of drag-reduction by polymers consists of the following three steps.

(i) An approximation of the turbulent mean velocity with polymers is obtained from the mean flow analysis presented in Section 8.2.3. Here, we have used the eddy viscosity of a turbulent flow of Newtonian fluids and we have neglected the second-order statistics of fluctuations in the mean constitutive equations.

(ii) Second-order statistics of velocity fluctuations and fluctuating components of the conformation tensor $\left(\overline{\mathbf{u}\mathbf{u}^T}, \Gamma, \Lambda\right)$ are obtained from the stochastically forced equations (8.13) linearized around the turbulent mean profiles determined in (i).

(iii) The second-order statistics $\left(\overline{\mathbf{u}\mathbf{u}^T}, \Gamma, \Lambda\right)$ are used in the mean flow equations (8.23) to determine the effect of fluctuations on the mean velocity, mean component of the conformation tensor, and thereby skin-friction drag. Appendix 8.7 contains the mean flow equations used to determine the modified turbulent mean profiles.

8.4 Results and discussion

In this section, we examine the effect of flow fluctuations on drag reduction, turbulent mean velocity, eddy viscosity, and turbulent kinetic energy. We also compare our predictions with DNS results of [7] and discuss the similarities and disagreement between the two. Finally, we study the mechanisms leading to polymer drag reduction by examining the equation for the turbulent kinetic energy.

In order to examine the influence of the Weissenberg number (We_τ) and the finite extensibility parameter (L) on the turbulent mean velocity and skin-friction drag, we confine our attention to the flows with $R_\tau = 186$, $\beta = 0.9$, and $D_0 = 3.25$. For these parameters, the second-order statistics of the turbulent flow of Newtonian fluids were obtained using DNS [8, 153]. As highlighted in Section 8.3, these statistics provide the basis for modeling statistics of forcing to the momentum equation that reproduce the energy spectrum in Newtonian turbulent channel flows.

The finite-dimensional approximations of the underlying operators are obtained using MATLAB Differentiation Matrix Suite [83], which utilizes pseudospectral methods to approximate differential operators. After discretization in the wall-normal direction, each operator in (8.16) becomes an $N \times N$ matrix, where N denotes the number of Chebyshev collocation points in y. All computations are performed in MATLAB and grid-point convergence is confirmed by running additional computations with larger number of grid points in y. The results presented here are computed using $N = 200$.

8.4.1 Drag reduction by polymers

In this section, we analyze the influence of fluctuations on the turbulent drag. This is achieved by obtaining the second-order statistics of the fluctuating velocity and conformation tensors from the covariance operator $\bar{X}$ (8.16). We then utilize the second-order statistics ($\overline{uv}_p$, Γ_{12}, Λ_{12}) as corrections to the mean flow equations (8.23) and determine the turbulent mean profiles. Note that $\overline{uv}_p$ represents the contribution to the Reynolds shear stress from polymers only and it is given by

$$\overline{uv}_p \;=\; \overline{uv}_{\text{total}} \;-\; \overline{uv}_{\text{Newton}}.$$

Here the total and Newtonian Reynolds shear stresses, $\overline{uv}_{\text{total}}$ and $\overline{uv}_{\text{Newton}}$, are determined from the covariance operators $\bar{X}$ (8.16) with $\beta = 0.9$ and $\beta = 1.0$, respectively. Finally, turbulent drag is computed from the turbulent mean velocity using (8.11).

The percent drag reduction as a function of the friction Weissenberg number is shown in figure 8.4(a). Figure 8.4(a) shows that the amount of drag reduction achievable by polymer increases as L increase. In addition, for a given L, the amount of drag reduction initially increases with the Weissenberg number but slightly decreases and saturates beyond a certain value. Our results suggest that the amount of drag reduction achievable by polymer is bounded by the Weissenberg number which directly relates to the amount of polymer concentration. This boundedness on the drag reduction by the polymer concentrations has been long observed to be the maximum drag reduction (MDR) or Virk asymptote [156]. Furthermore, we note that our results presented here is not observed in the model for Oldroyd-B fluids. For Oldroyd-B fluids, we observed no saturation in the amount of drag reduction induced by polymers as We_τ increases [144]. We believe that this is due to the nature of the Oldroyd-B model where polymer molecules are allowed them to stretch indefinitely.

We note that although our model-based analysis is capable of capturing the MDR characteristic of polymer turbulent flows, our analysis is not capable of correctly producing the amount of polymer drag reduction by polymer. Figure 8.4(a) shows a maximum drag reduction of approximately 33% versus 80% shown by direct numerical simulations of fully turbulent channel flows [7]. This discrepancy is possibly due to the simplistic selection of the spatial spectrum of the stochastic forcing in the evolution model. Further investigation into the selection of the spatial spectrum of the stochastic forcing is needed to fully understand its influence on turbulent drag reduction. Analysis of these factors is dedicated to future studies.

On the other hand, figure 8.4(b) shows the normalized drag reduction conducted by our analysis and the normalized polymer drag reduction data from direct numerical simulations of fully developed turbulent channel flow [7]. Results are normalized by their respective maximum achievable drag reduction. As evident of Figure 8.4(b), our model-based analysis is capable of capturing the essential trend of polymer drag reduction produced from DNS. This encouraging result suggests that our model-based method

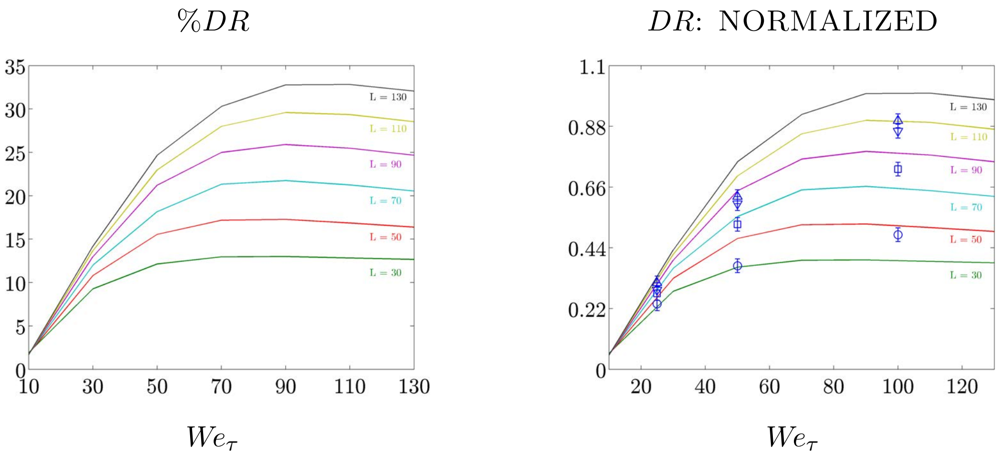

(a)

(b)

Figure 8.4: (a) Percent drag reduction as a function of the friction Weissenberg number. Results are obtained using the turbulent mean velocity U for flows with $R_\tau = 186$, $\beta = 0.9$, $D_0 = 3.75$, and $L = [30, 130]$ with second-order flow statistics $(\overline{uv}, \Gamma_{12}, \Lambda_{12})$ correction to the mean flow equations. (b) Drag reduction normalized by $\max\left(DR\left(We_\tau = 130, L\right)\right) = 0.33$. Symbols represent the normalized polymer drag reduction data from direct numerical simulations [7] of fully developed turbulent flow with $R_\tau = 125$, $\beta = 0.9$, $D_0 = 3.75$, $L = 30\,(\circ)$, $L = 60\,(\square)$, $L = 85\,(\bigtriangledown)$, $L = 120\,(\bigtriangleup)$.

can serve as a valuable tool for predicting the amount of drag reduction achievable by polymers at arbitrary set of flow parameters: We_τ, L, R_τ, and β. Our method provides an alternate way of analyzing polymer drag reduction without running time-consuming high-fidelity simulations.

8.4.2 Turbulent mean velocity and fluctuations' statistics

Here, we present the mean turbulent velocity, turbulent viscosity, and Reynolds stresses obtained using our model-based analysis. Figure 8.5 shows the turbulent mean flow velocity $U(y^+)$ as a function of the distance from the channel wall for various levels of drag reduction. We see that the turbulent mean velocity increases as the level of drag reduction increases. In addition, the log region of the velocity profiles (in the center of the channel) is shifted upward while the slope of the log law remains similar to the flow without polymers. We note that as drag reduction approaches the maximum drag reduction level, the slope of the log law increases from 2.5 to 12. The turbulent mean velocities presented in figure 8.5 are in agreement with the results from DNS of fully-developed turbulent channel flows of polymers [7].

Figure 8.6(a) shows the mean Reynolds shear stress as a function of the normalized

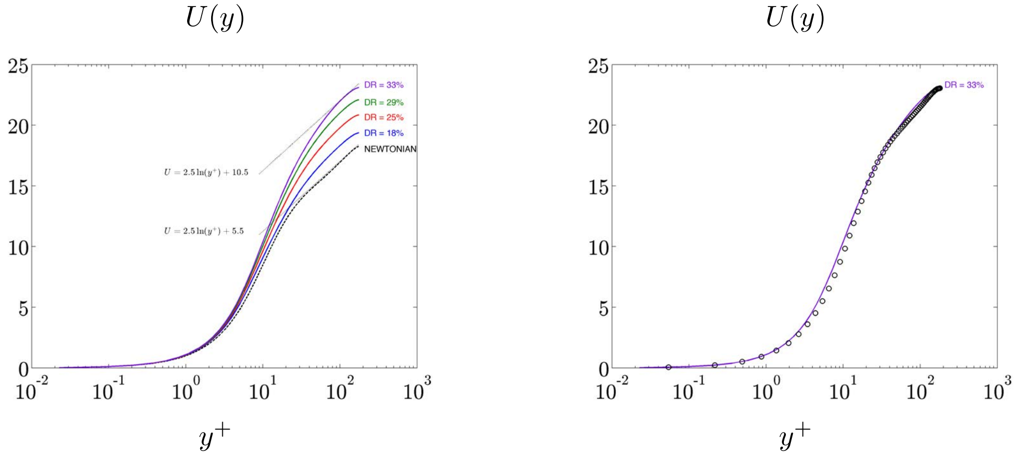

(a) (b)

Figure 8.5: Turbulent mean velocity obtained using method presented in Section 8.3 for flows with $R_\tau = 186$, $\beta = 0.9$, and $D_0 = 3.75$. Result for flow without polymers is represented by the dashed line. The symbol ($\circ$) represents data obtained using DNS for flows with $DR = 33\%$.

wall distance for the flow with $R_\tau = 186$, $\beta = 0.9$, $D_0 = 3.75$, and with $DR = 33\%$. Compared to the flow without polymers, the Reynolds shear stress decreases as DR increases. The corresponding plot for the root-mean-squared (RMS) velocity fluctuations is shown in figure 8.6(b). It is evident that as DR increases the streamwise RMS velocity fluctuations, u_{rms} increases while both the wall-normal and spanwise RMS velocity fluctuations, v_{rms} and w_{rms}, decrease compared to the flow without polymers, respectively. Furthermore, the corresponding plot for the turbulent viscosity is shown in figure 8.6(c). We see that the turbulent viscosity significantly decreases in the facility of channel's center as DR increases. Finally, we have also shown in figure 8.6(a) the second-order statistics obtained using high-fidelity simulations of polymer-induced turbulent channel flow with 33% drag reduction. As evident of figure 8.6(a), we can see that our model-based method is not capable of reproducing accurate turbulent statistics of velocity fluctuations. This demonstrates the limitation of the choice of noise modeling we chose for our body forcing. However, the second-order statistics of fluctuations can be improved with a better choice selection of the spectral density of the forcing [157]. We note that this demonstrates the flexibility of our model-based approach and greater understanding of the role of the spectral density of the forcing in polymer-induced drag reduction will be dedicated to future research.

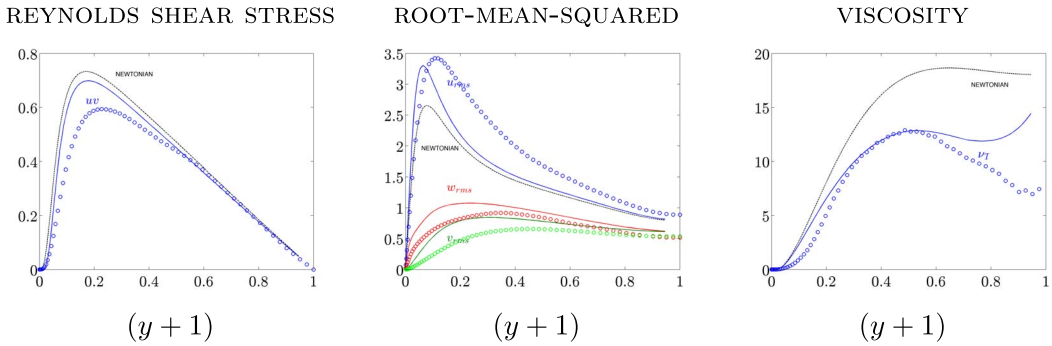

(a) (b) (c)

Figure 8.6: Turbulent mean viscosity, Reynolds shear stress, and root-mean-squared velocity fluctuations obtained using method presented in Section 8.3 for flows with $R_\tau = 186$, $\beta = 0.9$, $D_0 = 3.75$, and $DR = 33\%$. Results for the flow without polymers are represented by dashed lines. The symbol ($\circ$) represents data obtained from DNS for flows with 33% drag reduction.

8.4.3 Contribution of fluctuations' statistics to mean polymer stresses, turbulent velocity, and drag

We next examine the influence of second-order statistics on the mean polymer stresses and mean turbulent velocity. This is done by analyzing the contributions of the fluctuations' statistics to the mean equations (8.23). Careful examination of the mean equations (8.23) reveals that the polymer shear stress T_{12} and Reynolds shear stress $\overline{uv}$ drive the mean velocity equation and hence, directly influence drag reduction. We first examine the influence of polymers' finite extensibility L on T_{12} and $\overline{uv}$ for a fixed $We_\tau = 110$. Figure 8.7 shows the variation of the Reynolds shear stress ($\overline{uv}$) and polymer shear stress (T_{12}) as a function of the distance from the wall for $R_\tau = 186$, $\beta = 0.9$, $D_0 = 3.75$, $We_\tau = 110$, and $L = \{30, 70, 110, 130\}$. We can see that as L increases the Reynolds shear stress $\overline{uv}$ monotonically decreases while the polymer shear stress T_{12} monotonically increases. For fixed We_τ, this demonstrates that as finite extensibility of the polymer molecules increases, turbulent drag is reduced on twofolds. First, decrease in Reynolds shear stress indicates that bulk increases in the mean turbulent velocity which directly relates to decrease in drag. This is evident in the mean equation for the streamwise velocity (8.23a) where the sign multiplying Reynolds stress is negative. Second, in a similar argument, increase in the polymer shear stress indicates that drag is decreased. We note that the trend captured by our analysis agrees with data collected using high-fidelity numerical simulations [7].

Figure 8.8 shows the variation of Λ_{12}, Γ_{12}, and T_{12} as a function of the distance from the wall for $We_\tau = 110$ and $L = \{30, 70, 110, 130\}$. We see that as L increases all

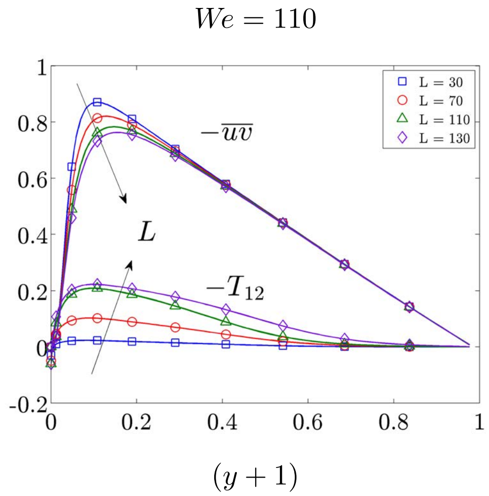

Figure 8.7: Variation of Reynolds shear stress ($\overline{uv}$) and polymer shear stress (T_{12}) as a function of the distance from the wall for $R_\tau = 186$, $\beta = 0.9$, $D_0 = 3.75$, $We_\tau = 110$, and $L = \{30, 70, 110, 130\}$.

three terms also monotonically increase. We can see that Λ_{12} contributes significantly more to the polymer shear stress T_{12} compared to Γ_{12}. This shows that the interactions between the fluctuating velocity gradient and the conformation tensors are the driving forces for drag reduction. We note that our observations depicted in figure 8.8 have also been seen in high-fidelity numerical simulations [7].

We next examine the influence of Weissenberg number We_τ on T_{12} and $\overline{uv}$. Figure 8.9 shows the variation of the Reynolds shear stress ($\overline{uv}$) and polymer shear stress (T_{12}) as a function of the distance from the wall for $L = 110$ and $We_\tau = \{30, 70, 110, 130\}$. Similarly, figure 8.9(a) shows that the Reynolds shear stress also decreases monotonically as We_τ increases. On the other hand, polymer shear stress T_{12} does not increase monotonically with the increase in We_τ, as evident of figure 8.9(b). Instead, T_{12} initially increases along the wall before decaying slightly as We_τ increases. However, away from the wall towards the channel's center, T_{12} increases as a function of We_τ. Furthermore, we observe that the total area under T_{12} curve in the wall-normal direction increases as We_τ increases and saturates when We_τ is larger than the finite extensibility of the polymer molecules. Our results demonstrate the role of the polymers' extensibility as the limiting factor in the the growth of each polymer molecule. We note that in Oldroyd-B fluids, the energy of the polymer stresses grow without bound as We_τ gets infinitely large [144].

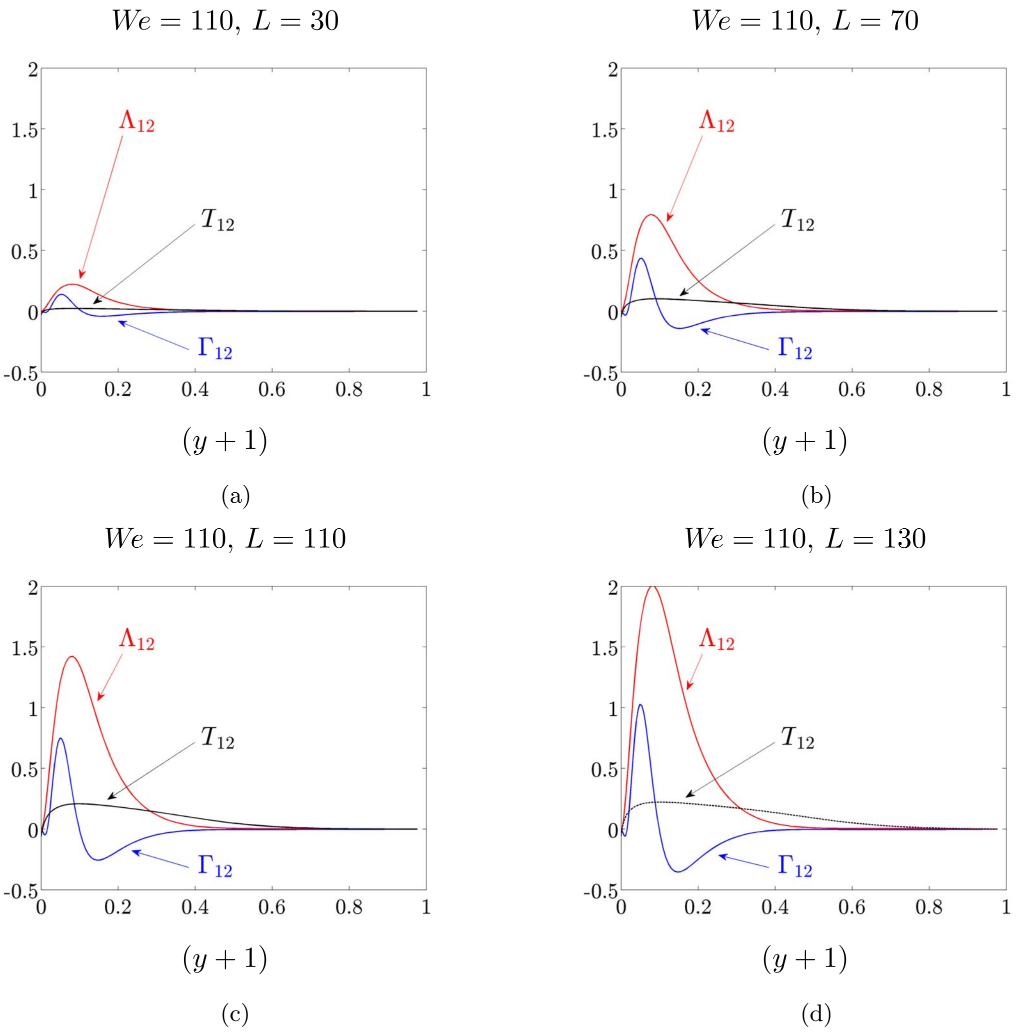

(a) (b) (c) (d)

Figure 8.8: Variation of Λ_{12}, Γ_{12}, and T_{12} as a function of the distance from the wall for $R_\tau = 186$, $\beta = 0.9$, $D_0 = 3.75$, $We_\tau = 110$, (a) $L = 30$, (a) $L = 70$, (a) $L = 110$, and (a) $L = 130$.

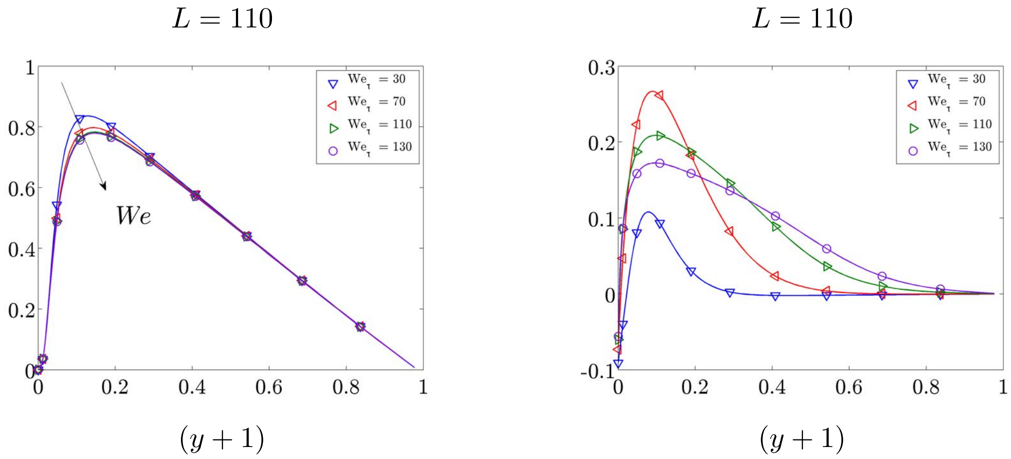

(a) (b)

Figure 8.9: Variation of (a) Reynolds shear stress ($\overline{uv}$) and (b) polymer shear stress (T_{12}) as a function of the distance from the wall for $R_\tau = 186$, $\beta = 0.9$, $D_0 = 3.75$, $L = 110$, and $We_\tau = \{30, 70, 110, 130\}$.

8.4.4 Energy amplification of velocity and polymer stress fluctuations

Given the zero-mean white stochastic forcing (in t) $\mathbf{f}(\boldsymbol{\kappa}, y, t)$, the ensemble average kinetic energy density of the statistical steady-state is determined by

$$E_v(\boldsymbol{\kappa}) \;=\; \lim_{t \to \infty} \langle \mathbf{u}(\boldsymbol{\kappa}, \cdot, t), \mathbf{u}(\boldsymbol{\kappa}, \cdot, t) \rangle, \tag{8.17}$$

where $\langle \cdot, \cdot \rangle$ denotes the $L_2[-1, 1]$ inner product and averaging in time, i.e.,

$$\begin{aligned} \langle \mathbf{u}, \mathbf{u} \rangle \;&=\; \mathcal{E}\left\{ \int_{-1}^{1} \mathbf{u}^*(\boldsymbol{\kappa}, y, t)\, \mathbf{u}(\boldsymbol{\kappa}, y, t)\, \mathrm{d}y \right\}, \\ \mathcal{E}\{u(\cdot, t)\} \;&=\; \lim_{T \to \infty} \frac{1}{T} \int_0^T u(\cdot, t + \xi)\, \mathrm{d}\xi. \end{aligned} \tag{8.18}$$

We note that $E_v(\boldsymbol{\kappa})$ determines the asymptotic level of variance maintained by the stochastic forcing in (8.13). In high-fidelity numerical simulations, this quantity is computed by running the simulations of the governing equations until statistical steady-state is reached. On the other hand, for the linear system (8.13), this quantity can be determined by using the autocorrelation operator $\bar{X}$ as

$$E_v(\boldsymbol{\kappa}) \;=\; \operatorname{trace}\left(\bar{X}_{11}(\boldsymbol{\kappa})\, \mathbf{C}_v^*(\boldsymbol{\kappa})\, \mathbf{C}_v(\boldsymbol{\kappa}) \right), \tag{8.19}$$

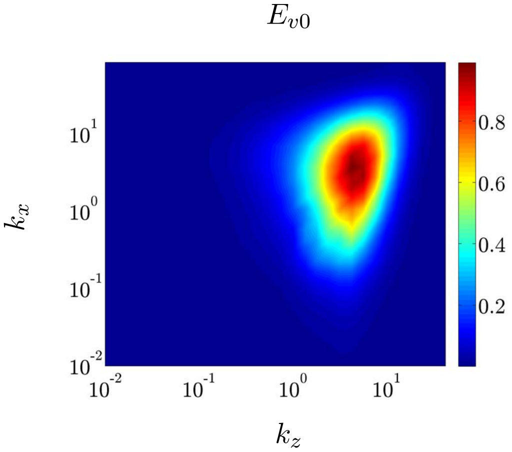

Figure 8.10: Premultiplied DNS-based energy spectrum of the turbulent flow of Newtonian fluids, $k_x k_z E_{v0}$, at $R_\tau = 186$ [8].

where $\bar{X}_{11}$ is the $(1,1)$-block of $\bar{X}$. Furthermore, the normalized ensemble average kinetic energy density is given by

$$\bar{E}_v(\boldsymbol{\kappa}) \;=\; \frac{E_v(\boldsymbol{\kappa})}{E_{v0}(\boldsymbol{\kappa})} \;=\; 1 \,+\, \bar{E}_{vp}(\boldsymbol{\kappa}), \tag{8.20}$$

where E_{v0} represents the two-dimensional energy spectrum of the turbulent channel flow of Newtonian fluids and $\bar{E}_{vp}$ denotes the contribution of polymers to the total kinetic energy density. Similarly, the normalized ensemble average energy density of the fluctuating conformation tensor is given by

$$\bar{E}_c(\boldsymbol{\kappa}) \;=\; \frac{E_c(\boldsymbol{\kappa})}{E_{v0}(\boldsymbol{\kappa})} \;=\; \frac{E_{c0}(\boldsymbol{\kappa})}{E_{v0}(\boldsymbol{\kappa})} + \frac{E_{cp}(\boldsymbol{\kappa})}{E_{v0}(\boldsymbol{\kappa})} \;=\; \bar{E}_{c0}(\boldsymbol{\kappa}) \,+\, \bar{E}_{cp}(\boldsymbol{\kappa}), \tag{8.21}$$

where E_{c0} and E_{cp} represent the contribution to the total energy density of the six components of the fluctuating conformation tensor from Newtonian fluids and polymers, and E_c is given by

$$E_c(\boldsymbol{\kappa}) \;=\; \mathrm{trace}\left(\bar{X}_{22}(\boldsymbol{\kappa})\,\mathbf{C}_c^*(\boldsymbol{\kappa})\,\mathbf{C}_c(\boldsymbol{\kappa})\right). \tag{8.22}$$

Figure 8.10 shows the premultiplied DNS-based energy spectrum of the turbulent flow of Newtonian fluids at $R_\tau = 186$ [8]. The energy spectrum is premultiplied by the spatial wavenumbers such that the area under the log-log plot is equal to the total energy of the velocity fluctuations. We see that the most energetic modes of the turbulent flow of Newtonian fluids take place at $k_x \approx 2.5$ and $k_z \approx 6.5$. Figure 8.11 shows the contribution to the normalized energy spectrum induced by polymers as a function of

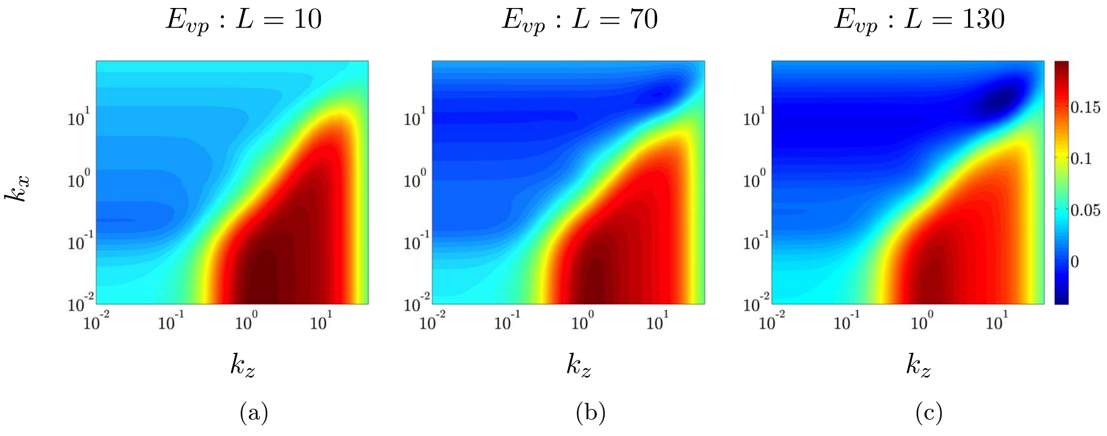

Figure 8.11: Contribution to the normalized energy spectrum of velocity fluctuations induced by polymers, $\bar{E}_{vp}(\boldsymbol{\kappa})$, for $We_\tau = 130$, $R_\tau = 186$, $\beta = 0.9$, $D_0 = 3.25$: (a) $L = 10$; (b) $L = 70$; and (c) $L = 130$. All figures are shown in log-log-log scale.

the spatial wavenumbers, $\bar{E}_{vp}(\boldsymbol{\kappa})$, for the flows with $We_\tau = 186$ and $L = \{10, 70, 130\}$. We can see that the energy of velocity fluctuations is amplified by polymer in all three flows and the area that is most amplified takes place at $k_x \approx 10^{-2}$ and $k_z \approx 2$. This most amplified area is the largest in the flow with $L = 10$ and gradually decreases in size and magnitude as L increases. On the other hand, the least amplified region of the flow with $L = 10$ gradually decreases in magnitude as L increases. Furthermore, this region becomes negative in magnitude which indicates that polymer is capable of reducing the kinetic energy of velocity fluctuations for flows with large enough We_τ and L. The region where polymer achieves the greatest reduction in kinetic energy takes place at $k_x \approx 10$ and $k_z \approx 10$. However, the total energy of the velocity fluctuations is still amplified by polymers. We note that the spatial distribution of the kinetic energy density is similar for other value of the Weissenberg number and, that the essential trends are captured in Figure 8.11.

Figure 8.12 shows the contribution to the normalized energy spectrum of the fluctuating conformation tensor from Newtonian fluids' dynamics for the flow with $We_\tau = 186$, $R_\tau = 186$, $\beta = 0.9$, $D_0 = 3.25$, and for $L = \{10, 70, 130\}$. From Newtonian fluids' dynamics, the energy density of the fluctuating conformation tensor is concentrated in the region with small spanwise wavenumbers and with $k_x \approx \mathcal{O}(10)$. As the polymer extensibility increases, this highly energized region is amplified further. On the other hand, the contribution to the normalized energy spectrum induced by polymers is shown in figure 8.13. For $L = 10$, we see that polymers' dynamics further amplify the energy of the polymer stress fluctuations for all pairs of streamwise and spanwise wavenumbers. However, using a sign-preserving logarithmic scale for $L = 70$ and $L = 130$,

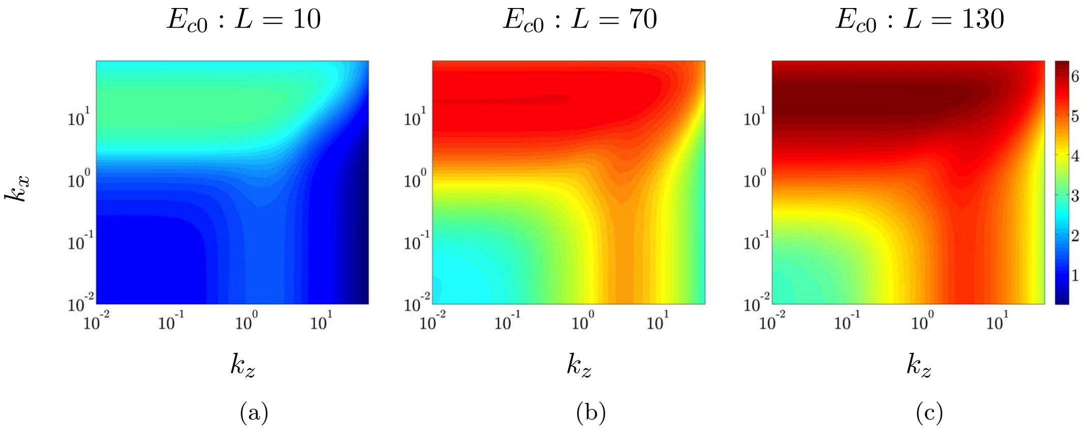

(a) (b) (c)

Figure 8.12: Contribution to the normalized energy spectrum of the fluctuating conformation tensor from Newtonian fluids' dynamics, $\bar{E}_{c0}(\boldsymbol{\kappa})$, for $We_\tau = 130$, $R_\tau = 186$, $\beta = 0.9$, $D_0 = 3.25$: (a) $L = 10$; (b) $L = 70$; and (c) $L = 130$. All figures are shown in log-log-log scale.

figures 8.13(b) and 8.13(c) show that the energy of the fluctuating conformation tensor is decreased in the region with small spanwise wavenumbers and with $k_x \approx \mathcal{O}(10)$ and is increased in the region with small streamwise wavenumbers and with $k_z \approx \mathcal{O}(1)$.

8.5 Concluding remarks

In this paper, we have introduced a model-based approach for studying polymer induced drag reduction. Our unique simulation-free method is different from current approaches where turbulence modeling is embedded in numerical simulations to study drag reduction induced by polymers. The key ingredient that enabled us to accomplished this is combining techniques from both turbulence modeling and linear systems theory. In particular, we have used the turbulent viscosity hypothesis with FENE-P constitutive equations to determine the influence of flow fluctuations on the mean velocity and polymer stresses, and consequently, drag reduction.

Our simulation-free method for analyzing polymer induced drag reduction consists of three main steps. In the first step, we augment the molecular viscosity with turbulent viscosity of turbulent flow of Newtonian fluids. We then determine the turbulent mean flow with polymers from the resulting model. In the second step, we study the dynamics of turbulent fluctuations around the aforementioned mean flow to determine the turbulent flow statistics. This crucial step is captured by considering the linearized equations in the presence of white-in-time stochastic forcing whose spatial spectrum is selected to be proportional to the turbulent kinetic energy of Newtonian fluids. Furthermore, the spatial spectral density tensors of flow fluctuations obtained from the solution of

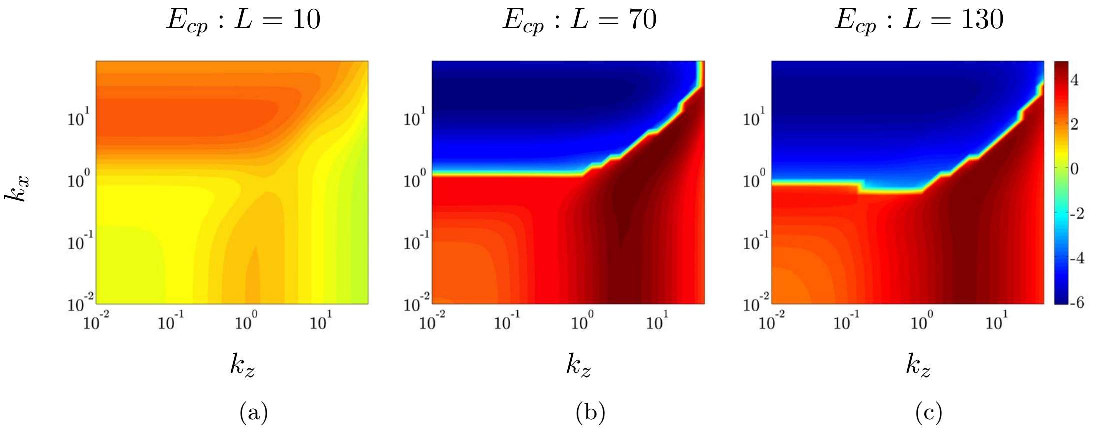

(a) (b) (c)

Figure 8.13: Contribution to the normalized energy spectrum of the fluctuating conformation tensor induced by polymers, $\bar{E}_{cp}(\boldsymbol{\kappa})$, for $We_\tau = 130$, $R_\tau = 186$, $\beta = 0.9$, $D_0 = 3.25$: (a) $L = 10$; (b) $L = 70$; and (c) $L = 130$. All figures are shown in sign preserving log-log-log scale.

the corresponding Lyapunov equations determine the effect of polymers on the dominant flow structures. Finally, in the third step, we use the turbulent flow statistics to determine the modified turbulent mean flow and analyze the influence of turbulent fluctuations on drag.

We have shown that our model-based analysis reliably predicts the drag-reducing trends induced by polymers. We demonstrated that drag reduction induced by polymer increases as both the finite extensibility of the polymer chains and the Weissenberg number increase. Our analysis indicates that drag reduction may be saturated at a fixed finite extensibility and as Weissenberg number increases infinitely large (and vice versa). Although our model does not reveal the underlying mechanisms responsible for this saturated level of drag reduction at large Weissenberg number, a more in-depth analysis similar to the approach developed by [158] may shed addition light into the maximum drag reduction by polymers.

Furthermore, we have demonstrated that our model-based approach is capable of reliably producing the correct mean turbulent velocity for a fixed drag reduction level. However, our analysis falls short in producing second-order statistics of velocity fluctuations of DNS. Although our model-based method is not capable of capturing all aspects of turbulent flow physics by polymers, this simple turbulence modeling (that only relies on turbulent viscosity hypothesis), in conjunction with eddy-viscosity-enhanced linearization of FENE-P model, has significant predictive capability of capturing full-scale phenomena. We note that the gap between theoretical predictions and experiments/simulations can be reduced by developing more sophisticated turbulence model.

In particular, the predictive power of the proposed approach can be enhanced by optimization of the power spectrum of the forcing [157].

8.6 Appendix: The underlying operators in a 3D pressure-driven channel flow of FENE-P fluids

In this appendix, we define the underlying operators appearing in (8.13) for a pressure-driven channel flow of FENE-P fluids. The components of operator **A**, defined in (8.14), are given by

$$
\begin{aligned}
\mathbf{A}_{11} \;&=\; \begin{bmatrix} A_{vv} & 0 \\ A_{\eta v} & A_{\eta\eta} \end{bmatrix}, \quad & \mathbf{A}_{12} \;&=\; \frac{1-\beta}{R_\tau} \begin{bmatrix} \Delta^{-1} & 0 \\ 0 & I \end{bmatrix} \bar{\mathbf{A}}_{12}, \\
\mathbf{A}_{21} \;&=\; \begin{bmatrix} \mathbf{A}_{21}^{1v} & \mathbf{A}_{21}^{1\eta} \\ \mathbf{A}_{21}^{2v} & \mathbf{A}_{21}^{2\eta} \end{bmatrix}, \quad & \mathbf{A}_{22} \;&=\; \begin{bmatrix} \mathbf{A}_{22}^{11} & \mathbf{A}_{22}^{12} \\ \mathbf{A}_{22}^{21} & \mathbf{A}_{22}^{22} \end{bmatrix},
\end{aligned}
$$

where

$$
\begin{aligned}
A_{vv} \;&=\; \Delta^{-1} \left(\mathrm{i}k_x \left(U'' \,-\, U\Delta \right) \,+\, \frac{\beta}{R_\tau} \left(\left(1 + \nu_{T0}\right) \Delta^2 \,+\, 2\nu_{T0}' \Delta \partial_y \,+\, \nu_{T0}'' \left(\partial_{yy} + k^2 \right) \right) \right) \\
A_{\eta\eta} \;&=\; -\mathrm{i}k_x U \,+\, \frac{\beta}{R_\tau} \left(\left(1 + \nu_{T0}\right) \Delta \,+\, \nu_{T0}' \partial_y \right), \quad A_{\eta v} \;=\; -\mathrm{i}k_x U', \\
\mathbf{A}_{21}^{1v} \;&=\; \frac{1}{k^2} \begin{bmatrix} k^2 \left(2\mathrm{i}k_x S_{12} \,+\, 2S_{22}\partial_y \,-\, S_{22}' \right) \\ \mathrm{i}k_z \left(k^2 S_{33} + S_{22}\partial_y \right) \,-\, k_x k_z S_{12} \partial_y \\ -\left(k^2 S_{33}' \,+\, 2k_z^2 S_{33} \partial_y \right) \end{bmatrix}, \quad \mathbf{A}_{21}^{1\eta} \;=\; \frac{1}{k^2} \begin{bmatrix} 0 \\ \mathrm{i}k_x S_{22} \partial_y \,-\, k_x^2 S_{12} \\ -2k_x k_z S_{33} \end{bmatrix},
\end{aligned}
$$

$$\mathbf{A}_{21}^{2v} \;=\; \frac{1}{k^2}\begin{bmatrix} -k_x k_z\left(S_{33} \,+\, S_{11}\partial_y\right) \,-\, \mathrm{i}k_z S_{12}\partial_{yy} \\ k_z^2 S_{12}\partial_y \,-\, k^2 S_{12}' \,+\, \mathrm{i}k_x k^2 S_{11} \,+\, \mathrm{i}k_x S_{22}\partial_{yy} \\ 2\mathrm{i}k_x S_{12}\partial_{yy} \,-\, k^2 S_{11}' \,-\, 2k_x^2 S_{11}\partial_y \end{bmatrix},$$

$$\mathbf{A}_{21}^{2\eta} \;=\; \frac{1}{k^2}\begin{bmatrix} k_z^2 S_{33} \,-\, k_x^2 S_{11} \,+\, \mathrm{i}k_x S_{12}\partial_y \\ k_x k_z S_{12} \,-\, \mathrm{i}k_z S_{22}\partial_y \\ 2k_x k_z S_{11} \,-\, 2\mathrm{i}k_z S_{12}\partial_y \end{bmatrix},$$

$$\bar{\mathbf{A}}_{12} \;=\; \frac{1}{We}\begin{bmatrix} A_{12}^{v1} & A_{12}^{v2} & A_{12}^{v3} & A_{12}^{v4} & A_{12}^{v5} & A_{12}^{v6} \\ A_{12}^{\eta 1} & A_{12}^{\eta 2} & A_{12}^{\eta 3} & A_{12}^{\eta 4} & A_{12}^{\eta 5} & A_{12}^{\eta 6} \end{bmatrix},$$

$$\mathbf{A}_{22}^{11} \;=\; \begin{bmatrix} H - \dfrac{\bar{f}^2}{We\bar{L}^2}S_{22} & 0 & -\dfrac{\bar{f}^2}{We\bar{L}^2}S_{22} \\ 0 & H & 0 \\ -\dfrac{\bar{f}^2}{We\bar{L}^2}S_{22} & 0 & H - \dfrac{\bar{f}^2}{We\bar{L}^2}S_{33} \end{bmatrix}, \quad H \;=\; -\mathrm{i}k_x \,-\, \frac{\bar{f}}{We} \,+\, \frac{D_0}{R_\tau}\Delta,$$

$$\mathbf{A}_{22}^{12} \;=\; \begin{bmatrix} 0 & 0 & -\dfrac{\bar{f}^2}{We\bar{L}^2}S_{22} \\ 0 & 0 & 0 \\ 0 & 0 & -\dfrac{\bar{f}^2}{We\bar{L}^2}S_{33} \end{bmatrix}, \quad \mathbf{A}_{22}^{21} \;=\; \begin{bmatrix} 0 & U' & 0 \\ U' - \dfrac{\bar{f}^2}{We\bar{L}^2}S_{12} & 0 & -\dfrac{\bar{f}^2}{We\bar{L}^2}S_{12} \\ -\dfrac{\bar{f}^2}{We\bar{L}^2}S_{11} & 0 & -\dfrac{\bar{f}^2}{We\bar{L}^2}S_{11} \end{bmatrix},$$

$$\mathbf{A}_{22}^{22} \;=\; \begin{bmatrix} H & 0 & 0 \\ 0 & H & -\dfrac{\bar{f}^2}{We\bar{L}^2}S_{12} \\ 0 & 2U' & H - \dfrac{\bar{f}^2}{We\bar{L}^2}S_{11} \end{bmatrix}.$$

Here, $k^2 \,=\, k_x^2 + k_z^2$, $\mathrm{i} \,=\, \sqrt{-1}$, $\Delta \,=\, \partial_{yy} - k^2$ with Dirichlet boundary conditions, $\Delta^2 = \partial_{yyyy} - 2k^2\partial_{yy} + k^4$ with both Dirichlet and Neumann boundary conditions, and prime denotes differentiation with respect to y, i.e., $(\cdot)' = \mathrm{d}(\cdot)/\mathrm{d}y$. Furthermore, A_{12}^{ij}-operators are determined by

$$\begin{aligned}
A_{12}^{v1} &= -k^2\left(\bar{f}' + \bar{f}\partial_y\right) + G_v, \quad A_{12}^{v2} = -\mathrm{i}k_z\left(\bar{f}'' + 2\bar{f}'\partial_y + \bar{f}\left(\partial_{yy} + k^2\right)\right), \\
A_{12}^{v3} &= k_z^2\left(\bar{f}' + \bar{f}\partial_y\right) + G_v, \quad A_{12}^{v4} = 2k_xk_z\left(\bar{f}' + \bar{f}\partial_y\right), \\
A_{12}^{v5} &= -\mathrm{i}k_x\left(\bar{f}'' + 2\bar{f}'\partial_y + \bar{f}\left(\partial_{yy} + k^2\right)\right), \quad A_{12}^{v6} = k_x^2\left(\bar{f}' + \bar{f}\partial_y\right) + G_v, \\
A_{12}^{\eta 1} &= G_\eta, \quad A_{12}^{\eta 2} = -\mathrm{i}k_x\left(\bar{f}' + \bar{f}\partial_y\right), \\
A_{12}^{\eta 3} &= k_xk_z\bar{f} + G_\eta, \quad A_{12}^{\eta 4} = \left(k_x^2 - k_z^2\right)\bar{f}, \\
A_{12}^{\eta 5} &= \mathrm{i}k_z\left(\bar{f}' + \bar{f}\partial_y\right), \quad A_{12}^{\eta 6} = -k_xk_z\bar{f} + G_\eta, \\
G_v &= \frac{1}{\bar{L}^2}\Bigg(k_x^2\left(2\bar{f}\bar{f}'S_{11} + \bar{f}^2S_{11}' + \bar{f}^2S_{11}\partial_y\right) - k_x^2\left(2\bar{f}\bar{f}'S_{22} + \bar{f}^2S_{22}' + \bar{f}^2S_{22}\partial_y\right) - \\
&\quad \mathrm{i}k_x\left(\left(\bar{f}^2S_{12}\right)'' + 2\left(2\bar{f}\bar{f}'S_{12} + \bar{f}^2S_{12}'\right)\partial_y\right)\Bigg), \\
G_\eta &= \frac{1}{\bar{L}^2}\Bigg(\mathrm{i}k_z\left(2\bar{f}\bar{f}'S_{12} + \bar{f}^2S_{12}' + \bar{f}^2S_{12}\partial_y\right) - k_xk_z\bar{f}^2\left(S_{11} - S_{22}\right)\Bigg).
\end{aligned}$$

The output operator in (8.13) is given by

$$\mathbf{C} = \left[\begin{array}{cc} \mathbf{C}_v^T & \mathbf{C}_r^T \end{array}\right]^T,$$

where

$$\mathbf{C}_{\mathbf{u}} = \left[\begin{array}{cc} \mathbf{C}_{\mathbf{u}} & \mathbf{O}_{3\times 6} \end{array}\right], \qquad \mathbf{C}_r = \left[\begin{array}{cc} \mathbf{O}_{6\times 2} & \mathbf{I}_{6\times 6} \end{array}\right].$$

Here, the operator $\mathbf{C}_{\mathbf{u}}$ maps well-normal velocity/vorticity vector $\boldsymbol{\psi}_1$ to the velocity fluctuation vector $\mathbf{u}$ and it is given by

$$\mathbf{C}_{\mathbf{u}} = \left[\begin{array}{cc} \left(\mathrm{i}k_x/k^2\right)\partial_y & -\mathrm{i}k_z/k^2 \\ I & 0 \\ \left(\mathrm{i}k_z/k^2\right)\partial_y & \mathrm{i}k_x/k^2 \end{array}\right].$$

8.7 Appendix: Mean flow equations with second-order statistics of flow fluctuations

Here, we present the mean flow equations:

$$0 \;=\; -\,P_x \,+\, \frac{\beta}{R_\tau}\big(\nu'_{T0}\,U' \,+\, (1+\nu_{T0})\,U''\big) \,+\, \frac{(1-\beta)}{R_\tau}\,T'_{12} \,-\, \overline{uv}'_p, \tag{8.23a}$$

$$0 \;=\; -\,\frac{1}{We}\,\bar{f}R_{12} \,+\, R_{22}\,U' \,+\, \frac{D_0}{R_\tau}R''_{12} \,+\, \Lambda_{12} \,+\, \Gamma_{12}, \tag{8.23b}$$

$$0 \;=\; -\,\frac{1}{We}\big(\bar{f}R_{22} \,-\, 1\big) \,+\, \frac{D_0}{R_\tau}R''_{22} \,+\, \Lambda_{22} \,+\, \Gamma_{22}, \tag{8.23c}$$

$$0 \;=\; -\,\frac{1}{We}\big(\bar{f}R_{33} \,-\, 1\big) \,+\, \frac{D_0}{R_\tau}R''_{33} \,+\, \Lambda_{33} \,+\, \Gamma_{33}, \tag{8.23d}$$

$$0 \;=\; -\,\frac{1}{We}\big(\bar{f}R_{11} \,-\, 1\big) \,+\, 2\,R_{12}\,U' \,+\, \frac{D_0}{R_\tau}R''_{11} \,+\, \Lambda_{11} \,+\, \Gamma_{11}, \tag{8.23e}$$

The contribution to Reynolds shear stress coming from polymers is repsentated by $\overline{uv}_p$ and it is given by

$$\overline{uv}_p \;=\; \overline{uv}_{\text{total}} \,-\, \overline{uv}_{\text{Newton}}.$$

The total and Newtonian Reynolds shear stresses, $\overline{uv}_{\text{total}}$ and $\overline{uv}_{\text{Newton}}$, are determined from the covariance operators $\bar{X}$ (8.16) with $\beta = 0.9$ and $\beta = 1.0$, respectively.

Part III

Computational tools for analysis of spatially distributed systems

Chapter 9

Computation of frequency responses for linear time-invariant PDEs on a compact interval

In this chapter, we develop mathematical framework and computational tools for calculating frequency responses of linear time-invariant partial differential equations (PDEs) in which an independent spatial variable belongs to a compact interval. In conventional studies this computation is done numerically using spatial discretization of differential operators in the evolution equation. Instead, we introduce an alternative method that avoids the need for finite-dimensional approximation of the underlying operators. This method recasts the frequency response operator as a two point boundary value problem and uses state-of-the-art automatic spectral collocation techniques for solving the resulting boundary value problems with accuracy comparable to machine precision. Our approach has two advantages over currently available schemes: first, it avoids numerical instabilities encountered in systems with differential operators of high order and, second, it alleviates difficulty in implementing boundary conditions. We provide examples from Newtonian and viscoelastic fluid dynamics to illustrate utility of the proposed method.

9.1 Introduction

In many physical systems there is a need to examine the effects of exogenous disturbances on the variables of interest. The frequency response analysis represents an effective means for quantifying the system's performance in the presence of a stimulus, and it characterizes the steady-state response of a stable system to persistent harmonic forcing. At each temporal frequency, the frequency response of finite dimensional linear time-invariant systems with scalar input and output is a complex number that determines the magnitude and phase of the output relative to the input. In systems with many inputs and outputs (multi-variable systems), the frequency response is a complex matrix whose dimension is determined by the number of inputs and outputs. In systems with infinite dimensional input and output spaces, considered here, the frequency response is an operator. It is well-known that the singular values of the frequency response matrix (in multi-variable systems) or the frequency response operator (in infinite dimensional systems) represent proper generalization of the magnitude characteristics for single-input single-output systems. At a specific frequency, the largest singular value determines the largest amplification from the input forcing to the desired output. Furthermore, the associated left and right principal singular functions identify the spatial distributions of the output (that exhibits this largest amplification) and the input (that has the strongest influence on the system's dynamics), respectively.

In this chapter, we study the frequency responses of linear time-invariant partial differential equations (PDEs) in which an independent spatial variable belongs to a compact interval. We are interested in computing the largest singular value of the frequency response operator and its corresponding singular functions. Computation of frequency responses for PDEs is typically done numerically using finite-dimensional approximations of the operators in the evolution equation. Pseudo-spectral methods represent a powerful tool for discretization of spatial differential operators, and they possess superior numerical accuracy compared to approximation schemes based on finite differences [32–35]. In spite of their advantages, pseudo-spectral methods may produce unreliable results and even fail to converge upon grid refinement when dealing with systems that contain differential operators of high order; this lack of convergence is attributed to the loss of accuracy arising from ill-conditioning of the discretized differentiation matrices [36]. Furthermore, implementation of general boundary conditions may be challenging.

To alleviate these difficulties, we introduce a method that avoids the need for finite dimensional approximations of differential operators in the evolution equation. This is accomplished by recasting the frequency response operator as a two point boundary value problem (TPBVP) that is given by either an input-output differential equation of a high order or by an equivalent system of first order differential equations (i.e., spatial state-space representation). Furthermore, we present a procedure for converting these differential representations into the corresponding systems of integral equations. This transformation facilitates the use of recently developed computing environment, Chebfun [37], that is capable of solving boundary value problems and eigenvalue problems with superior accuracy. Our mathematical framework in conjunction with Chebfun's state-of-the-art numerical algorithms has two main advantages over standard methods: first, it alleviates numerical ill-conditioning encountered in systems with differential operators of high order; and second, it enables easy implementation of a wide range of boundary conditions.

Chebfun is a collection of powerful algorithms for numerical computations that involve continuous and piecewise-continuous functions. Instead of working in a finite dimensional setting, Chebfun allows users to symbolically represent functions and operators in their infinite dimensional form with simple and compact MATLAB syntaxes. This provides an elegant high-level language for solving linear and nonlinear boundary value and eigenvalue problems with few lines of code. Internally, functions are computed numerically using automatic Chebyshev polynomial interpolation techniques, and the operators are approximated using automatic spectral collocation methods. Finite dimensional approximations of functions and operators are automatically refined in order to obtain accurate and convergent representations. Furthermore, once the boundary conditions are specified Chebfun makes sure that they are automatically satisfied internally when solving differential or integral equations.

The proposed method has many potential applications in numerical analysis, physics, and engineering, especially in systems with generators that do not commute with their adjoints [31]. In these systems, standard modal analysis may fail to capture amplification of exogenous disturbances, low stability margins, and large transient responses. In contrast, singular value decomposition of the frequency response operator represents an effective tool for identifying these non-modal aspects of the system's dynamics. In particular, wall-bounded shear flows of both Newtonian and viscoelastic fluids have non-normal dynamical generators of high spatial order and the ability to accurately compute frequency responses for these systems is of paramount importance; additional examples of systems with non-normal generators, for which the tools developed here are particularly well-suited, can be found in the outstanding book by Trefethen and Embree [31] and the references therein. The utility of non-modal analysis in understanding the dynamics of infinitesimal fluctuations around laminar flow conditions has been well-documented; see [52, 61, 75, 89] for Newtonian fluids and [114–117] for viscoelastic fluids. In viscoelastic fluids with large polymer relaxation times, analysis is additionally complicated by the fact that pseudo-spectral methods exhibit spurious numerical instabilities [125, 126]. We use examples from fluid mechanics to demonstrate the ease of incorporating boundary conditions and superior accuracy of our method compared to conventional finite dimensional approximation schemes.

The following presentation is organized as follows. In Section 9.2, we formulate the problem and discuss the notion of a frequency response for PDEs. In Section 9.3, we present the method for converting the frequency response operator into a TPBVP that can be posed as an input-output differential equation or as a spatial state-space representation. In Section 9.4, we show how to transform a family of differential equations into equivalent integral equations and describe the use of Chebfun's indefinite integration operator for determining the eigenvalues and corresponding eigenfunctions of the resulting integral equations. In Section 9.5, we demonstrate the utility of our developments by providing two examples from Newtonian and viscoelastic fluid dynamics. We conclude with a brief summary of the chapter in Section 9.6, and relegate the mathematical developments to the appendices.

9.2 Motivating examples and problem formulation

In this section, we provide two examples that are used to motivate our developments and to illustrate the classes of systems that we consider. These examples are used throughout the chapter to explain the problem setup and utility of the proposed method. We then describe the class of PDEs that we study and briefly review the notion of a frequency response operator.

9.2.1 Motivating examples

We next present two physical examples: the one-dimensional (1D) diffusion equation, and the system of PDEs that governs the dynamics of the flow fluctuations in an inertialess channel flow of viscoelastic fluids. The 1D diffusion equation has simple dynamics and it is used to illustrate mathematical framework developed in the chapter. The example from viscoelastic fluid mechanics is used to demonstrate utility of our approach on a system that is known to produce spurious numerical instabilities. We show how numerical difficulties encountered in the computation of the frequency responses can be overcome using the developed framework in conjunction with state-of-the-art automatic spectral collocation techniques.

One-dimensional diffusion equation

Let a one-dimensional diffusion equation with homogenous Dirichlet boundary conditions and zero initial conditions be subject to spatially and temporally distributed forcing $d(y,t)$,

$$\begin{array}{rcl} \phi_t(y,t) & = & \phi_{yy}(y,t) \; + \; d(y,t), \\ \phi(\pm 1,t) & = & 0, \\ \phi(y,0) & = & 0, \;\; y \in [-1, \, 1]\,. \end{array} \tag{9.1}$$

Throughout the chapter, the spatially independent variable is denoted by y, the time is denoted by t, and the subscripts denote differentiation with respect to time/space. Considering ϕ as the field of interest, the frequency response operator for this system (from input d to output ϕ) is given by

$$\mathcal{T}(\omega) \; = \; \Big(\mathrm{i}\omega I \; - \; D^{(2)}\Big)^{-1}, \tag{9.2}$$

where $D^{(2)}$ is the second derivative operator with homogenous Dirichlet boundary conditions, I is the identity operator, ω is the temporal frequency, and i is the imaginary unit.

It is well known that the second derivative operator with Dirichlet boundary conditions is self-adjoint with a complete set of orthonormal eigenfunctions,

$$v_n(y) = \sin\left((n\pi/2)(y+1)\right), \;\; n = \{1, 2, \ldots\}.$$

This information can be used to diagonalize operator $D^{(2)}$ in $\mathcal{T}(\omega)$ which facilitates straightforward determination of the frequency response. For systems with spatially varying coefficients and non-normal generators the frequency response analysis is typically done numerically using finite dimensional approximations of the differential operators. For example, the pseudospectral method [83] with N collocation points can be used to transform the frequency response operator (9.2) of system (9.1) into an $N \times N$ matrix. However, for systems with differential operators of high order, spectral differentiation matrices may be poorly conditioned and implementation of boundary conditions may be challenging. In this chapter, numerical approximation of differential operators in the evolution equation is avoided by first recasting the system into corresponding two point boundary value problems and then using state-of-the-art techniques for solving the resulting boundary value problems with accuracy comparable to machine precision.

Alternatively, by applying the temporal Fourier transform on system (9.1) we obtain the following input-output differential equation

$$\begin{aligned} \hat{\phi}''(y,\omega) \,-\, \mathrm{i}\omega\hat{\phi}(y,\omega) \;&=\; -\,\hat{d}(y,\omega), && (9.3\mathrm{a}) \\ \hat{\phi}(\pm 1,\omega) \;&=\; 0, && (9.3\mathrm{b}) \end{aligned}$$

where $\hat{d}$ and $\hat{\phi}$ are the Fourier transformed input and output fields, and $\hat{\phi}' = \mathrm{d}\hat{\phi}/\mathrm{d}y$. At each ω, (9.3a) is a second-order ordinary differential equation (in y) subject to the boundary conditions (9.3b). Equivalently, by defining $x_1 = \hat{\phi}$ and $x_2 = \hat{\phi}'$, (9.3) can be brought into a system of first order differential equations

$$\mathcal{T}(\omega): \left\{ \begin{aligned} \begin{bmatrix} x_1'(y) \\ x_2'(y) \end{bmatrix} \;&=\; \begin{bmatrix} 0 & 1 \\ \mathrm{i}\omega & 0 \end{bmatrix} \begin{bmatrix} x_1(y) \\ x_2(y) \end{bmatrix} + \begin{bmatrix} 0 \\ -1 \end{bmatrix} d(y), \\ \phi(y) \;&=\; \begin{bmatrix} 1 & 0 \end{bmatrix} \begin{bmatrix} x_1(y) \\ x_2(y) \end{bmatrix}, \\ \begin{bmatrix} 0 \\ 0 \end{bmatrix} \;&=\; \begin{bmatrix} 1 & 0 \\ 0 & 0 \end{bmatrix} \begin{bmatrix} x_1(-1) \\ x_2(-1) \end{bmatrix} + \begin{bmatrix} 0 & 0 \\ 1 & 0 \end{bmatrix} \begin{bmatrix} x_1(1) \\ x_2(1) \end{bmatrix}. \end{aligned} \right. \qquad (9.4)$$

We will utilize structures of the TPBVPs (9.3) and (9.4) in conjunction with recently developed automatic spectral collocation techniques to study the frequency response across ω.

Inertialess channel flow of viscoelastic fluids

We next consider a system that describes the dynamics of two-dimensional velocity and polymer stress fluctuations in an inertialess channel flow of viscoelastic fluids; see figure 9.1 for geometry. The dynamics of infinitesimal fluctuations around the mean

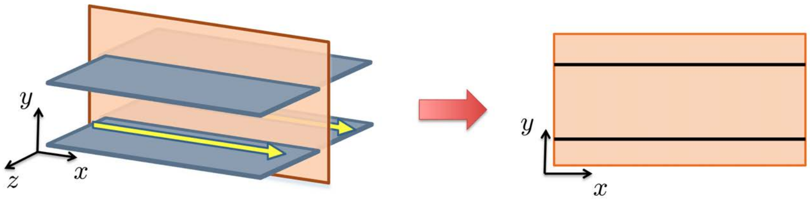

Figure 9.1: We consider the dynamics of flow fluctuations in the (x, y)-plane of the channel.

flow $(\bar{\mathbf{v}},\, \bar{\boldsymbol{\tau}})$ are given by

$$
\begin{aligned}
0 \;&=\; -\,\boldsymbol{\nabla} p \,+\, (1-\beta)\,\boldsymbol{\nabla}\cdot\boldsymbol{\tau} \,+\, \beta\,\boldsymbol{\nabla}^2\mathbf{v} \,+\, \mathbf{d}, && \text{(9.5a)}\\
0 \;&=\; \boldsymbol{\nabla}\cdot\mathbf{v}, && \text{(9.5b)}\\
\boldsymbol{\tau}_t \;&=\; \boldsymbol{\nabla}\mathbf{v} \,+\, (\boldsymbol{\nabla}\mathbf{v})^T \,-\, \boldsymbol{\tau} \,+\, We\,(\boldsymbol{\tau}\cdot\boldsymbol{\nabla}\bar{\mathbf{v}} \,+\, \bar{\boldsymbol{\tau}}\cdot\boldsymbol{\nabla}\mathbf{v}\\
&\quad +\, (\bar{\boldsymbol{\tau}}\cdot\boldsymbol{\nabla}\mathbf{v})^T \,+\, (\boldsymbol{\tau}\cdot\boldsymbol{\nabla}\bar{\mathbf{v}})^T \,-\, \mathbf{v}\cdot\boldsymbol{\nabla}\bar{\boldsymbol{\tau}} \,-\, \bar{\mathbf{v}}\cdot\boldsymbol{\nabla}\boldsymbol{\tau}\,). && \text{(9.5c)}
\end{aligned}
$$

In shear driven flow, $\bar{\mathbf{v}}$ and $\bar{\boldsymbol{\tau}}$ are

$$
\bar{\mathbf{v}} \;=\; \begin{bmatrix} y \\ 0 \end{bmatrix}, \quad \bar{\boldsymbol{\tau}} \;=\; \begin{bmatrix} \bar{\tau}_{11} & \bar{\tau}_{12} \\ \bar{\tau}_{12} & \bar{\tau}_{22} \end{bmatrix} \;=\; \begin{bmatrix} 2We & 1 \\ 1 & 0 \end{bmatrix},
$$

$\mathbf{v} \;=\; \begin{bmatrix} u & v \end{bmatrix}^T$, p, and $\boldsymbol{\tau}$ are the velocity, pressure, and stress fluctuations; u and v are velocities in x and y directions; $\boldsymbol{\nabla}$ is the gradient; and $\boldsymbol{\nabla}^2 = \boldsymbol{\nabla}\cdot\boldsymbol{\nabla}$ is the Laplacian. System (9.5) is driven by spatially distributed and temporally varying body force fluctuations $\mathbf{d} = \begin{bmatrix} d_1 & d_2 \end{bmatrix}^T$ with d_1 and d_2 representing the forcing in x and y. The non-dimensional parameters in (9.5) are the ratio of the solvent to the total viscosity $\beta \in (0, 1)$, and the ratio of the fluid relaxation time to the characteristic flow time We (the Weissenberg number).

Static-in-time momentum (9.5a) and continuity (9.5b) equations describe the motion of incompressible fluids in the Stokes flow, i.e., at zero Reynolds number. The constitutive equation (9.5c) captures the influence of the velocity gradients on the dynamics of stress fluctuations in dilute polymer solutions [17]. For background material on the use of frequency response analysis in understanding the dynamics of viscoelastic fluids, we refer the reader to [114–117] and the references therein.

By expressing the velocity fluctuations in terms of the stream function ψ,

$$
u \;=\; \partial_y \psi, \quad v \;=\; -\partial_x \psi,
$$

pressure can be removed form the equations (9.5). Furthermore, by applying the Fourier transform in x and t on (9.5c) and by substituting the resulting expression for stresses into the equation for ψ, we arrive at the following ordinary differential equation (ODE) in y for the stream function,

$$\mathcal{T}(\omega) : \begin{cases} \left(D^{(4)} + a_3(y) D^{(3)} + a_2(y) D^{(2)} + a_1(y) D^{(1)} + a_0(y)\right) \hat{\psi}(y) \; = \\ \left(\mathbf{b}_1(y)\, \mathbf{D}^{(1)} + \mathbf{b}_0(y)\right) \hat{\mathbf{d}}(y), \\ \begin{bmatrix} \hat{u}(y) \\ \hat{v}(y) \end{bmatrix} \; = \; \begin{bmatrix} D^{(1)} \\ -\mathrm{i} k_x \end{bmatrix} \hat{\psi}(y), \\ 0 \; = \; \hat{\psi}(y = \pm 1) \; = \; \hat{\psi}'(y = \pm 1), \end{cases} \tag{9.6}$$

where $D^{(k)} = \partial^k / \partial y^k$, k_x is the horizontal wavenumber, and

$$\mathbf{D}^{(1)} \; = \; \begin{bmatrix} D^{(1)} & 0 \\ 0 & D^{(1)} \end{bmatrix}.$$

The coefficients $\{a_i(y), \mathbf{b}_j(y)\}$ in (9.6) are reported in 9.10. The system of equations (9.6) is parameterized by ω, k_x, β, and We. For notational convenience, we have suppressed the dependence of $\hat{\psi}$, $\hat{\mathbf{d}}$, $\hat{u}$, and $\hat{v}$ on these four parameters.

In Section 9.5, we show that spatial discretization of the operators in (9.5) using the pseudo-spectral method [83] can produce erroneous frequency responses. In contrast, transformation of the system into a TPBVP followed by the use of Chebfun environment [37] yields reliable results.

9.2.2 Problem formulation

We now formulate the problem for PDEs with the evolution equation

$$\mathcal{E}\, \boldsymbol{\phi}_t(y,t) \; = \; \mathcal{F}\, \boldsymbol{\phi}(y,t) \; + \; \mathcal{G}\, \mathbf{d}(y,t), \tag{9.7a}$$

$$\boldsymbol{\varphi}(y,t) \; = \; \mathcal{H}\, \boldsymbol{\phi}(y,t), \tag{9.7b}$$

where $t \in [0, \infty)$ and $y \in [a, b]$ denote the temporal and spatial variables. The spatially distributed and temporally varying state, input, and output fields are represented by $\boldsymbol{\phi}$, $\mathbf{d}$, and $\boldsymbol{\varphi}$, respectively. At each t, $\mathbf{d}(\cdot, t)$ and $\boldsymbol{\varphi}(\cdot, t)$ denote the square-integrable vector-valued functions, and $\{\mathcal{E}, \mathcal{F}, \mathcal{G}, \mathcal{H}\}$ are matrices of differential operators with, in general, spatially varying coefficients. For example, the ijth entry of the operator $\mathcal{F}$ can be expressed as

$$\mathcal{F}_{ij} \; = \; \sum_{k\,=\,0}^{n_{ij}} f_{ij,k}(y)\, D^{(k)},$$

where each $f_{ij,k}$ is a function that is at least k times continuously differentiable on the interval $[a, b]$ [159], $D^{(k)} = \partial^k / \partial y^k$, and n_{ij} is the order of the highest derivative in $\mathcal{F}_{ij}$.

The application of the temporal Fourier transform yields the frequency response operator of system (9.7)

$$\mathcal{T}(\omega) \;=\; \mathcal{H}\,(\mathrm{i}\omega\mathcal{E} \;-\; \mathcal{F})^{-1}\,\mathcal{G}. \tag{9.8}$$

For a stable system (9.7), $\mathcal{T}(\omega)$ describes the steady-state response to harmonic input signals across the temporal frequency ω. Namely, if the input is harmonic in t, i.e.,

$$\mathbf{d}(y,t) \;=\; \hat{\mathbf{d}}(y,\omega)\,\mathrm{e}^{\mathrm{i}\omega t},$$

with $\hat{\mathbf{d}}(\cdot,\omega)$ denoting a square-integrable spatial distribution in y, then the output is also harmonic in t with the same frequency but with a modified amplitude and phase

$$\begin{aligned}\boldsymbol{\varphi}(y,t) \;&=\; \left(\left[\mathcal{T}(\omega)\,\hat{\mathbf{d}}(\cdot,\omega)\right](y)\right)\mathrm{e}^{\mathrm{i}\omega t} \;=\; \hat{\boldsymbol{\varphi}}(y,\omega)\,\mathrm{e}^{\mathrm{i}\omega t}\\ &=\; \left(\int_a^b \mathcal{T}_{\mathrm{ker}}(y,\xi;\omega)\,\hat{\mathbf{d}}(\xi,\omega)\,\mathrm{d}\xi\right)\mathrm{e}^{\mathrm{i}\omega t}.\end{aligned}$$

The amplitude and phase of the output at the frequency ω are precisely determined by the frequency response operator $\mathcal{T}(\omega)$, with $\mathcal{T}_{\mathrm{ker}}$ denoting the kernel representation of the operator $\mathcal{T}$.

For the class of systems that we consider, the kernel representation of the frequency response operator $\mathcal{T}_{\mathrm{ker}}(\,\cdot\,,\,\cdot\,;\omega)$ is a bounded matrix valued function on $[a,b] \times [a,b]$. This implies that the operator $\mathcal{T}(\omega)$ can be represented using the singular value (i.e., Schmidt) decomposition [160],

$$\hat{\boldsymbol{\varphi}}(y,\omega) \;=\; \left[\mathcal{T}(\omega)\,\hat{\mathbf{d}}(\cdot,\omega)\right](y) \;=\; \sum_{n\,=\,1}^{\infty}\sigma_n(\omega)\,\hat{\mathbf{u}}_n(y,\omega)\left\langle\hat{\mathbf{v}}_n,\hat{\mathbf{d}}\right\rangle, \tag{9.9}$$

where $\langle\cdot,\cdot\rangle$ is the standard $L_2\,[a,b]$ inner product,

$$\langle\hat{\mathbf{v}}_1,\hat{\mathbf{v}}_2\rangle \;=\; \int_a^b \hat{\mathbf{v}}_1^*(y)\,\hat{\mathbf{v}}_2(y)\,\mathrm{d}y,$$

and $\hat{\mathbf{v}}_1^*(y)$ is the complex-conjugate-transpose of the vector $\hat{\mathbf{v}}_1(y)$. In (9.9), $\{\hat{\mathbf{u}}_n\}$ and $\{\hat{\mathbf{v}}_n\}$ denote the left and the right singular functions of the operator $\mathcal{T}$ associated with the singular value σ_n. These are obtained from the eigenvalue decomposition of the operators $\mathcal{T}\,\mathcal{T}^\star$ and $\mathcal{T}^\star\,\mathcal{T}$,

$$\begin{aligned}\left[\mathcal{T}(\omega)\,\mathcal{T}^\star(\omega)\,\hat{\mathbf{u}}_n(\cdot,\omega)\right](y) \;&=\; \sigma_n^2(\omega)\,\hat{\mathbf{u}}_n(y,\omega),\\ \left[\mathcal{T}^\star(\omega)\,\mathcal{T}(\omega)\,\hat{\mathbf{v}}_n(\cdot,\omega)\right](y) \;&=\; \sigma_n^2(\omega)\,\hat{\mathbf{v}}_n(y,\omega),\end{aligned}$$

where $\mathcal{T}^\star$ is the adjoint of the operator $\mathcal{T}$. The singular values are positive numbers arranged in descending order,

$$\sigma_1 \;\geq\; \sigma_2 \;\geq\; \cdots \;>\; 0,$$

and they are determined by the square root of the non-zero eigenvalues of $\mathcal{T}\mathcal{T}^\star$ (or $\mathcal{T}^\star\mathcal{T}$). On the other hand, the singular functions $\{\hat{\mathbf{u}}_n\}$ and $\{\hat{\mathbf{v}}_n\}$ form the orthonormal bases for the spaces of square integrable functions that the output $\hat{\boldsymbol{\varphi}}$ and the input $\hat{\mathbf{d}}$ belong to.

From (9.9) we see that the action of the operator $\mathcal{T}(\omega)$ on $\hat{\mathbf{d}}(y,\omega)$ is determined by the linear combination of the left singular functions $\{\hat{\mathbf{u}}_n\}$. The product between the singular values, σ_n, and the inner product of the input $\hat{\mathbf{d}}$ and the right singular function $\hat{\mathbf{v}}_n$, $\left\langle \hat{\mathbf{v}}_n, \hat{\mathbf{d}} \right\rangle$, yields the corresponding weights. Thus, for $\hat{\mathbf{d}} = \hat{\mathbf{v}}_m$, the output is in the direction of $\hat{\mathbf{u}}_m$ and its energy is determined by σ_m^2,

$$\hat{\mathbf{d}}(y,\omega) \;=\; \hat{\mathbf{v}}_m(y,\omega) \quad\Rightarrow\quad \hat{\boldsymbol{\varphi}}(y,\omega) \;=\; \sigma_m(\omega)\,\hat{\mathbf{u}}_m(y,\omega),$$

implying that at any frequency ω the largest singular value $\sigma_1(\omega)$ quantifies the largest energy of the output for unit energy inputs. This largest energy can be achieved by selecting $\hat{\mathbf{d}}(y,\omega) = \hat{\mathbf{v}}_1(y,\omega)$, and the most energetic spatial output profile resulting from the action of $\mathcal{T}(\omega)$ is given by $\hat{\boldsymbol{\varphi}}(y,\omega) = \sigma_1(\omega)\,\hat{\mathbf{u}}_1(y,\omega)$.

In linear dynamical systems, spectral decomposition of the dynamical generators is typically used to identify instability. Appearance of the eigenvalues with positive real part implies exponential temporal growth of infinitesimal fluctuations and the associated eigenfunctions characterize spatial patterns of these growing modes. For systems with normal dynamical generators (i.e., operators that *commute* with their adjoints) the eigenfunctions are mutually orthogonal and the eigenvalues provide complete information about system's response. However, for systems with non-normal generators eigenvalues may give misleading information about system's responses. Even in the stable regime, non-normality can cause (i) substantial transient growth of fluctuations before their asymptotic decay; (ii) significant amplification of ambient disturbances; and (iii) substantial decrease of stability margins. We note that singular value decomposition of the frequency response operator represents an effective tool for capturing these non-modal aspects of the system's response.

In what follows, we describe the procedure for reformulating the frequency response operator (9.8) into corresponding two point boundary value problems that are given by either an input-output differential equation or by a spatial state-space representation. These can be solved with superior accuracy using recently developed computational tools [37]. We illustrate the utility of our developments on an example from viscoelastic fluid dynamics, where standard finite dimensional approximation techniques fail to produce reliable results.

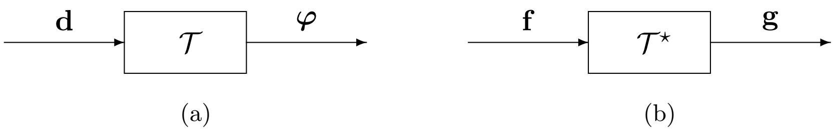

Figure 9.2: Block diagrams of (a) the frequency response operator $\mathcal{T}$: $\mathbf{d} \mapsto \boldsymbol{\varphi}$; and (b) the adjoint operator $\mathcal{T}^\star$: $\mathbf{f} \mapsto \mathbf{g}$.

9.3 Two point boundary value representations of $\mathcal{T}$, $\mathcal{T}^\star$, and $\mathcal{T}\mathcal{T}^\star$

In this section, we first describe the procedure for determining the two point boundary value representations of the frequency response operator (9.8). These are given by either a high-order input-output differential equation or by a system of first-order differential equations in spatial variable y. We then discuss the procedure for obtaining corresponding representations of the adjoint operator $\mathcal{T}^\star$ and the operator $\mathcal{T}\mathcal{T}^\star$.

9.3.1 Representations of the frequency response operator $\mathcal{T}$

The application of the temporal Fourier transform to (9.7) yields

$$\begin{aligned} (\mathrm{i}\omega\mathcal{E} \, - \, \mathcal{F})\, \boldsymbol{\phi}(y,\omega) \;&=\; \mathcal{G}\, \mathbf{d}(y,\omega), && (9.10\text{a}) \\ \boldsymbol{\varphi}(y,\omega) \;&=\; \mathcal{H}\, \boldsymbol{\phi}(y,\omega), && (9.10\text{b}) \end{aligned}$$

where we have omitted hats from the Fourier transformed fields for notational convenience (a convention that we adopt from now on). System (9.10) represents an ω-parameterized family of ordinary differential equations (ODEs) in y, with boundary conditions at a and b. From the definitions of the operators $\{\mathcal{E},\, \mathcal{F},\, \mathcal{G},\, \mathcal{H}\}$ described in Section 9.2.2, (9.10) can be represented by the following system of differential equations

$$\mathcal{T}: \left\{ \begin{aligned} [\,\mathcal{A}_0\, \boldsymbol{\phi}\,]\,(y) \;&=\; [\,\mathcal{B}_0\, \mathbf{d}\,]\,(y), \\ \boldsymbol{\varphi}(y) \;&=\; [\,\mathcal{C}_0\, \boldsymbol{\phi}\,]\,(y), \\ 0 \;&=\; \mathcal{N}_0\, \boldsymbol{\phi}\,(y), \end{aligned} \right. \qquad (9.11)$$

where

$$
\begin{aligned}
\mathcal{A}_0 \;&=\; \sum_{i=0}^{n} \boldsymbol{\alpha}_i(y)\,\mathbf{D}^{(i)},\;\; \mathcal{B}_0 \;=\; \sum_{i=0}^{m} \boldsymbol{\beta}_i(y)\,\mathbf{D}^{(i)},\;\; \mathcal{C}_0 \;=\; \sum_{i=0}^{k} \boldsymbol{\gamma}_i(y)\,\mathbf{D}^{(i)},\\
\mathcal{N}_0 \;&=\; \sum_{i=0}^{\ell} \left(\mathbf{W}_{a,i}\,\mathbf{E}_a \;+\; \mathbf{W}_{b,i}\,\mathbf{E}_b\right)\mathbf{D}^{(i)},\\
\mathbf{D}^{(i)} \;&=\; \begin{bmatrix} D^{(i)} & & \\ & \ddots & \\ & & D^{(i)} \end{bmatrix},\;\; \boldsymbol{\phi} \;=\; \begin{bmatrix} \phi_1 \\ \vdots \\ \phi_s \end{bmatrix},\;\; \mathbf{d} \;=\; \begin{bmatrix} d_1 \\ \vdots \\ d_r \end{bmatrix},\;\; \boldsymbol{\varphi} \;=\; \begin{bmatrix} \varphi_1 \\ \vdots \\ \varphi_p \end{bmatrix}.
\end{aligned}
$$

Here, $D^{(i)}\phi_j \;=\; \mathrm{d}^i\phi_j/\mathrm{d}y^i$, $\mathbf{E}_a$ and $\mathbf{E}_b$ denote the point evaluation functionals at the boundaries, e.g.,

$$\mathbf{E}_a\,\boldsymbol{\phi}\,(y) \;=\; \boldsymbol{\phi}(a),$$

and $\{\mathbf{W}_{a,i},\; \mathbf{W}_{b,i}\}$ are constant matrices that specify the boundary conditions on $\boldsymbol{\phi}$. For notational convenience we have omitted the dependence on ω in (9.11), which is a convention that we adopt from now on. Here, n, m, k, and ℓ denote the highest differential orders of the operators $\mathcal{A}_0$, $\mathcal{B}_0$, $\mathcal{C}_0$, and $\mathcal{N}_0$, respectively. If the number of components in $\boldsymbol{\phi}$, $\mathbf{d}$, and $\boldsymbol{\varphi}$ is given by s, r, and p, then $\{\boldsymbol{\alpha}_i(y)\}$ are matrices of size $s \times s$ with entries determined by the coefficients of the operator $(\mathrm{i}\omega\mathcal{E} - \mathcal{F})$; $\{\boldsymbol{\beta}_i(y)\}$ are matrices of size $s \times r$ with entries determined by the coefficients of the operator $\mathcal{G}$; and $\{\boldsymbol{\gamma}_i(y)\}$ are matrices of size $p \times s$ with entries determined by the coefficients of the operator $\mathcal{H}$. We also normalize the coefficient of the highest derivative of each ϕ_i to one, i.e.,

$$\alpha_{n_i,ii} \;=\; 1,\;\; i \;=\; 1,\ldots,s,$$

where $\alpha_{n_i,ii}$ is the iith component of the matrix $\boldsymbol{\alpha}_{n_i}$, and n_i identifies the highest derivative of ϕ_i. In order to make sure that the input field $\mathbf{d}$ in (9.11) does not directly influence the boundary conditions and the output field $\boldsymbol{\varphi}$, we impose the following technical assumptions on system (9.11),

$$\ell \;<\; n,\;\; m \;<\; n \,-\, \ell,\;\; k \;<\; n \,-\, m.$$

This assumption is satisfied in most physical problems of interest.

Alternatively we can bring (9.11) into a system of first-order differential equations (in y). This can be done by introducing state variables, $\{\mathbf{x}_i(y)\}$, where each of the states represents a linear combination of $\boldsymbol{\phi}$ and $\mathbf{d}$, and their derivatives up to a certain order. A procedure for converting a high-order two point boundary value realization (9.11) with spatially varying coefficients to a system of first-order ODEs is described in 9.7. This transformation yields the *spatial* state-space representation of the frequency response operator $\mathcal{T}$

$$\mathcal{T} : \left\{ \begin{array}{rcl} \mathbf{x}'(y) & = & \mathbf{A}_0(y)\,\mathbf{x}(y) \;+\; \mathbf{B}_0(y)\,\mathbf{d}(y), \\ \boldsymbol{\varphi}(y) & = & \mathbf{C}_0(y)\,\mathbf{x}(y), \\ 0 & = & \mathbf{N}_a\,\mathbf{x}(a) \;+\; \mathbf{N}_b\,\mathbf{x}(b), \end{array} \right. \tag{9.12}$$

where $\mathbf{x}$ is the state vector, $\mathbf{A}_0$, $\mathbf{B}_0$, and $\mathbf{C}_0$ are matrices with, in general, spatially varying entries, $\mathbf{N}_a$ and $\mathbf{N}_b$ are constant matrices that specify the boundary conditions, and $\mathbf{x}' = \mathrm{d}\mathbf{x}/\mathrm{d}y$. To avoid redundancy in boundary conditions, $\mathbf{N}_a$ and $\mathbf{N}_b$ are chosen so that the matrix $\left[\begin{array}{cc} \mathbf{N}_a & \mathbf{N}_b \end{array}\right]$ has a full row rank. We note that (9.12) is well-posed (that is, it has a unique solution for any input $\mathbf{d}$) if and only if [161]

$$\det\left(\mathbf{N}_a \;+\; \mathbf{N}_b\,\mathbf{\Phi}_0(b,a)\right) \;\neq\; 0,$$

where $\mathbf{\Phi}_0(y,\eta)$ is the state transition matrix of $\mathbf{A}_0(y)$,

$$\frac{\mathrm{d}\mathbf{\Phi}_0(y,\eta)}{\mathrm{d}y} \;=\; \mathbf{A}_0(y)\,\mathbf{\Phi}_0(y,\eta), \quad \mathbf{\Phi}_0(\eta,\eta) \;=\; I,$$

and $\det(\cdot)$ is the determinant of a given matrix.

For the 1D diffusion equation of Section 9.2.1, the input-output differential equation and the corresponding spatial state-space representation of the frequency response operator are given by (9.3) and (9.4), respectively. Note that the boundary conditions (9.3b) can be rewritten into the form required by (9.11),

$$\left(\left[\begin{array}{c} 1 \\ 0 \end{array}\right] E_{-1} \;+\; \left[\begin{array}{c} 0 \\ 1 \end{array}\right] E_1 \right) \phi(y) \;=\; \left[\begin{array}{c} 0 \\ 0 \end{array}\right].$$

9.3.2 Representations of the adjoint operator $\mathcal{T}^\star$

We next describe the procedure for obtaining the two point boundary value representations of the adjoint of the frequency response operator, $\mathcal{T}$, $\mathcal{T}^\star$: $\mathbf{f} \mapsto \mathbf{g}$; see figure 9.2(b). As shown above, the operator $\mathcal{T}$ can be recast into the input-output differential equation (9.11), and the corresponding representation of $\mathcal{T}^\star$ is given by

$$\mathcal{T}^\star : \left\{ \begin{array}{rcl} \left[\,\mathcal{A}_0^\star\,\boldsymbol{\psi}\,\right](y) & = & \left[\,\mathcal{C}_0^\star\,\mathbf{f}\,\right](y), \\ \mathbf{g}(y) & = & \left[\,\mathcal{B}_0^\star\,\boldsymbol{\psi}\,\right](y), \\ 0 & = & \mathcal{N}_0^\star\,\boldsymbol{\psi}\,(y). \end{array} \right. \tag{9.13}$$

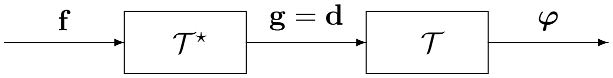

Figure 9.3: A cascade connection of $\mathcal{T}^\star$ and $\mathcal{T}$ with $\mathcal{T}\mathcal{T}^\star$: $\mathbf{f} \mapsto \boldsymbol{\varphi}$.

Here, the adjoint operators are [159, 162]

$$\begin{aligned}
[\,\mathcal{A}_0^\star\, \boldsymbol{\psi}\,](y) &= \sum_{i\,=\,0}^{n} (-1)^i \left[\mathbf{D}^{(i)} \left(\boldsymbol{\alpha}_i^*\, \boldsymbol{\psi}\right)\right](y), \\
[\,\mathcal{C}_0^\star\, \mathbf{f}\,](y) &= \sum_{i\,=\,0}^{k} (-1)^i \left[\mathbf{D}^{(i)} \left(\boldsymbol{\gamma}_i^*\, \mathbf{f}\right)\right](y), \\
[\,\mathcal{B}_0^\star\, \boldsymbol{\psi}\,](y) &= \sum_{i\,=\,0}^{m} (-1)^i \left[\mathbf{D}^{(i)} \left(\boldsymbol{\beta}_i^*\, \boldsymbol{\psi}\right)\right](y), \\
[\,\mathcal{N}_0^\star\, \boldsymbol{\psi}\,](y) &= \sum_{i\,=\,0}^{\ell} \left(\mathbf{W}_{a,i}^\star\, \mathbf{E}_a \,+\, \mathbf{W}_{b,i}^\star\, \mathbf{E}_b\right) \left[\mathbf{D}^{(i)}\, \boldsymbol{\psi}\right](y),
\end{aligned}$$

where $\boldsymbol{\alpha}_i^*$, $\boldsymbol{\beta}_i^*$, and $\boldsymbol{\gamma}_i^*$ are the complex-conjugate-transposes of the matrices $\boldsymbol{\alpha}_i$, $\boldsymbol{\beta}_i$, and $\boldsymbol{\gamma}_i$. The boundary conditions on the adjoint variable $\boldsymbol{\psi}$ are determined so that the boundary terms vanish when determining the adjoint of the operator $\mathcal{A}_0$. A procedure describing how to determine the boundary conditions of the adjoint system is given in [159].

On the other hand, the state-space representation of the adjoint of the operator $\mathcal{T}$ is given in [161]

$$\mathcal{T}^\star : \left\{ \begin{aligned}
\mathbf{z}'(y) &= -\mathbf{A}_0^*(y)\, \mathbf{z}(y) \,-\, \mathbf{C}_0^*(y)\, \mathbf{f}(y), \\
\mathbf{g}(y) &= \mathbf{B}_0^*(y)\, \mathbf{z}(y), \\
0 &= \mathbf{M}_a\, \mathbf{z}(a) \,+\, \mathbf{M}_b\, \mathbf{z}(b),
\end{aligned} \right. \tag{9.14}$$

where $\mathbf{A}_0^*$, $\mathbf{B}_0^*$, and $\mathbf{C}_0^*$ denote the complex-conjugate-transposes of the matrices $\mathbf{A}_0$, $\mathbf{B}_0$, and $\mathbf{C}_0$. The boundary condition matrices $\mathbf{M}_a$ and $\mathbf{M}_b$ are determined so that $\left[\begin{array}{cc} \mathbf{M}_a & \mathbf{M}_b \end{array}\right]$ has a full row rank and

$$\left[\begin{array}{cc} \mathbf{M}_a & \mathbf{M}_b \end{array}\right] \left[\begin{array}{c} \mathbf{N}_a^* \\ -\mathbf{N}_b^* \end{array}\right] \;=\; 0. \tag{9.15}$$

A procedure for selecting $\mathbf{M}_a$ and $\mathbf{M}_b$ that satisfy these two requirements is described in [163]. Furthermore, we note that the well-posedness of the adjoint representation (9.14) is guaranteed by the well-posedness of $\mathcal{T}$.

For the 1D diffusion equation of Section 9.2.1, the adjoint of the operator $\mathcal{T}(\omega)$

described by (9.3) has the following input-output representation

$$\mathcal{T}^{\star}(\omega):\left\{\begin{array}{rcl}\left(D^{(2)}+\mathrm{i}\omega I\right)\psi(y) &=& f(y),\\ g(y) &=& -\psi(y),\\ \left(\left[\begin{array}{c}1\\0\end{array}\right]E_{-1}+\left[\begin{array}{c}0\\1\end{array}\right]E_{1}\right)\psi(y) &=& \left[\begin{array}{c}0\\0\end{array}\right].\end{array}\right. \tag{9.16}$$

As specified in (9.14), the state-space representation of $\mathcal{T}^{\star}(\omega)$ is determined by taking the appropriate complex-conjugate-transposes of the corresponding matrices in (9.4) with the following boundary condition matrices

$$M_1 = \left[\begin{array}{cc}0&1\\0&0\end{array}\right],\; M_2 = \left[\begin{array}{cc}0&0\\0&1\end{array}\right].$$

9.3.3 Representations of $\mathcal{T}\mathcal{T}^{\star}$

From the above described representations of $\mathcal{T}$ and $\mathcal{T}^{\star}$, we can determine corresponding representations of the operator $\mathcal{T}\mathcal{T}^{\star}$: $\mathbf{f}\mapsto\boldsymbol{\varphi}$. As illustrated in figure 9.3, this operator represents a cascade connection of the frequency response operator $\mathcal{T}$ and its adjoint $\mathcal{T}^{\star}$. The input-output differential equation for $\mathcal{T}\mathcal{T}^{\star}$ is obtained by equating the output of $\mathcal{T}^{\star}$ in (9.13) with the input of $\mathcal{T}$ in (9.11), i.e., $\mathbf{d}=\mathbf{g}$, yielding

$$\mathcal{T}\mathcal{T}^{\star}:\left\{\begin{array}{rcl}[\,\mathcal{A}\,\boldsymbol{\xi}\,](y) &=& [\,\mathcal{B}\,\mathbf{f}\,](y),\\ \boldsymbol{\varphi}(y) &=& [\,\mathcal{C}\,\boldsymbol{\xi}\,](y),\\ 0 &=& \mathcal{N}\,\boldsymbol{\xi}\,(y),\end{array}\right. \tag{9.17}$$

where

$$\boldsymbol{\xi}(y) = \left[\begin{array}{c}\boldsymbol{\phi}(y)\\ \boldsymbol{\psi}(y)\end{array}\right],\; \mathcal{A} = \left[\begin{array}{cc}\mathcal{A}_0 & -\mathcal{B}_0\,\mathcal{B}_0^{\star}\\ 0 & \mathcal{A}_0^{\star}\end{array}\right],$$

$$\mathcal{N} = \left[\begin{array}{cc}\mathcal{N}_0 & 0\\ 0 & \mathcal{N}_0^{\star}\end{array}\right],\; \mathcal{B} = \left[\begin{array}{c}0\\ \mathcal{C}_0^{\star}\end{array}\right],\; \mathcal{C} = \left[\begin{array}{cc}\mathcal{C}_0 & 0\end{array}\right].$$

Similarly, the spatial state-space representation of $\mathcal{T}\mathcal{T}^{\star}$ is obtained by equating the input $\mathbf{d}$ in (9.12) to the output $\mathbf{g}$ in (9.14), which yields

$$\mathcal{T}\mathcal{T}^{\star}:\left\{\begin{array}{rcl}\mathbf{q}'(y) &=& \mathbf{A}(y)\,\mathbf{q}(y) \;+\; \mathbf{B}(y)\,\mathbf{f}(y),\\ \boldsymbol{\varphi}(y) &=& \mathbf{C}(y)\,\mathbf{q}(y),\\ 0 &=& \mathbf{L}_a\,\mathbf{q}(a) \;+\; \mathbf{L}_b\,\mathbf{q}(b),\end{array}\right. \tag{9.18}$$

with

$$\begin{aligned}
\mathbf{q}(y) &= \begin{bmatrix} \mathbf{x}(y) \\ \mathbf{z}(y) \end{bmatrix}, \qquad \mathbf{A}(y) = \begin{bmatrix} \mathbf{A}_0(y) & \mathbf{B}_0(y)\,\mathbf{B}_0^*(y) \\ 0 & -\mathbf{A}_0^*(y) \end{bmatrix}, \\
\mathbf{B}(y) &= \begin{bmatrix} 0 \\ -\mathbf{C}_0^*(y) \end{bmatrix}, \quad \mathbf{C}(y) = \begin{bmatrix} \mathbf{C}_0(y) & 0 \end{bmatrix}, \\
\mathbf{L}_a &= \begin{bmatrix} \mathbf{N}_a & 0 \\ 0 & \mathbf{M}_a \end{bmatrix}, \quad \mathbf{L}_b = \begin{bmatrix} \mathbf{N}_b & 0 \\ 0 & \mathbf{M}_b \end{bmatrix}.
\end{aligned}$$

Since a cascade connection of two well-posed systems is well-posed, the existence and uniqueness of solutions of (9.17) and (9.18) is guaranteed by the well-posedness of the corresponding two point boundary value representations of $\mathcal{T}$ and $\mathcal{T}^\star$.

We next present a procedure for computing the largest singular value of $\mathcal{T}$ using the above representations of the operator $\mathcal{T}\mathcal{T}^\star$.

9.4 Computation of the largest singular value of $\mathcal{T}$

In this section, we utilize the structure of the two point boundary value representations (9.17) and (9.18) of $\mathcal{T}\mathcal{T}^\star$ to develop a method for computing the largest singular value of the frequency response operator $\mathcal{T}(\omega)$,

$$\sigma_{\max}^2\left(\mathcal{T}(\omega)\right) \;=\; \lambda_{\max}\left(\mathcal{T}(\omega)\,\mathcal{T}^\star(\omega)\right),$$

where $\lambda_{\max}(\cdot)$ denotes the largest eigenvalue of a given operator. In what follows, we present the procedure for computing the eigenvalues of $\mathcal{T}\mathcal{T}^\star$ using both input-output (9.17) and state-space (9.18) representations of $\mathcal{T}\mathcal{T}^\star$. This is done by first recasting the system of differential equations into a corresponding integral formulation; we then employ recently developed automatic Chebyshev spectral collocation method [37] to solve the eigenvalue problem for the resulting integral equation. Note that the eigenfunction corresponding to the largest singular value identifies the output of the system that is most amplified in the presence of disturbances. Similar procedure can be used to determine the principal eigenfunction of the operator $\mathcal{T}^\star\mathcal{T}$, thereby yielding the input that has the largest influence on the system's output.

The solution to a two point boundary value problem (9.17) can be obtained numerically by approximating the differential operators using, e.g., a pseudo-spectral collocation technique [32–35]. For differential equations of a high-order, the resulting finite-dimensional approximations may be poorly conditioned. This difficulty can be overcome by converting a high-order differential equation into a corresponding integral equation [164]. This conversion utilizes indefinite integration operators that are characterized by condition numbers that remain bounded upon discretization refinement. The procedure for achieving this conversion, described in Section 9.4.2, extends the result of [165] from a scalar case to a system of high-order differential equations. Furthermore, in Section 9.4.3 we show how a spatial state-space representation (9.18) can be transformed to an equivalent integral form. We then employ Chebfun's function eigs to perform the eigenvalue decomposition of the resulting system of equations.

9.4.1 An illustrative example

We first illustrate the procedure for converting a differential equation into its corresponding integral form using the 1D diffusion equation (9.3),

$$\left(D^{(2)} - \mathrm{i}\omega I\right)\phi(y) \;=\; -\,d(y), \tag{9.19a}$$

$$\left(\left[\begin{array}{c} 1 \\ 0 \end{array}\right] E_{-1} + \left[\begin{array}{c} 0 \\ 1 \end{array}\right] E_{1}\right)\phi(y) \;=\; \left[\begin{array}{c} 0 \\ 0 \end{array}\right]. \tag{9.19b}$$

System (9.19) can be converted into an equivalent integral equation by introducing an auxiliary variable

$$\nu(y) \;=\; \left[D^{(2)}\,\phi\right](y). \tag{9.20}$$

Integration of (9.20) yields

$$\begin{array}{rcl} \phi'(y) & = & \displaystyle\int_{-1}^{y} \nu(\eta_1)\,\mathrm{d}\eta_1 \;+\; k_1 \;=\; \left[J^{(1)}\,\nu\right](y) \;+\; k_1, \\ \phi(y) & = & \displaystyle\int_{-1}^{y}\left(\int_{-1}^{\eta_2} \nu(\eta_1)\,\mathrm{d}\eta_1\right)\mathrm{d}\eta_2 \;+\; k_1\,(y\,+\,1) \;+\; k_2 \\ & = & \left[J^{(2)}\,\nu\right](y) \;+\; K^{(2)}\,\mathbf{k}, \end{array} \tag{9.21}$$

where $J^{(1)}$ and $J^{(2)}$ denote the indefinite integration operators of degrees one and two, the vector $\mathbf{k} = \left[\begin{array}{cc} k_2 & k_1 \end{array}\right]^T$ contains the constants of integration which are to be determined from the boundary conditions (9.19b), and

$$K^{(2)} \;=\; \left[\begin{array}{cc} 1 & (y+1) \end{array}\right].$$

The integral form of the 1D diffusion equation is obtained by substituting (9.21) into (9.19),

$$\left(I - \mathrm{i}\omega J^{(2)}\right)\nu(y) \;-\; \mathrm{i}\omega\,K^{(2)}\,\mathbf{k} \;=\; -\,d(y), \tag{9.22a}$$

$$\left[\begin{array}{cc} 1 & 0 \\ 1 & 2 \end{array}\right]\left[\begin{array}{c} k_2 \\ k_1 \end{array}\right] \;+\; \left(\left[\begin{array}{c} 1 \\ 0 \end{array}\right] E_{-1} + \left[\begin{array}{c} 0 \\ 1 \end{array}\right] E_{1}\right)\left[J^{(2)}\nu\right](y) \;=\; \left[\begin{array}{c} 0 \\ 0 \end{array}\right]. \tag{9.22b}$$

Now, by observing that

$$E_{-1}\left[J^{(1)}\nu\right](y) \;=\; \int_{-1}^{-1}\nu(\eta)\,\mathrm{d}\eta \;=\; 0,$$

we can use (9.22b) to express the constants of integration $\mathbf{k}$ in terms of ν,

$$\begin{bmatrix} k_2 \\ k_1 \end{bmatrix} \;=\; -\frac{1}{2}\begin{bmatrix} 2 & 0 \\ -1 & 1 \end{bmatrix}\begin{bmatrix} 0 \\ 1 \end{bmatrix} E_1\left[J^{(2)}\,\nu\right](y) \;=\; \begin{bmatrix} 0 \\ -1/2 \end{bmatrix} E_1\left[J^{(2)}\,\nu\right](y). \tag{9.23}$$

Finally, substitution of (9.23) into (9.22a) yields an equation for ν,

$$\left(I \,-\, \mathrm{i}\omega J^{(2)} \,+\, \frac{1}{2}\mathrm{i}\omega\,(y\,+\,1)\,E_1 J^{(2)}\right)\nu(y) \;=\; -d(y). \tag{9.24}$$

Invertibility of the matrix that multiplies the integration constants $\mathbf{k} = \begin{bmatrix} k_2 & k_1 \end{bmatrix}^T$ in (9.22b) facilitated derivation of an explicit expression for $\mathbf{k}$ in terms of ν. For the 1D reaction-diffusion equation with homogenous Neumann boundary conditions,

$$\left(D^{(2)} \,-\, cI \,-\, \mathrm{i}\omega I\right)\phi(y) \;=\; -\,d(y), \tag{9.25a}$$

$$\left(\begin{bmatrix} 1 \\ 0 \end{bmatrix} E_{-1} + \begin{bmatrix} 0 \\ 1 \end{bmatrix} E_1\right)\left[D^{(1)}\phi\right](y) \;=\; \begin{bmatrix} 0 \\ 0 \end{bmatrix}, \tag{9.25b}$$

substitution of (9.21) to (9.25) yields

$$\left(I \,-\, (\mathrm{i}\omega \,+\, c)\,J^{(2)}\right)\nu(y) \,-\, (\mathrm{i}\omega \,+\, c)\,K^{(2)}\,\mathbf{k} \;=\; -\,d(y), \tag{9.26a}$$

$$\begin{bmatrix} 0 & 1 \\ 0 & 1 \end{bmatrix}\begin{bmatrix} k_2 \\ k_1 \end{bmatrix} \,+\, \begin{bmatrix} 0 \\ 1 \end{bmatrix} E_1\left[J^{(1)}\nu\right](y) \;=\; \begin{bmatrix} 0 \\ 0 \end{bmatrix}. \tag{9.26b}$$

A positive reaction rate c in (9.25a) ensures stability in the presence of Neumann boundary conditions.

Lack of invertibility of the matrix that multiplies the integration constants in (9.26b) is an obstacle to determining $\mathbf{k}$ explicitly in terms of ν. Instead, the dependence of ν on $\mathbf{k}$ and d can be obtained from (9.26a),

$$\nu(y) \;=\; \left(I \,-\, (\mathrm{i}\omega \,+\, c)\,J^{(2)}\right)^{-1}\left((\mathrm{i}\omega \,+\, c)\,K^{(2)}\,\mathbf{k} \,-\, d(y)\right). \tag{9.27}$$

Now, substitution of (9.27) to (9.26b) yields

$$\mathbf{k} \;=\; \mathbf{G}^{-1}\begin{bmatrix} 0 \\ 1 \end{bmatrix} E_1\,J^{(1)}\left(I \,-\, (\mathrm{i}\omega \,+\, c)\,J^{(2)}\right)^{-1} d(y), \tag{9.28}$$

where the matrix $\mathbf{G}$ is given by

$$\mathbf{G} \;=\; \begin{bmatrix} 0 & 1 \\ 0 & 1 \end{bmatrix} + \begin{bmatrix} 0 \\ 1 \end{bmatrix} E_1\, J^{(1)} \left(I \,-\, (\mathrm{i}\omega \,+\, c)\, J^{(2)}\right)^{-1} (\mathrm{i}\omega \,+\, c)\, K^{(2)}.$$

Finally, an equation for ν is obtained by substituting (9.28) into (9.26a),

$$\begin{gathered} \left(I \,-\, (\mathrm{i}\omega \,+\, c)\, J^{(2)}\right) \nu(y) \;= \\ \left((\mathrm{i}\omega \,+\, c)\, K^{(2)}\, \mathbf{G}^{-1} \begin{bmatrix} 0 \\ 1 \end{bmatrix} E_1\, J^{(1)} \left(I \,-\, (\mathrm{i}\omega \,+\, c)\, J^{(2)}\right)^{-1} \,-\, I \right) d(y). \end{gathered} \tag{9.29}$$

Systems (9.24) and (9.29) only contain indefinite integration operators and point evaluation functionals which are known to be well-conditioned. This is a major advantage compared to their corresponding input-output differential equations (9.19) and (9.25).

9.4.2 Integral form of a system of high-order differential equations

We now present the procedure for converting a system of high-order differential equations (9.17),

$$\mathcal{T}\mathcal{T}^{\star} : \begin{cases} [\,\mathcal{A}\,\boldsymbol{\xi}\,]\,(y) \;=\; [\,\mathcal{B}\,\mathbf{f}\,]\,(y), \\ \quad \boldsymbol{\varphi}(y) \;=\; [\,\mathcal{C}\,\boldsymbol{\xi}\,]\,(y), \\ \qquad\; 0 \;=\; \mathcal{N}\,\boldsymbol{\xi}\,(y), \end{cases} \tag{9.30}$$

to an equivalent integral form. The input and output vectors $\mathbf{f}(y)$ and $\boldsymbol{\varphi}(y)$ have p elements, $\boldsymbol{\xi}(y)$ is a $2s$-vector, and the operators in (9.30) are given by

$$\begin{aligned} \mathcal{A} \;&=\; \sum_{i\,=\,0}^{n} \mathbf{a}_i(y)\,\mathbf{D}^{(i)}, \quad & \mathcal{B} \;&=\; \sum_{i\,=\,0}^{k} \mathbf{b}_i(y)\,\mathbf{D}^{(i)}, \\ \mathcal{C} \;&=\; \sum_{i\,=\,0}^{k} \mathbf{c}_i(y)\,\mathbf{D}^{(i)}, \quad & \mathcal{N} \;&=\; \sum_{i\,=\,0}^{\ell} (\mathbf{Y}_{a,i}\,\mathbf{E}_a \,+\, \mathbf{Y}_{b,i}\,\mathbf{E}_b)\,\mathbf{D}^{(i)}. \end{aligned}$$

As illustrated in Section 9.4.1, instead of trying to find the solution $\boldsymbol{\xi}$ to (9.17) directly, we introduce two auxiliary variables, $\boldsymbol{\nu}$ and $\mathbf{k}$. The ith component of the vector $\boldsymbol{\nu}(y) = \left[\; \nu_1(y) \quad \ldots \quad \nu_{2s}(y) \;\right]^T$ is determined by

$$\nu_i(y) \;=\; \left[D^{(n_i)}\,\xi_i\right](y), \tag{9.31}$$

where n_i denotes the highest derivative of ξ_i in

$$[\,\mathcal{A}\,\boldsymbol{\xi}\,]\,(y) \;=\; [\,\mathcal{B}\,\mathbf{f}\,]\,(y).$$

Integration of (9.31) yields

$$\left[D^{(j)}\xi_i\right](y) \;=\; \left[J^{(n_i-j)}\nu_i\right](y) \,+\, K^{(n_i-j)}\,\mathbf{k}_i,\;\; j=0,\ldots,n_i, \tag{9.32}$$

where $\mathbf{k}_i \in \mathbb{C}^{n_i}$ is the vector of integration constants which are to be determined from the boundary conditions, $J^{(n_i)}$ is the indefinite integration operator of degree n_i with $J^{(0)}=0$, and $K^{(n_i)}$ is the matrix with columns that span the vector space of polynomials of degree less than n_i,

$$\begin{aligned} K^{(n_i)} \;&=\; \left[\; K_0(y) \quad K_1(y) \quad \cdots \quad K_{n_i-1}(y) \;\right], \quad K^{(0)} \;=\; 0, \\ K_0(y) \;=\; 1,\;\; K_j(y) \;&=\; \frac{1}{j!}\,(y-a)^j\,,\;\; j \;\geq\; 1. \end{aligned}$$

Substitution of (9.32) into (9.30) yields the integral representation of the operator $\mathcal{T}\mathcal{T}^\star$,

$$\mathcal{T}\mathcal{T}^\star : \left\{ \begin{array}{l} \begin{bmatrix} \mathcal{L}_{11} & \mathcal{L}_{12} \\ \mathcal{L}_{21} & \mathcal{L}_{22} \end{bmatrix} \begin{bmatrix} \boldsymbol{\nu} \\ \mathbf{k} \end{bmatrix} \;=\; \begin{bmatrix} \mathcal{B} \\ 0 \end{bmatrix} \mathbf{f}, \\ \boldsymbol{\varphi} \;=\; \left[\; \mathcal{P}_1 \quad \mathcal{P}_2 \;\right] \begin{bmatrix} \boldsymbol{\nu} \\ \mathbf{k} \end{bmatrix}, \end{array} \right. \tag{9.33}$$

where

$$\begin{aligned} \mathcal{L}_{11} \;&=\; \sum_{i=0}^{n} \mathbf{a}_i(y)\,\mathbf{J}^{(n-i)}, & \mathcal{L}_{12} \;&=\; \sum_{i=0}^{n} \mathbf{a}_i(y)\,\mathbf{K}^{(n-i)}, \\ \mathcal{L}_{21} \;&=\; \sum_{i=0}^{\ell} \mathbf{Y}_{b,i}\,\mathbf{E}_b\,\mathbf{J}^{(n-i)}, & \mathcal{L}_{22} \;&=\; \sum_{i=0}^{\ell} \left(\mathbf{Y}_{a,i}\,\mathbf{E}_a \,+\, \mathbf{Y}_{b,i}\,\mathbf{E}_b\right)\mathbf{K}^{(n-i)}, \\ \mathcal{P}_1 \;&=\; \sum_{i=0}^{k} \mathbf{c}_i(y)\,\mathbf{J}^{(n-i)}, & \mathcal{P}_2 \;&=\; \sum_{i=0}^{k} \mathbf{c}_i(y)\,\mathbf{K}^{(n-i)}, \end{aligned}$$

$$\begin{aligned} \mathbf{J}^{(n-i)} \;&=\; \begin{bmatrix} J^{(n_1-i)} & & \\ & \ddots & \\ & & J^{(n_{2s}-i)} \end{bmatrix}, \quad \mathbf{K}^{(n-i)} \;=\; \begin{bmatrix} K^{(n_1-i)} & & \\ & \ddots & \\ & & K^{(n_{2s}-i)} \end{bmatrix}, \\ J^{(i)} \;&=\; 0,\;\; K^{(i)} \;=\; 0, \quad i \;\leq\; 0. \end{aligned}$$

Using (9.33) we can determine an expression for the integration constants,

$$\mathcal{L}_{22}\,\mathbf{k} \;=\; -\left[\,\mathcal{L}_{21}\,\boldsymbol{\nu}\,\right](y). \tag{9.34}$$

If the matrix $\mathcal{L}_{22}$ is invertible, equation (9.34) in conjunction with (9.33) yields

$$\boldsymbol{\nu}(y) \;=\; \Big[\big(\mathcal{L}_{11} \,-\, \mathcal{L}_{12}\,\mathcal{L}_{22}^{-1}\,\mathcal{L}_{21}\,\big)^{-1}\,(\mathcal{B}\,\mathbf{f})\Big]\,(y), \tag{9.35a}$$

$$\boldsymbol{\varphi}(y) \;=\; \big[\big(\mathcal{P}_1 \,-\, \mathcal{P}_2\,\mathcal{L}_{22}^{-1}\,\mathcal{L}_{21}\,\big)\,\boldsymbol{\nu}\big]\,(y), \tag{9.35b}$$

and the representation of the operator $\mathcal{T}\mathcal{T}^\star$ is obtained by substituting (9.35a) into (9.35b). Thus, determination of the left singular functions $\{\mathbf{u}_n\}$ of the operator $\mathcal{T}$ amounts to solving the following eigenvalue problem

$$\Big[\big(\mathcal{P}_1 \,-\, \mathcal{P}_2\,\mathcal{L}_{22}^{-1}\,\mathcal{L}_{21}\,\big)\;\big(\mathcal{L}_{11} \,-\, \mathcal{L}_{12}\,\mathcal{L}_{22}^{-1}\,\mathcal{L}_{21}\,\big)^{-1}\,(\mathcal{B}\,\mathbf{u}_n)\Big]\,(y) \;=\; \sigma_n^2\,\mathbf{u}_n(y), \tag{9.36}$$

where σ_n denotes the corresponding singular value of $\mathcal{T}$.

On the other hand, if $\mathcal{L}_{22}$ is singular, we can determine an expression for $\boldsymbol{\nu}$ in terms of $\mathbf{k}$ and $\mathbf{f}$ from (9.33),

$$\boldsymbol{\nu}(y) \;=\; \big[\mathcal{L}_{11}^{-1}\,\mathcal{B}\,\mathbf{f}\big]\,(y) \,-\, \mathcal{L}_{11}^{-1}\,\mathcal{L}_{12}\,\mathbf{k}. \tag{9.37}$$

Furthermore, substitution of (9.37) into (9.34) yields

$$\mathbf{k} \;=\; -\mathbf{G}^{-1}\mathcal{L}_{21}\;\big[\mathcal{L}_{11}^{-1}\,\mathcal{B}\,\mathbf{f}\big]\,(y), \tag{9.38}$$

where the matrix $\mathbf{G}$ is given by

$$\mathbf{G} \;=\; \mathcal{L}_{22} - \mathcal{L}_{21}\,\mathcal{L}_{11}^{-1}\,\mathcal{L}_{12}.$$

This expression for $\mathbf{k}$ in conjunction with (9.33) yields

$$\boldsymbol{\nu}(y) \;=\; \big[\mathcal{L}_{11}^{-1}\,\big(\mathcal{B} \,+\, \mathcal{L}_{12}\,\mathbf{G}^{-1}\,\mathcal{L}_{21}\,\mathcal{L}_{11}^{-1}\mathcal{B}\big)\,\mathbf{f}\big]\,(y), \tag{9.39a}$$

$$\boldsymbol{\varphi}(y) \;=\; [\mathcal{P}_1\,\boldsymbol{\nu}]\,(y) \,-\, \big[\mathcal{P}_2\,\mathbf{G}^{-1}\,\mathcal{L}_{21}\,\mathcal{L}_{11}^{-1}\,\mathcal{B}\,\mathbf{f}\big]\,(y). \tag{9.39b}$$

The integral representation of the operator $\mathcal{T}\mathcal{T}^\star$ can be obtained by substituting (9.39a) into (9.39b), and the left singular pair $(\sigma_n, \mathbf{u}_n)$ of the operator $\mathcal{T}$ is determined from the solution to the following eigenvalue problem

$$\big[\big(\mathcal{P}_1\,\mathcal{L}_{11}^{-1} \,+\, \mathcal{P}_1\,\mathcal{L}_{11}^{-1}\,\mathcal{L}_{12}\,\mathbf{G}^{-1}\,\mathcal{L}_{21}\,\mathcal{L}_{11}^{-1} \,-\, \mathcal{P}_2\,\mathbf{G}^{-1}\,\mathcal{L}_{21}\,\mathcal{L}_{11}^{-1}\big)\,(\mathcal{B}\,\mathbf{u}_n)\big]\,(y) \;=\; \sigma_n^2\,\mathbf{u}_n(y). \tag{9.40}$$

9.4.3 Integral form of a spatial state-space representation

We next describe a procedure for transforming a spatial state-space representation (9.18),

$$\mathcal{T}\mathcal{T}^\star : \left\{ \begin{array}{rcl} \mathbf{q}'(y) & = & \mathbf{A}(y)\,\mathbf{q}(y) \;+\; \mathbf{B}(y)\,\mathbf{f}(y), \\ \boldsymbol{\varphi}(y) & = & \mathbf{C}(y)\,\mathbf{q}(y), \\ 0 & = & \mathbf{L}_a\,\mathbf{q}(a) \;+\; \mathbf{L}_b\,\mathbf{q}(b), \end{array} \right. \tag{9.41}$$

into a system of first-order integral equations. In a similar manner as in Section 9.4.2, we introduce two auxiliary variables $\boldsymbol{\nu}$ and $\mathbf{k}$ so that

$$\boldsymbol{\nu}(y) \;=\; \mathbf{q}'(y) \quad \Rightarrow \quad \mathbf{q}(y) = [\,\mathbf{J}\,\boldsymbol{\nu}\,]\,(y) \;+\; \mathbf{k}, \tag{9.42}$$

where $\mathbf{J}$ is a block diagonal matrix of the first order indefinite integration operators $J^{(1)}$,

$$\mathbf{J} \;=\; \begin{bmatrix} J^{(1)} & & \\ & \ddots & \\ & & J^{(1)} \end{bmatrix}.$$

Substitution of (9.42) into (9.41) yields a system of first order integral equations for the operator $\mathcal{T}\mathcal{T}^\star$,

$$\boldsymbol{\nu}(y) \;=\; \mathbf{A}(y)\;[\,\mathbf{J}\,\boldsymbol{\nu}\,]\,(y) \;+\; \mathbf{A}(y)\,\mathbf{k} \;+\; \mathbf{B}(y)\,\mathbf{f}(y), \tag{9.43a}$$

$$\boldsymbol{\varphi}(y) \;=\; \mathbf{C}(y)\,[\,\mathbf{J}\,\boldsymbol{\nu}\,]\,(y) \;+\; \mathbf{C}(y)\,\mathbf{k}, \tag{9.43b}$$

$$0 \;=\; (\mathbf{L}_a\,\mathbf{E}_a \;+\; \mathbf{L}_b\,\mathbf{E}_b)\,[\,\mathbf{J}\,\boldsymbol{\nu}\,]\,(y) \;+\; (\mathbf{L}_a \;+\; \mathbf{L}_b)\,\mathbf{k}. \tag{9.43c}$$

An expression for $\boldsymbol{\nu}$ in terms of the forcing $\mathbf{f}$ and the integration constants $\mathbf{k}$ can be obtained from (9.43a),

$$\boldsymbol{\nu}(y) \;=\; \Big[(\mathbf{I} - \mathbf{A}\,\mathbf{J})^{-1}\,(\mathbf{B}\,\mathbf{f})\Big]\,(y) \;+\; \Big[(\mathbf{I} - \mathbf{A}\,\mathbf{J})^{-1}\,\mathbf{A}\Big]\,(y)\;\mathbf{k}. \tag{9.44}$$

Furthermore, substitution of (9.44) into (9.43c) yields

$$\mathbf{k} \;=\; -\mathbf{H}^{-1}\,\mathbf{L}_b\,\mathbf{E}_b\,\Big[\mathbf{J}\,(\mathbf{I} - \mathbf{A}\,\mathbf{J})^{-1}\,\mathbf{B}\,\mathbf{f}\Big]\,(y), \tag{9.45}$$

where $\mathbf{H}$ is a matrix given by

$$\mathbf{H} \;=\; \mathbf{L}_b\,\mathbf{E}_b\,\Big[\mathbf{J}\,(\mathbf{I} - \mathbf{A}\,\mathbf{J})^{-1}\,\mathbf{A}\Big]\,(y) \;+\; \mathbf{L}_a \;+\; \mathbf{L}_b.$$

Finally, substitution of (9.44) and (9.45) into (9.43b) yields

$$\begin{aligned}\boldsymbol{\varphi}(y) \;=\; & \Big[\mathbf{C}\,\mathbf{J}\,(\mathbf{I}\,-\mathbf{A}\,\mathbf{J})^{-1}\,\mathbf{B}\,\mathbf{f}\Big]\,(y) \;-\; \Big[\mathbf{C}\,\mathbf{H}^{-1}\,\mathbf{L}_b\,\mathbf{E}_b\,\mathbf{J}\,(\mathbf{I}\,-\mathbf{A}\,\mathbf{J})^{-1}\,\mathbf{B}\,\mathbf{f}\Big]\,(y) \\ & -\;\Big[\mathbf{C}\,\mathbf{J}\,(\mathbf{I}\,-\mathbf{A}\,\mathbf{J})^{-1}\,\mathbf{A}\,\mathbf{H}^{-1}\,\mathbf{L}_b\,\mathbf{E}_b\,\mathbf{J}\,(\mathbf{I}\,-\mathbf{A}\,\mathbf{J})^{-1}\,\mathbf{B}\,\mathbf{f}\Big]\,(y),\end{aligned} \tag{9.46}$$

where invertibility of the matrix $\mathbf{H}$ follows from the well-posedness of the two-point boundary value problem (9.41). Thus, the singular values σ_n and the associated left singular functions $\mathbf{u}_n$ of $\mathcal{T}$ can be obtained by solving the following eigenvalue problem

$$\begin{aligned}& \Big[\mathbf{C}\,\mathbf{J}\,(\mathbf{I}\,-\mathbf{A}\,\mathbf{J})^{-1}\,\mathbf{B}\,\mathbf{u}_n\Big]\,(y) \;-\; \Big[\mathbf{C}\,\mathbf{H}^{-1}\,\mathbf{L}_b\,\mathbf{E}_b\,\mathbf{J}\,(\mathbf{I}\,-\mathbf{A}\,\mathbf{J})^{-1}\,\mathbf{B}\,\mathbf{u}_n\Big]\,(y) \\ & -\;\Big[\mathbf{C}\,\mathbf{J}\,(\mathbf{I}\,-\mathbf{A}\,\mathbf{J})^{-1}\,\mathbf{A}\,\mathbf{H}^{-1}\,\mathbf{L}_b\,\mathbf{E}_b\,\mathbf{J}\,(\mathbf{I}\,-\mathbf{A}\,\mathbf{J})^{-1}\,\mathbf{B}\,\mathbf{u}_n\Big]\,(y) \;=\; \sigma_n^2\,\mathbf{u}_n(y).\end{aligned} \tag{9.47}$$

In summary, the principal left singular pair of the operator $\mathcal{T}$ can be determined by rewriting either the input-output differential equation (9.17) or the system of first-order differential equations (9.18) representing $\mathcal{T}\mathcal{T}^\star$ into their respective integral forms (9.33) and (9.43). The resulting eigenvalue problems (9.36) and (9.47) are solved using Chebfun [37]. The detailed discussion on how Chebfun can be used to solve the eigenvalue problems (9.36) and (9.47) is relegated to 9.8.

9.5 Examples

We next use our method to study frequency responses of two systems from fluid mechanics: the three-dimensional incompressible channel flow of Newtonian fluids, and the two-dimensional inertialess channel flow of viscoelastic fluids. In the latter example, we show how numerical instabilities encountered when using finite dimensional approximation techniques can be alleviated. The utility of theoretical and computational tools of this work goes beyond fluids; they can be used to examine dynamics of a broad class of physical systems with normal or non-normal dynamical generators, and spatially constant or varying coefficients.

9.5.1 Three-dimensional incompressible channel flows of Newtonian fluids

We first study the dynamics of infinitesimal three-dimensional fluctuations in a pressure-driven channel flow with base velocity $U(y) = 1 - y^2$; see figure 9.4 for geometry. As shown in [77], the linearized Navier-Stokes (NS) equations can be brought to the evolution form (9.7) with state $\boldsymbol{\phi} = \begin{bmatrix} \phi_1 & \phi_2 \end{bmatrix}^T$, where ϕ_1 and ϕ_2 are the normal velocity and vorticity fluctuations. Furthermore, $\mathbf{d} = \begin{bmatrix} d_1 & d_2 & d_3 \end{bmatrix}^T$ and $\boldsymbol{\varphi} = \begin{bmatrix} u & v & w \end{bmatrix}^T$ are the input and output fields whose components represent the body forcing and velocity fluctuations in the three spatial directions, x, y, and z. Owing to translational

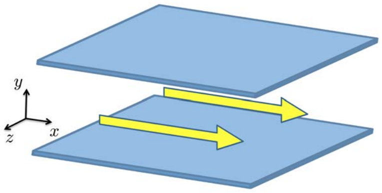

Figure 9.4: Channel flow geometry.

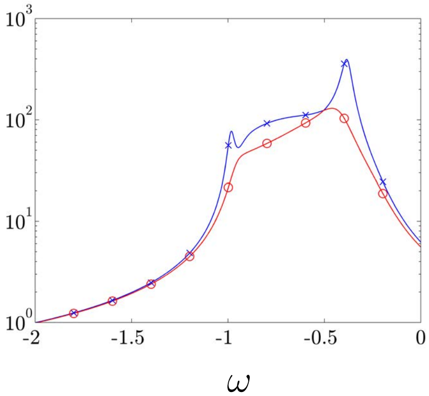

Figure 9.5: Two largest singular values of the frequency response operator for the linearized Navier-Stokes equations as a function of the temporal frequency ω in the flow with $R = 2000$, $k_x = 1$, and $k_z = 1$: blue $\times$, $\sigma_1(\mathcal{T})$; and red $\circ$, $\sigma_2(\mathcal{T})$.

invariance in x and z, (9.7) is parameterized by the corresponding wave numbers k_x and k_z with the boundary conditions on the normal velocity and vorticity,

$$\begin{array}{rcl} \phi_1(k_x, \pm 1, k_z, t) & = & D^{(1)}\phi_1(k_x, \pm 1, k_z, t) \;\; = \;\; 0, \\ \phi_2(k_x, \pm 1, k_z, t) & = & 0, \qquad k_x, k_z \in \mathbb{R}, \quad t \geq 0. \end{array}$$

The operators in (9.7) are given in 9.9 and, for any pair of k_x and k_z, they are matrices of differential operators in $y \in [-1, 1]$.

In what follows, we set the Reynolds number to $R = 2000$, $k_x = k_z = 1$ and compute the singular values of $\mathcal{T}$ using the method developed in Section 9.4.2. Figure 9.5 shows two largest singular values, σ_1 and σ_2, of the frequency response operator $\mathcal{T}$ for the linearized NS equations as a function of the temporal frequency ω. The largest singular value σ_1 exhibits two distinct peaks at $\omega \approx -1$ and $\omega \approx -0.4$. These peaks are caused by different physical mechanisms which can be uncovered by investigating responses from individual forcing to individual velocity components [77]. The discussion of these mechanisms is beyond the scope of this dissertation.

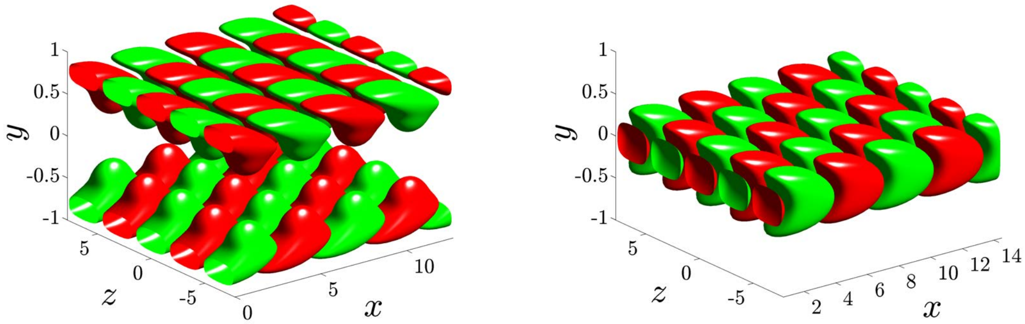

(a) (b)

Figure 9.6: Streamwise velocity fluctuation development for largest singular value of the frequency response operator in a pressure-driven channel flow with R $= 2000$, $k_x = k_z = 1$, (a) $\omega = -0.385$, and (b) $\omega = -0.982$. High and low velocity regions are represented by red and green colors. Isosurfaces of u are taken at ± 0.55.

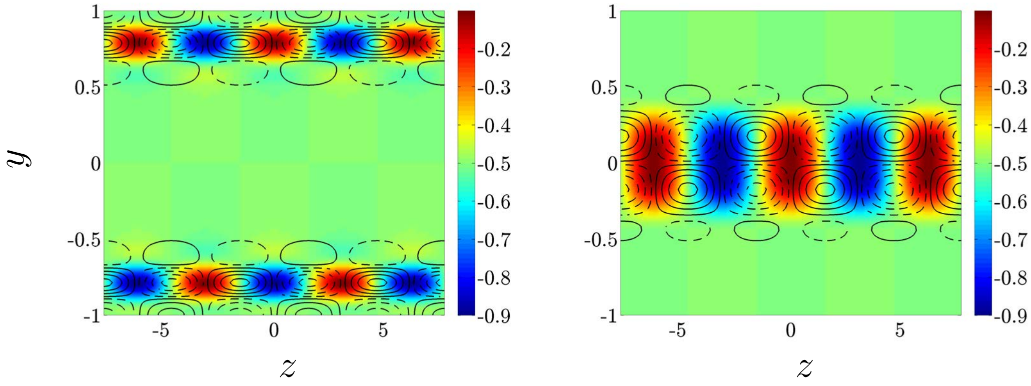

(a) (b)

Figure 9.7: Streamwise velocity (color plots) and vorticity, $\omega_x = \partial_y w - \partial_z v$, (contour lines) fluctuation development for largest singular value of the frequency response operator in the cross section of a pressure-driven channel flow with $R = 2000$, $k_x = k_z = 1$, (a) $\omega = -0.385$, and (b) $\omega = -0.982$. Red color represents high speed and blue color represents low speed streaks.

Figure 9.6 shows the isosurface plots of the most amplified streamwise velocity fluctuations corresponding to the two peaks shown in figure 9.5. These structures are purely harmonic in x, z, and t, and their profiles in y are determined by the the left principal singular functions of the frequency response operator at $\omega = -0.385$ and $\omega = -0.982$. For $\omega = -0.385$, u is localized in the near-wall region. On the other hand, for $\omega = -0.982$ the fluctuations occupy the center of the channel. The development of the streamwise velocity (color plots), and streamwise vorticity $\omega_x = \partial_y w - \partial_z v$ (contour lines) fluctuations in the channel's cross-section is shown in figure 9.7. For $\omega = -0.385$, the most amplified set of fluctuations results in pairs of counter rotating streamwise vortices that generate high and low velocity in the vicinity of the lower and upper walls. In contrast, for $\omega = -0.982$ there is a large concentration of arrays of counter rotating streamwise vortices in the center of the channel. Even though the spatial patterns identified by our analysis represent an idealized view of the flow, their utility in understanding the early stages of transition to turbulence has been well-documented [89].

9.5.2 Inertialess channel flow of viscoelastic fluids

We next compute the frequency responses of the inertialess flow of viscoelastic fluids presented in Section 9.2.1. This example illustrates the utility of our method in situations where standard finite dimensional approximations may fail to produce accurate results. For this example, the input-output and spatial state-space representations of the frequency response operator are given in 9.10. We compute the largest singular value using the procedure described in Section 9.4 and provide comparison of our results with those obtained using a pseudo-spectral collocation method [83].

It is well-known that inertialess flows of viscoelastic fluids exhibit spurious numerical instabilities at high-Weissenberg numbers [125, 126]. In view of this, we fix $k_x = 1$, $\beta = 0.5$, and $\omega = 0$ and examine the effects of the Weissenberg number, We, on the frequency response. We first compute the largest singular value of $\mathcal{T}$ using a pseudo-spectral collocation method [83]. This is achieved by approximating the operators in the input-output representation (9.17) of $\mathcal{T}\mathcal{T}^\star$ with differentiation matrices of different sizes. Figure 9.8(a) shows that $\sigma_{\max}$ converges as the number of collocation points, N, increases from 50 to 200 for $1 \leq We \leq 9$. However, for $We > 9$ the increased number of collocation points in y does not necessarily produce convergent results; see figure 9.8(b). Furthermore, in certain cases, the eigenvalues of the operator $\mathcal{T}\mathcal{T}^\star$ computed using pseudo-spectral method have large negative values. This is clearly at odds with the fact that $\mathcal{T}\mathcal{T}^\star$ is a non-negative self-adjoint operator, which indicates that the negative eigenvalues arise from numerical artifacts.

Figures 9.8(c) and 9.8(d) show the largest singular value of the operator $\mathcal{T}$ computed using the method of Section 9.4. For $1 \leq We \leq 9$, the largest singular values obtained in Chebfun for both input-output and spatial state-space integral representations of $\mathcal{T}\mathcal{T}^\star$ are equal to each other and they agree with the results of pseudo-spectral method; see

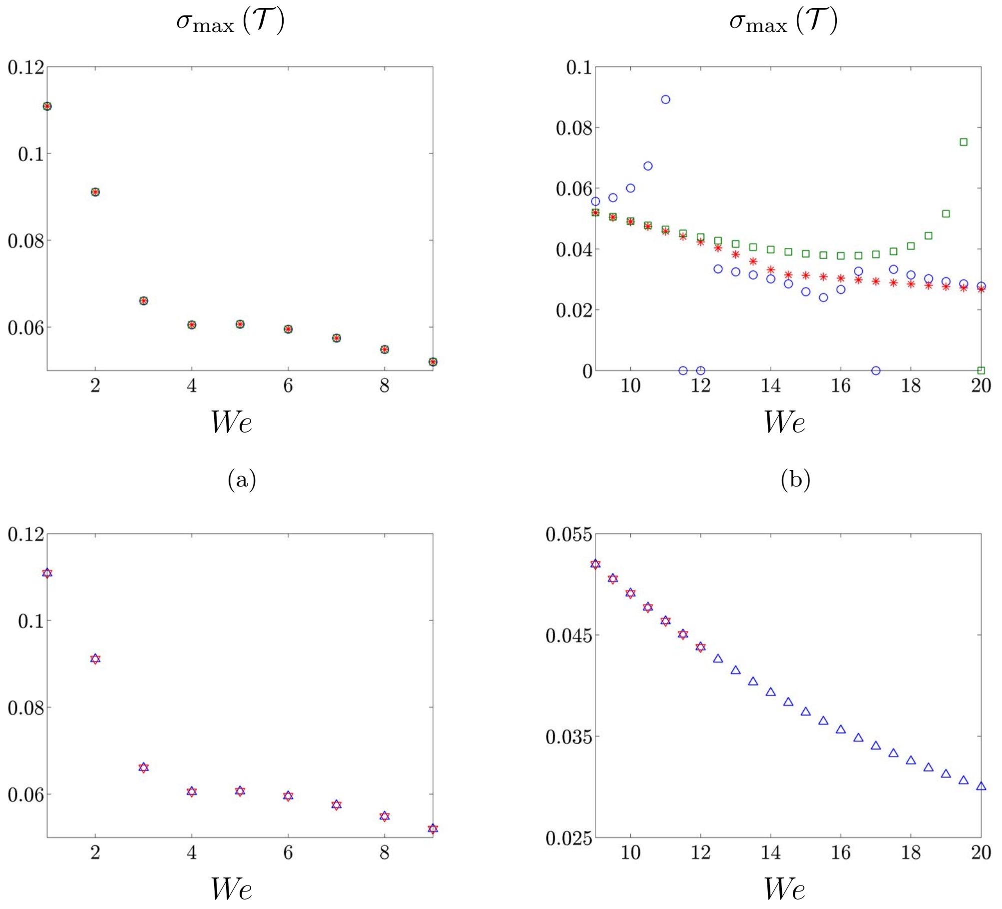

(a) (b)

(c) (d)

Figure 9.8: The largest singular values of the frequency response operator for an inertialess shear-driven channel flow of viscoelastic fluids as a function of We at $k_x = 1$, $\beta = 0.5$, and $\omega = 0$. Results are obtained using: (a) and (b) Pseudo-spectral method with $N = 100$, blue ∘; $N = 150$, red *; and $N = 200$, green □; (c) and (d) Chebfun with integral forms of input-output differential equations, blue △; and spatial state-space representations, red ▽.

figure 9.8(c). For $We > 9$ we see that the largest singular value computed using Chebfun exhibits nice trends as We increases. Furthermore, automatic Chebyshev spectral collocation method employed by Chebfun makes sure that grid point convergence of the singular values is satisfied. We note that the singular values computed using the input-output and spatial state-space integral representations of $\mathcal{T}\mathcal{T}^\star$ are equal to each other for $We \leq 12$. On the laptop used for computations, MATLAB has experienced memory issues when solving the eigenvalue problem in the state-space formulation (9.47) for $We > 12$. These memory issues may arise from solving a large system of linear equations internally in Chebfun. We have not observed any problems with memory when solving eigenvalue problem obtained from the the input-output equation in its integral form (9.36). We further note that the singular values can be computed accurately using the input-output integral representation at much higher Weissenberg numbers.

We next present the principal singular functions corresponding to the streamwise and normal velocity fluctuations in a flow with $We = 20$. These are obtained using pseudo-spectral method and Chebfun with the input-output integral representation. Figures 9.9(a) and 9.9(b) show the spatial profiles of velocity fluctuations that experience the largest amplification in the presence of disturbances. These profiles are obtained using pseudo-spectral method with different number of collocation points. Note the lack of convergence as the number of collocation points is increased. On the other hand, Chebfun does not suffer from numerical instabilities, and the corresponding principal singular functions exhibit nice symmetry with respect to the center of the channel; see figures 9.9(c) and 9.9(d). Similar trends are observed for larger values of We.

9.6 Concluding remarks

We have developed a method for computing the principal singular value and the corresponding singular functions of the frequency response operator for distributed systems with a spatial variable that belongs to a compact interval. Our method avoids the need for numerical approximation of differential operators in the evolution equation. This is achieved by recasting the frequency response operator as a two point boundary value problem, a formulation well-suited for employing Chebfun computing environment. When dealing with spatial differential operators of high order our method exhibits two advantages over conventional techniques: numerical ill-conditioning associated with high-order differential matrices is overcome; and boundary conditions are easily implemented and satisfied. We have provided examples from Newtonian and viscoelastic fluid dynamics to illustrate the utility of our developments.

Our method has been enhanced by the development of easy-to-use MATLAB functions which take the system's coefficients and boundary condition matrices as inputs and yield the desired number of left (or right) singular pairs as the output. The coefficients and boundary conditions of the adjoint systems are automatically implemented within the code using the method described in this chapter. The burden of finding the adjoint

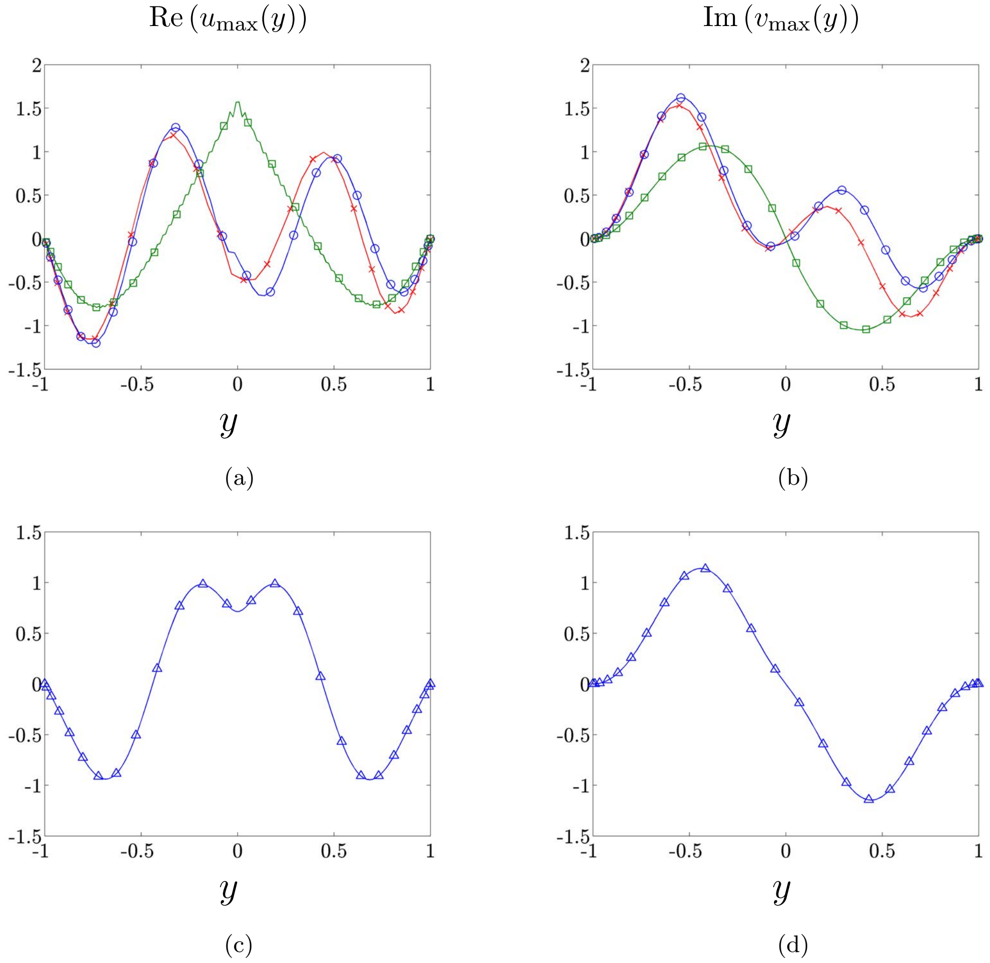

(a) (b) (c) (d)

Figure 9.9: Principal singular functions of the frequency response operator for inertialess shear-driven flow of viscoelastic fluids with $We = 20$, $k_x = 1$, and $\beta = 0.5$. First column: real part of $u_{\max}$; second column: imaginary part of $v_{\max}$. Results are obtained using: (a) and (b) Pseudo-spectral method with $N = 50$, red ×; $N = 100$, blue $\circ$; $N = 200$, green $\square$; (c) and (d) Chebfun with integral form of input-output differential equations.

operators and boundary conditions is thus removed from the user who can instead focus on interpreting results and understanding the essential physics.

Even though we have confined our attention to computation of the frequency responses for PDEs, the developed framework allows users to employ Chebfun as a tool for determining singular value decomposition of compact operators that admit two point boundary value representations. In particular, our approach paves the way for overloading MATLAB's command svds, from matrices to compact operators.

While the body of the chapter focuses on PDEs with distributed input and output fields, by considering an Euler-Bernoulli beam with boundary actuation in 9.11, we illustrate how Chebfun can be used to compute frequency responses of systems with boundary inputs. This problem turns out to be much simpler than the problems with distributed inputs, and it can be implemented with only few lines of code in Chebfun. We also use this example to demonstrate the utility of integral formulation in producing accurate results even for systems with poorly scaled coefficients.

In all examples that we considered, it is much more efficient to compute the eigenvalue pairs for a system of high-order integral equations (9.36) than for a system of first-order integral equations (9.47). We believe that larger number of dependent variables is reducing efficiency of computations that rely on spatial state-space representation. We note that Chebfun automatically adjust the number of collocation points in order to obtain solutions with an *a priori* specified tolerance. The computational speed can be increased by lowering this tolerance using the following command in MATLAB

```
chebfunpref('res', tolerance).
```

Our ongoing efforts are focused on employing Chebfun as a tool for computing the peak (over temporal frequency) of the largest singular value of the frequency response operator. In systems and controls literature, $\sup_{\omega} \sigma_{\max} (\mathcal{T}(\omega))$ is known as the H_∞ norm and its computation requires identification of purely imaginary eigenvalues of a Hamiltonian operator in conjunction with bisection [119,120]. In addition to quantifying the worst-case amplification of purely harmonic (in time) deterministic (in space) disturbances, the inverse of the H_∞ norm determines the size of an unstructured modeling uncertainty that can destabilize the nominal system. Thus, large frequency response peaks indicate small stability margins (i.e., poor robustness properties to modeling imperfections), and they are a reliable predictor of systems in which small modeling imperfections can introduce instability. This interpretation of the H_∞ norm is closely related to the notion of pseudospectra of linear operators [31] and it has been used to provide useful insight into dynamics of systems with non-normal generators [75, 89].

All MATLAB codes for computing frequency responses are available for download at

www.umn.edu/∼mihailo/software/chebfun-svd/

9.7 Appendix: Conversion to a spatial state-space realization

We next describe how a high-order ODE with spatially varying coefficients can be converted to a family of first-order ODEs (9.12). We consider the following ordinary differential equation with boundary conditions:

$$\begin{aligned}
\phi^{(n)}(y) \;&=\; -\sum_{i=0}^{n-1} \alpha_i(y)\,\phi^{(i)}(y) \,+\, \sum_{i=0}^{m} \beta_i(y)\,d^{(i)}(y),\;\; m \,<\, n \,-\, \ell, && \text{(9.48a)}\\
\varphi(y) \;&=\; \sum_{i=0}^{k} \gamma_i(y)\,\phi^{(i)}(y),\;\; k \,<\, n \,-\, m, && \text{(9.48b)}\\
0 \;&=\; \sum_{i=0}^{\ell} N_{i,a}\,\phi^{(i)}(a) \,+\, N_{i,b}\,\phi^{(i)}(b),\;\; \ell \,<\, n, && \text{(9.48c)}
\end{aligned}$$

where $\phi^{(i)} = \mathrm{d}^i\phi/\mathrm{d}y^i$. Since coefficients $\{\beta_i(y)\}$ in (9.48a) are spatially varying, the standard observer and controller canonical forms cannot be used to obtain a system of first-order ODEs (9.12). Instead, we introduce a new variable $w(y)$,

$$w(y) = \sum_{i=0}^{m} \beta_i(y)\,d^{(i)}(y), \tag{9.49}$$

and substitute (9.49) into (9.48a) to obtain

$$\phi^{(n)}(y) = -\sum_{i=0}^{n-1} \alpha_i(y)\,\phi^{(i)}(y) \,+\, w(y), \tag{9.50}$$

Here, a state-space realization of (9.50) is given by the controller canonical form,

$$\begin{aligned}
\mathbf{z}'(y) \;&=\; \mathbf{A}_1(y)\,\mathbf{z}(y) \,+\, \mathbf{e}_n\,w(y), && \text{(9.51a)}\\
\phi(y) \;&=\; \mathbf{e}_1^T\,\mathbf{z}(y), && \text{(9.51b)}
\end{aligned}$$

where

$$\mathbf{A}_1(y) \;=\; \left[\begin{array}{c|c} \mathbf{0}_{(n-1)\times 1} & \mathbf{I}_{(n-1)\times(n-1)} \\ \hline -\alpha_0(y) & -\alpha_1(y) \;\;\cdots\;\; -\alpha_{n-1}(y) \end{array}\right],$$

and $\mathbf{e}_i$ is the ith unit vector. It is a standard fact that the solution to (9.51) is given by

$$\mathbf{z}(y) \;=\; \mathbf{\Phi}_1(y,a)\,\mathbf{z}(a) \,+\, \int_a^y \mathbf{\Phi}_1(y,\eta)\,\mathbf{e}_n\,w(\eta)\,\mathrm{d}\eta, \tag{9.52}$$

where $\mathbf{\Phi}_1(y,\eta)$ is the state-transition matrix of $\mathbf{A}_1(y)$. Substituting (9.49) into (9.52) yields

$$\mathbf{z}(y) \;=\; \mathbf{\Phi}_1(y,a)\,\mathbf{z}(a) \,+\, \int_a^y \left(\mathbf{\Phi}_1(y,\eta)\,\mathbf{e}_n\left(\sum_{i\,=\,0}^{m}\beta_i(\eta)\,d^{(i)}(\eta)\right)\right)\mathrm{d}\eta. \tag{9.53}$$

Application of integration by parts to the integral in (9.53) along with a change of variables leads to the following two point boundary value state-space representation of (9.48)

$$\begin{aligned} \mathbf{x}'(y) &= \mathbf{A}_0(y)\,\mathbf{x}(y) \,+\, \mathbf{B}_0\,d(y), && (9.54\text{a})\\ \varphi(y) &= \mathbf{C}_0\,\mathbf{x}(y), && (9.54\text{b})\\ 0 &= \mathbf{N}_a\,\mathbf{x}(a) \,+\, \mathbf{N}_b\,\mathbf{x}(b), && (9.54\text{c}) \end{aligned}$$

where

$$\begin{aligned} \mathbf{x}(y) &= \mathbf{z}(y) \,-\, \sum_{i\,=\,0}^{m\,-\,1}\left(\sum_{j\,=\,1}^{m\,-\,i}\mathbf{Q}_{j-1}(\beta_{i+j}(y))\right)d^{(i)}(y),\\ \mathbf{A}_0(y) &= \mathbf{A}_1(y), \;\; \mathbf{B}_0(y) \;=\; \sum_{i\,=\,0}^{m}\mathbf{Q}_i(\beta_i(y)),\\ \mathbf{C}_0(y) &= \Big[\underbrace{\gamma_0(y)\;\;\cdots\;\;\gamma_k(y)}_{k\,+\,1}\;\underbrace{0\;\;\cdots\;\;0}_{n\,-\,k\,-\,1}\Big],\\ \mathbf{N}_a &= \begin{bmatrix} N_{0,a} & & \\ & \ddots & \\ & & N_{\ell,a}\end{bmatrix}, \;\; \mathbf{N}_b \;=\; \begin{bmatrix} N_{0,b} & & \\ & \ddots & \\ & & N_{\ell,b}\end{bmatrix}. \end{aligned}$$

We note that, for a given function β, $\mathbf{Q}_i$ can be recursively determined from

$$\begin{aligned} \mathbf{Q}_i(\beta(y)) &= \mathbf{A}_1(y)\,\mathbf{Q}_{i\,-\,1}(\beta(y)) \,-\, \frac{\mathrm{d}}{\mathrm{d}y}\mathbf{Q}_{i\,-\,1}(\beta(y)), \quad i = 1,\,\ldots,\,m,\\ \mathbf{Q}_0(\beta(y)) &= \mathbf{e}_n\,\beta(y). \end{aligned}$$

9.8 Appendix: Implementation of eigenvalue problems in integral formulation using Chebfun

The eigenvalue problems (9.36) and (9.47) derived in Sections 9.4.2 and 9.4.3 are solved using Chebfun. Here, we show how to implement the functions and operators in Chebfun to solve (9.36); a similar procedure can be used to solve (9.47). The eigenvalue problem (9.36) requires the construction of a number of operators and quasimatrices (terminology used by the authors of Chebfun to denote vectors of functions). The operator $\mathcal{A}$ in (9.30) is represented by the coefficients $\mathbf{a}_i(y)$ which are functions determining columns of a quasimatrix. For example, consider the differential equations representing the operator $\mathcal{T}\mathcal{T}^\star$ for the 1D diffusion equation

$$\begin{aligned}
\begin{bmatrix} D^{(2)} - \mathrm{i}\omega I & -I \\ 0 & D^{(2)} + \mathrm{i}\omega I \end{bmatrix} \begin{bmatrix} \xi_1(y) \\ \xi_2(y) \end{bmatrix} &= \begin{bmatrix} 0 \\ I \end{bmatrix} f(y), \\
\phi(y) &= \begin{bmatrix} I & 0 \end{bmatrix} \begin{bmatrix} \xi_1(y) \\ \xi_2(y) \end{bmatrix}, \\
\begin{bmatrix} 1 & 0 \\ 0 & 0 \end{bmatrix} \begin{bmatrix} \xi_1(-1) \\ \xi_1'(-1) \end{bmatrix} + \begin{bmatrix} 0 & 0 \\ 1 & 0 \end{bmatrix} \begin{bmatrix} \xi_1(+1) \\ \xi_1'(+1) \end{bmatrix} &= \begin{bmatrix} 0 \\ 0 \end{bmatrix}, \\
\begin{bmatrix} 1 & 0 \\ 0 & 0 \end{bmatrix} \begin{bmatrix} \xi_2(-1) \\ \xi_2'(-1) \end{bmatrix} + \begin{bmatrix} 0 & 0 \\ 1 & 0 \end{bmatrix} \begin{bmatrix} \xi_2(+1) \\ \xi_2'(+1) \end{bmatrix} &= \begin{bmatrix} 0 \\ 0 \end{bmatrix}.
\end{aligned} \tag{9.55}$$

The code used to generate operator $\mathcal{A}$ for the 1D diffusion equation is given by

```
%% Operator A for the 1D diffusion equation
dom = domain(-1,1);     % domain of functions
fone = chebfun(1,dom);  % fone(y) = 1
fzero = chebfun(0,dom); % fzero(y) = 0

% w is the temporal frequency and 1i is the imaginary unit
% (1,1) element of operator A
% -i*w*xi_1 + 0*D^{(1)}*xi_1 + 1*D^{(2)}*xi_1
A11 = [-1i*w*fone, fzero, fone];
% (1,2) element of operator A
% -1*xi_2 + 0*D^{(1)}*xi_2 + 0*D^{(2)}*xi_2
A12 = [-fone, fzero, fzero];
% (2,1) element of operator A
% 0*xi_1 + 0*D^{(1)}*xi_1 + 0*D^{(2)}*xi_1
A21 = [fzero, fzero, fzero];
% (2,2) element of operator A
% i*w*xi_1 + 0*D^{(1)}*xi_1 + 1*D^{(2)}*xi_1
A22 = [1i*w*fone, fzero, fone];

% form operator A using cell-array construction
A = {A11, A12; A21, A22};
```

The variable dom denotes the domain of the functions, and fone and fzero represent unit and zero functions. The dimension of each Chebfun's function in MATLAB is $\infty \times 1$, where the first index represents the continuous variable y. Hence, the quasimatrices

A11, A12, A21, and A22 have dimensions $\infty \times 3$. Since the dimension of quasimatrices prohibits the construction of matrix of functions, we instead utilize MATLAB's cell arrays (using curly brackets) to represent the operator $\mathcal{A}$. The boundary condition matrices are given by

```
Ya1 = [1, 0; 0, 0];  Ya2 = [1, 0; 0, 0];
Yb1 = [0, 0; 1, 0];  Yb2 = [0, 0; 1, 0];
Ya  = {Ya1; Ya2};    Yb  = {Yb1; Yb2};
```

The code used to generate the quasimatrix $\mathbf{K}^{(n)}$ is given by

```
n = size(A,1); % number of states in your system of ODEs
% determine the highest differential order of each component of \xi
% in the equations
ni = zeros(n,1);
for j = 1:n
ni(j) = size( A{j,j}, 2) - 1;
end
% indefinite integration operator
J = cumsum(dd);
%% Construct each component of K
Ki = chebfun(1,dd);
for j = 2 : max(ni)
Ki(:,j) = J*Ki(:, j-1);
end
% construct quasimatrix K using cell-array
for j = 1:n
K{j} = Ki(:, 1:ni(j));
end
```

The indefinite integration operator is obtained using Chebfun's command cumsum. The variable ni contains the highest differential order of each state ξ_i in the system. We next determine the matrix $\mathcal{L}_{22}$ appearing in (9.33) by applying the boundary condition operator $\mathcal{N}$ to $\mathbf{K}$. The following code is used to generate $\mathcal{L}_{22}$

```
%% Determine the matrix L_{22}
% loop through each component of \xi
for j = 1:n
% quasimatrix K associated with \xi_{j}
Kj = K{j};
L22{j} = Ya{j} + Yb{j}*toeplitz([1 zeros(1, ni(j)-1)], Kj( b, : ));
end
```

The qausimatrix $\mathcal{L}_{12}$ is obtained by multiplying coefficients of the operator $\mathcal{A}$ with the quasimatrix $\mathbf{K}$,

```
%% Determine the functional operator L_{12}
% loop through each component of L_{12}, which has size n x n
for i = 1:n
for j = 1:n
% initialize the (i,j) component of L_{12} and
% get the quasimatrix K associated with \xi_{j}
L12ij = 0; Kj = K{j};
% get the (i,j) component of operator A
Aij = A{i,j};
for indni = 1 : ni(j)
L12ij = L12ij + diag( Aij(:, ind) )*Kj;
Kj = [  chebfun(0,dd), Kj(:, 1:ni(j) - 1) ];
end
L12{i, j} = L12ij;
end
end
```

The operator $\mathcal{L}_{11}$ in (9.33) is realized using the following MATLAB's commands

```
%% Determine the operator L_{11}
% loop through each component of L_{11}, which has size n x n
for i = 1 : n
for j = 1 : n
% get the (i,j) component of A
Aij = A{i,j};
% initialize (i,j) component of L11 with Aij_0
L11ij = diag( Aij(:,1) );
for indni = 1 : ni(j) - 1
L11ij = L11ij*J + diag( Aij(:, indni + 1) );
end
L11ij = L11ij*J + diag( Aij(:, ni(j) + 1) );
L11{i,j} = L11ij;
end
end
```

The boundary point evaluation functional E_b is easily constructed by

```
Eb = linop(@(n) [zeros(1,n-1) 1], @(u) feval(u,b), dd);
```

In a similar manner, the operator $\mathcal{L}_{21}$ is realized by

```
%% Determine the operator L_{21}
% loop through each component of L_{21} which has size of n x 1
for j = 1:n
```

```
% get the j component of the boundary condition matrix Yb
Ybj = Yb{j};
L21j = Ybj(:,1)*Eb;
for indni = 1 : ni(j) - 1
L21j = L21j*J + Ybj(:, ind+1)*Eb;
end
L21{j} = L21j*J;
end
```

We note that the operators $\mathcal{P}_1$ and $\mathcal{P}_2$ in (9.33) can be constructed using similar procedure. We have shown how to construct all operators and quasimatrices appearing in (9.33). However, the eigenvalue problem (9.36) requires the operator $\mathcal{L}_{12}\,\mathcal{L}_{22}^{-1}\,\mathcal{L}_{21}$. This operator can only be realized using explicit construction [165] because Chebfun syntax does not allow this expression to be formed directly.

```
%% determining the operator H = L_{12} L_{22}^{-1} L_{21}
% looping through each component of H which has size of n x n
for i = 1:n
for j = 1:n
L12ij = L12{i,j};
L22j = L22{j};
L21j = L21{j};

% m-by-m discretization of H (discretized form)
mat = @(m) L12ij( chebpts(m,dom), : )*( L22j \ L21j(m) );
% functional expression of H (functional form)
op = @(v) L12ij*( L22j \ (L21j*v) );
% explicit construction of a linear operator in Chebfun
H{i,j} = linop(mat,op,dom);
end
end
```

A similar procedure is used to construct the operator $\mathcal{P}_2\,\mathcal{L}_{22}^{-1}\,\mathcal{L}_{21}$. Finally, Chebfun's eigenvalue solver (eigs) is used to compute the eigenvalues and eigenfunctions. We note that we use similar method to construct the operators for the spatial state-space representation of the eigenvalue problem discussed in Section 9.4.3. For brevity, they are not presented here. All codes for solving the eigenvalue problems in the integral formulation using Chebfun are available at

www.umn.edu/∼mihailo/software/chebfun-svd/.

9.9 Appendix: Representations of the frequency response operator for the linearized Navier-Stokes equations

In this section, we provide the input-output and spatial state-space representations of the frequency response operator for the linearized NS equations. The input-output differential equations for the three-dimensional incompressible channel flow are given by

$$\mathcal{T}: \left\{ \begin{array}{l} \big(\mathbf{a}_4\,\mathbf{D}^{(4)} \,+\, \mathbf{a}_2(y)\,\mathbf{D}^{(2)} \,+\, \mathbf{a}_0(y)\big)\,\boldsymbol{\phi}(y) \;=\; \big(\mathbf{b}_1\,\mathbf{D}^{(1)} \,+\, \mathbf{b}_0\big)\,\mathbf{d}(y), \\ \left[\begin{array}{c} u \\ v \\ w \end{array}\right] \;=\; \big(\mathbf{c}_1\,\mathbf{D}^{(1)} \,+\, \mathbf{c}_0\big)\,\boldsymbol{\phi}(y), \\ 0 = \big((\mathbf{W}_{-1,1}\,\mathbf{E}_{-1} \,+\, \mathbf{W}_{1,1}\,\mathbf{E}_1)\mathbf{D}^{(1)} \,+\, (\mathbf{W}_{-1,0}\,\mathbf{E}_{-1} \,+\, \mathbf{W}_{1,0}\,\mathbf{E}_1)\big)\,\boldsymbol{\phi}(y), \end{array} \right. \tag{9.56}$$

where

$$\mathbf{a}_4(y) \;=\; \left[\begin{array}{cc} 1 & 0 \\ 0 & 0 \end{array}\right], \;\; \mathbf{a}_2(y) \;=\; \left[\begin{array}{cc} a_{2,1}(y) & 0 \\ 0 & 1 \end{array}\right], \;\; \mathbf{a}_0(y) \;=\; \left[\begin{array}{cc} a_{0,1}(y) & 0 \\ -\mathrm{i}k_z\,U'(y) & a_{0,2}(y) \end{array}\right],$$

$$\begin{aligned} a_{2,1}(y) \;&=\; -\big(2\kappa^2 \,+\, \mathrm{i}k_x R\,U(y) \,+\, \mathrm{i}\omega R\big)\,, \\ a_{0,1}(y) \;&=\; \kappa^4 \,+\, \mathrm{i}k_x\kappa^2 R\,U(y) \,+\, \mathrm{i}k_x R\,U''(y) \,+\, \mathrm{i}\omega\kappa^2 R, \\ a_{0,2}(y) \;&=\; -\big(\kappa^2 \,+\, \mathrm{i}k_x R\,U(y) \,+\, \mathrm{i}\omega R\big)\,,\;\; \kappa^2 \;=\; k_x^2 + k_z^2, \end{aligned}$$

$$\begin{aligned} \mathbf{b}_1 \;&=\; \left[\begin{array}{ccc} \mathrm{i}k_x R & 0 & \mathrm{i}k_z R \\ 0 & 0 & 0 \end{array}\right], \;\; \mathbf{b}_0 \;=\; \left[\begin{array}{ccc} 0 & \kappa^2 R & 0 \\ -\mathrm{i}k_z R & 0 & \mathrm{i}k_x R \end{array}\right], \\ \mathbf{c}_1^T \;&=\; \frac{1}{\kappa^2}\left[\begin{array}{ccc} \mathrm{i}k_x & 0 & \mathrm{i}k_z \\ 0 & 0 & 0 \end{array}\right], \;\; \mathbf{c}_0^T \;=\; \frac{1}{\kappa^2}\left[\begin{array}{ccc} 0 & \kappa^2 & 0 \\ -\mathrm{i}k_z & 0 & \mathrm{i}k_x \end{array}\right], \\ \mathbf{W}_{-1,0} \;&=\; \left[\begin{array}{cccccc} 1 & 0 & 0 & 0 & 0 & 0 \\ 0 & 0 & 0 & 0 & 1 & 0 \end{array}\right]^T, \;\; \mathbf{W}_{1,0} \;=\; \left[\begin{array}{cccccc} 0 & 1 & 0 & 0 & 0 & 0 \\ 0 & 0 & 0 & 0 & 0 & 1 \end{array}\right]^T, \\ \mathbf{W}_{-1,1} \;&=\; \left[\begin{array}{cccccc} 0 & 0 & 1 & 0 & 0 & 0 \\ 0 & 0 & 0 & 0 & 0 & 0 \end{array}\right]^T, \;\; \mathbf{W}_{1,1} \;=\; \left[\begin{array}{cccccc} 0 & 0 & 0 & 1 & 0 & 0 \\ 0 & 0 & 0 & 0 & 0 & 0 \end{array}\right]^T. \end{aligned}$$

The spatial state-space representation of $\mathcal{T}$ is obtained by rewriting (9.56) into a system of first-order differential equations given by (9.12) with the following matrices

$$\mathbf{A}_0 = \begin{bmatrix} 0 & 1 & 0 & 0 & 0 & 0 \\ 0 & 0 & 1 & 0 & 0 & 0 \\ 0 & 0 & 0 & 1 & 0 & 0 \\ -a_{0,1}(y) & 0 & -a_{2,1}(y) & 0 & 0 & 0 \\ 0 & 0 & 0 & 0 & 0 & 1 \\ \mathrm{i}k_z R U'(y) & 0 & 0 & 0 & -a_{0,2}(y) & 0 \end{bmatrix}, \; \mathbf{B}_0 = \begin{bmatrix} 0 & 0 & 0 \\ 0 & 0 & 0 \\ \mathrm{i}k_x R & 0 & \mathrm{i}k_z R \\ 0 & \kappa^2 R & 0 \\ 0 & 0 & 0 \\ -\mathrm{i}k_z R & 0 & \mathrm{i}k_x R \end{bmatrix},$$

$$\mathbf{C}_0 = \frac{1}{\kappa^2} \begin{bmatrix} 0 & \mathrm{i}k_x & 0 & 0 & -\mathrm{i}k_z & 0 \\ \kappa^2 & 0 & 0 & 0 & 0 & 0 \\ 0 & \mathrm{i}k_z & 0 & 0 & \mathrm{i}k_x & 0 \end{bmatrix},$$

$$\mathbf{N}_1 = \begin{bmatrix} 0_{2\times 2} & 0_{2\times 2} & 0_{2\times 1} & 0_{2\times 1} \\ I_{2\times 2} & 0_{2\times 2} & 0_{2\times 1} & 0_{2\times 1} \\ 0_{1\times 2} & 0_{1\times 2} & 0 & 0 \\ 0_{1\times 2} & 0_{1\times 2} & 1 & 0 \end{bmatrix}, \; \mathbf{N}_{-1} = \begin{bmatrix} I_{2\times 2} & 0_{2\times 2} & 0_{2\times 1} & 0_{2\times 1} \\ 0_{2\times 2} & 0_{2\times 2} & 0_{2\times 1} & 0_{2\times 1} \\ 0_{1\times 2} & 0_{1\times 2} & 1 & 0 \\ 0_{1\times 2} & 0_{1\times 2} & 0 & 0 \end{bmatrix},$$

The input-output and state-space representations of the adjoint of the operator $\mathcal{T}$ can be determined using the procedure presented in Section 9.3.2.

9.10 Appendix: Representations of the frequency response operator for the inertialess channel flow of viscoelastic fluids

We next show how to formulate the input-output and spatial state-space representations of the frequency response operator for the inertialess flow of viscoelastic fluids. We begin by rewriting (9.6) into the input-output representation (9.11),

$$\mathcal{T}: \begin{cases} \left(D^{(4)} + a_3(y)\, D^{(3)} + a_2(y)\, D^{(2)} + a_1(y)\, D^{(1)} + a_0(y)\right) \psi(y) \\ = \left(\mathbf{b}_1(y)\, \mathbf{D}^{(1)} + \mathbf{b}_0(y)\right) \mathbf{d}(y), \\ \begin{bmatrix} u \\ v \end{bmatrix} = \left(\mathbf{c}_1\, D^{(1)} + \mathbf{c}_0\right) \psi(y), \\ 0 = \left((\mathbf{W}_{-1,1}\, E_{-1} + \mathbf{W}_{1,1}\, E_1) D^{(1)} + (\mathbf{W}_{-1,0}\, E_{-1} + \mathbf{W}_{1,0}\, E_1)\right) \psi(y), \end{cases} \tag{9.57}$$

where

$$
\begin{aligned}
a_0(y) \;&=\; \frac{k_x^4}{a_4(y)}\left(\beta \,-\, \frac{2\,We^2\,(\beta\,-\,1)\,\big(2We^2\,+\,1\big)}{(\mathrm{i}k_x We\,y\,+\,\mathrm{i}\omega\,+\,1)^3} \,-\, \frac{(\beta\,-\,1)\,\big(2We^2\,+\,1\big)}{\mathrm{i}k_x We\,y\,+\,\mathrm{i}\omega\,+\,1}\right),\\
a_1(y) \;&=\; \frac{1}{a_4(y)}\frac{2\,\mathrm{i}k_x^3\,We\,(\beta\,-\,1)\,(\mathrm{i}\omega\,+\,\mathrm{i}k_x We\,y)\,\big(\mathrm{i}k_x We\,y\,+\,\mathrm{i}\omega\,-\,2We^2\,+\,1\big)}{(\mathrm{i}k_x We\,y\,+\,\mathrm{i}\omega\,+\,1)^3},\\
a_2(y) \;&=\; \frac{1}{a_4(y)}\left(-\,2\,\beta\,k_x^2 \,+\, \frac{2\,k_x^2\,(\beta\,-\,1)\,\big(We^2\,+\,1\big)}{\mathrm{i}k_x We\,y\,+\,\mathrm{i}\omega\,+\,1} \,-\, \frac{4\,(\beta\,-\,1)\,k_x^2\,We^2}{(\mathrm{i}k_x We\,y\,+\,\mathrm{i}\omega\,+\,1)^2}\right.\\
&\qquad\left. +\,\frac{2\,(\beta\,-\,1)\,k_x^2\,We^2}{(\mathrm{i}k_x We\,y\,+\,\mathrm{i}\omega\,+\,1)^3}\right),\\
a_3(y) \;&=\; -\,\frac{1}{a_4(y)}\frac{2\,\mathrm{i}k_x We\,(\beta\,-\,1)\,(\mathrm{i}k_x We\,y\,+\,\mathrm{i}\omega)}{(\mathrm{i}k_x We\,y\,+\,\mathrm{i}\omega\,+\,1)^2}, \quad a_4(y) \;=\; \frac{\beta\,\mathrm{i}k_x We\,y\,+\,\beta\,\mathrm{i}\omega\,+\,1}{\mathrm{i}k_x We\,y\,+\,\mathrm{i}\omega\,+\,1},\\
b_1(y) \;&=\; -\,\frac{1}{\beta\,a_4(y)}, \quad b_0(y) = \frac{\mathrm{i}k_x}{\beta\,a_4(y)}, \quad \mathbf{b}_1(y) = \left[\begin{array}{cc} b_1(y) & 0 \end{array}\right], \quad \mathbf{b}_0(y) = \left[\begin{array}{cc} 0 & b_0(y) \end{array}\right],\\
\mathbf{c}_1 \;&=\; \left[\begin{array}{cc} 1 & 0 \end{array}\right]^T, \quad \mathbf{c}_0 = \left[\begin{array}{cc} 0 & -\mathrm{i}k_x \end{array}\right]^T, \quad \left[\begin{array}{cccc} \mathbf{W}_{-1,1} & \mathbf{W}_{1,1} & \mathbf{W}_{-1,0} & \mathbf{W}_{1,0} \end{array}\right] = \mathbf{I}_{4\times 4}.
\end{aligned}
$$

The spatial state-space representation of $\mathcal{T}$ is obtained by rewriting (9.57) into a system of first-order differential equations. Using the procedure described in 9.7 yields

$$
\mathbf{A}_0 \;=\; \left[\begin{array}{cccc}
0 & 1 & 0 & 0\\
0 & 0 & 1 & 0\\
0 & 0 & 0 & 1\\
-a_0(y) & -a_1(y) & -a_2(y) & -a_3(y)
\end{array}\right], \;
\mathbf{B}_0 = \left[\begin{array}{cc}
0 & 0\\
0 & 0\\
b_1(y) & 0\\
-b_1'(y) - a_3(y)\,b_1(y) & b_0(y)
\end{array}\right],
$$

$$
\mathbf{C}_0 \;=\; \left[\begin{array}{cccc}
0 & 1 & 0 & 0\\
-\mathrm{i}k_x & 0 & 0 & 0
\end{array}\right], \;
\mathbf{N}_{-1} \;=\; \left[\begin{array}{cc}
I_{2\times 2} & 0_{2\times 2}\\
0_{2\times 2} & 0_{2\times 2}
\end{array}\right], \;
\mathbf{N}_1 \;=\; \left[\begin{array}{cc}
0_{2\times 2} & 0_{2\times 2}\\
I_{2\times 2} & 0_{2\times 2}
\end{array}\right].
$$

The input-output and state-space representations of the adjoint of the operator $\mathcal{T}$ can be determined using the procedure described in Section 9.3.2.

9.11 Appendix: Frequency response of an Euler-Bernoulli beam

In this section, we consider an Euler-Bernoulli beam that is clamped at the left end and subject to a boundary actuation $u(t)$ at the other end; see figure 9.10 for an illustration.

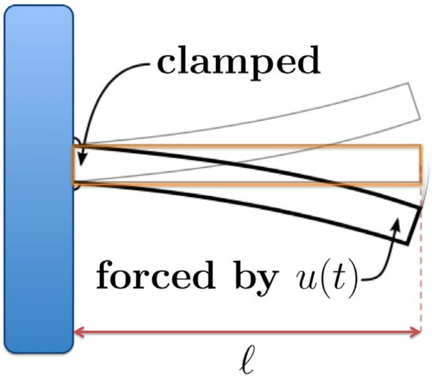

Figure 9.10: An Euler-Bernoulli beam that is clamped at the left end and subject to a boundary actuation at the other end.

The vertical displacement of the beam $\phi(y,t)$ is governed by [166],

$$\mu\,\phi_{tt}(y,t) \;+\; \frac{\alpha\,E_I}{\ell^4}\,\phi_{tyyyy}(y,t) \;+\; \frac{E_I}{\ell^4}\,\phi_{yyyy}(y,t) \;=\; 0, \;\; y \in [\,0,1\,], \tag{9.59a}$$

$$\phi(0,t) \;=\; \phi_y(0,t) \;=\; 0, \tag{9.59b}$$

$$\phi_{yy}(1,t) \;=\; 0, \quad \frac{\alpha\,E_I}{\ell^3}\,\phi_{tyyy}(1,t) \;+\; \frac{E_I}{\ell^3}\,\phi_{yyy}(1,t) \;=\; u(t). \tag{9.59c}$$

Here, the input $u(t)$ denotes the force acting on the tip of the beam, ℓ is the length of the beam, μ is the mass per unit length of the beam, E_I is the flexural stiffness, and α is the Voigt damping factor.

Equation (9.59) can be used to model the movement of a micro-cantilever in atomic force microscopy applications [167] with

$$\begin{array}{rclrcl} \ell & = & 240 \times 10^{-6}\,\text{m}, & \mu & = & 1.88 \times 10^{-7}\,\text{kg/m}, \\ E_I & = & 7.55 \times 10^{-12}\,\text{Nm}^2, & \alpha & = & 5 \times 10^{-8}\,\text{s}. \end{array} \tag{9.60}$$

In contrast to the body of the chapter, the forcing $u(t)$ does not enter to the equation as an additive input but as a boundary condition. We next show how easily frequency response in this case can be computed using `Chebfun`.

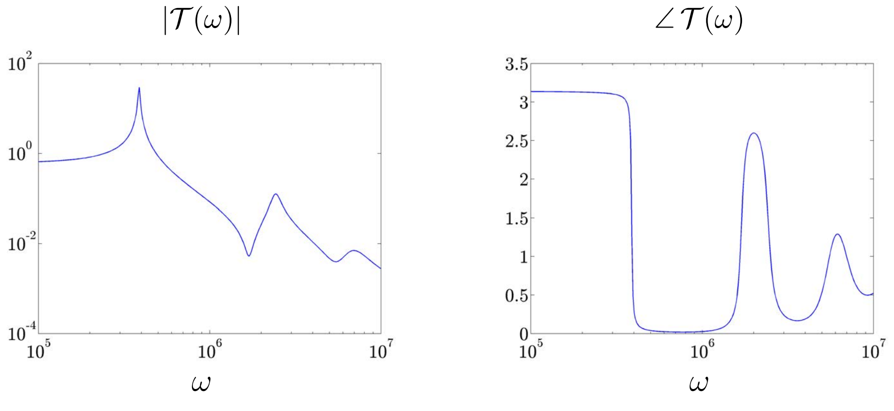

(a) (b)

Figure 9.11: Frequency response of the Euler-Bernoulli beam (9.59)-(9.60) with the output determined by the vertical displacement of the beam at the right end. (a) magnitude of the frequency response $|\mathcal{T}(\omega)|$; (b) phase of the frequency response $\angle\mathcal{T}(\omega)$.

Application of the temporal Fourier transform to (9.59) yields

$$\mathcal{T}(\omega) : \left\{ \begin{array}{l} \dfrac{E_I}{\ell^4}(1 \,+\, \mathrm{i}\,\omega\,\alpha)\; \phi''''(y,\omega) \;-\; \mu\,\omega^2\,\phi(y,\omega) \;=\; 0, \\ \phi(0,\omega) \;=\; \phi'(0,\omega) \;=\; 0, \\ \phi''(1,\omega) \;=\; 0, \quad \dfrac{E_I}{\ell^3}(1 \,+\, \mathrm{i}\,\omega\,\alpha)\; \phi'''(1,\omega) \;=\; u(\omega). \end{array} \right. \tag{9.61}$$

At each ω, the mapping from $u(\omega)$ to $\phi(y,\omega)$ can be obtained by computing the solution to (9.61) with $u(\omega) = 1$ using Chebfun. The energy of the beam is determined by

$$E(\omega) \;=\; \frac{1}{2}\left(\left\langle \phi''(\cdot,\omega), \phi''(\cdot,\omega)\right\rangle \;+\; \omega^2\left\langle \phi(\cdot,\omega), \phi(\cdot,\omega)\right\rangle\right),$$

and it can be simply computed with the aid of Chebun's functions diff and cumsum. On the other hand, if the output is given by the vertical displacement at the right end of the beam, the frequency response is simply determined by the magnitude and phase of the complex number $\phi(1,\omega)$; see figure 9.11.

For parameters given by (9.60), even the use of Chebfun's differential operators to construct

$$\mathcal{A}_0 \;=\; \frac{E_I}{\ell^4}(1 \,+\, \mathrm{i}\,\omega\,\alpha)\, D^{(4)} \;-\; \mu\,\omega^2\, I,$$

with appropriate boundary conditions may lead to unfavorable conditioning of differentiation matrices. This can be alleviated by determining and solving instead the integral form of (9.61). The procedure for achieving this closely follows the method presented in Section 9.4.2. The MATLAB code used for computing the frequency response with integral formulation can be found at www.umn.edu/∼mihailo/software/chebfun-svd/.

References

[1] M. Matsubara and P. H. Alfredsson. Disturbance growth in boundary layers subjected to free-stream turbulence. *J. Fluid Mech*, 430:149–168, 2001.

[2] T. Min, S. M. Kang, J. L. Speyer, and J. Kim. Sustained sub-laminar drag in a fully developed channel flow. *J. Fluid Mech.*, 558:309–318, 2006.

[3] R. Moarref and M. R. Jovanović. Controlling the onset of turbulence by streamwise traveling waves. Part 1: Receptivity analysis. *J. Fluid Mech.*, 663:70–99, November 2010.

[4] T. Yoshino, Y. Suzuki, and N. Kasagi. Drag reduction of turbulence air channel flow with distributed micro sensors and actuators. *J. Fluid Sci. Tech.*, 3(1):137–148, 2008.

[5] A. Groisman and V. Steinberg. Elastic turbulence in a polymer solution flow. *Nature*, 405:53–55, 2000.

[6] A. Groisman and V. Steinberg. Efficient mixing at low reynolds numbers using polymer additives. *Nature*, 410:905 – 908, 2001.

[7] C. F. Li, V. K. Gupta, R. Sureshkumar, and B. Khomami. Turbulent channel flow of dilute polymeric solutions: Drag reduction scaling and an eddy viscosity model. *J. Non-Newtonian Fluid Mech.*, 139:177–189, 2006.

[8] J. C. Del Alamo and J. Jiménez. Spectra of the very large anisotropic scales in turbulent channels. *Phys. Fluids*, 15(6):41–44, 2003.

[9] R. G. Larson. Turbulence without inertia. *Nature*, 405:27–28, 2000.

[10] R. G. Larson. Instabilities in viscoelastic flows. *Rheol. Acta.*, 31:213–263, 1992.

[11] J. Kim, P. Moin, and R. Moser. Turbulence statistics in fully developed channel flow at low Reynolds number. *J. Fluid Mech.*, 177:133–166, 1987.

[12] M. P. Simens, J. Jimenez, S. Hoyas, and Y. Mizuno. A high-resolution code for turbulent boundary layers. *J. Comp. Phys.*, 228:4218–4231, 2009.

[13] J. C. del Álamo, J. Jiménez, Zandonade P., and Moser R. D. Scaling of the energy spectra of turbulent channels. *J. Fluid Mech.*, 500:135–144, 2004.

[14] T. Tsukahara, H. Kawamura, and K. Shingai. DNS of turbulent Couette flow with emphasis on the large-scale structure in the core region. *J. Turbulence*, 7(019), 2006.

[15] S. Hoyas and J. Jimenez. Reynolds number effects on the Reynolds-stress budgets in turbulent channels. *Phys. of Fluids*, 20:796–811, 2008.

[16] R. B. Bird, C. F. Curtiss, R. C. Armstrong, and O. Hassager. *Dynamics of Polymeric Liquids*. Wiley, 1987. vol. 2.

[17] R. G. Larson. *The Structure and Rheology of Complex Fluids*. Oxford University Press, 1999.

[18] A. Groisman and V. Steinberg. Elastic turbulence in curvilinear flows of polymer solutions. *New J. Phys.*, 6:29, 2004.

[19] B. Yesilata. Nonlinear dynamics of a highly viscous and elastic fluid in pipe flow. *Fluid Dyn. Res.*, 31:41–64, 2002.

[20] B. Yesilata. Temporal nature of polymeric flows near circular pipe-exit. *Polym. Plast. Technol. Eng.*, 48(7):723–729, 2009.

[21] D. Bonn, F. Ingremeau, Y. Amarouchene, and H. Kellay. Large velocity fluctuations in small-reynolds-number pipe flow of polymer solutions. *Phys. Rev. E*, 84(4):045301(R), 2011.

[22] E. D. Burger, W. R. Munk, and H. A. Wahl. Flow increase in the Trans Alaska pipeline through use of a polymeric drag-reducing additive. *J. Petrol. Technol.*, 34(2):377–386, 1982.

[23] C. M. White and M. G. Mungal. Mechanics and prediction of turbulent drag reduction with polymer additives. *Annu. Rev. Fluid Mech.*, 40:235–256, 2008.

[24] R. Sureshkumar, A. N. Beris, and R. A. Handler. Direct numerical simulation of the turbulent channel flow of a polymer solution. *Phys. Fluids*, 9:743, 1997.

[25] Y. Dubief, C. M. White, V. E. Terrapon, E. S. G. Shaqfeh, P. Moin, and S. K. Lele. New answers on the interaction between polymers and vortices in turbulent flows. *Flow, Turbulence and Combustion*, 74(4):311–329, 2005.

[26] L. Xi and M. D. Graham. Turbulent drag reduction and multistage transitions in viscoelastic minimal flow units. *J. Fluid Mech.*, 647:421–452, 2010.

[27] P. A. Stone, F. Waleffe, and M. D. Graham. Toward a structural understanding of turbulent drag reduction: nonlinear coherent states in viscoelastic shear flows. *Phys. Rev. Lett.*, 89(20):208301, 2002.

[28] Y. Dubief, C. M. White, V. E. Terrapon, E. S. G. Shaqfeh, P. Moin, and S. K. Lele. On the coherent drag-reducing and turbulence-enhancing behaviour of polymers in wall flows. *J. Fluid Mech.*, 514:271–280, 2004.

[29] C. D. Dimitropoulos, Y. Dubief, E. S. G. Shaqfeh, P. Moin, and S. K. Lele. Direct numerical simulation of polymer-induced drag reduction in turbulent boundary layer flow. *Phys. Fluids*, 17:011705, 2005.

[30] W. Li and M. D. Graham. Polymer induced drag reduction in exact coherent structures of plane poiseuille flow. *Phys. Fluids*, 19:083101, 2007.

[31] L. N. Trefethen and M. Embree. *Spectral and Pseudospectra: the Behavior of Nonnormal Matrices and Operators.* Princeton University Press, 2005.

[32] C. Canuto, M. Y. Hussaini, A. Quarteroni, and T. A. Zang. *Spectral Methods in Fluid Dynamics.* Springer, 1988.

[33] J. P. Boyd. *Chebyshev and Fourier Spectral Methods.* Springer, 1989.

[34] L. N. Trefethen. *Finite Difference and Spectral Methods for Ordinary and Partial Differential Equations.* unpublished text, 1996. available at `http://www.comlab.ox.ac.uk/nick.trefethen/pdetext.html`.

[35] L. N. Trefethen. *Spectral Methods in MATLAB.* SIAM, 2000.

[36] W. Heinrichs. Improved condition number for spectral methods. *Math. Comput.*, 53(187):103–119, 1989.

[37] Lloyd. N. Trefethen, Nicholas Hale, Rodrigo B. Platte, Tobin. A. Driscoll, and Ricardo Pachón. Chebfun version 4. University of Oxford, 2011. `http://www.maths.ox.ac.uk/chebfun/`.

[38] J. F. Gibson. Channelflow: a spectral Navier-Stokes solver in C++. *Tech. Rep.*, 2007. Georgia Institute of Technology, `www.channelflow.org`.

[39] M. R. Jovanović and B. Bamieh. The spatio-temporal impulse response of the linearized Navier-Stokes equations. In *Proceedings of the 2001 American Control Conference*, pages 1948–1953, Arlington, VA, 2001.

[40] M. R. Jovanović. *Modeling, analysis, and control of spatially distributed systems.* PhD thesis, University of California, Santa Barbara, 2004.

[41] P. Moin and J. Kim. Tackling turbulence with supercomputers. *Sci. Am.*, 276(1):46–52, 1997.

[42] R. Peyret. *Spectral Methods for Incompressible Viscous Flow.* Springer, 2002.

[43] J. Kim, P. Moin, and R. Moser. Turbulence statistics in fully developed channel flow at low reynolds number. *J. Fluid Mech.*, 177:133–166, 1987.

[44] L. Kleiser and U. Schumann. Treatment of incompressibility and boundary conditions in 3-D numerical spectral simulations of plane channel flows. In *3rd GAMM Conf. Numerical Methods in Fluid Mech.*, volume 1, pages 165–173, 1980.

[45] M. Crouzeix. Une méthode multipas implicite-explicite pour l'approximation des équations d'évolution paraboliques. *Numer. Math.*, 35(3):257–276, 1980.

[46] I. Marusic, D. D. Joseph, and K. Mahesh. Laminar and turbulent comparisons for channel flow and channel control. *J. Fluid Mech.*, 570:467–477, 2007.

[47] J. Hœpffner and K. Fukagata. Pumping or drag reduction? *J. Fluid Mech.*, 635:171–187, 2009.

[48] T. R. Bewley. A fundamental limit on the balance of power in a transpiration-controlled channel flow. *J. Fluid Mech.*, 632:443–446, 2009.

[49] K. Fukagata, K. Sugiyama, and N. Kasagi. On the lower bound of net driving power in controlled duct flows. *Physica D: Nonlinear Phenomena*, 238(13):1082–1086, 2009.

[50] M. Quadrio and P. Ricco. Critical assessment of turbulent drag reduction through spanwise wall oscillations. *J. Fluid Mech.*, 521(-1):251–271, 2004.

[51] I. G. Currie. *Fundamental mechanics of fluids.* CRC Press, 2003.

[52] P.J̃. Schmid and D.S̃. Henningson. *Stability and Transition in Shear Flows.* Springer-Verlag, 2001.

[53] M. S. Chong, A. E. Perry, and B. J. Cantwell. A general classification of three-dimensional flow fields. *Phys. Fluid A*, 2:765–777, 1990.

[54] N. D. Sandham and L. Kleiser. The late stages of transition to turbulence in channel flow. *J. Fluid Mech.*, 245:319–348, 1992.

[55] H. M. Blackburn, N. N. Mansour, and B. J. Cantwell. Topology of fine-scale motions in turbulent channel flow. *J. Fluid Mech.*, 310:269–292, 1996.

[56] T. R. Bewley, P. Moin, and R. Temam. DNS-based predictive control of turbulence: an optimal benchmark for feedback algorithms. *J. Fluid Mech.*, 447:179–225, 2001.

[57] X. Wu and P. Moin. Direct numerical simulation of turbulence in a nominally zero-pressure-gradient flat-plate boundary layer. *J. Fluid Mech.*, 630:5–41, 2009.

[58] A. E. Perry and M. S. Chong. A description of eddying motions and flow patterns using critical-point concepts. *Ann. Rev. Fluid Mech.*, 19:125–155, 1987.

[59] M. S. Chong, J. Soria, A. E. Perry, J. Chacin, B. J. Cantwell, and Y. Na. Turbulence structures of wall-bounded shear flow found using DNS data. *J. Fluid Mech.*, 357:225–247, 1998.

[60] U. Brosa. Turbulence without strange attractor. *J. Stat. Phys.*, 55(5):1303–1312, 1989.

[61] S. Grossmann. The onset of shear flow turbulence. *Rev. Mod. Phys.*, 72:603–618, 2000.

[62] B. Hof, J. Westerweel, T. M. Schneider, and B. Eckhardt. Finite lifetime of turbulence in shear flows. *Nature*, 443(7):59–62, 2006.

[63] D. Borrero-Echeverry, M. F. Schatz, and R. Tagg. Transient turbulence in Taylor-Couette flow. *Phys. Rev. E*, 81(2):25301, 2010.

[64] M. R. Jovanović, R. Moarref, and D. You. Turbulence suppression in channel flows by means of a streamwise traveling wave. In *Proceedings of the 2006 Summer Program*, pages 481–494, Center for Turbulence Research, Stanford University/NASA, 2006.

[65] M. R. Jovanović. Turbulence suppression in channel flows by small amplitude transverse wall oscillations. *Phys. Fluids*, 20(1):014101 (11 pages), January 2008.

[66] A. Scotti and U. Piomelli. Numerical simulation of pulsating turbulent channel flow. *Phys. Fluids*, 13(5):1367–1384, 2001.

[67] F. Waleffe. Exact coherent structures in channel flow. *J. Fluid Mech.*, 435:93–102, 2001.

[68] J. Jiménez, G. Kawahara, M. P. Simens, M. Nagata, and M. Shiba. Characterization of near-wall turbulence in terms of equilibrium and "bursting" solutions. *Phys. Fluids*, 17(1):015105, 2005.

[69] R. R. Kerswell. Recent progress in understanding the transition to turbulence in a pipe. *Nonlinearity*, 18:R17–R44, 2005.

[70] H. Choi, P. Moin, and J. Kim. Active turbulence control for drag reduction in wall-bounded flows. *J. Fluid Mech.*, 262:75–110, 1994.

[71] H. Choi, R. Temam, P. Moin, and J. Kim. Feedback control for unsteady flow and its application to the stochastic Burgers equation. *J. Fluid Mech.*, 253:509–543, 1993.

[72] T. Bewley and P. Moin. Optimal control of turbulent channel flows. *Active Control of Vibration and Noise, ASME-DE*, 75, 1994.

[73] J. Kim and T. R. Bewley. A linear systems approach to flow control. *Annu. Rev. Fluid Mech.*, 39:383–417, 2007.

[74] K. M. Butler and B. F. Farrell. Three-dimensional optimal perturbations in viscous shear flow. *Phys. Fluids A*, 4:1637–1650, 1992.

[75] L. N. Trefethen, A. E. Trefethen, S. C. Reddy, and T. A. Driscoli. Hydrodynamic stability without eigenvalues. *Science*, 261:578–584, 1993.

[76] B. Bamieh and M. Dahleh. Energy amplification in channel flows with stochastic excitations. *Phys. Fluids*, 13:3258–3269, 2001.

[77] M. R. Jovanović and B. Bamieh. Componentwise energy amplification in channel flows. *J. Fluid Mech.*, 534:145–183, July 2005.

[78] B. K. Lieu, R. Moarref, and M. R. Jovanović. Controlling the onset of turbulence by streamwise traveling waves. Part 2: Direct numerical simulations. *J. Fluid Mech.*, 663:100–119, November 2010.

[79] M. Högberg, T.R̃. Bewley, and D.S̃. Henningson. Linear feedback control and estimation of transition in plane channel flow. *J. Fluid Mech.*, 481:149–175, 2003.

[80] M. Fardad, F. Lin, and M. R. Jovanović. On the optimal design of structured feedback gains for interconnected systems. In *Proceedings of the 48th IEEE Conference on Decision and Control*, pages 978–983, Shanghai, China, 2009.

[81] F. Lin, M. Fardad, and M. R. Jovanović. Augmented Lagrangian approach to design of structured optimal state feedback gains. *IEEE Trans. Automat. Control*, 56(12):2923–2929, December 2011.

[82] K. Zhou, J. C. Doyle, and K. Glover. *Robust and Optimal Control*. Prentice Hall, 1996.

[83] J. A. C. Weideman and S. C. Reddy. A MATLAB differentiation matrix suite. *ACM T. Math. Software*, 26(4):465–519, 2000.

[84] A. Hanifi, P.J. Schmid, and D.S. Henningson. Transient growth in compressible boundary layer flow. *Phys. Fluids*, 8(3):826–837, 1996.

[85] B. Bamieh, F. Paganini, and M.Ã. Dahleh. Distributed control of spatially invariant systems. *IEEE Transactions on Automatic Control*, 47(7):1091–1107, July 2002.

[86] S. Boyd and L. Vandenberghe. *Convex Optimization.* Cambridge University Press, 2004.

[87] B. F. Farrell and P. J. Ioannou. Stochastic forcing of the linearized Navier-Stokes equations. *Phys. Fluids A*, 5:2600–2609, 1993.

[88] S.C̃. Reddy and D.S̃. Henningson. Energy growth in viscous channel flows. *J. Fluid Mech.*, 252:209–238, 1993.

[89] P. J. Schmid. Nonmodal stability theory. *Annu. Rev. Fluid Mech.*, 39:129–162, 2007.

[90] P. S. Klebanoff, K. D. Tidstrom, and L. M. Sargent. The three-dimensional nature of boundary-layer instability. *J. Fluid Mech.*, 12:1–34, 1962.

[91] P. Andersson, M. Berggren, and D. S. Henningson. Optimal disturbances and bypass transition in boundary layers. *Phys. of Fluids*, 11:134–150, 1999.

[92] J. Jiménez and P. Moin. The minimal flow unit in near-wall turbulence. *J. Fluid Mech.*, 225:213–240, 1991.

[93] J. M. Hamilton, J. Kim, and F. Waleffe. Regeneration mechanisms of near-wall turbulence structures. *J. Fluid Mech.*, 287:317–348, 1995.

[94] J. Jiménez and A. Pinelli. The autonomous cycle of near-wall turbulence. *J. Fluid Mech.*, 389:335–359, 1999.

[95] K. J. Kim and R. J Adrian. Very large scale motion in the outer layer. *Phys. of Fluids*, 11(2):417–422, 1999.

[96] J. F. Morrison, B. J. McKeon, W. Jiang, and A. J. Smits. Scaling of the streamwise velocity component in turbulent pipe flow. *J. Fluid Mech.*, 508:99–131, 2004.

[97] M. Guala, S. E. Hommema, and R. J. Adrian. Large-scale and very-large-scale motions in turbulent pipe flow. *J. Fluid Mech.*, 554:521–542, 2006.

[98] N. Hutchins and I. Marusic. Evidence of very long meandering structures in the logarithmic region of turbulent boundary layers. *J. Fluid Mech.*, 579:1–28, 2007.

[99] N. Hutchins and I. Marusic. Large-scale influences in near-wall turbulence. *Phil. Trans. Royal Soc. London A*, 365:647–664, 2007.

[100] R. Mathis, N. Hutchins, and I. Marusic. Large-scale amplitude modulation of the small-scale structures of turbulent boundary layers. *J. Fluid Mech.*, 628:311–337, 2009.

[101] D. F. Gayme, B. J. McKeon, A. Papachristodoulou, B. Bamieh, and J. C. Doyle. Streamwise constant model of turbulence in plane Couette flow. *J. Fluid Mech.*, 665:99–119, 2010.

[102] B. Farrell and P. Ioannou. Dynamics of streamwise rolls and streaks in turbulent wall-bounded shear flow. *J. Fluid Mech.*, 708:149–196, 2012.

[103] D. F. Gayme. *A Robust Control Approach to Understanding Nonlinear Mechanisms in Shear Flow Turbulence.* PhD thesis, Caltech, Pasadena, CA, USA, 2010.

[104] J. F. Gibson. Channelflow: A spectral Navier-Stokes simulator in C++. Technical report, U. New Hampshire, 2012. `Channelflow.org`.

[105] R. Peyret. *Spectral Methods for Incompressible Flows.* Springer-Verlag, 2002.

[106] C. Canuto, M.Y. Hussaini, A. Quateroni, and T.A. Zhang. *Spectral Methods in Fluid Dynamics.* Springer-Verlag, 1988.

[107] T. A. Zang and M. Y. Hussaini. Numerical experiments on subcritical transition mechanism. In *AIAA, Aerospace Sciences Meeting*, Reno, NV, 1985.

[108] P. E. Arratia, C. C. Thomas, J. Diorio, and J. P. Gollub. Elastic instabilities of polymer solutions in cross-channel flow. *Phys. Rev. Lett.*, 96:144502:1–4, 2006.

[109] J. M. Ottino and S. Wiggins. Introduction: mixing in microfluidics. *Phil. Trans. R. Soc. Lond. A*, 362:923–935, 2004.

[110] R. G. Larson, E. S. G. Shaqfeh, and S. J. Muller. A purely elastic instability in Taylor-Couette flow. *J. Fluid Mech.*, 218:573–600, 1990.

[111] L. Pan, A. Morozov, and P. Arratia. Nonlinear elastic instabilities in parallel shear flows. In *Bulletin of the American Physical Society*, Baltimore, MD, 2011.

[112] B. Meulenbroek, C. Storm, A. N. Morozov, and W. van Saarloos. Weakly nonlinear subcritical instability of visco-elastic poiseuille flow. *J. Non-Newtonian Fluid Mech.*, 116:235–268, 2004.

[113] A. N. Morozov and W. van Saarloos. Subcritical finite-amplitude solutions for plane couette flow of viscoelastic fluids. *Phys. Rev. Lett.*, 95:024501, 2005.

[114] N. Hoda, M. R. Jovanović, and S. Kumar. Energy amplification in channel flows of viscoelastic fluids. *J. Fluid Mech.*, 601:407–424, April 2008.

[115] N. Hoda, M. R. Jovanović, and S. Kumar. Frequency responses of streamwise-constant perturbations in channel flows of Oldroyd-B fluids. *J. Fluid Mech.*, 625:411–434, April 2009.

[116] M. R. Jovanović and S. Kumar. Transient growth without inertia. *Phys. Fluids*, 22(2):023101 (19 pages), February 2010.

[117] M. R. Jovanović and S. Kumar. Nonmodal amplification of stochastic disturbances in strongly elastic channel flows. *J. Non-Newtonian Fluid Mech.*, 166(14-15):755–778, August 2011.

[118] M. D. Chilcott and J. M. Rallison. Creeping flow of dilute polymer solutions past cylinders and spheres. *J. Non-Newtonian Fluid Mech.*, 29:381–432, 1988.

[119] S. Boyd, V. Balakrishnan, and P. Kabamba. A bisection method for computing the h_∞ norm of a transfer matrix and related problems. *Math. Control Signal.*, 2(3):207–219, 1989.

[120] N. A. Bruinsma and M. Steinbuch. A fast algorithm to compute the H_∞-norm of a transfer function matrix. *Syst. Control Lett.*, 14:287–293, 1990.

[121] B. K. Lieu and M. R. Jovanović. Computation of frequency responses for linear time-invariant PDEs on a compact interval. *J. Comput. Phys.*, 250:246–269, October 2013.

[122] W. Schoppa and F. Hussain. Coherent structure generation in near-wall turbulence. *J. Fluid Mech.*, 453:57–108, 2002.

[123] F. Waleffe. On a self-sustaining process in shear flows. *Phys. Fluids*, 9:883, 1997.

[124] B. K. Lieu, M. R. Jovanovic, and S. Kumar. Worst-case amplification of disturbances in inertialess flows of viscoelastic fluids. In *Preprints of the 18th IFAC World Congress*, pages 14458–14463, Milano, Italy, 2011.

[125] R. Kupferman. On the linear stability of plane Couette flow for an Oldroyd-B fluid and its numerical approximation. *J. Non-Newtonian Fluid Mech.*, 127(2-3):169–190, 2005.

[126] M. D. Graham. Effect of axial flow on viscoelastic Taylor-Couette instability. *J. Fluid Mech.*, 360(1):341–374, 1998.

[127] P. V. Kokotović, H. K. Khalil, and J. O'Reilly. *Singular Perturbation Methods in Control: Analysis and Design.* SIAM, 1999.

[128] P. S. Virk. Drag reduction fundamentals. *AIChE J.*, 21:625 – 656, 1975.

[129] J. W. Hoyt. The effect of additives on fluid friction. *Trans. ASME D: J. Basic Eng.*, 94:258–285, 1972.

[130] J. L. Lumley. Drag reduction by additives. *Annu. Rev. Fluid Mech.*, 1(1):367–384, 1969.

[131] J. L. Lumley. Drag reduction in turbulent flow by polymer additives. *J. Polym. Sci. Macromol. Rev.*, 7(1):263–290, 1973.

[132] F. T. M. Nieuwstadt and J. M. J. den Toonder. Drag reduction by additives - a review. *CISM Courses and Lectures*, pages 269–316, 2001.

[133] C. M. White, V. S. R. Somandepalli, and M. G. Mungal. The turbulence structure of drag-reduced boundary layer flow. *Exp. Fluids*, 36(1):62–69, 2004.

[134] P. K. Ptasinski, F. T. M. Nieuwstadt, B. H. A. A. Van den Brule, and M. A. Hulsen. Experiments in turbulent pipe flow with polymer additives at maximum drag reduction. *Flow Turbul. Combust.*, 66(2):159–182, 2001.

[135] M. D. Warholic, D. K. Heist, M. Katcher, and T. J. Hanratty. A study with particle-image velocimetry of the influence of drag-reducing polymers on the structure of turbulence. *Exp. Fluids*, 31(5):474–483, 2001.

[136] Y. Hou, V. S. R. Somandepalli, and M. G. Mungal. A technique to determine total shear stress and polymer stress profiles in drag reduced boundary layer flows. *Exp. Fluids*, 40(4):589–600, 2006.

[137] J. E. Koskie and W. G. Tiederman. Polymer drag reduction of a zero pressure gradient boundary layer. *Phys. Fluids A*, 3:2471–73, 1991.

[138] C. D. Dimitropoulos, R. Sureshkumar, and A. N. Beris. Direct numerical simulation of viscoelastic turbulent channel flow exhibiting drag reduction: effect of the variation of rheological parameters. *J. Non-Newtonian Fluid Mech.*, 79:433 – 468, 1998.

[139] T. Min, J. Y. Yoo, H. Choi, and D. D. Joseph. Drag reduction by polymer additives in a turbulent channel flow. *J. Fluid Mech.*, 486:213–238, 2003.

[140] R. Moarref and M. R. Jovanović. Model-based design of transverse wall oscillations for turbulent drag reduction. *J. Fluid Mech.*, 707:205–240, September 2012.

[141] J. C. Del Alamo and J. Jimenez. Linear energy amplification in turbulent channels. *J. Fluid Mech.*, 559:205–213, 2006.

[142] C. Cossu, G. Pujals, and S. Depardon. Optimal transient growth and very large-scale structures in turbulent boundary layers. *J. Fluid Mech.*, 619:79–94, 2009.

[143] G. Pujals, M. García-Villalba, C. Cossu, and S. Depardon. A note on optimal transient growth in turbulent channel flows. *Phys. Fluids*, 21(1):015109, 2009.

[144] B. K. Lieu and M. R. Jovanović. Analysis of drag reduction by polymers in a turbulent channel flow. In *Proceedings of the 2012 Summer Program*, pages 65–74, Center for Turbulence Research, Stanford University/NASA, 2012.

[145] K. D. Housiadas and A. N. Beris. An efficient fully implicit spectral scheme for DNS of turbulent viscoelastic channel flow. *J. Non-Newtonian Fluid Mech.*, 122:243 – 262, 2004.

[146] R. Sureshkumar and A. N. Beris. Effect of artificial stress diffusivity on the stability of numerical calculations and the flow dynamics of time-dependent viscoelastic flows. *J. Non-Newtonian Fluid Mech.*, 60:53 – 80, 1995.

[147] W. D. McComb. *The Physics of Fluid Turbulence.* Oxford University Press, 1991.

[148] P. A. Durbin and B. A. P. Reif. *Theory and Modeling of Turbulent Flows.* Wiley, 2000.

[149] P. A. Durbin. Separated flow computations with the k-ϵ-v^2 model. *AIAA Journal*, 33(4):659–664, 1995.

[150] F. T. Pinho, C. F. Li, B. A. Younis, and R. Sureshkumar. A low reynolds number turbulence closure for viscoelastic fluids. *J. Non-Newtonian Fluid Mech.*, 154:89–108, 2008.

[151] G. Iaccarino, E. S. G. Shaqfeh, and Y. Dubief. Reynolds-averaged modeling of polymer drag reduction in turbulent flows. *J. Non-Newtonian Fluid Mech.*, 165:376–384, 2010.

[152] W. C. Reynolds and W. G. Tiederman. Stability of turbulent channel flow with application to malkus's theory. *J. Fluid Mech.*, 27(2):253–272, 1967.

[153] J. C. Del Alamo, J. Jiménez, P. Zandonade, and R. D. Moser. Scaling of the energy spectra of turbulent channels. *J. Fluid Mech.*, 500(1):135–144, 2004.

[154] M. R. Jovanović and T. T. Georgiou. Reproducing second order statistics of turbulent flows using linearized navier-stokes equations with forcing. *Bulletin of the American Physical Society*, 55, 2010.

[155] M. R. Jovanović and B. Bamieh. Modelling flow statistics using the linearized Navier-Stokes equations. In *Proceedings of the 40th IEEE Conference on Decision and Control*, pages 4944–4949, Orlando, FL, 2001.

[156] P. S. Virk, E. W. Merril, H. S. Mickley, K. A. Smith, and E. L. Mollo-Christensen. The tom's phenomenon: turbulent pipe flow of dilute polymer solutions. *J. Fluid Mech.*, 20:22–30, 1967.

[157] A. Zare, M. R. Jovanović, and T. T. Georgiou. Completion of partially known turbulent flow statistics. In *Proceedings of the 2014 American Control Conference*, pages 1680–1685, Portland, OR, 2014.

[158] B. K. Lieu, M. R. Jovanović, and S. Kumar. Worst-case amplification of disturbances in inertialess Couette flow of viscoelastic fluids. *J. Fluid Mech.*, 723:232–263, May 2013.

[159] M. Renardy and R. C. Rogers. *An Introduction to Partial Differential Equations.* Springer, 2004.

[160] A. W. Naylor and G. R. Sell. *Linear Operator Theory in Engineering and Science.* Springer, 2000.

[161] I. Gohberg and M. A. Kaashoek. Time varying linear systems with boundary conditions and integral operators. I. The transfer operator and its properties. *Integral Equations and Operator Theory*, 7(3):325–391, 1984.

[162] P. E. Crouch, F. Lamnabhi-Lagarrigue, and A. J. Van der Schaft. Adjoint and Hamiltonian input-output differential equations. *IEEE T. Automat. Contr.*, 40(4):603–615, 1995.

[163] M. R. Jovanović and B. Bamieh. A formula for frequency responses of distributed systems with one spatial variable. *Syst. Control Lett.*, 55(1):27–37, January 2006.

[164] L. Greengard. Spectral integration and two-point boundary value problems. *SIAM J. Numer. Anal.*, 28(4):1071–1080, 1991.

[165] T. A. Driscoll. Automatic spectral collocation for integral, integro-differential, and integrally reformulated differential equations. *J. Comput. Phys.*, 229:5980–5998, 2010.

[166] R. W. Clough and J. Penzien. *Dynamics of Structures.* McGraw-Hill, 1993.

[167] M. Fardad, M. R. Jovanović, and M. V. Salapaka. Damping mechanisms in dynamic mode atomic force microscopy applications. In *Proceedings of the 2009 American Control Conference*, pages 2272–2277, Saint Louis, MO, 2009.